

**METAL-OXIDE NANOCOMPOSITE FOR TUNABLE PHYSICAL  
PROPERTIES**

by

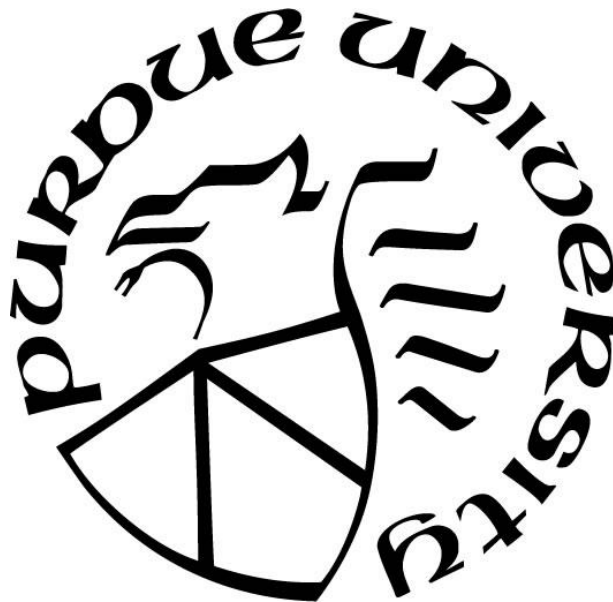
**Shikhar Misra**

**A Dissertation**

*Submitted to the Faculty of Purdue University*

*In Partial Fulfillment of the Requirements for the degree of*

**Doctor of Philosophy**



School of Materials Engineering

West Lafayette, Indiana

August 2020

**THE PURDUE UNIVERSITY GRADUATE SCHOOL**  
**STATEMENT OF COMMITTEE APPROVAL**

**Dr. Haiyan Wang, Chair**

School of Materials Engineering

**Dr. John Blendell**

School of Materials Engineering

**Dr. Kenneth H. Sandhage**

School of Materials Engineering

**Dr. Zhihong Chen**

School of Electrical and Computer Engineering

**Approved by:**

Dr. David Bahr

*Dedicated to my family and friends*

## ACKNOWLEDGMENTS

A PhD is a long journey and it could not be done without the help and support of many people. The people around me have helped me grow as a researcher and as a person and I would like to thank everyone who contributed to my progress.

I would like to sincerely thank my advisor, Dr. Haiyan Wang, for her professional advice and guidance throughout my Ph.D. study. I have benefited a lot from her insightful suggestions, extensive knowledge and passion for science. She provided me with enough freedom to pursue independent projects that I was interested in along with very useful research and discussion. She is one of the most energetic people I have ever met who helped me develop passion and interest about thin film science and technology. I also appreciate her great care, encouragement, support and trust for my research and life. Working with Dr. Wang has made me more experienced, independent, hard-working and mature. I feel grateful to work in her group, and really appreciate all her advice both in academics and about life.

I would like to thank my thesis committee: Dr. John Blendell, Dr. Kenneth Sandhage and Dr. Zhihong Chen for their valuable suggestions and guidance in my research. Dr. Blendell's class on tensor mathematics and Dr. Sandhage's class on thermodynamics established the fundamental understanding of materials science, which I ended up using in my research and beyond. Collaborating with Dr. Chen also taught me about the several challenges in thin film growth. I really appreciate their time and effort in helping me on my research projects.

I also want to thank the current and past group members: Bethany, Bruce, Di, Han, Hongyi, Jie, Jijie, Juanjuan, Juncheng, Leigang, Matias, Meng, Robynne, Xin, Xing, Xingyao, Xuejing, Zhimin, Zihao for their collaboration as well as valuable discussion, which helped a lot throughout my research. Special thanks to Leigang for being my mentor in my first year and teaching me useful and important skills such as thin film deposition, characterization techniques and making publishable figures. I also want to thank them for the friendship, support and collaboration during my study. I also like to acknowledge the faculty and staff in the Materials Engineering department: Donna Bystorm, Rosemary Son, Stacey Coar, and Vicki Cline for help with the administrative work.

Thanks to all my friends at Purdue, US and India who have supported me throughout my PhD journey and made this a memorable journey. Thanks are due to Shivam, Ankit, Tapaswi,

Jaehun, Prabhat, Vivek, Shashwat, Mridul, Milind, Abhishek, Amogh, Krishna, Debashis, Kei, Jonova, Alejandro, Angel, Nes, Saaketh, Ankit, Abhinav, Aditya, Salman, and Harkirat.

Lastly, and most importantly, I would like to thank my parents Shri Ram Mohan Misra and Smt Anjula Misra for their unlimited unconditional love, care and encouragement. Thanks to my brother, Dr. Prakhar Misra for constantly motivating me through my tough times and for the important guidance and support throughout my PhD journey and life.

# TABLE OF CONTENTS

LIST OF TABLES .....	9
LIST OF FIGURES .....	10
NOMENCLATURE .....	17
ABSTRACT.....	19
1. INTRODUCTION .....	20
1.1 Epitaxial growth of thin films .....	20
1.1.1 Growth thermodynamics for single phase nanocrystalline thin film.....	20
1.1.2 Growth mechanism of two-phase nanocomposites .....	22
Nucleation and growth .....	22
Spinodal Decomposition .....	26
1.2 Morphological Control in thin films .....	28
1.2.1 Interfacial strain .....	29
1.2.2 Substrate selection .....	31
1.2.3 Relative composition of the phases .....	31
1.2.4 Surface energy of phases with each other and with substrate .....	32
1.3 Vertically Aligned Nanocomposite (VAN) thin films.....	33
1.3.1 Overview of VAN thin films .....	33
1.3.2 Strain Engineering in VAN thin films .....	35
1.3.3 Advantages of VAN thin films .....	36
1.4 Materials Systems .....	37
1.4.1 Titanium Dioxide (TiO <sub>2</sub> ) .....	37
1.4.2 Barium Titanate (BaTiO <sub>3</sub> ) .....	38
1.4.3 Zinc Oxide (ZnO) .....	40
1.5 Functionality .....	41
1.5.1 Ferroelectricity.....	41
1.5.2 Plasmonics .....	44
1.5.3 Hyperbolic Metamaterials .....	48
1.6 Self-assembled metal-dielectric nanocomposite thin films .....	52
1.6.1 Particle in Matrix and Vertically Aligned Nanocomposite .....	55

1.6.2	Strain Compensation Model .....	57
	Linear strain compensation model .....	58
	Areal strain compensation model .....	59
1.6.3	Case Studies .....	61
1.7	Research Motivation .....	64
2.	RESEARCH METHODOLOGY .....	66
2.1	Pulsed Laser Deposition .....	66
2.2	Structural Characterization .....	68
	2.2.1 X-Ray Diffraction .....	68
	2.2.2 Transmission Electron Microscopy .....	69
	2.2.3 Atomic Force Microscopy .....	71
2.3	Optical Characterization .....	73
	2.3.1 UV-Vis-NIR Spectroscopy .....	73
	2.3.2 Ellipsometer .....	74
3.	TAILORABLE AU NANOPARTICLES EMBEDDED IN EPITAXIAL TiO <sub>2</sub> THIN FILMS FOR TUNABLE OPTICAL PROPERTIES .....	76
	3.1 Overview .....	76
	3.2 Introduction .....	76
	3.3 Results and Discussion .....	78
	3.4 Conclusion .....	95
	3.5 Experimental Section .....	96
4.	SELF-ASSEMBLED ORDERED THREE-PHASE Au-BaTiO <sub>3</sub> -ZnO VERTICALLY ALIGNED NANOCOMPOSITES ACHIEVED BY A TEMPLATING METHOD .....	98
	4.1 Overview .....	98
	4.2 Introduction .....	98
	4.3 Results and Discussion .....	101
	4.4 Conclusion .....	118
	4.5 Experimental Section .....	119
5.	MORPHOLOGICAL CONTROL OF THE SELF-ASSEMBLED THREE-PHASE Au-BaTiO <sub>3</sub> -ZnO METAMATERIAL FOR TUNABLE OPTICAL PROPERTIES .....	121
	5.1 Overview .....	121

5.2	Introduction.....	121
5.3	Results and Discussion .....	123
5.4	Conclusion .....	134
5.5	Experimental Details.....	134
6.	STABILITY STUDY OF SELF-ASSEMBLED ORDERED THREE PHASE Au-BaTiO <sub>3</sub> -ZnO BY IN-SITU HEATING IN TRANSMISSION ELECTRON MICROSCOPY .....	136
6.1	Overview.....	136
6.2	Introduction.....	136
6.3	Results and Discussion .....	139
6.4	Conclusions.....	150
6.5	Experimental Details.....	151
7.	SUMMARY AND FUTURE WORK .....	152
	REFERENCES .....	154
	PUBLICATIONS.....	175

## LIST OF TABLES

Table 1-1: List of VAN systems grouped by their functionalities.....	35
Table 3-1. Quantitative analysis of the XPS spectrum .....	91

## LIST OF FIGURES

Figure 1-1: Transition energy for the transformation of TiO <sub>2</sub> anatase phase to TiO <sub>2</sub> rutile phase on (a) (001) LAO substrate and (b) (1-102) Al <sub>2</sub> O <sub>3</sub> substrate. Inset shows the enlarged graph near the transition point <sup>1</sup> .....	22
Figure 1-2: Schematic showing various processes involved in nucleation and growth on surfaces .....	24
Figure 1-3: Schematic showing different growth modes: (a) Volmer-Weber (VW) (island) growth, (b) Frank-Van der Merwe (FM) (multilayer) growth and (c) Stranski-Krastanov (SK) growth ..	24
Figure 1-4: Film nucleation process on the substrate .....	25
Figure 1-5: Cross-section and planar TEM images showing the checkerboard structure in Bi <sub>0.5</sub> Sm <sub>0.5</sub> FeO <sub>3</sub> thin films <sup>8</sup> .....	27
Figure 1-6: Cross-section TEM images (a,b), EDS imaging (c,d) and HAADF-STEM images showing the TiO <sub>2</sub> -VO <sub>2</sub> phase-separated heterostructure on (001) (a,c,e) and (100) (b,d,f) oriented rutile TiO <sub>2</sub> substrates <sup>7</sup> .....	28
Figure 1-7: (a) Plan-view, (b) STEM and (c) HRTEM images of STO <sub>0.5</sub> :MgO <sub>0.5</sub> VAN. (d) shows FFT of image (c) <sup>12</sup> .....	30
Figure 1-8: (a) HRSTEM image showing interface of BFMO layered structure with BFMO interlayer <sup>14</sup> and (b) HRTEM showing the interface of highly strained BFMO film <sup>15</sup> .....	30
Figure 1-9: Temperature-strain phase diagram for BaTiO <sub>3</sub> <sup>17</sup> .....	31
Figure 1-10: Morphology of BiFeO <sub>3</sub> -CoFe <sub>2</sub> O <sub>4</sub> nanocomposite with (a-d) CFO pillars) having (001) end facet with the film grown on (001) STO substrate and (e-h) BFO pillars having (111) end facet with the film grown on (111) STO substrate <sup>18</sup> .....	32
Figure 1-11: Plan-view TEM images of LSMO-CeO <sub>2</sub> VAN with CeO <sub>2</sub> pillars on (a) as-received and (b,c) annealed STO (001) substrate <sup>22</sup> .....	33
Figure 1-12: 1-3 type approach. CFO nanopillars embedded in BTO matrix show enhanced ferroelectric properties <sup>13</sup> .....	34
Figure 1-13: Schematic of the crystal structure of TiO <sub>2</sub> showing the rutile and anatase phase <sup>58,59</sup> .....	38
Figure 1-14: Schematic of the BaTiO <sub>3</sub> crystal structure showing the phase transition from the tetragonal to cubic phase .....	39
Figure 1-15: Schematic of the crystal structure of ZnO showing its three phases: rocksalt, zinc blende, and wurtzite <sup>65</sup> .....	40
Figure 1-16: Schematic of the BaTiO <sub>3</sub> crystal structure showing the tetragonal distortion on applying voltage .....	42

Figure 1-17. (a) Non-switchable ferroelectric domains observed using DF-TEM. STEM-HAADF image shows the displacement of atoms and ferroelectric hysteresis loop (b) Mapping of electrostatic potential and electric field mapping <sup>72</sup> .....	43
Figure 1-18: Comparison of the variation of <i>a</i> and <i>c</i> lattice parameters of pure BaTiO <sub>3</sub> and BaTiO <sub>3</sub> :Sm <sub>2</sub> O <sub>3</sub> composite as function of temperature <sup>27</sup> .....	44
Figure 1-19: Surface plasmon resonance in gold nanoparticle <sup>73</sup> .....	45
Figure 1-20: (a) Schematic showing semiconductor photocatalysis in the presence and absence of plasmon (b) Mechanism of plasmon-induced charge transfer <sup>80</sup> (c) Hydrogen and oxygen gas evolution in the presence and absence of plasmon <sup>78</sup> .....	48
Figure 1-21: Iso-frequency curves for (a) metal, (b) isotropic dielectric, (c) hyperbolic material with one sheet, and (d) hyperbolic material with two sheets .....	50
Figure 1-22: Schematic of the hyperlens consisting of alternating Ag/Al <sub>2</sub> O <sub>3</sub> multilayers and the simulation of sub-diffraction-limited optics <sup>84</sup> .....	51
Figure 1-23. Overview of the metal-dielectric nanocomposites. Schematic illustration of the (a1) top-down design/fabrication techniques showing the nanoimprint lithography, focused ion beam and electron-beam lithography as labeled, and (a2) bottom-up techniques showing the self-assembly, templated self-assembly, particle-in-matrix and anodized alumina oxide template method. The various applications of the metal-dielectric nanocomposites are highlighted in (b). They can be used as metamaterials, multiferroics, SERS application and lab-on-a-chip. <sup>72,113-115</sup> .....	53
Figure 1-24: Particle-in-matrix design. (a) Cross-section STEM of the Au-VO <sub>2</sub> nanocomposite thin film deposited on Al <sub>2</sub> O <sub>3</sub> (0001) substrate and (b) HR-STEM of the Au nanoparticle embedded in VO <sub>2</sub> . <sup>39</sup> .....	56
Figure 1-25: Vertically aligned nanocomposite. (a) X-ray diffraction of the Au-BaTiO <sub>3</sub> nanocomposite, (b) Cross-section, (c) plan-view STEM image and its corresponding (d) EDS elemental map distribution. HR-STEM (e) plan-view image and (f) cross-section image of the Au nanopillar. (g) Enlarged image of the vertical Au-BTO interface and the schematic illustration of the lattice matching relationship. <sup>41,96</sup> .....	57
Figure 1-26: Linear and Areal strain compensation model. Schematic illustration of lattice matching relationship for the (a) linear and (d) areal strain compensation model. (b) In-plane lattice constant and (e) area for the metal and oxide phases as a function of oxide mole fraction. The dashed line joining the metal and oxide phases are the reported VAN systems and indicate the tunability of the in-plane strain on the substrate. Substrate are marked with a solid black line. (c) Plot showing the reported metal-oxide VAN systems plotted with their lattice parameters and (f) areal strain. The orange portions represent the region where both tensile and compressive strains are present while the blue shaded portion represent the region where either both tensile or compressive strain is present. The VAN systems marked with red star indicate highly spatially ordered systems. ....	59
Figure 1-27: Case study I. (a) Cross-section EF-TEM image of the Co-CeO <sub>2</sub> showing the Co nanowires. (b) HR-TEM image of a Co nanowire and (c1)-(c3) the corresponding SAED patterns of the three regions marked in (b). (d) Cross-section STEM image of Co-BaZrO <sub>3</sub> nanocomposite.	

(e) HR-STEM plane-view image and (f) cross-section image. (g) shows an enlarged portion of the vertical interface between Co and BaZrO<sub>3</sub>.<sup>33,35,111</sup> ..... 62

Figure 1-28: Case study II. X-ray diffraction of Ni-CeO<sub>2</sub> nanocomposite thin film, (b) Cross-section STEM-EDS map showing the elemental distribution, (c) HR-STEM cross-section image and (d) plan-view image showing the two different growth orientation of the Ni pillars. (e) X-ray diffraction of the Ni-Ba(Zr<sub>0.8</sub>Y<sub>0.2</sub>)O<sub>3</sub> nanocomposite thin film, (f) Cross-section STEM image, (g) Plan-view STEM image and (h) the corresponding HR-STEM image showing the Ni growth orientation.<sup>32,34</sup> ..... 63

Figure 1-29: Case study III. X-ray diffraction of the Fe-(La<sub>0.5</sub>Sr<sub>0.5</sub>)FeO<sub>3</sub> nanocomposite thin film deposited with different laser energy. (b) Cross-section STEM image and (c) the corresponding Fe EDS map. (d) Plan-view TEM image showing the distribution of Fe pillars. (e) X-ray diffraction of the Fe-BaTiO<sub>3</sub> nanocomposite thin film deposited at different laser frequency. (f) Cross-section STEM image and (g) the corresponding Fe EDS map. (d) Plan-view TEM image showing the faceted structure of Fe pillars.<sup>139, 36</sup> ..... 64

Figure 2-1. Schematic of the pulsed laser deposition system<sup>143</sup> ..... 67

Figure 2-2. Illustration of the Brag's law for lattice planes with inter-atomic spacing  $d$ <sup>144</sup> ..... 69

Figure 2-3. Ray diagrams for the two basic operation modes in TEM showing the diffraction mode (left) and the imaging mode (right)<sup>145</sup> ..... 70

Figure 2-4. Schematic set-up for atomic force microscope<sup>146</sup> ..... 72

Figure 2-5. Schematic setup of the PFM<sup>147</sup> ..... 73

Figure 2-6. Setup of the UV-Vis-NIR spectrophotometer<sup>148</sup> ..... 74

Figure 2-7. Schematic setup of the ellipsometer..... 75

Figure 3-1. Cross-sectional STEM images showing Au NPs embedded in epitaxial TiO<sub>2</sub> thin film for growth temperature of (a) 700 °C, (b) 500 °C, (c) 300 °C and (d) mixed temperature. .... 79

Figure 3-2. STEM images of Au-TiO<sub>2</sub> nanocomposite at (a) 700 °C, (b) 500 °C, (c) 300 °C and (d) mixed temperatures..... 81

Figure 3-3. Statistics of the Au NP size distribution as a function of deposition temperature..... 82

Figure 3-4. SAED of Au-TiO<sub>2</sub> nanocomposite for the growth temperature of 700 °C..... 83

Figure 3-5. (a) XRD patterns of Au-TiO<sub>2</sub> nanocomposite at different growth temperature and (b) the variation in FWHM of TiO<sub>2</sub> (004) peak, (c) Au (002) peak. .... 83

Figure 3-6. Rocking curve for the (004) TiO<sub>2</sub> peak indicating the FWHM of 0.64 ..... 84

Figure 3-7. (a) Normalized transmittance spectra of the TiO<sub>2</sub> and Au-TiO<sub>2</sub> nanocomposite films for varied growth temperature and (b) their corresponding band gap calculated using Tauc plot. Marked region in (a) is shown as an inset in (b). ..... 86

Figure 3-8. (a) Unnormalized transmittance spectra of the TiO<sub>2</sub> and Au-TiO<sub>2</sub> nanocomposite films for varied growth temperature, and (b) the absorption coefficient ..... 87

Figure 3-9. (a) Experimental setup used to measure the angular dependent transmission and reflection, (b) transmission spectra for the sample grown at mixed temperature at varying angles, (c) transmittance at 20° and -20° and (d) reflectance at varying angles ..... 87

Figure 3-10. Angular dependent transmittance spectra for the Au-TiO<sub>2</sub> sample grown at (a) 700 °C and (b) 500 °C ..... 88

Figure 3-11. (a) Cross-sectional STEM image of the Au-TiO<sub>2</sub> film grown on STO (001) at 700 °C, (b) approximate geometry used to simulate the absorption spectra, (c) Experimental absorption spectra and (d) calculated absorption spectra showing the surface and bulk contribution of Au NPs, (e) absorption map corresponding to incident illumination at 585 nm and (f) 710 nm. .... 89

Figure 3-12. High resolution XPS spectra of (a) Ti 2p and (b) Au 4f of Au-TiO<sub>2</sub> nanocomposite thin film..... 90

Figure 3-13. Experimental (solid) and fitted (dot) components of the ellipsometric parameter Psi ( $\psi$ ) for the (a) Au-TiO<sub>2</sub> sample deposited at 300 °C and (b) TiO<sub>2</sub> deposited at 700 °C..... 92

Figure 3-14. (a) Experimental (solid) and fitted (dot) components of the ellipsometric parameter Psi ( $\psi$ ) for the TiO<sub>2</sub>-Au sample deposited at 700 °C. Inset shows the ellipsometer measurement setup. The ellipsometer parameters  $\psi$  and  $\Delta$  (not shown here) were measured at different angles to improve the accuracy of the fitted model (b) Real and imaginary part of the permittivity for the TiO<sub>2</sub> and TiO<sub>2</sub>-Au sample deposited at 700 °C and 300 °C, (c) Absorption spectra for methylene blue for different irradiation times with the Au-TiO<sub>2</sub> film grown at 500 °C and (d) normalized absorbance plotted against the irradiation time for the three different films along with the reference MB solution. Inset shows the mechanism of plasmon-induced charge transfer. Electrons near the Au Fermi level are excited to surface plasmon state and get transferred to TiO<sub>2</sub> conduction band where the electron-driven hydrogen evolution half-reaction takes place. .... 94

Figure 4-1. Growth mechanism schematic of (a) two-phase BTO-ZnO vertically aligned nanocomposite (VAN), (b) random three-phase Au-BTO-ZnO, and (c) ordered three-phase Au-BTO-ZnO. In (a), regions of BTO and ZnO get nucleated aside each other giving rise to a self-assembled BTO-ZnO VAN. (b) shows three separate regions of nucleation for Au, BTO and ZnO. (c) shows the two-step growth of ordered three phase nanocomposite. Au NPs are capped at the end of ZnO pillars giving rise to the ordered three-phase 'nanoman' structure. .... 100

Figure 4-2. Microstructure study of the random three-phase Au-BTO-ZnO nanocomposite. (a) 3D schematic illustration of the random three-phase Au-BTO-ZnO nanocomposite, (b) plan-view scanning transmission electron microscopy (STEM) image with the corresponding EDS mapping showing distribution of the phases, (c) atomic-scale high resolution STEM (HRSTEM) plan-view image showing the three phases, (d) cross-sectional STEM image with the corresponding EDS mapping, and (e) HRSTEM image showing the lattice spacing and growth direction of BTO. 101

Figure 4-3. SAED of (a) random and (b) ordered three phase Au-BTO-ZnO nanocomposite .. 102

Figure 4-4. XRD  $\theta$ -2 $\theta$  scan of the three different nanocomposite designs deposited on SrTiO<sub>3</sub> (001) ..... 103

Figure 4-5. Microstructure study of the ordered three-phase Au-BTO-ZnO nanocomposite. (a) 3D schematic illustration of the ordered three-phase Au-BTO-ZnO nanocomposite, (b) plan-view

STEM image with the corresponding EDS mapping showing distribution of the phases, and (c) cross-sectional STEM image with the corresponding EDS mapping .....	104
Figure 4-6. EDS elemental maps for Sr and Ti for both random and ordered three-phase nanocomposite .....	104
Figure 4-7. Auto-correlation maps for (a-b) random and (c-d) ordered three-phase nanocomposite .....	105
Figure 4-8. (a) Phase diagram of Au and ZnO showing the eutectic temperature at 650°C. <sup>189,190</sup> The growth temperature used for the deposition was 700°C. (b) 2-step growth process employing the EAVLS mechanism enabling the growth of ordered vertically aligned three-phase nanocomposite, (c) atomic-scale HRSTEM cross-section image showing the templated Au-BTO and STO epitaxial interface before the growth of second layer, and (d) atomic-scale HRSTEM image showing the Au NP capping the ZnO NW and surrounded by the BTO matrix indicative of the VLS mechanism.....	106
Figure 4-9. Conventional VLS mechanism enabling the growth of crystalline ZnO NW using Au NPs as catalysts.....	107
Figure 4-10. (a) STEM image of the BTO-ZnO two phase nanocomposite, (b) composition EDS mapping showing the VAN structure, (c) HRTEM image showing the phase contrast between BTO and ZnO, and (d) HRSTEM image showing the inter-planar spacing of BTO to be 4.1Å.....	108
Figure 4-11. Nanocomposite multifunctionalities. (a) The optical transmission spectra for the three different nanocomposite design, (b) PFM out-of-plane phase map for the ordered three-phase nanocomposite obtained after poling with +5V (bright contrast) and -5V (dark contrast) over an area of 5x5 $\mu\text{m}^2$ , (c) piezoelectric coefficient $d_{33}$ -voltage ( $d_{33}$ -V) curves for the three different nanocomposite designs confirming their switchable and ferroelectric behavior, and (d) comparison of the BTO $c$ lattice parameter (calculated using XRD) and its corresponding piezoelectric coefficient ( $d_{33}$ ). .....	110
Figure 4-12. (a) random and (b) ordered three phase Au-BTO-ZnO nanocomposite deposited on MgO (001) substrate used for the optical transmittance measurements. ....	111
Figure 4-13. a) PFM amplitude and (b) phase hysteresis loops for all the three nanocomposite designs.....	111
Figure 4-14. Nanocomposite optical properties. (a)-(c) Experimental (solid) and fitted (dot) components of the ellipsometric parameter $\psi$ for the three different nanocomposite designs. The ellipsometer parameters $\psi$ and $\Delta$ (not shown here) were measured at different angles to improve the accuracy of the fitted model. (d)-(f) Corresponding real part of the in-plane and out-of-plane permittivity. Inset shows their corresponding iso-frequency curves (at 650 nm) where $k_0=\omega^2/c^2$ is the wavenumber in vacuum, $k_x$ , $k_y$ and $k_z$ are the [100], [010], and [001] components of the wave vector, respectively. (d) and (e) shows an ellipsoidal surface while (f) shows a hyperbolic response in the visible and near-infrared regime. ....	112
Figure 4-15. In-plane and out-of-plane imaginary permittivity for (a) two phase BTO-ZnO nanocomposite, (b) random three-phase Au-BTO-ZnO nanocomposite, and (c) ordered three-phase Au-BTO-ZnO nanocomposite .....	114

Figure 4-16. Experimental and calculated absorption for (a) random and (b) ordered three phase nanocomposite. ....	115
Figure 4-17. Real (n) and imaginary (k) part of the refractive index for (a)-(b) two-phase nanocomposite, (c)-(d) random three-phase nanocomposite, and (e)-(f) ordered three-phase nanocomposite. ....	116
Figure 4-18. Real and imaginary part of the permittivity for Au-BTO film of 50 nm thickness deposited on SrTiO <sub>3</sub> (001) substrate. ....	117
Figure 4-19. (a) STEM image and (b)-(c) EDS map showing phase distribution of the elements. ....	118
Figure 5-1. X-ray diffraction of the ordered three-phase Au-BaTiO <sub>3</sub> -ZnO nanocomposite thin films. XRD plots as a function of (a) temperature, (b) Au-BaTiO <sub>3</sub> template thickness and (c) deposition frequency. (d) c lattice parameter of BaTiO <sub>3</sub> and ZnO plotted as a function of deposition frequency. (e)-(f) Reciprocal space maps (RSM) around the SrTiO <sub>3</sub> (002) peak for the 2Hz/2Hz and 10Hz/10Hz samples, respectively. ....	124
Figure 5-2. X-ray Diffraction graph of Au-BTO thin film showing no peak splitting in BTO..	126
Figure 5-3. Cross-sectional EDS elemental maps as function of substrate, varied from (a) LAO, (b) STO, and (c) MgO .....	127
Figure 5-4. (a)-(d) Cross-sectional EDS elemental maps as function of deposition frequency of Au-BaTiO <sub>3</sub> template layer and BaTiO <sub>3</sub> -ZnO layer. (e) Plot of the Au pillar width and (f) Au nanoparticle aspect ratio as a function of frequency.....	128
Figure 5-5. HR-STEM image of the BaTiO <sub>3</sub> -SrTiO <sub>3</sub> interface of three-phase Au-BaTiO <sub>3</sub> -ZnO sample deposited at (a) 2Hz/2Hz and (b) 10Hz/10Hz and their corresponding Fourier transform images in (c) and (d) respectively. ....	129
Figure 5-6. STEM image showing the lines used for calculating the Au pillar diameter.....	129
Figure 5-7. Cross-sectional EDS elemental maps as function of Au-BaTiO <sub>3</sub> template thickness, varied from (a) 20 nm, (b) 40 nm, and (c) 60 nm and their corresponding Zn EDS map in (d)-(f). ....	130
Figure 5-8. X-ray diffraction of the three-phase Au-BaTiO <sub>3</sub> -ZnO deposited on MgO, STO and LAO .....	131
Figure 5-9. Cross-sectional EDS elemental maps of the three-phase Au-BaTiO <sub>3</sub> -ZnO nanocomposite thin films, deposited at (a) 500°C, (b) 600°C, and (c) 700°C.....	132
Figure 5-10. Polar plot of the measured SHG intensity as a function of incident polarization angle with output polarization fixed at (a) 90° (S-out) and (b) 0° (P-out). Real part of the in-plane ( $\epsilon'_{  }$ ) and out-of-plane ( $\epsilon'_{\perp}$ ) permittivity as a function of (c) frequency and (d) Au-BaTiO <sub>3</sub> template thickness.....	133
Figure 6-1. Schematic illustration of the (a) ordered three-phase Au-BaTiO <sub>3</sub> -ZnO nanocomposite. Heating profiles showing the (b) <i>ex-situ</i> annealing in air, (c) in vacuum, and during <i>in-situ</i> heating in TEM to investigate the thermal stability of the nanocomposite thin film. ....	138

Figure 6-2. X-ray Diffraction. XRD plots of the as-deposited, air annealed and vacuum annealed three-phase Au-BaTiO<sub>3</sub>-ZnO nanocomposite. .... 139

Figure 6-3. Raman Spectroscopy of the as-deposited, air annealed and vacuum annealed three-phase Au-BaTiO<sub>3</sub>-ZnO nanocomposite. .... 140

Figure 6-4. *Ex-situ* annealing of the ordered three-phase Au-BaTiO<sub>3</sub>-ZnO nanocomposite. (a) Cross-sectional STEM image of the as-deposited Au-BaTiO<sub>3</sub>-ZnO nanocomposite, Cross-sectional STEM image and the corresponding EDS map after *ex-situ* annealing in (b) air and (c) vacuum..... 141

Figure 6-5. *In-situ* heating of Au-BaTiO<sub>3</sub>-ZnO in TEM. Cross-sectional STEM image along with the initial and final EDS map during the *in-situ* heating in TEM from room temperature (RT) to 650°C of the (a)-(d) four selected regions. Scale bar corresponds to 20 nm ..... 142

Figure 6-6. STEM image of the Au NP showing the curvature at RT..... 144

Figure 6-7. Tunable optical properties. Real part of the in-plane ( $\epsilon'_{100}=\epsilon'_{010}$ ) and out-of-plane ( $\epsilon'_{001}$ ) permittivity for the as-deposited, air-annealed, and vacuum annealed Au-BaTiO<sub>3</sub>-ZnO thin films. .... 145

Figure 6-8. Microstructure of the as-deposited Au-BaTiO<sub>3</sub>-ZnO nanocomposite. (a) HR-STEM image of the BaTiO<sub>3</sub>-ZnO vertical interface and its corresponding (b) Fourier-transform image showing the presence of dislocations at the BaTiO<sub>3</sub>-ZnO vertical interface. Schematic illustration showing the two possible domain-matching epitaxy (DME) at the BaTiO<sub>3</sub>-ZnO vertical interface with (c) 5 BTO (002): 4 ZnO (0002) and (d) 6 BTO (002): 5 ZnO (0002) lattice matching relationship..... 147

Figure 6-9. Microstructure of the vacuum-deposited Au-BaTiO<sub>3</sub>-ZnO nanocomposite. (a) STEM image of the vacuum-annealed Au-BaTiO<sub>3</sub>-ZnO nanocomposite, (b) its corresponding EDS elemental map and (c) EDS line-scan with the labeled stoichiometry. (d) HR-STEM image of the pure Au pillar and (e) of the pillar with stoichiometry Au<sub>0.92</sub>Zn<sub>0.08</sub> with its (f) corresponding Fourier-transform image. (g) HR-STEM image of Au-BaTiO<sub>3</sub> and BaTiO<sub>3</sub>-ZnO vertical interface with (h) its corresponding Fourier-transform image..... 148

Figure 6-10. (a) STEM image of the vacuum annealed three-phase Au-BaTiO<sub>3</sub>-ZnO nanocomposite, (b) its corresponding EDS map and (c) the EDS line-scan showing the pillar compositions. .... 149

Figure 6-11. The Au-Zn (bulk) phase diagram<sup>210</sup> ..... 150

## NOMENCLATURE

AFM	Atomic force microscopy
CVD	Chemical vapor deposition
DME	Domain matching epitaxy
EDS	Energy dispersive X-ray spectroscopy
EMA	Effective medium approximation
ENZ	Epsilon near zero
FE	Ferroelectric
FFT	Fast fourier transform
FWHM	Full-width-half-maximum
HAADF	High angle annular dark field
HMM	Hyperbolic metamaterial
HR-STEM	High-resolution scanning transmission electron microscopy
HR-TEM	High-resolution transmission electron microscopy
MB	Methylene blue
MSE	Mean squared error
PFM	Piezoresponse force microscopy
PLD	Pulsed laser deposition
PVD	Physical vapor deposition
MR	Magnetoresistance
NP	Nanoparticle
NW	Nanowire
RSM	Reciprocal space mapping
SAED	Selected area electron diffraction
SHG	Second harmonic generation
SPR	Surface plasmon resonance
STEM	Scanning transmission electron microscopy
TEM	Transmission electron microscopy
VAN	Vertically aligned nanocomposite

VLS	Vapor-liquid-solid
XPS	X-ray photoelectron spectroscopy
XRD	X-ray diffraction
UV-Vis-NIR	Ultraviolet-visible-near-infrared

## ABSTRACT

Understanding how light interacts with the matter is essential for developing future optoelectronic devices. Furthermore, tuning such light-matter interaction requires designing new material platforms that is essential for developing devices which are functional in different light wavelength regimes. Among these designs, particle-in-matrix, multilayer or nanowire morphology, consisting of metal and dielectric materials, have been demonstrated for achieving improved physical and optical properties, such as ferroelectricity, ferromagnetism and negative refraction. For example, Au-TiO<sub>2</sub> two phase nanocomposite has been explored in this dissertation as a way of achieving enhanced photocatalysis. However, due to the availability of a limited range of structures in terms of crystallinity and morphology in the two-phase nanocomposites, a greater design flexibility and structural complexity along with versatile growth techniques are needed for developing next generation integrated photonic and electronic devices. This can be achieved by incorporating a third phase through the three phase nanocomposite designs by judicious selection of materials and functionalities.

In this dissertation, a new nanocomposite design having three different phases has been introduced: Au, BaTiO<sub>3</sub> and ZnO, which grow in a highly ordered ‘nanoman’-like structure. More interestingly, the three phases in the novel ‘nanoman’-like structure combine to give an emergent new property which are not found individually in the three phases. The ordered ‘nanoman’-like structures enable a high degree of tunability in their optical and electrical properties, including the hyperbolic dispersion in the visible and near infrared regime, in addition to the prominent ferroelectric/piezoelectric properties. Moreover, the growth kinetics and the thermal stability (using in-situ Transmission Electron Microscopy) of the ‘nanoman’ structures has also been studied. This study introduces a new growth paradigm of fabricating three-phase nanocomposite that will surely generate wide interests with potential applications to different systems. The ordered three-phase ‘nanoman’ structures present enormous opportunities for novel complex nanocomposite designs towards future optical, electrical and magnetic property tuning.

# 1. INTRODUCTION

Self-assembled nanocomposite thin films offer an interesting way towards functionality coupling and achieving novel physical properties. In this chapter, the growth mechanisms of single phase and two-phase nanocomposite thin films are discussed followed by the discussion on the factors influencing thin film morphologies. The background of vertically aligned nanocomposites (VAN), functionality and new metal-dielectric nanocomposites is also discussed.

## 1.1 Epitaxial growth of thin films

Thin film growth differs significantly as compared to bulk material processing methods. For example, rutile is the more thermodynamically stable phase of  $\text{TiO}_2$  in the bulk form. However, when it is grown on single crystal  $\text{SrTiO}_3$  (STO) (001) or  $\text{LaAlO}_3$  (LAO)(001), the metastable anatase phase is formed. Moreover, when grown on  $(11\bar{2}0)$   $\text{Al}_2\text{O}_3$ , the thermodynamically stable rutile phase is formed<sup>1</sup>. The most thermodynamically stable grows on the substrate regardless of whether that phase is present in the target or not<sup>2</sup>. This phenomenon is termed as the epitaxial stabilization in thin films. The following section presents the growth thermodynamics of single-phase thin films.

### 1.1.1 Growth thermodynamics for single phase nanocrystalline thin film

For a nucleus of the growing phase, the Gibbs free energy of formation can be written as:

$$\Delta G_f = \Delta gV + \sigma S + \Delta G^{stress} \quad (1.1)$$

where  $\Delta g$  is the specific Gibbs' energy of the bulk material,  $V$  is the volume of the nucleus,  $\sigma$  is the surface energy,  $S$  is the surface area of the nucleus and  $\Delta G^{stress}$  is the additional energy term due to the stress imposed on the growing phase by the surface.<sup>1</sup> For simplification, let's assume a square shaped nucleus with side  $d$  and height  $h$  growing on a square like film-substrate interface with lattice parameter of  $a_f$  and  $a_s$  for film and substrate respectively. Let's consider two competing phases 1 (') (e.g.: anatase) and 2 (") (e.g.: rutile) where  $\Delta g'' < \Delta g'$  but 1 grows coherently while 2 grows incoherently on a particular substrate.

$$\Delta G_f' = \Delta g' d^2 h + \sigma_c' d^2 + \sigma_v'(d^2 + 4dh) + h \frac{\mu}{1-\nu} \varepsilon^2 d^2 \quad (1.2)$$

$$\Delta G_f'' = \Delta g'' d^2 h + \sigma_{ic}^s'' d^2 + \sigma^v'' (d^2 + 4dh) \quad (1.3)$$

where  $\sigma_c^s'$  and  $\sigma_{ic}^s''$  refers to the surface energy of coherent nucleating phase and incoherent nucleating with the substrate respectively.  $\sigma^v'$  and  $\sigma^v''$  refers to the surface energy of the nucleating phase with the vapor which is assumed to be the same for both the coherent and incoherent phases ( $\sigma^v'' = \sigma^v'$ ). Therefore, it is assumed that the energy contribution by edges and surfaces of islands is the same for both phases.  $\varepsilon$  is the strain in the growing nucleus due to the lattice mismatch between the film and substrate given by  $(a_f - a_s/a_s)$ . The energy contribution due to strain is not present for the incoherent phase due to the higher  $\sigma_{ic}^s''$  as compared to  $\sigma_c^s'$  (10-100 times larger). Therefore, free energy per unit surface associated with the transfer from a coherent to an incoherent phase,  $\Delta E$  is given by:

$$\Delta E_f = \frac{\Delta G_f''}{d^2} - \frac{\Delta G_f'}{d^2} \quad (1.4)$$

$$\Delta E = h[(\Delta g'' - \Delta g') - \frac{\mu}{1-\nu} \varepsilon^2] + (\sigma_{ic}^s'' - \sigma_c^s') \quad (1.5)$$

Hence, when  $\Delta E$  is negative, transformation from the coherent phase to incoherent phase will take place. The first term is negative while the second term is positive. Since, there is a  $h$  dependence on the first term, the Gibbs free energy of formation is positive (the second term is dominant) during the initial growth period. In other words, the system tries to minimize its overall energy by growing coherent phase (anatase) as opposed to the more thermodynamically stable incoherent phase (rutile). This phenomenon is essentially called epitaxial stabilization. Once the film growth process starts, the negative term starts increasing until a height where  $\Delta E$  is zero. This is the critical height after which the system prefers to grow the more thermodynamically stable phase. The transition energy term varies quadratically with the lattice mismatch term  $\varepsilon$  (of the coherent phase) while it varies linearly with other variables such as surface energy and free energy difference. Hence, if the lattice mismatch of the coherent phase is small, then it can lead to a high critical thickness. The effect of dislocations and grain boundary on the free energy term have been neglected<sup>1</sup>.

Figure 1-1 shows the transformation energy for TiO<sub>2</sub> from anatase to rutile polymorph using eq. 1.5.<sup>1</sup> As seen in Figure 1-1a, metastable anatase phase grows epitaxially on (001) LAO

up to a critical thickness value corresponding to  $\Delta E=0$ , after which rutile phase starts to grow. However, in Figure 1-1b, thermodynamically stable epitaxial rutile phase is formed from the beginning on  $(11\bar{2}0)$   $\text{Al}_2\text{O}_3$  with no formation of anatase polymorph observed.

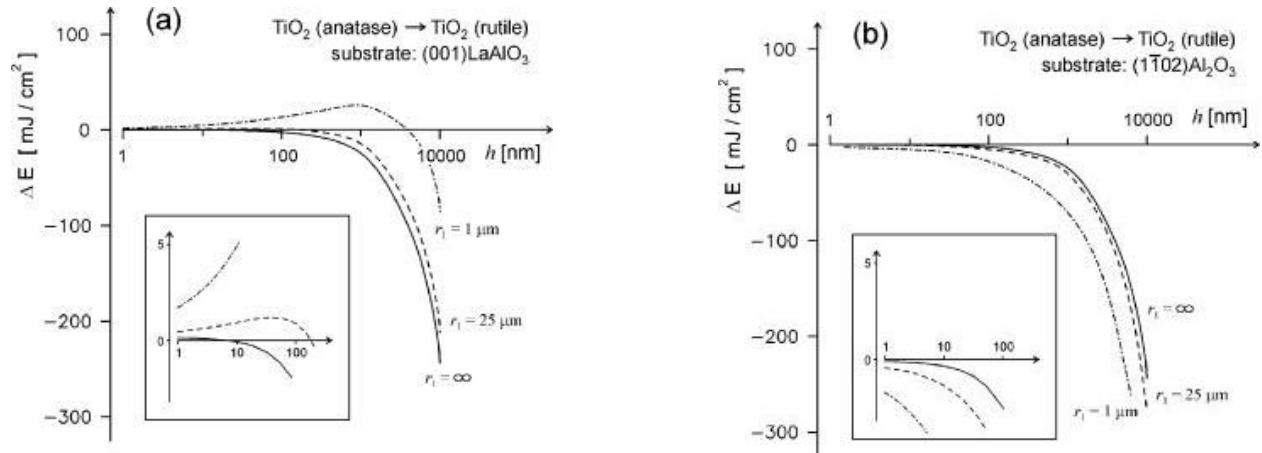


Figure 1-1: Transition energy for the transformation of TiO<sub>2</sub> anatase phase to TiO<sub>2</sub> rutile phase on (a) (001) LAO substrate and (b) (1-102) Al<sub>2</sub>O<sub>3</sub> substrate. Inset shows the enlarged graph near the transition point<sup>1</sup>

### 1.1.2 Growth mechanism of two-phase nanocomposites

Typically, two phase nanocomposites exist in three different thin-film forms: (i) nanoparticles in matrix (0-3 type), (ii) multilayer (2-2 type) and (iii) vertically aligned nanocomposites (VAN) (1-3 type). All the designs allow control over the interface quality, microstructure and strain<sup>3</sup>. The formation of two-phase nanocomposite thin films takes place through two main mechanisms: (i) nucleation and growth and (ii) spinodal decomposition. These are the two main processes to obtain phase segregation from a uniform solid solution. In nucleation and growth process, small clusters of one phase begin to form in the matrix of the second phase resulting in a random distribution of the phases. While in spinodal decomposition, small composition fluctuation makes the solid solution thermodynamically unstable resulting in a sinusoidal composition fluctuation<sup>2</sup>. The following section will explore each of these processes in detail with related examples.

#### *Nucleation and growth*

When the adatoms condense on the substrate, they may either re-evaporate or diffuse along the surface. Diffusion along the surface can again lead to either re-evaporation or adsorption at special sites such as edges or kinks as shown in Figure 1-2. During the film growth, interdiffusion of the substrate and film atoms occurs to smoothen the film/substrate interface<sup>4</sup>.

If the film growth is considered as a thermodynamic equilibrium process, then surface processes such as condensation and re-evaporation must be balanced. However, since the film growth takes place, the growth process must be a non-equilibrium kinetic process. Therefore, the thin film deposited may not be the most thermodynamically stable one, since the growth process is kinetically determined. Nevertheless, it is possible to use equilibrium thermodynamic arguments (as shown earlier) even though the overall growth process is a non-equilibrium kinetic process<sup>4</sup>.

There are generally three possible thin film growth modes: (i) island or Volmer-Weber (VW) mode, (ii) layer or Frank-van der Merwe (FM) mode and (iii) layer plus island or Stranski-Krastanov (SK) mode. The schematics of these growth modes is given in Figure 1-3. In VW mode, formation of small clusters or islands occurs due to the stronger bonding of the deposited adatoms to each other than the substrate. Typical example of this growth mode includes the growth of metal and semiconductor films on oxide substrates. While the opposite is true in case of Frank-van der Merwe mode, in which adatoms are more strongly bonded to the substrate than to each other leading to formation of multilayers. This growth mode is observed in the epitaxial growth of oxide and semiconductor materials. In Stranski-Krastanov mode, formation of islands takes place after the formation of few monolayers. Factors such as change in lattice mismatch, symmetry or orientation of the intermediate can be the cause of the subsequent island growth typically after 5-6 monolayers. This is the most common growth mode and has been observed in various metal-oxide and metal-metal systems<sup>5</sup>.

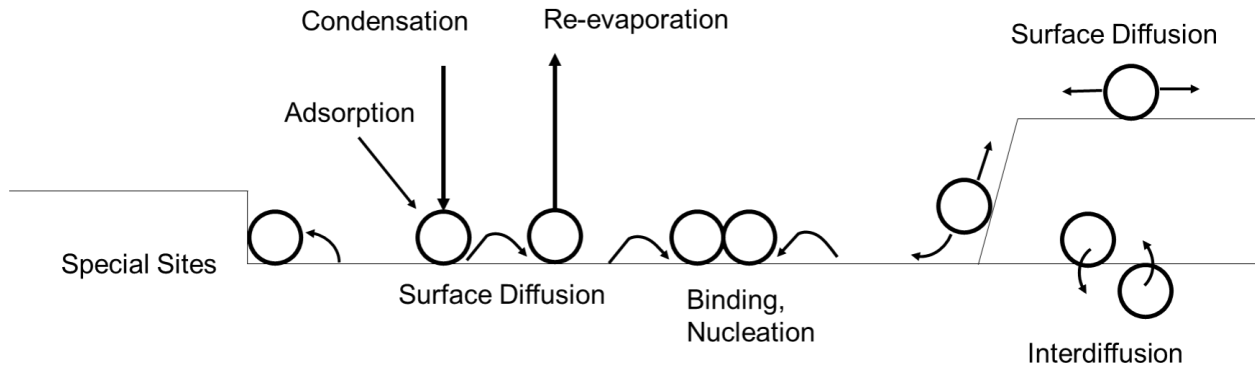


Figure 1-2: Schematic showing various processes involved in nucleation and growth on surfaces

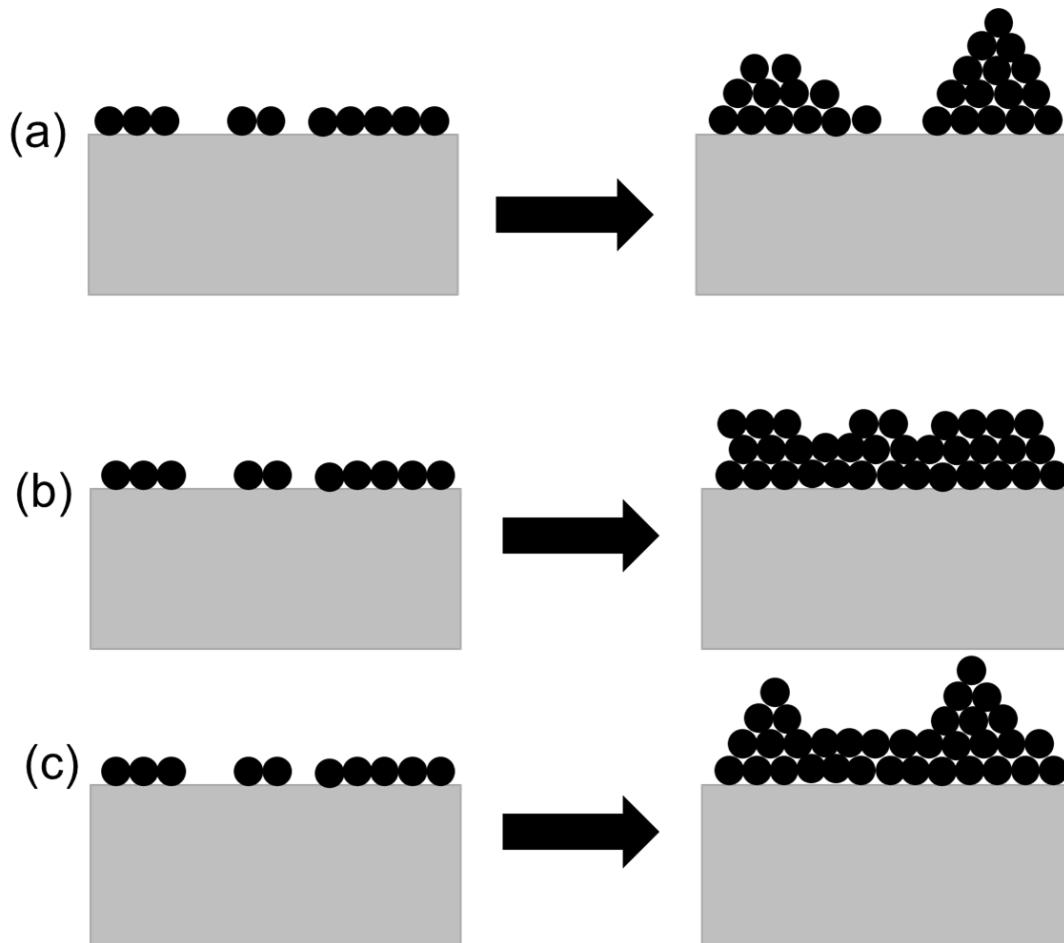


Figure 1-3: Schematic showing different growth modes: (a) Volmer-Weber (VW) (island) growth, (b) Frank-Van der Merwe (FM) (multilayer) growth and (c) Stranski-Krastanov (SK) growth

A classification between the layer and island growth modes can be made in terms of the surface tension of film/substrate ( $\gamma_{FS}$ ), substrate/vacuum ( $\gamma_{SV}$ ) and film/vacuum interface ( $\gamma_{FV}$ ). For a contact angle  $\theta$  (in Figure 1-4), the relationship is given by:

$$\gamma_{SV} = \gamma_{SF} + \gamma_{FV} \cos \theta \quad (1.6)$$

For the island growth mode:  $\theta > 0$ ,  $\gamma_{SV} < \gamma_{FV} + \gamma_{FS}$

For the layer growth mode:  $\theta = 0$ ,  $\gamma_{SV} > \gamma_{FV} + \gamma_{FS}$

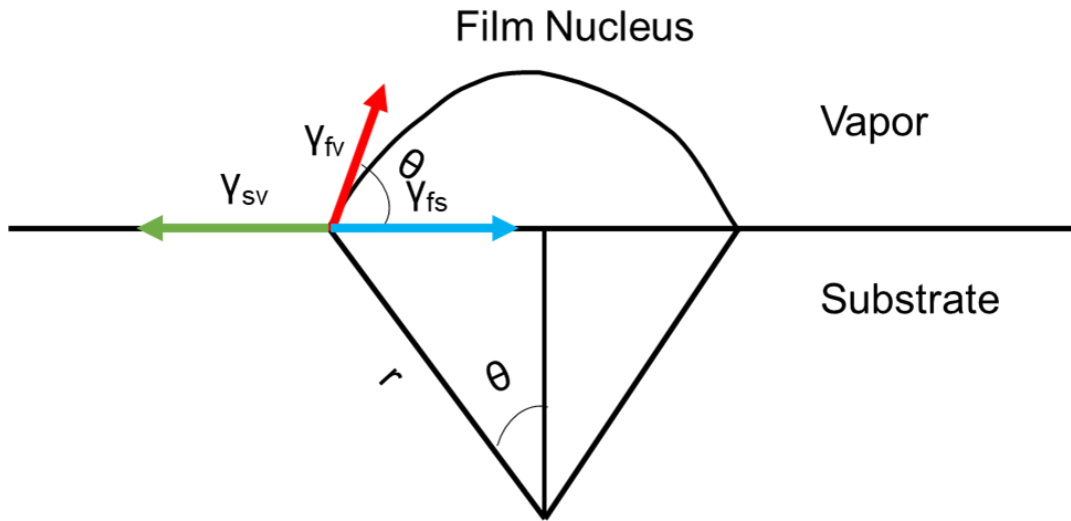


Figure 1-4: Film nucleation process on the substrate

In case of homoepitaxy,  $\gamma_{FS}=0$  since the substrate and the film are essentially the same material leading to a high-quality growth. Therefore, to obtain high quality multilayer deposition in case of heteroepitaxy, surface energy difference between film and substrate should be small. Typically, a material with low surface energy wets the surface with higher surface energy. During the film growth process, nucleation is preferred at specific sites such as step edges, defects, kinks etc. After a critical nucleus size is achieved, it can start to grow. The growth process depends on kinetic parameters such as growth rate, temperature (which changes the diffusion coefficient), pressure etc. of the system<sup>5</sup>.

For fabricating two phase nanocomposites, the two phases must be immiscible in each other. The size, distribution and orientation of the phases is strongly dependent on (i) composition ratio of phases A and B, (ii) the surface energies and crystallographic relations between each phase and the substrate and between the two phases, and c) the growth kinetics<sup>2</sup>.

The overall strain in the nanocomposite thin film is the sum of individual strain from both phase A and B interfaces with the substrate. Therefore, the composition ratio A:B plays an important role in determining the final microstructure. For many demonstrated VAN systems, phase and compositions are chosen such as to minimum the average in-plane strain<sup>6</sup>.

### ***Spinodal Decomposition***

If the two phases are immiscible in each other, i.e., they do not form a solid solution, then the two phases will grow on the substrate by nucleation and growth. If the two phases form a solid solution (show miscibility), then a single phase will grow by nucleation and growth. However, if the two phases possess a positive enthalpy of mixing and show miscibility at high temperatures with a tendency towards clustering at low temperature, then complete mixing of both the phases is energetically not favorable. In such situations, the solution can spinodally decompose into a mixture of two phases with different composition in order minimize the overall free energy.<sup>2</sup>

Unlike phase separation *via* nucleation and growth process, spinodal decomposition doesn't require nucleation and is completely controlled by diffusion which leads to spontaneous phase separation with nanoscale composition fluctuation. Moreover, the interfaces between the separated phases remain coherent which can lead to essentially better physical properties such as reduced light scattering for optical application. Spinodal decomposition leads to creation of regions with slightly different lattice parameter which leads to the development of local strain. In order to minimize this strain, often spinodally decomposed systems produce self-assembled and highly spatially ordered nanostructured thin films. This mechanism also offers a unique approach for the scalable fabrication of nanostructured materials with controlled structural properties at the nanoscale. Given enough time, the system will become a mixture of two discrete phases with compositions determined by the free energy minima<sup>7</sup>.

Spinodal systems generally consist of two phases having similar crystal structures and properties and produce self-assembled, highly ordered microstructures. Typically, oxides exhibit wide miscibility with each other, hence have a great potential to undergo spinodal decomposition and to show self-assembled, high spatial ordering. Spinodal decomposition has been observed in both bulk oxide material and oxide thin films. The following section discusses about few examples which are prevalent in oxide thin films<sup>2</sup>.

Spinodal decomposition leading to the formation of two phase nanocomposites has been shown in various oxide systems such as 1:1  $\text{BiFeO}_3:\text{Sm}_2\text{O}_3$ <sup>8</sup> in a checkerboard morphology as shown in Figure 1-5. The phase separation is quite distinct to be observed in X-ray Diffraction which suggests that the final phases are close to the free energy minima which is possible to achieve in reasonable timescales because of the rapid growth kinetics. Checkerboard structure has also been demonstrated in  $\text{Zn}(\text{Mn},\text{Ga})_2\text{O}_4$  films with regularly spaced and alternating orthorhombic (Mn-rich) and rotated tetragonal (Mn-poor) regions<sup>9</sup>. By forming this type of structure, the system can effectively minimize its strain energy due to the lattice mismatch between the two phases and can also minimize the misfit dislocations.

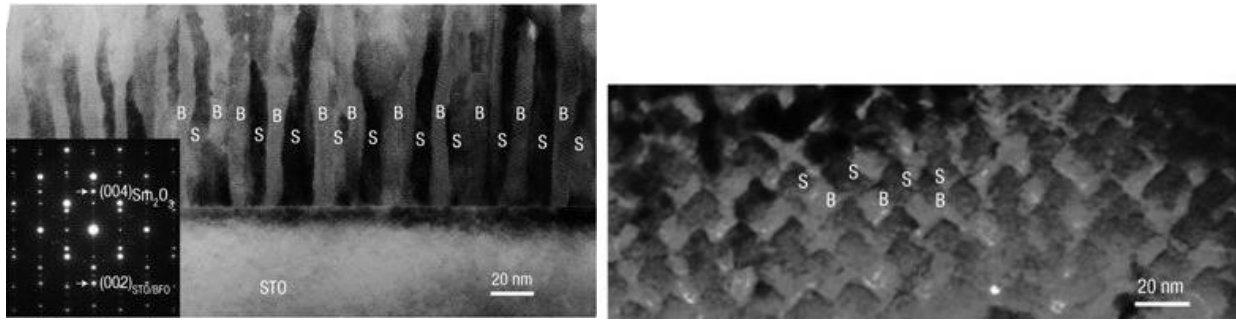


Figure 1-5: Cross-section and planar TEM images showing the checkerboard structure in  $\text{Bi}_{0.5}\text{Sm}_{0.5}\text{FeO}_3$  thin films<sup>8</sup>

Recently, spinodal decomposition has also been shown in the  $\text{TiO}_2\text{-VO}_2$  system to obtain self-assembled multilayer and vertically aligned nanostructures both by sputtering and pulsed laser deposition (PLD) techniques. Spinodal decomposition in  $\text{TiO}_2\text{-VO}_2$  system has been shown in bulk form as early as 1998 but only recently have they been studied in much greater detail both in bulk and thin film form. *Sun et al.*<sup>10</sup> demonstrated the growth of amorphous  $\text{TiO}_2\text{-VO}_2$  by room temperature sputtering process. However, annealing the film at 500 °C for 10 hrs gives rise to the multilayer  $\text{TiO}_2\text{-VO}_2$  structure by spinodal decomposition as shown in Figure 1-6. The lattice mismatch between  $\text{TiO}_2$  and  $\text{VO}_2$  is 0.61% along  $a$  axis and 3.3% along  $c$  axis, therefore, the phases get separated along the  $c$  direction in order to minimize the strain energy. This highly anisotropic stress is also useful in lowering the transition temperature of  $\text{VO}_2$ . Since both  $\text{TiO}_2$  and  $\text{VO}_2$  exhibit different optical properties, this combination can lead to an interesting metamaterial design. For example, this system has been proposed to be used in smart windows and enhanced optical switching. Following this work, *Chen et al.*<sup>7</sup> showed the spinodal decomposition in the

same system using PLD. However, the authors also reported the possibility to make a multilayer or vertically separated phases. Since the modulation is always along the c direction (in the substrate reference frame), by changing the orientation of the substrate, it is possible to change the morphology of the film. Growth of thin films on (001) and (100)  $\text{TiO}_2$  substrates followed by annealing gives rise to a multilayers and vertical pillar morphology respectively with periodicity of 15-20 nm. Similarly, other spinodal systems such as  $\text{ZrO}_2\text{-SiO}_2$ ,  $\text{Y}_2\text{O}_3\text{-SiO}_2$ ,  $\text{HfO}_2\text{-SiO}_2$ ,  $\text{Al}_2\text{O}_3\text{-SiO}_2$ ,  $\text{Al}_2\text{O}_3\text{-Cr}_2\text{O}_3$  and  $\text{AlN-SiC}$  are known to exist in bulk forms but haven't been studied in detail thin film form<sup>11</sup>.

Thus, spinodal decomposition shows the potential of producing self-assembled films with high spatial ordering. Minimization of interfacial and strain energy and substrate surface directed spinodal decomposition (substrate orientation) are the main factors that are responsible for controlling the morphology of growth.

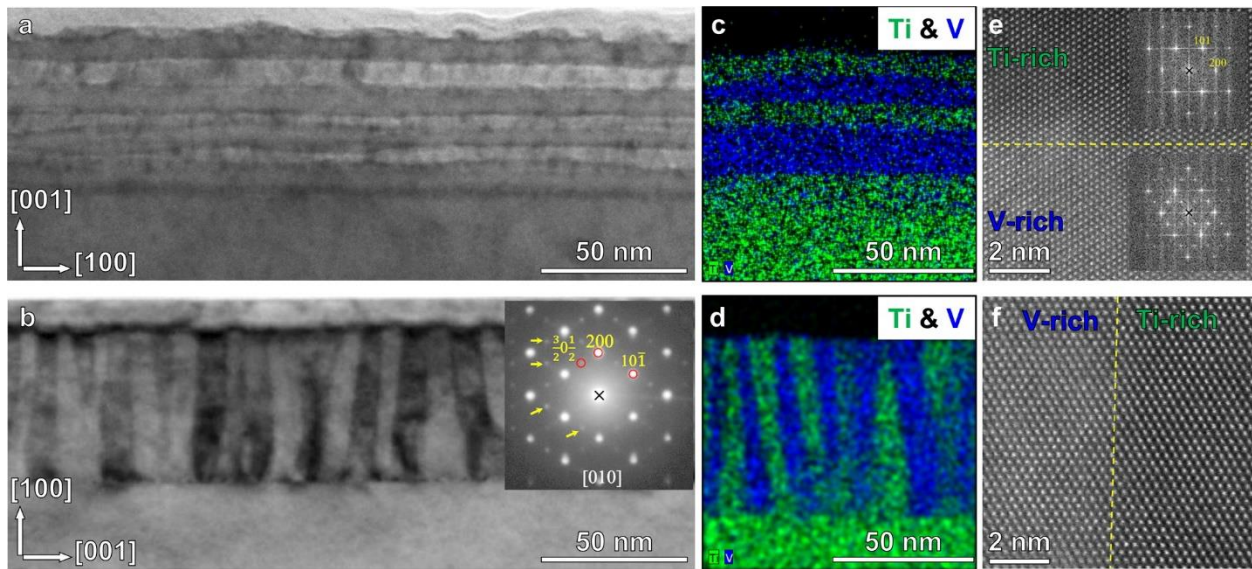


Figure 1-6: Cross-section TEM images (a,b), EDS imaging (c,d) and HAADF-STEM images showing the  $\text{TiO}_2\text{-VO}_2$  phase-separated heterostructure on (001) (a,c,e) and (100) (b,d,f) oriented rutile  $\text{TiO}_2$  substrates<sup>7</sup>

## 1.2 Morphological Control in thin films

As mentioned previously, morphological control is critical for tuning the physical properties of the nanocomposite. The following section discusses the important factors that play a crucial role in determining the morphology of the nanocomposite. Most of the study has focused on tuning the

morphology of oxide-oxide nanocomposite systems, therefore the following section mainly discusses about them.

### 1.2.1 Interfacial strain

From the epitaxial stabilization model for thin films, a quadratic dependence of strain on the free energy was obtained. Therefore, the system tries to minimize its interfacial strain energy arising due to the lattice mismatch of one phase with the substrate and with the other phase by changing its orientation or its polymorphic form. In this regard, the design of VAN offers several advantages. This is mainly because of the vertical strain control owing to the larger vertical interfacial area as opposed to the single interface with the substrate in the case of layered structures. The vertical strain coupling between the phases can be maintained up to a large thickness range. The vertical interfacial strain effects have been demonstrated in the STO:MgO<sup>12</sup>, BTO-CFO<sup>13</sup> and BTO-Sm<sub>2</sub>O<sub>3</sub><sup>8</sup> nanocomposites. (STO)<sub>0.5</sub>:(MgO)<sub>0.5</sub> VAN on STO shows a perfect lattice matching epitaxy both in-plane (with the substrate) and with the phases. HRTEM images shown in Figure 1-7 shows the film/substrate interface with no obvious misfit dislocations observed from the FFT image. Although there is a 7.3% lattice mismatch between STO and MgO, no dislocations are observed here since the VAN systems can accommodate much larger strains in the system<sup>12</sup>.

Moreover, *Chen et al.*<sup>14</sup> and *Choi et al.*<sup>15</sup> showed both layered supercell and tetragonal structures respectively from the same starting Bi<sub>2</sub>FeMnO<sub>6</sub> (BFMO) phase by taking advantage of the related interfacial and strain parameters.<sup>16</sup> The layered BFMO322 (Bi:Fe:Mn=3:2:2) grows pseudomorphically initially as a highly strained interlayer. After a critical thickness of 3-5 nm, misfit dislocations form to accommodate the strain to form a new equilibrium layered supercell BFMO322 structure shown in Figure 1-8(a).<sup>14</sup> While factors such as slow growth rates, narrow temperature window and thinner films (around 30 nm) helps maintain the strain coherency, high crystallinity and phase purity throughout the film essential for the growth of tetragonal phase as shown in figure 8(b).<sup>15</sup>

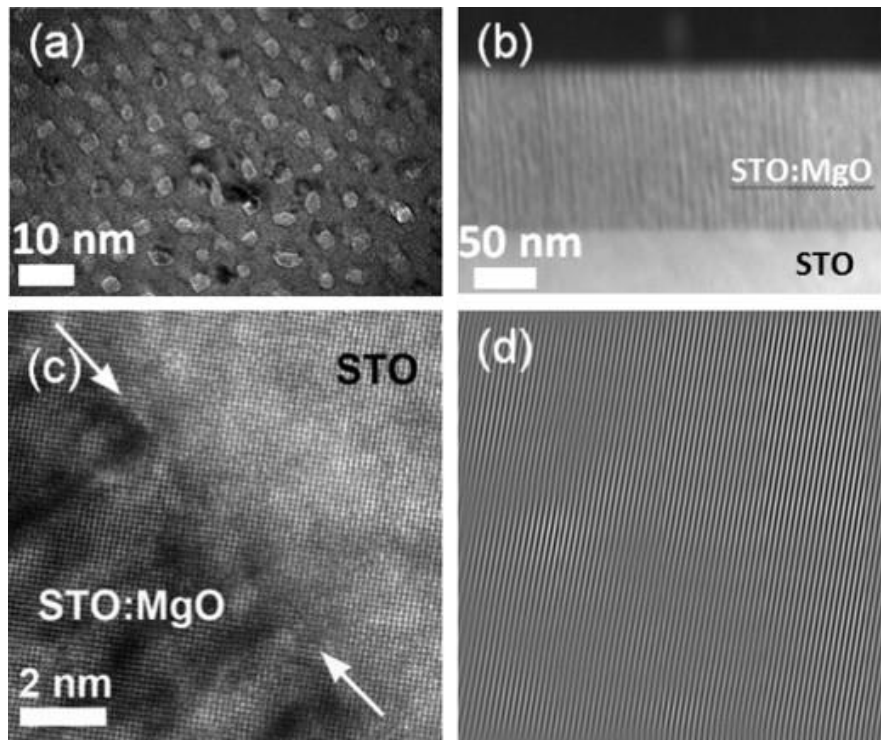


Figure 1-7: (a) Plan-view, (b) STEM and (c)HRTEM images of  $\text{STO}_{0.5}\text{MgO}_{0.5}$  VAN. (d) shows FFT of image (c)<sup>12</sup>

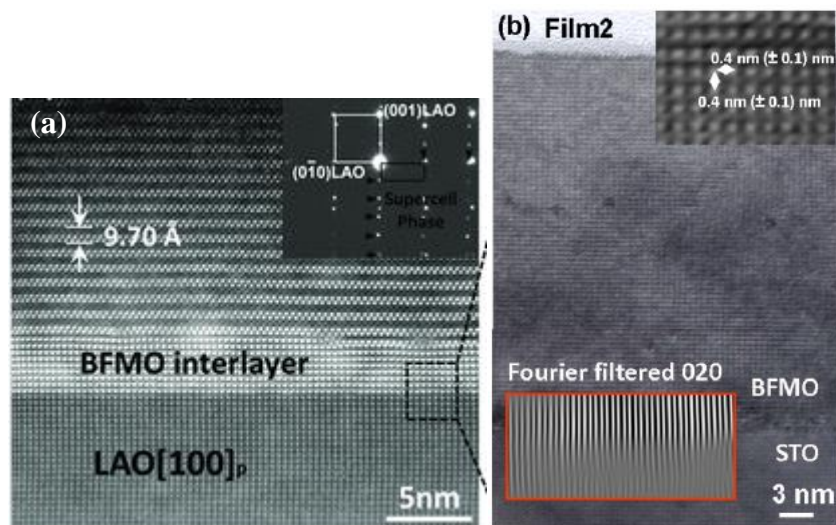


Figure 1-8: (a) HRSTEM image showing interface of BFMO layered structure with BFMO interlayer<sup>14</sup> and (b) HRTEM showing the interface of highly strained BFMO film<sup>15</sup>

### 1.2.2 Substrate selection

A good lattice match with the substrate is essential for the epitaxial growth of films. Previously discussed example of  $\text{TiO}_2$  grown as metastable anatase phase on STO (001) and LAO (001) but grown as rutile phase on  $\text{Al}_2\text{O}_3$  (1-102) show how the selection of substrate can affect the film growth. Further, the example of  $\text{TiO}_2\text{-VO}_2$  nanocomposite shows the effect of substrate orientation on the film morphology. Figure 1-9 shows the temperature-strain phase diagram for  $\text{BaTiO}_3$  (BTO).<sup>17</sup> It is shown that by changing the in-plane strain (i.e. by changing the substrate), it is possible to modify the crystal structure of BTO from a non-centrosymmetric structure (ferroelectric) to a centrosymmetric structure (paraelectric). Therefore, this approach can be exploited heavily to improve the physical properties of the materials.

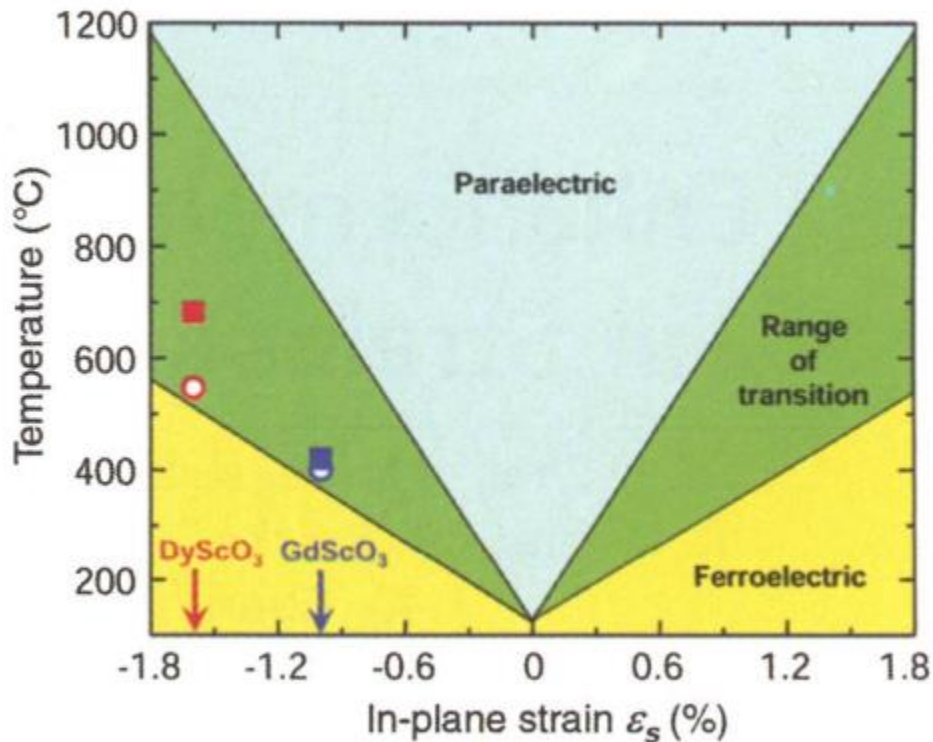


Figure 1-9: Temperature-strain phase diagram for  $\text{BaTiO}_3$ <sup>17</sup>

### 1.2.3 Relative composition of the phases

For many demonstrated VAN systems, phase and compositions are chosen such as to minimum average in-plane strain<sup>6</sup>. For example,  $\text{BiFeO}_3\text{:CoFe}_2\text{O}_4$  (BFO:CFO) system in the

composition ratio between 65:35-33:67 has been shown to exhibit VAN structure as shown in Figure 1-10. The phase orientation is determined by the minimization of the surface energy. For the film grown on STO (001), BFO becomes the matrix as the interfacial energy between BFO and STO (001) is low. CFO forms pyramidal crystallites with {111} faces growing out of plane as these are its lowest surface energy faces. However, for the film grown on STO (111), situation is reversed and now BFO forms pyramidal crystallites while CFO forms the matrix. Moreover, increasing the growth temperature increases the diffusion which increases the pillar diameter<sup>18</sup>.

For low composition ratios of phase A and B (10:90 or 90:10), either randomly distributed nanoparticles having coherent or semi-coherent interfaces (high growth rate and low growth temperature)<sup>19</sup> or self-assembled columnar arrangement of nanoparticles (slow growth rate and high growth temperature) is formed<sup>20</sup>.

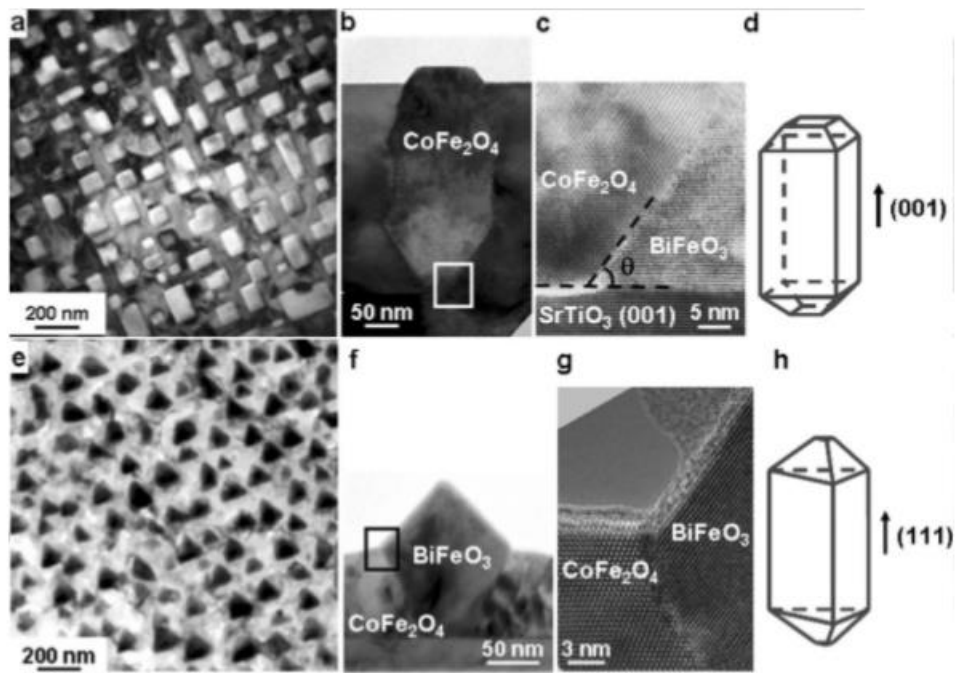


Figure 1-10: Morphology of BiFeO<sub>3</sub>-CoFe<sub>2</sub>O<sub>4</sub> nanocomposite with (a-d) CFO pillars) having (001) end facet with the film grown on (001) STO substrate and (e-h) BFO pillars having (111) end facet with the film grown on (111) STO substrate<sup>18</sup>

#### 1.2.4 Surface energy of phases with each other and with substrate

As mentioned previously, minimization of surface energy is one of the ways to minimize the overall energy of the system. Competition between surface energy and orientation-dependent

strain energy together determines the final phases and film morphology.<sup>21</sup> More recently, effect of surface energy of the substrate/film interface on the film morphology was shown in the LSMO-CeO<sub>2</sub> nanocomposite. *Fan et al.*<sup>22</sup> showed that by annealing the STO (001) substrate, CeO<sub>2</sub> showed preferential nucleation and growth on SrO terminated area ((011) out-of-plane) and TiO<sub>2</sub> terminated area ((001) out-of-plane) with long-range ordering as opposed to random ordering on untreated substrates as shown in Figure 1-11. The different orientation of CeO<sub>2</sub> nanopillars are due to the different surface energy of SrO and TiO<sub>2</sub> terminated area. Moreover, the ordered nanocomposite also showed much better ferromagnetic properties compared to the random structure.

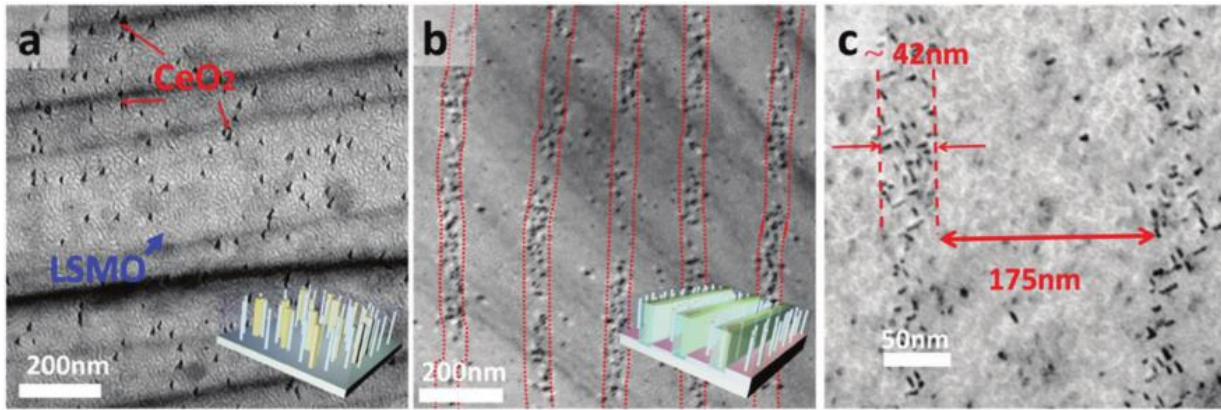


Figure 1-11: Plan-view TEM images of LSMO-CeO<sub>2</sub> VAN with CeO<sub>2</sub> pillars on (a) as-received and (b,c) annealed STO (001) substrate<sup>22</sup>

### 1.3 Vertically Aligned Nanocomposite (VAN) thin films

#### 1.3.1 Overview of VAN thin films

Vertically aligned nanocomposites (VAN) thin films are self- assembled structures in which both the phases grow epitaxially on the substrate in the out-of-plane direction. Both the phases grow alternatively and are vertically coupled through an epitaxial relationship or through domain matching epitaxy (DME). The lattice coupling at the vertical interface between the two phases and the lateral film/substrate interface play an important role for the growth of VAN thin films. Nanocomposite thin films typically exist in three different designs: (i) Nanoparticles in matrix (0-3 type), (ii) Multilayer (2-2 type), and (iii) Vertically aligned nanocomposites (VAN) (1-3 type).<sup>23</sup>

Among them, VAN thin films have attracted a lot of research interest due to their unique property of tuning the vertical strain by changing the film thickness.

Several studies have been done on two phase oxide-oxide VAN structures. The two-phase VAN system was first demonstrated in the  $\text{La}_{0.67}\text{Ca}_{0.33}\text{MnO}_3$ : MgO (LCMO:MgO) thin films in 2002.<sup>24</sup> Tunable magnetotransport properties were obtained by doing a systematic strain tuning by varying the MgO concentration. In 2004, a new  $\text{BaTiO}_3$ :  $\text{CoFe}_2\text{O}_4$  (BTO: CFO) system was demonstrated with spinel CFO pillars embedded as vertical pillars in the BTO matrix.<sup>13</sup> This system exhibited room temperature multiferroic properties by coupling the properties of ferroelectric properties of BTO and ferromagnetic properties of CFO along the vertical interfaces of the VAN structure. Figure 1-12 shows a plane view transmission electron microscopy (TEM) image of a BTO-CFO nanocomposite in which CFO grows as a nanopillar. Similarly, other systems such as CFO:BFO and BTO:YMO have also been demonstrated as VAN structure.<sup>25,26</sup> Also, different VAN structure with different morphologies such as nanocheckerboard, nanomaze and nanopillar in matrix have been reported.<sup>2</sup> Table 1-1 summarizes the different oxide-oxide VAN systems with crystal-structure and functionalities that have been demonstrated.

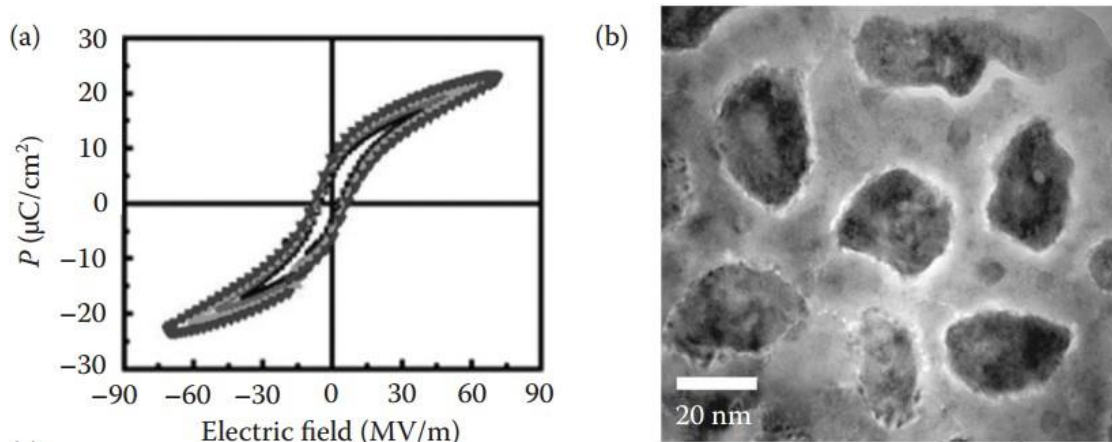


Figure 1-12: 1-3 type approach. CFO nanopillars embedded in BTO matrix show enhanced ferroelectric properties<sup>13</sup>

Table 1-1: List of VAN systems grouped by their functionalities

Functionalities	VAN Systems
Ferroelectric	BaTiO <sub>3</sub> : Sm <sub>2</sub> O <sub>3</sub> <sup>27</sup> BiFeO <sub>3</sub> : Sm <sub>2</sub> O <sub>3</sub> <sup>8</sup> BaTiO <sub>3</sub> : CeO <sub>2</sub> <sup>28</sup>
Magnetic and magnetotransport	La <sub>0.7</sub> Sr <sub>0.3</sub> MnO <sub>3</sub> (LSMO): ZnO <sup>29</sup> LSMO: CeO <sub>2</sub> <sup>22</sup> LSMO: CuO <sup>30</sup> LSMO: NiO <sup>31</sup> Ni: CeO <sub>2</sub> <sup>32</sup> Co: CeO <sub>2</sub> <sup>33</sup> Ni: BaZr <sub>0.8</sub> Y <sub>0.2</sub> O <sub>3</sub> <sup>34</sup> La <sub>1-x</sub> Ca <sub>x</sub> MnO <sub>3</sub> : MgO <sup>24</sup> Co: BaZrO <sub>3</sub> <sup>35</sup> Fe: BaTiO <sub>3</sub> <sup>36</sup> Ni: SrTiO <sub>3</sub> <sup>37</sup>
Multiferroic	BiFeO <sub>3</sub> : CoFe <sub>2</sub> O <sub>4</sub> <sup>25</sup> BaTiO <sub>3</sub> : CoFe <sub>2</sub> O <sub>4</sub> <sup>13</sup>
Exchange Bias	LSMO: BiFeO <sub>3</sub> <sup>38</sup> LSMO: NiO <sup>31</sup>
Optical	BiFeO <sub>3</sub> : Sm <sub>2</sub> O <sub>3</sub> <sup>8</sup> Au-VO <sub>2</sub> <sup>39</sup> Au-LiNbO <sub>3</sub> <sup>40</sup> Au: BaTiO <sub>3</sub> <sup>41</sup> Cu: ZnO <sup>42</sup> Au: ZnO <sup>43</sup>

### 1.3.2 Strain Engineering in VAN thin films

Two types of strain exist in the VAN thin films: (i) substrate induced in-plane strain at the film/substrate interface, and (ii) out-of-plane strain along the vertical interface of the pillar/matrix interface. The in-plane strain is the sum of strain from both the pillar/substrate interface and matrix/substrate interface. In order to reduce the in-plane strain, the pillar or the matrix can show matching relationship in one of the following three possibilities: (i) cube-on-cube with no in-plane rotation, (ii) cube-on-cube with 45° in-plane rotation, and (iii) irregular matching with some in-plane rotation. Case (i) occurs in systems when both the film and substrate are cubic/pseudo cubic and have a lattice parameter close to 1:1 or 2:1 ratio. Examples of such systems include BTO:CFO, BFO:CFO, and BFO:LSMO on STO (001) substrate.<sup>13,38,44</sup> When the lattice parameter ratio of the film and substrate is close to  $\sqrt{2}$ : 1, then case (ii) occurs in systems such as BTO:CeO<sub>2</sub>, BTO:YMO,

BTO:Sm<sub>2</sub>O<sub>3</sub> and LSMO:CeO<sub>2</sub> on STO (001) substrate.<sup>26–28,45</sup> However, when the film and substrate have different crystal structure and a large lattice mismatch, then case (iii) takes place in systems such as LSMO:ZnO on STO (001) substrate.<sup>29,46</sup>

Substrate-induced strain exists only up to a few nm (~50 nm) after which film relaxation occurs through the formation of dislocations in single phase thin films. In contrast, the out-of-plane strain present at the vertical interface of pillar/matrix can exist in a much thicker film (up to few μm) in VAN thin films. Vertical strain between the two phases can be greatly reduced through domain matching epitaxy (DME). For example, in LSMO:ZnO VAN structure, five of LSMO (001) planes match with six of ZnO (11 $\bar{2}$ 0) planes to reduce the vertical to ~0.5%.<sup>46</sup> In addition, different secondary phases can be explored to tune the vertical strain of the primary phase. For example, the out-of-plane lattice parameter of LSMO is 3.86 Å on STO substrate, which can be increased to 3.89 Å in the LSMO:ZnO VAN system and further to 3.95 Å in the LSMO:YSZ system.<sup>6</sup> Therefore, strain tuning of both the lateral and vertical strain can successfully tailor the microstructure of the film and its physical properties.

### 1.3.3 Advantages of VAN thin films

The growth of VAN thin films offers several advantages. VAN architecture allows the growth of materials with high lattice mismatch with the substrate. During VAN growth, both the phases synergistically work to reduce the mismatch induced strain (both in-plane and out-of-plane) within the film. Usually, material with a large lattice mismatch with the substrate grows with poor epitaxial quality or even as polycrystalline films. For example, Sm-doped CeO<sub>2</sub> (SDC) single phase film grows as a polycrystalline film on Nb-doped STO (001) substrate since SDC has a fluorite structure as compared to the perovskite structure of STO.<sup>47</sup> Interestingly, good epitaxy film is formed when SDC is grown with STO as the secondary phase to form VAN. This is due to the vertical interface coupling between SDC and STO, which helps stabilize the SDC phase. Since the two phases are vertically strained, the films can be strained up to a larger thickness as compared to the single-phase thin films in the VAN architecture.

VAN thin films allow easy integration of different functionality, including ferroelectric, ferromagnetic, photocatalytic, superconducting and optical properties. In addition, VAN also allow tunability of these physical properties by changing the pillar density, pillar diameter and pillar morphology. For example, (La<sub>0.7</sub>Sr<sub>0.3</sub>MnO<sub>3</sub>)<sub>0.67</sub>:(CuO)<sub>0.33</sub> (LSMO:CuO) has been

demonstrated as VAN to exhibit magnetoresistance (MR) properties.<sup>30</sup> Interestingly, by changing the growth kinetics (i.e. deposition frequency) and substrate-induced strain (by choosing different substrates), the MR% can be tuned from ~9% to ~80%. Therefore, VAN systems provide a lot of opportunities for materials selection to attain tunable physical properties.

## 1.4 Materials Systems

### 1.4.1 Titanium Dioxide (TiO<sub>2</sub>)

TiO<sub>2</sub> has been heavily researched upon for its photocatalytic properties<sup>48</sup> and its application in water-splitting<sup>49</sup>, water purification,<sup>50</sup> degradation of pollutants and organic molecules<sup>51</sup>, and solar cells<sup>52</sup>. Moreover, it has found numerous other applications such as in memristor<sup>53</sup>, gas sensor<sup>54</sup>, electrochromic devices<sup>55</sup>, optical coatings<sup>56</sup>, and cosmetic products<sup>57</sup>. In bulk, TiO<sub>2</sub> mainly crystallizes in three major crystal structures: (i) Rutile (tetragonal, a=b=4.58 Å, c=2.95 Å), (ii) Anatase (tetragonal, a=b=3.78 Å, c=9.50 Å), and (iii) Brookite (rhombohedral, a=5.44 Å, b=9.17 Å, c=5.14 Å). However, only the rutile and anatase phases of TiO<sub>2</sub> are important for the photocatalytic applications. In both the structures, the titanium atom is surrounded by a distorted oxygen octahedra as shown in Figure 1-13.<sup>58,59</sup>

Fabricating TiO<sub>2</sub> in thin film offers the flexibility of stabilizing either rutile or anatase phase depending on the specific application. For example, STO (001) is effective in stabilizing the anatase phase up to a critical thickness while Al<sub>2</sub>O<sub>3</sub> (0001) is effective in stabilizing the rutile phase. The photocatalytic properties of TiO<sub>2</sub> is limited by its high bandgap (3 eV for rutile and 3.2 eV for anatase phase), due to which it is activated only in the UV regime. Since the solar electromagnetic spectrum comprises 48% of visible light and only 5% of ultraviolet light, a very small portion of the spectrum is captured<sup>60</sup>. Depositing TiO<sub>2</sub> as thin films also helps tune the band gap by controlling the stoichiometry, oxygen defects, and strain on the TiO<sub>2</sub> film.

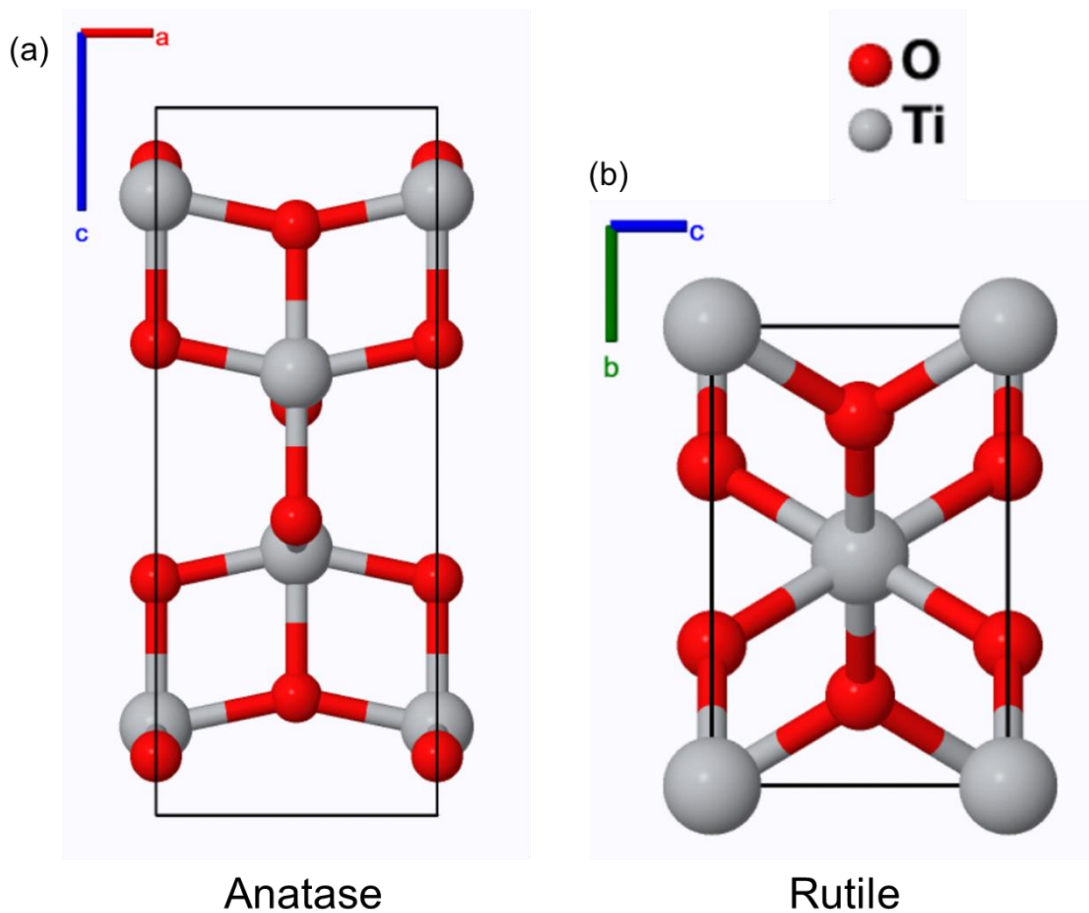


Figure 1-13: Schematic of the crystal structure of  $\text{TiO}_2$  showing the rutile and anatase phase<sup>58,59</sup>

#### 1.4.2 Barium Titanate ( $\text{BaTiO}_3$ )

$\text{BaTiO}_3$  (BTO) is a typical perovskite of the type  $\text{ABO}_3$ . It crystallizes as a tetragonal structure ( $a=b=3.994 \text{ \AA}$ ,  $c=4.038 \text{ \AA}$ ) at room temperature with a  $c/a$  ratio in between 1.0 and 1.005. The Ba atoms are present at the corners while the face center is occupied by the O atoms. Ti atom is slightly displaced from the body center (driven by the Gold-Schmidt factor) which gives rise to an inherent dipole in the unit cell. Due to the non-centrosymmetric crystal structure of BTO, it possesses piezoelectricity (bulk  $d_{33}$  value of  $80 \text{ pm/V}$ ).<sup>61</sup> In addition, it also has the property of the spontaneous polarization reversal on reversing the applied electric field, which gives rise to its ferroelectric nature. When heated above its Curie temperature ( $T_c=120^\circ\text{C}$ ), the crystal structure transforms from a less symmetric tetragonal structure to a more symmetric cubic structure as shown in Figure 1-14. This increase in symmetry changes the BTO structure from the non-centrosymmetric structure to a centrosymmetric structure.

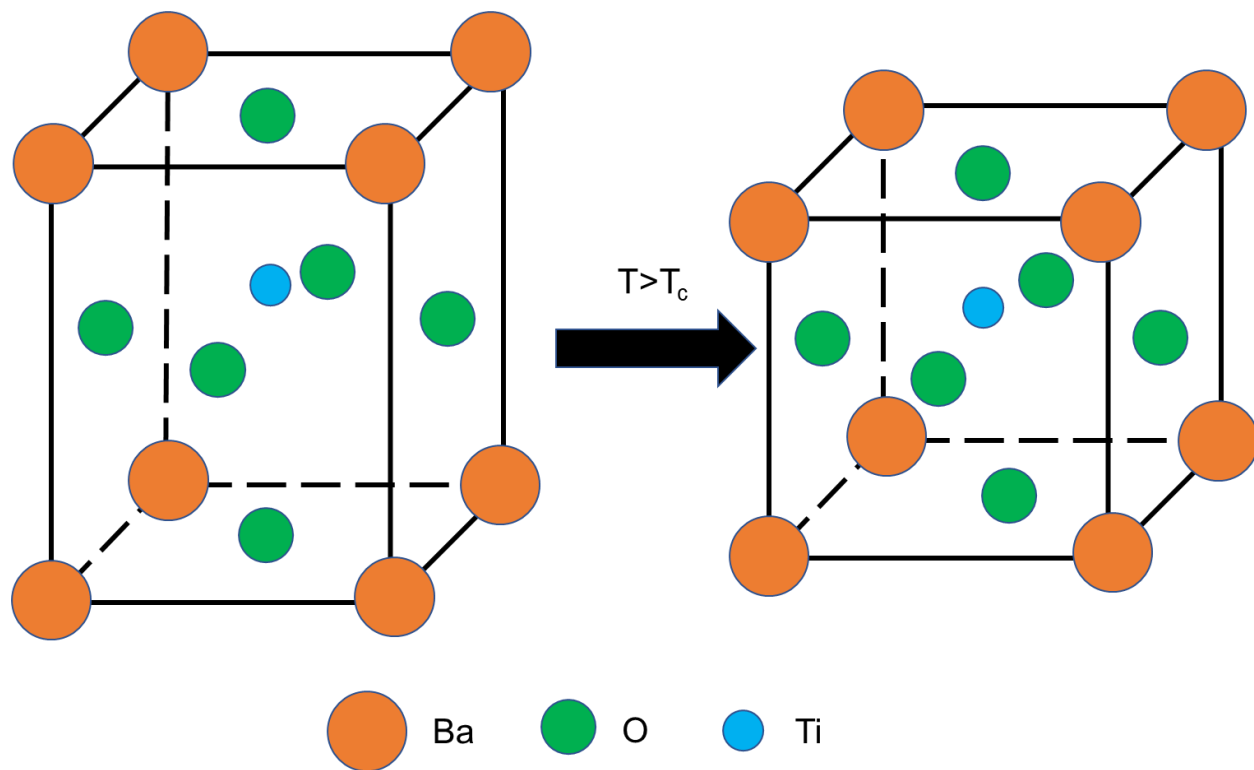


Figure 1-14: Schematic of the BaTiO<sub>3</sub> crystal structure showing the phase transition from the tetragonal to cubic phase

However, the Curie temperature of BTO can be effectively tuned by applying substrate-induced strain on the film. From the temperature-strain phase diagram of BTO<sup>62</sup>, it is evident that metastable phases can also become stable due to strain. For example,  $T_c$  can be increased from 120°C to 800°C by applying a 2.5% tensile strain on the BTO film. Such strain can also be maintained up to a larger thickness by introducing secondary phases such as ZnO, present as vertical pillars. Thus, tuning the strain in BTO also tunes its ferroelectric to paraelectric transition temperature.

In addition, BTO also possesses a high anisotropic dielectric constant with  $\epsilon_a/\epsilon_c$  to be around 20:1 at room temperature.<sup>63</sup> This is mainly due to the different double-well potential present along the  $a$  and  $c$  axis, which is discussed in more detail in section 1.5.1. Owing to its high permittivity, dielectric constant and spontaneous polarization at room temperature, BTO is widely used as thin film capacitors, dynamic random-access memories, chemical sensors, optical modulators, waveguides and microwave devices.<sup>64</sup>

### 1.4.3 Zinc Oxide (ZnO)

ZnO is a direct wide bandgap ( $E_g=3.3$  eV) semiconductor with many applications in piezoelectric transducers, photocatalysts, luminescence and actuators. In bulk form, ZnO exists in three different crystal structures: (i) wurtzite, (ii) zinc blende, and (iii) rocksalt, as shown in Figure 1-15.<sup>65</sup> Under ambient temperature and pressure, the hexagonal wurtzite phase is the thermodynamically most stable and can be obtained on different single-crystalline substrates such as STO, MgO and sapphire by various deposition parameters. The wurtzite unit cell is hexagonal with  $a=b=3.25$  Å,  $c=5.21$  Å with  $c/a$  ratio to be 1.633. However, from the epitaxial stabilization model for thin films, the cubic zinc blende phase can be obtained with a cubic (001) ZnS buffer layer. While the rocksalt phase can only be obtained at relatively high pressure.<sup>66,67</sup>

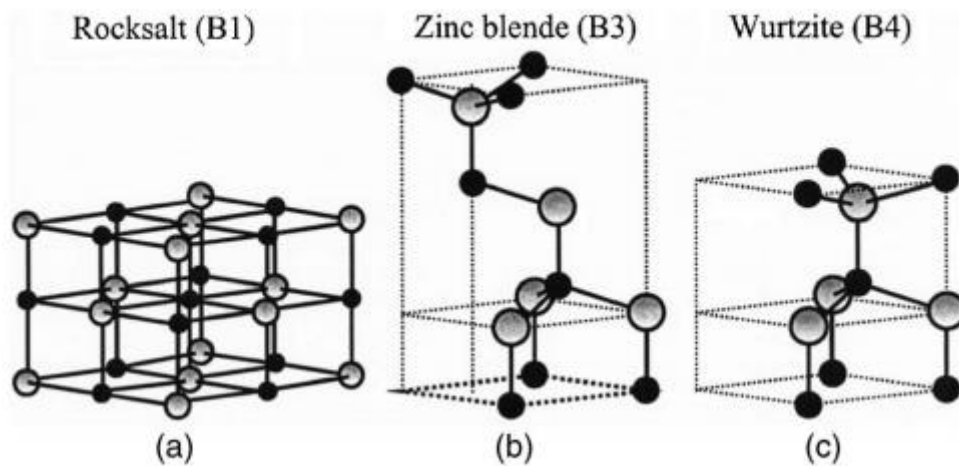


Figure 1-15: Schematic of the crystal structure of ZnO showing its three phases: rocksalt, zinc blende, and wurtzite<sup>65</sup>

ZnO has been synthesized in a variety of nanostructures, including nanorods, nanowires, nanorings and highly ordered nanowires. These structures have been obtained using chemical vapor deposition (CVD), metal-organic CVD, aqueous solution growth, electrodeposition and pulsed laser deposition. For example, highly ordered ZnO nanowires can be obtained using Au catalyzed growth of ZnO using CVD via the Vapor-Liquid-Solid (VLS) mechanism. In addition, controlling the defects in ZnO is very critical for its application in opto-electronic devices. ZnO is naturally a n-type semiconductor due to the presence of intrinsic defects including oxygen vacancies and zinc interstitials which act as a donor. The n-type conductivity can also arise from

the hydrogen which gets unintentionally doped and acts as a shallow donor. Therefore, controlling the intrinsic defects and doping of ZnO can drastically change its ionic conductivity, thereby making ZnO very useful for applications such as sensors, LEDs and solar cells.

## 1.5 Functionality

### 1.5.1 Ferroelectricity

Ferroelectricity is a property shown by materials to exhibit spontaneous polarization which can be reversed on the application of electric field. Out of the 32-point groups, ferroelectricity is shown by only those materials who belong to the 10 polar point groups. Therefore, a material must be non-centrosymmetric in order to exhibit ferroelectricity. Since a small electric field can create a large polarization, the dielectric constant of ferroelectric materials is generally very high ( $\epsilon_r > 1000$ ). If a ferroelectric material is heated above a critical temperature (called Curie temperature), it changes its crystal structure, becoming centrosymmetric thereby losing its spontaneous polarization. Now that the material has become paraelectric, it behaves Curie-Weiss law which relates the electric susceptibility to the Curie temperature. However, the dielectric permittivity shows an anomalous increase around the Curie temperature. This increase simply means that it is easiest to increase the electric polarization when the material is undergoing a change from ferroelectric to paraelectric.<sup>68</sup>

The switching mechanism in ferroelectrics can be explained based on Landau theory. From thermodynamics, free energy can be expanded in terms of polarization if we ignore the strain energy. Solving the free energy for its minima, we can get the equilibrium free energy which depend on the sign of the coefficient  $a$  (eq. 3.2). When  $a > 0$ , free energy has a minimum at  $P=0$  for  $E=0$  and behaves as a paraelectric material. However, when  $a < 0$ , the free energy minimizes at some finite polarization  $P(\neq 0)$ . As expected, below the Curie temperature, there are two minimum states of free energy at some finite polarization. The polarization can be switched overcoming the free energy barrier which is generally done by providing electric field. However, above the Curie temperature, the free energy minimizes when the polarization is zero. This means that there is no polarization when there is no electric field. Hence, the material is paraelectric above  $T_c$ .<sup>63,64,69,70</sup>

$$f = f_0 + \frac{\partial f}{\partial P} P + \frac{\partial^2 f}{\partial P^2} \frac{P^2}{2!} + \frac{\partial^3 f}{\partial P^3} \frac{P^3}{3!} + \frac{\partial^4 f}{\partial P^4} \frac{P^4}{4!} + \frac{\partial^5 f}{\partial P^5} \frac{P^5}{5!} + \frac{\partial^6 f}{\partial P^6} \frac{P^6}{6!} + \dots - PE \quad (1.7)$$

$$f = aP^2 + bP^4 + cP^6 + \dots \quad (1.8)$$

Ferroelectricity is typically possessed by perovskite materials of the type  $ABO_3$  such as  $BaTiO_3$  and  $PbTiO_3$ . The crystal structure of  $BaTiO_3$  is shown in Figure 1-16. On the application of an electric field,  $Ti^{4+}$  ion undergoes a displacement along the  $c$  axis from its equilibrium position. This causes an increased interaction with two (out of six)  $O^{2-}$  ions, along the  $c$  axis, which gives rise to a dipolar polarization. A deep double-well potential ( $\Delta E=11.7$  meV) is present along the  $c$ -axis as compared to the very shallow double-well potential ( $\Delta E=0.8$  meV) present along the  $a$ -axis, therefore, making the shorter axis to be more polarizable.<sup>71</sup> This is due to the increased interaction of two out of the six  $O^{2-}$  ions (along the  $c$ -axis) with  $Ti^{4+}$  ions, thereby, reducing their electronic polarizabilities. This causes the permittivity of  $BaTiO_3$  to be larger along the  $a$  axis as compared to the  $c$  axis.

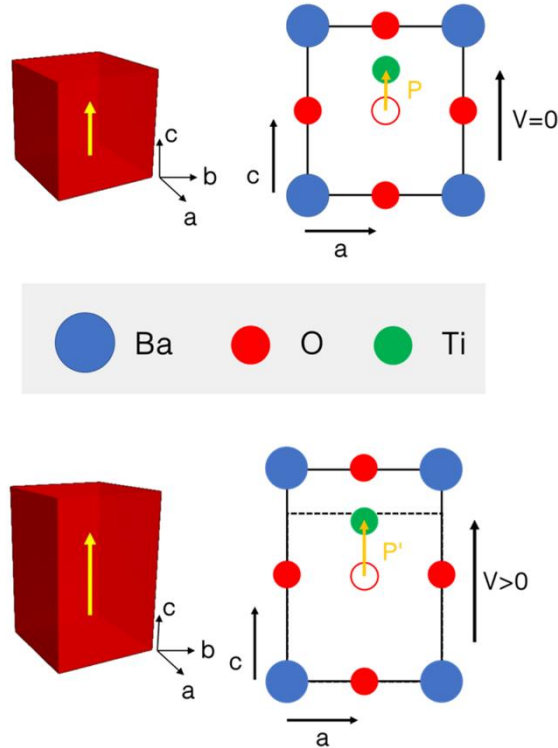


Figure 1-16: Schematic of the  $BaTiO_3$  crystal structure showing the tetragonal distortion on applying voltage

The ferroelectric properties of materials can be typically tuned by applying substrate induced lateral strain or nanocomposite induced vertical strain. Figure 1-17 shows one such design where a ferroelectric PZT film is epitaxially grown on the Nb-doped STO (conducting) substrate. On applying bias on the substrate, non-switchable domains are observed near the interface of substrate and film using dark field transmission electron microscopy (TEM) and scanning TEM (STEM). The contrast of the  $180^\circ$  head-to-head domain switching in DF TEM is confirmed using STEM where we can see shifting in the position of atom leading to up and down polarization ( $P_{up}$  and  $P_{down}$ ). The P-E hysteresis loop also confirms the rapid switching in negative biasing as observed in TEM. Electric field distribution shown in Figure 1-17b helps explain this effect. Essentially, electric field is concentrated near the substrate and film during positive biasing while no fields are found near the interface for negative bias. This unidirectional bias field doesn't generate enough field for polarization switching under negative bias. Therefore, PZT/Nb-STO yields only  $P_{up}$  which is thus nonswitchable. Such a kind of nanocomposite can find application in imprint applications and retention loss.<sup>72</sup>

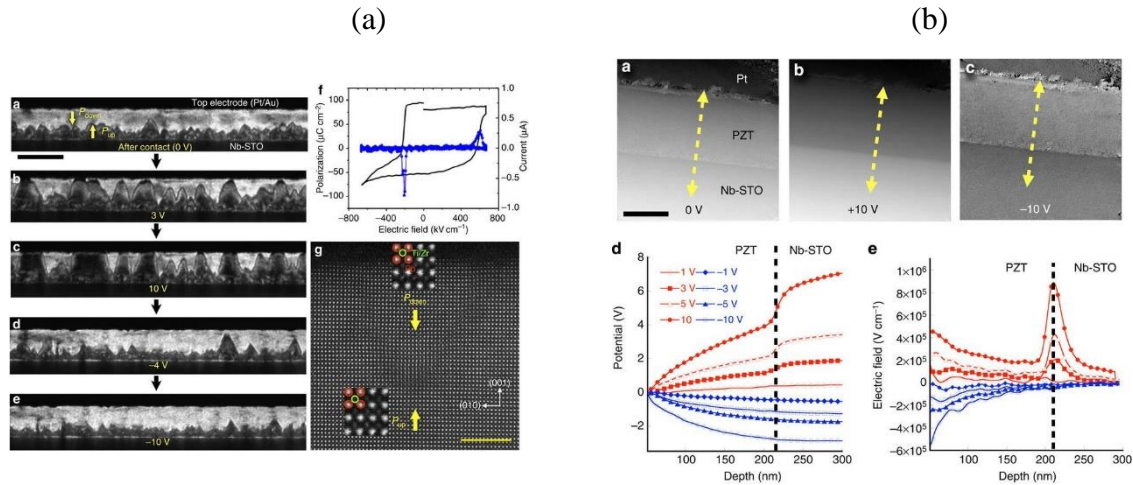


Figure 1-17. (a) Non-switchable ferroelectric domains observed using DF-TEM. STEM-HAADF image shows the displacement of atoms and ferroelectric hysteresis loop (b) Mapping of electrostatic potential and electric field mapping<sup>72</sup>

Another way to tune the ferroelectric properties is by applying vertical strain using VAN. VAN structures can sustain vertical strain up to a large film thickness due to strain coupling between the vertical phases. Figure 1-18 shows the  $c$  lattice parameter of the  $\text{BaTiO}_3\text{-Sm}_2\text{O}_3$  (BTO-Smog) VAN.<sup>27</sup> It can be seen that the BTO-SmO nanocomposite of 800 nm thickness maintains its

tetragonal distortion up to 800°C, due to the presence of uniform and vertical strain coupling between the 10 nm columnar SmO pillars and the surrounding BTO matrix.

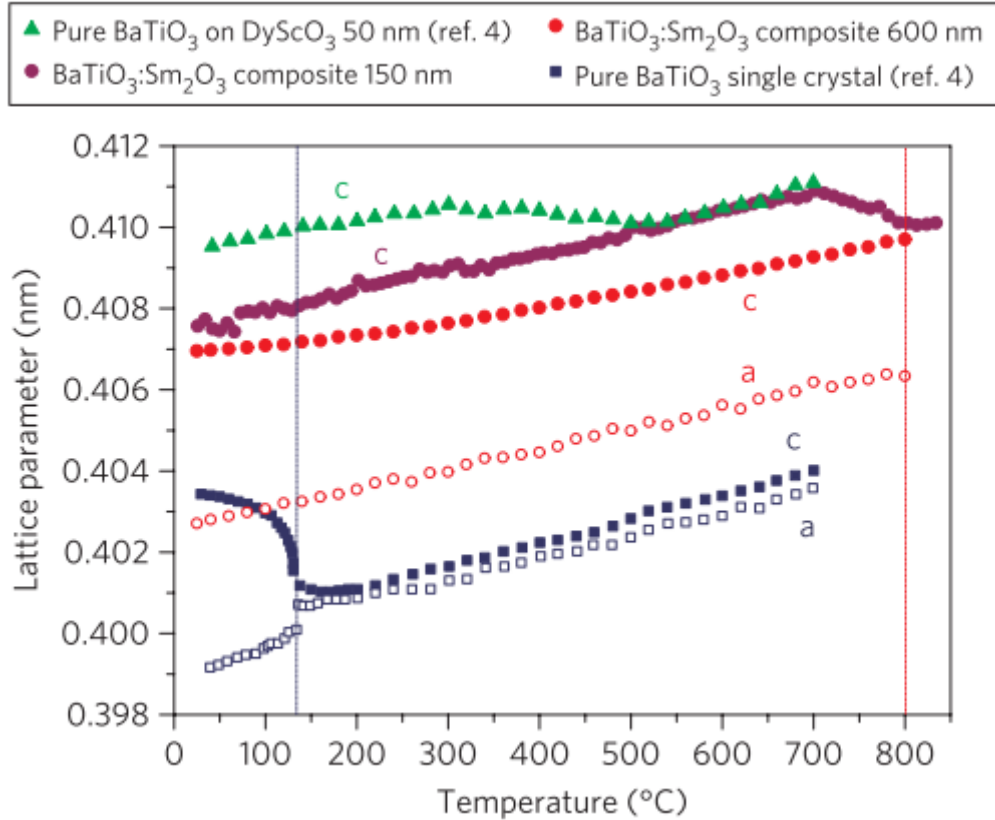


Figure 1-18: Comparison of the variation of  $a$  and  $c$  lattice parameters of pure BaTiO<sub>3</sub> and BaTiO<sub>3</sub>:Sm<sub>2</sub>O<sub>3</sub> composite as function of temperature<sup>27</sup>

### 1.5.2 Plasmonics

Application of nanocomposites can also be based on photon-matter interaction by which they can be extensively used in plasmonics. Plasmonics is essentially the study of interaction between free electrons in metal and electromagnetic field as shown in Figure 1-19.<sup>73</sup> Electric field in an electromagnetic wave varies sinusoidally which causes the free electrons to oscillate sinusoidally. Electron motion is confined by the metal-dielectric boundary thus limiting its oscillation path. These oscillating free electrons are called surface plasmons. Consequently, when frequency of light matches the resonant frequency of oscillating particles, surface plasmons show an enhanced optical interaction between particle and incident light. This effect is called Surface Plasmon

Resonance (SPR). At SPR frequency, plasmonic structures can interact with light more than 50 times as compared in the off-resonance state because of induced electromagnetic forces.

The mechanism of the optical scattering and absorption properties of metal nanoparticles was first proposed by Gustav Mie in 1908. Since then, a lot of work has been done experimentally and theoretically to understand the optical effect with shape and size. For example, if the size of a nanoparticle is larger, we require a larger wavelength of light in order to oscillate the free electrons in the material. Thus, surface plasmon resonance frequency can be tuned by the shape and size of plasmonic nanoparticles.<sup>74</sup>

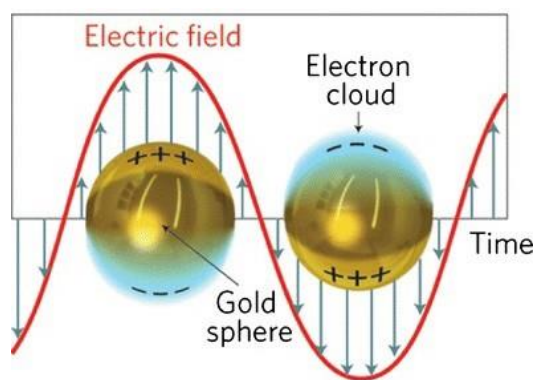


Figure 1-19: Surface plasmon resonance in gold nanoparticle<sup>73</sup>

A plasmonic particle can interact with light through 2 ways: (i) absorption of light by the particle and (ii) scattering of light away from the incident direction. Their sum is called extinction. Absorption and scattering efficiency become large when material permittivity reaches twice the negative permittivity of medium. Fortunately, metals show negative permittivity and thus show plasmonic behavior. However, very few metals such as Au, Ag, Cu, Pd and Pt show resonance in visible region. Au and Ag show strong resonance while Pd and Pt show weak and Cu is very susceptible to forming oxides and is not stable.<sup>75</sup>

It is also important to model the optical response of these plasmonic metals to gain an insight into their optical properties. The refractive index and permittivity response of the metals can be modeled by using a Drude-Lorentz model.<sup>76</sup> The permittivity response of a Lorentz oscillator is modeled by considering the driving force (incoming electromagnetic radiation), damping force (collisions with other electrons) and the spring constant (restoring force) and is given by:

$$\epsilon_r(\omega) - 1 = \frac{\omega_p^2(\omega_0^2 - \omega^2)}{(\omega_0^2 - \omega^2)^2 + \omega^2\gamma^2} \quad \epsilon_r(\omega) - 1 = \frac{\omega_p^2(\omega_0^2 - \omega^2)}{(\omega_0^2 - \omega^2)^2 + \omega^2\gamma^2} \quad (1.9)$$

where  $\omega$  is the frequency of the electromagnetic radiation,  $\epsilon_r(\omega)$  and  $\epsilon_i(\omega)$  is the real and imaginary part of the permittivity as a function of  $\omega$ , respectively,  $\omega_p$  is the plasmonic frequency,  $\omega_0$  is the resonance frequency and  $\gamma$  is the damping constant. For a bulk plasma, the plasmonic frequency  $\omega_p$  is given by:

$$\omega_p^2 = \frac{ne^2}{\epsilon_0 m} \quad (1.10)$$

where  $n$  is the charge carrier density,  $e$  is the electronic charge,  $\epsilon_0$  is permittivity of free space and  $m$  is the electron mass. Evidently, the plasma frequency is proportional to the number of electron density and is different for different materials. Due to presence of a large number of free electrons in metals, the restoring force for electrons can be assumed to be 0, i.e.,  $\omega_0=0$ , which gives rise to a Drude-Lorentz model as follows:

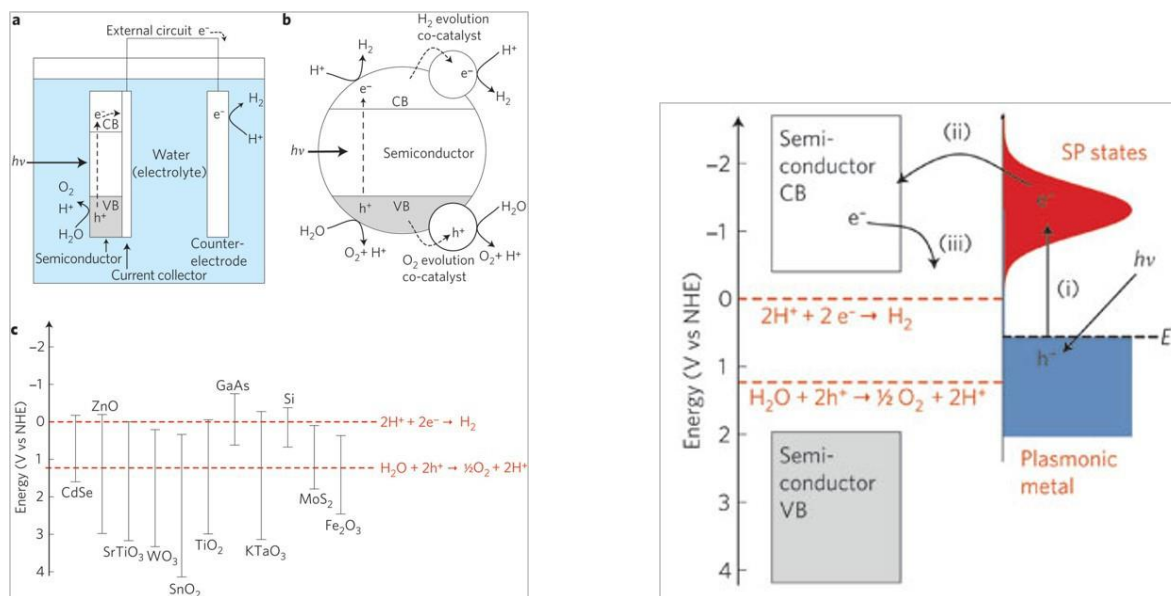
$$\epsilon_m = 1 - \frac{\omega_p^2}{\omega^2 + i\gamma\omega} \quad (1.11)$$

If the incident frequency is below the plasma frequency, the charge carriers can screen out the electric field and the incident wave is reflected. Therefore, the permittivity of metal is negative below the plasma frequency, which is particularly useful since it allows resonances to be set-up.

Nowadays, plasmonics is finding a range of applications from invisibility cloaks, superlenses, photocatalysts and photovoltaics which can be made more efficient.<sup>77-86</sup> Around 44% of the solar light lies in the visible region which is why the noble plasmonic materials such as Ag and Au become important. Figure 1-20a illustrates the semiconductor photocatalysis in the presence and absence of plasmon.<sup>80</sup> In this work, photocatalyst is used in water-splitting stimulated by UV-Vis light. Water-splitting process requires two half reactions to take place: hydrogen-evolution half reaction at cathode and oxygen-evolution half reaction at anode. Most of the catalysts of interest have their conduction band just near 0V on the near-hydrogen scale (NHE) scale. Ideally, it should be between -1V and 0V so that electrons can be provided for the hydrogen-evolution half reaction.

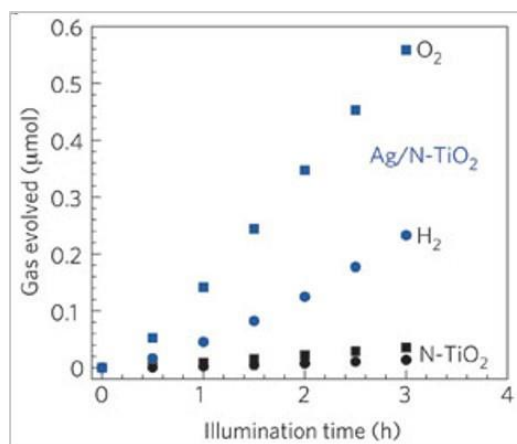
Many semiconductors which are good catalysts as shown in Figure 1-20 but cannot provide electrons for hydrogen-evolution half reaction. Although, they are good catalysts, but they have a huge band gap because of which they can only absorb 7% of the solar spectrum which lies in the UV region. Therefore, plasmonic nanostructures is the natural choice to make use of the visible spectrum and to provide energetic electrons to complete hydrogen-evolution half reaction.

Plasmonic-metal nanostructures in semiconductor can excite electrons near the fermi level to surface plasmon (SP) states shown in Figure 1-20b.<sup>80</sup> Since the electronic energy states are aligned, electrons get transferred from the SP states to semiconductor particle which can drive the hydrogen-evolution half-reaction. Efficiency of water-splitting by this nanocomposite structure is proven by measuring the hydrogen and oxygen gas evolved in plasmonic (more) and non-plasmonic (less) nanostructures (Figure 1-20c).<sup>78</sup> Hence, using plasmonic nanoparticles can efficiently couple light harvesting and catalytic function.



(a)

(b)



(c)

Figure 1-20: (a) Schematic showing semiconductor photocatalysis in the presence and absence of plasmon (b) Mechanism of plasmon-induced charge transfer<sup>80</sup>(c) Hydrogen and oxygen gas evolution in the presence and absence of plasmon<sup>78</sup>

### 1.5.3 Hyperbolic Metamaterials

Metamaterials are artificially structured materials with properties not found in nature. Among them, electromagnetic metamaterials are composed of sub-wavelength building blocks arranged in an ordered fashion that can be used for exotic optical properties. The ordered building blocks give rise to an emergent new property which are not found in the constituent materials. Metamaterials offer extensive opportunities for engineering the light-matter interaction, ideal for

achieving exotic optical properties including optical magnetism,<sup>87</sup> negative refraction,<sup>88</sup> and hyperbolic dispersion<sup>89</sup> which have potential applications in the field of optical computing, cloaking and sub-diffraction imaging.

One such class of metamaterials is hyperbolic metamaterial (HMM), which can be realized with the use of metal-dielectric nanocomposites. HMM derive their name from the iso-frequency surface of the extraordinary wave which is given by:

$$\frac{k_x^2 + k_y^2}{\epsilon_{\perp}} + \frac{k_z^2}{\epsilon_{\parallel}} = \frac{\omega^2}{c^2} \quad (1.12)$$

where  $\omega$  and  $c$  is the frequency and the speed of light and  $k$  is the wavevector of the electromagnetic wave. All the variables except  $\epsilon_{\perp}$  and  $\epsilon_{\parallel}$  are positive, since they are squared. When both  $\epsilon_{\perp}$  and  $\epsilon_{\parallel}$  are positive, the iso-frequency surface is an ellipsoid. When both  $\epsilon_{\perp}$  and  $\epsilon_{\parallel}$  are negative, the material behaves as a metal and doesn't support any propagation of wavevectors. However, when either of  $\epsilon_{\perp}$  or  $\epsilon_{\parallel}$  is negative and is of opposite sign as compared to the other, the iso-frequency opens into a hyperboloid, either with one sheet or two sheets. Specifically, when  $\epsilon_{\perp} < 0$  and  $\epsilon_{\parallel} > 0$ , the HMM is defined as a class 1 hyperbolic metamaterial, with its iso-frequency surface being a hyperboloid of one sheet. Similarly, when  $\epsilon_{\perp} > 0$  and  $\epsilon_{\parallel} < 0$ , the HMM is defined as a class 2 hyperbolic metamaterial, with its iso-frequency surface being a hyperboloid of two sheets as shown in Figure 1-21.

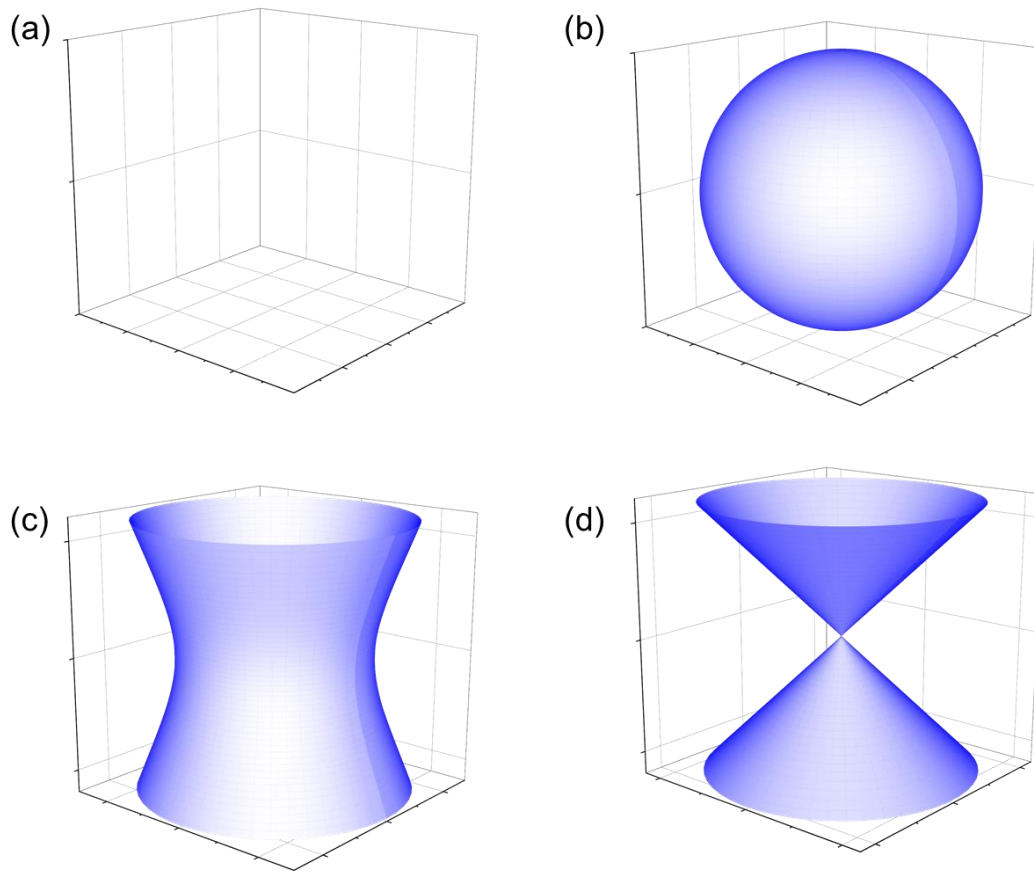


Figure 1-21: Iso-frequency curves for (a) metal, (b) isotropic dielectric, (c) hyperbolic material with one sheet, and (d) hyperbolic material with two sheets

Very few naturally hyperbolic metamaterials, since they require highly anisotropic structure. Since metal has a negative permittivity and dielectric has a positive permittivity at optical frequencies, HMM have a highly anisotropic structure, composed of metal and dielectric units. They can be fabricated either as metal-dielectric layers stacked alternatively on top of each other (2-2 design) and as metallic nanopillars embedded in the dielectric matrix as a VAN structure (1-3 design). The unit cells of the HMM for both the designs should be far below the operating wavelength. The major advantage of using the VAN design over the 2-2 multilayer design is the low optical losses and high transmission due to the lesser metal fill fraction needed to achieve the HMM property. The iso-frequency surface of HMM is hyperbolic, so they can support the propagation of extremely high wavevectors at that wavelength, which are normally evanescent and decay exponentially in air or vacuum.<sup>90,91</sup> Therefore, there are no evanescent waves in hyperbolic

which gives rise to many applications including sub-diffraction imaging, sub-wavelength modes and enhanced photonic density of states.

One of the first demonstration of HMM was done using 16 Ag/Al<sub>2</sub>O<sub>3</sub> multilayers, each with a thickness of 35 nm, deposited on a quartz substrate with a half-cylindrical cavity using electron-beam evaporation as shown in Figure 1-22.<sup>84</sup> Upon illumination of this metamaterial with an incident light of wavelength  $\lambda=365$  nm, the metamaterial was able to resolve to image features with a spacing as small as 125 nm. The same objects could not be imaged with the same instrumental setup without the HMM present. Such property of HMM can be useful in applications such as nanolithography and bio-molecular imaging.

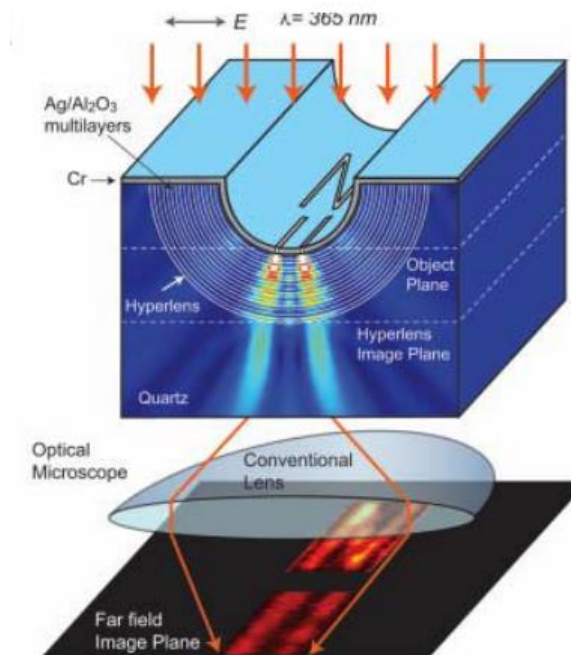


Figure 1-22: Schematic of the hyperlens consisting of alternating Ag/Al<sub>2</sub>O<sub>3</sub> multilayers and the simulation of sub-diffraction-limited optics<sup>84</sup>

Another way to fabricate the HMMs is through the self-assembly process by co-growing metallic and dielectric phases. Recently, a self-assembled two-phase Au-BTO epitaxial thin film on STO (001) has been demonstrated. The Au-BTO system forms a VAN with Au present as vertical pillars embedded in the BTO matrix. Due to the highly anisotropic structure of the nanocomposite, the nanocomposite shows metallic properties in the out-of-plane direction and dielectric properties in the in-plane direction. This property is shown by the permittivity response

in which the out-of-plane permittivity becomes negative at high wavelengths while the in-plane permittivity remains positive throughout the wavelength regime.

An interesting feature of the HMM is the existence of a wavelength regime where the effective medium dielectric constant is near zero. At these specific wavelengths, a component of the permittivity tensor goes through zero and are called epsilon-near-zero (ENZ) wavelength. In addition, tuning the effective electromagnetic response of the hyperbolic metamaterials by changing the ENZ wavelength is technologically important for realizing nonlinear material response in different wavelength regimes.<sup>92,93</sup> ENZ wavelength can be usually tuned by controlling the deposition parameters, post-annealing, dopant concentration, and varying the periodicity and width of the metallic phase.<sup>94,95</sup> Recent studies on tunable hyperbolic metamaterials, including Au-BaTiO<sub>3</sub> (Au-BTO) and Au-ZnO have focused on tuning the ENZ wavelength by varying the geometry and deposition conditions such as oxygen partial pressure and deposition frequency.<sup>43,96</sup> In these studies, careful microstructural control modulates the free electron density in the out-of-plane direction, thereby tuning the hyperbolic dispersion characteristic of the metal-dielectric nanocomposites.

## **1.6 Self-assembled metal-dielectric nanocomposite thin films**

Self-assembled nanocomposite thin films offer an interesting way towards functionality coupling and achieving novel physical properties. An extensive research has been conducted in the field of complex functional oxides and oxide-based nanocomposite, and functionalities ranging from ferromagnetic, ferroelectric, multiferroic, insulating, semiconducting, superconducting, and nonlinear optical effects have been demonstrated.<sup>13,14,22,27,45,46,97–102</sup> These functionalities and novel properties arise *via* intercoupling between charge, spin, orbital and lattice degree of freedom. Recently, ordered metal-dielectric hybrid structures have attracted considerable research interest due to their potential applications in optical metamaterials, catalysis, magnetic data storage, and energy storage applications.<sup>40,42,43,85,103–111</sup> Figure 1-23 shows the common fabrication techniques and applications for the metal-dielectric nanocomposites. Top-down fabrication techniques include e-beam lithography, nanoimprint lithography and focused ion beam for fabricating and designing oxide-metal nanocomposites.<sup>112–117</sup> For example, nanoimprint lithography can be used to pattern a substrate with sub-10 nm resolution,<sup>118</sup> over a large scale, which can be subsequently coupled with physical vapor deposition (PVD) techniques to fabricate metal-dielectric

nanocomposites. In addition, bottom-up approaches such as self-assembly, templated self-assembly and anodized alumina template method can also be used for the growth of metal-dielectric nanocomposites.<sup>41,106,119–121</sup> For example, PVD techniques can be used to fabricate a self-assembled metal-dielectric nanocomposite as a VAN or as a particle in matrix. Different combinations of metal-dielectric nanocomposites can find a wide variety of uses ranging from metamaterials, multiferroics, surface enhanced spectroscopy such as fluorescence, Raman spectroscopy and second harmonic generation to lab-on-a-chip applications, among many others as shown in Figure 1-23.<sup>41,84,91,122–130</sup>

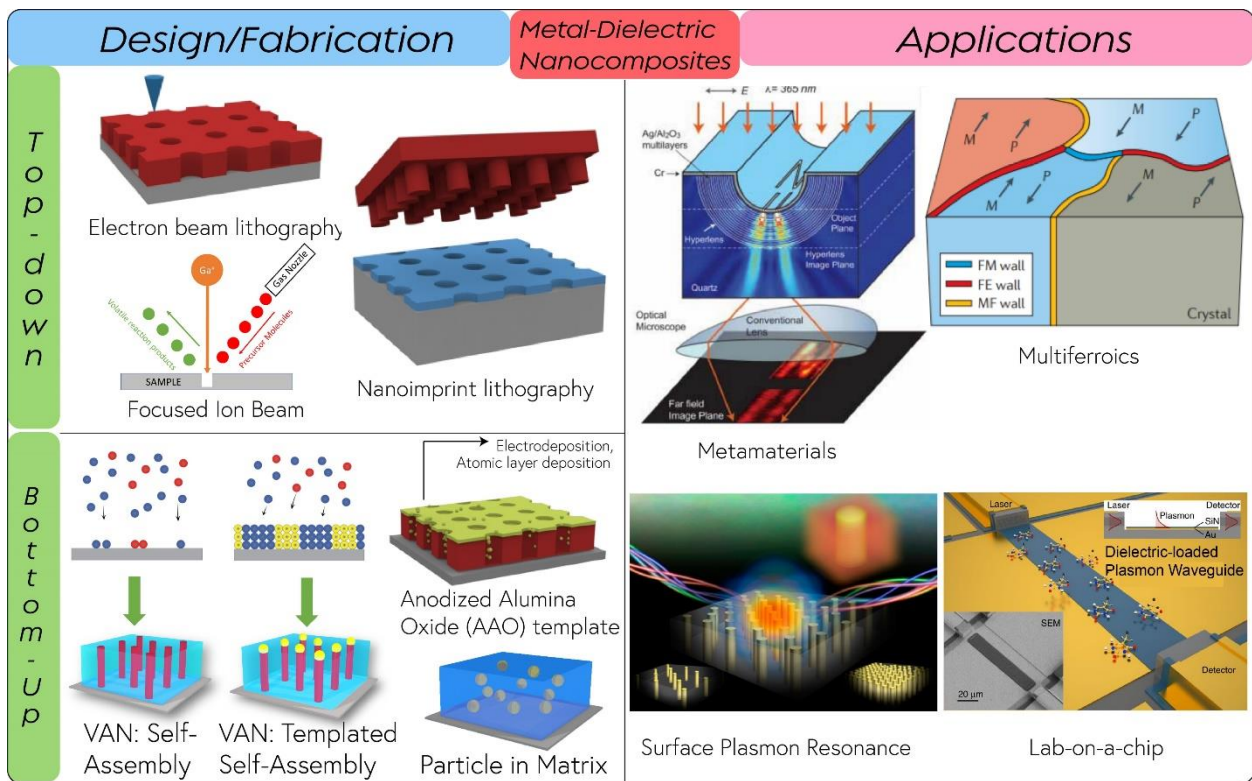


Figure 1-23. Overview of the metal-dielectric nanocomposites. Schematic illustration of the (a1) top-down design/fabrication techniques showing the nanoimprint lithography, focused ion beam and electron-beam lithography as labeled, and (a2) bottom-up techniques showing the self-assembly, templated self-assembly, particle-in-matrix and anodized alumina oxide template method. The various applications of the metal-dielectric nanocomposites are highlighted in (b). They can be used as metamaterials, multiferroics, SERS application and lab-on-a-chip.<sup>72,113–115</sup>

Typically, the metal-dielectric nanocomposite shows three types of morphology: (i) 0-3 particle in matrix, (ii) 2-2 multilayer, and (iii) 1-3 vertically aligned nanocomposite (VAN).

Among the 3 different common types of morphology, VAN are particularly interesting due their highly anisotropic and high interface-to-volume ratio, enabling fascinating physical properties. The vertical strain at the pillar/matrix heterointerface in vertically aligned nanocomposites (VAN), provides an extra degree of freedom for tuning the strain and physical properties. The in-plane strain can be tuned independently from the out-of-plane strain, with the stiffer phase dominating the final in-plane and out-of-plane state. The growth of VAN thin films offers several advantages. VAN architecture allows the epitaxial growth of materials with high lattice mismatch with the substrate.<sup>32,34,35,42</sup> Since the two phases are vertically strained, the films can be strained up to a larger thickness as compared to the single-phase thin films in the VAN architecture.<sup>27</sup> In addition, VAN thin films allow easy integration of different functionality, including ferroelectric, ferromagnetic, photocatalytic, superconducting and optical properties. Recently, several VAN systems have been demonstrated in a range of oxide-oxide systems where two different oxides grow as a VAN architecture using a single-step pulsed laser deposition (PLD) process.<sup>18,26,28–30,131</sup> For example, systems such as BaTiO<sub>3</sub>: CoFe<sub>2</sub>O<sub>4</sub>, BaTiO<sub>3</sub>: Sm<sub>2</sub>O<sub>3</sub> and La<sub>0.7</sub>Sr<sub>0.3</sub>MnO<sub>3</sub> (LSMO): ZnO have demonstrated room temperature multiferroicity, enhanced ferroelectricity and magnetoresistance respectively.<sup>13,27,46</sup> In comparison, self-assembled metal-oxide nanocomposites offer more opportunities in terms of functionality coupling such as magneto-optical, electro-optic and magneto-electric properties.

However, several challenges arise to achieve self-assembled metal-dielectric nanocomposites in epitaxial thin film form, due to the vastly different deposition conditions for oxides and metals. Difference in growth kinetics, surface wetting, (surface energy), oxygen diffusion as well as the potential inter-diffusion between the metal and oxides, make it very challenging to achieve epitaxial self-assembled metal-oxide nanocomposites. Very recently, several self-assembled metal-dielectric VAN systems have been successfully demonstrated such as Co-BaZrO<sub>3</sub>, Fe-BaTiO<sub>3</sub>, Au-BaTiO<sub>3</sub>, Ni-Ba(Zr<sub>0.8</sub>Y<sub>0.2</sub>)O<sub>3</sub>, etc.<sup>35,41,132</sup> Such VAN systems have the capability to couple the electric, magnetic and optical properties and give rise to an emergent new property which is not found in either of the phases. The formation of these self-assembled nanocomposites is driven by a combination of strain and surface energy minimization. Usually, the nanocomposite formation takes place by nucleation and growth during which strain energy play the major role in determining the final morphology during the initial seeding period due to the square dependence on strain as compared to the linear dependence on surface energy.

In this review, we first discuss the two different types of morphology, namely, particle in matrix and vertically aligned nanocomposite with some representative examples. In part I, two strain compensation models are proposed based on linear strain minimization and areal strain minimization. Based on the model, several case studies are discussed, comparing the microstructure and morphology of the different metal-dielectric nanocomposites by changing the dielectric phase. In part II, specific examples highlighting the coupling between the electrical, magnetic and optical properties are discussed of the metal-dielectric nanocomposites having both particle in matrix and VAN morphology.

### 1.6.1 Particle in Matrix and Vertically Aligned Nanocomposite

Metal-dielectric nanocomposites typically self-assemble as particle in matrix or as vertically aligned nanocomposite. Usually different crystal structures of metal and dielectric gives rise to the nanoparticles in matrix type nanocomposite, since it is difficult to maintain the vertical epitaxial relationship between different crystal structures.<sup>103,108,133–136</sup> Figure 1-24 shows a representative example of the metal nanoparticles in matrix. Figure 1-24a shows the Au-VO<sub>2</sub> nanocomposite (deposited on *c*-cut sapphire substrate) in which Au nanoparticles are uniformly distributed within the VO<sub>2</sub> matrix.<sup>39</sup> Au has a face-centered cubic crystal structure while VO<sub>2</sub> exist as a rutile structure at room temperature. VO<sub>2</sub> shows a highly textured growth, corresponding to the (020) plane along the *b* axis while Au NPs grow along the (111) plane, due to its lowest surface energy, along the out-of-plane direction. The plan-view HR-STEM images shown in Figure 1-24b shows the hexagonal lattice structure of Au particles, confirmed by the fast Fourier transform images (inset). The orientation relationship between Au and VO<sub>2</sub> is determined to be Au(011)//VO<sub>2</sub>(001) and Au(111)//VO<sub>2</sub>(020).

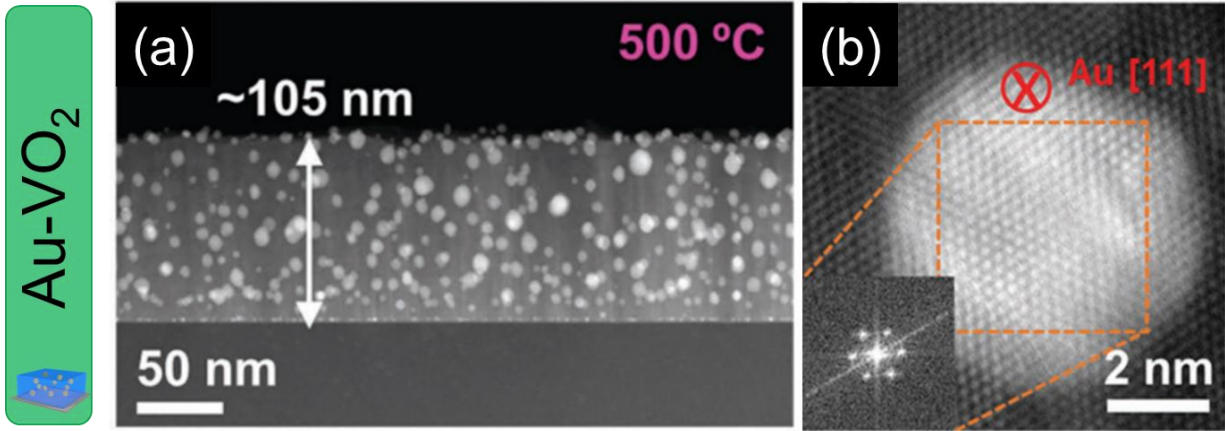


Figure 1-24: Particle-in-matrix design. (a) Cross-section STEM of the Au-VO<sub>2</sub> nanocomposite thin film deposited on Al<sub>2</sub>O<sub>3</sub> (0001) substrate and (b) HR-STEM of the Au nanoparticle embedded in VO<sub>2</sub>.<sup>39</sup>

A representative example of the metal-dielectric vertically aligned nanocomposite is Au-BaTiO<sub>3</sub> (Au-BTO) shown in Figure 1-25.<sup>41,96</sup> The Au phase is present as vertical pillars embedded in the BTO matrix (Figure 1-25b). The X-Ray Diffraction plot in Figure 3a shows the epitaxial growth of BTO on STO along the [001] direction while Au grows primarily along the [001] and [111] direction. The plan-view STEM image (Figure 1-25c) shows the faceted growth of Au nanopillars and the EDS elemental mapping (Figure 1-25d) shows no obvious inter-diffusion between the phases. The plan-view HR-STEM micrograph along the BTO <001> zone axis, shown in Figure 1-25e, shows the twin boundary in the Au pillar with inclined {111} planes, indicating that the Au pillar grows along the [011] orientation. From the cross-section HR-STEM image in Figure 3f, the Au pillar shows growth along the [002] out-of-plane direction. The enlarged image of the Au-BTO vertical interface (Figure 1-25g) shows the presence of coherent interface with a 1:1 lattice matching relationship. Based on the XRD and HR-STEM image analysis, the lattice matching relationship is determined to be (002)Au|| (002)BTO|| (002)STO, (022)Au|| (002)BTO|| (002)STO, and (111)Au|| (002)BTO|| (002)STO. Further, the Au pillar geometry can be modified by varying the growth kinetics such as deposition frequency and laser energy. Therefore, VAN architecture allows the vertical interface coupling between the two phases and maintains the strain in the film up to a much greater thickness as compared to single-phase thin films.

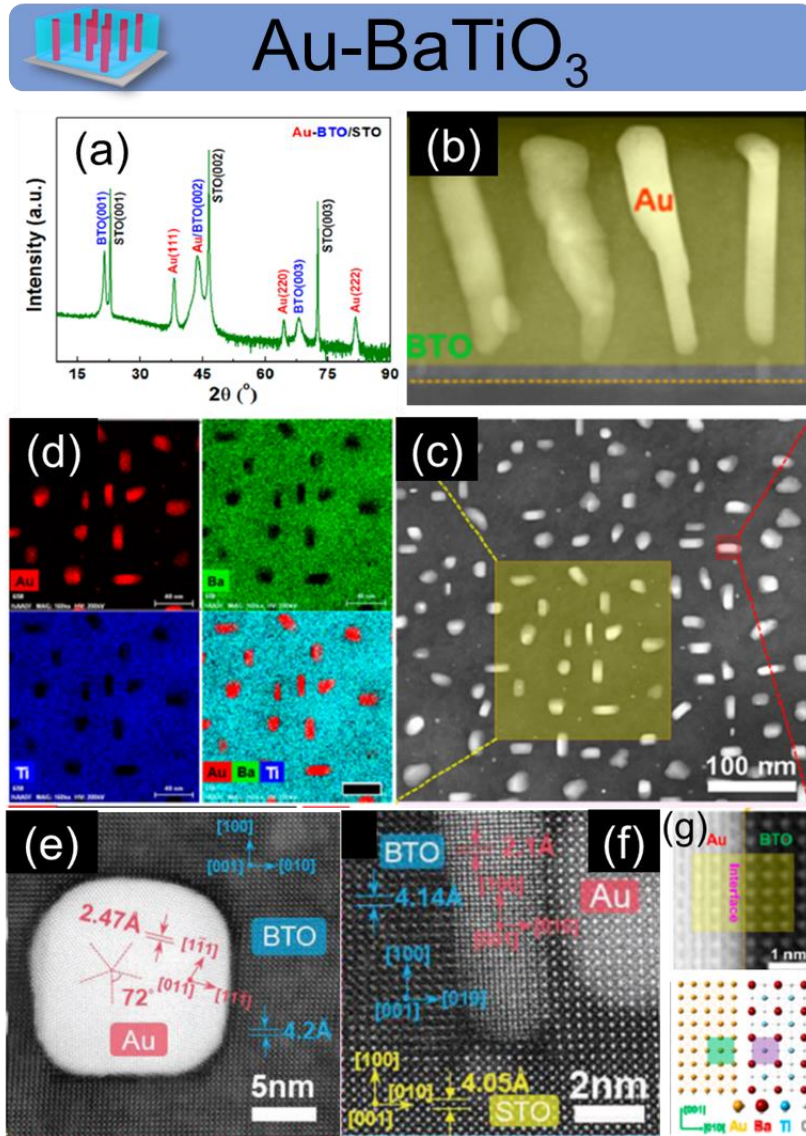


Figure 1-25: Vertically aligned nanocomposite. (a) X-ray diffraction of the Au-BaTiO<sub>3</sub> nanocomposite, (b) Cross-section, (c) plan-view STEM image and its corresponding (d) EDS elemental map distribution. HR-STEM (e) plan-view image and (f) cross-section image of the Au nanopyllar. (g) Enlarged image of the vertical Au-BTO interface and the schematic illustration of the lattice matching relationship.<sup>41,96</sup>

## 1.6.2 Strain Compensation Model

As mentioned earlier, the total in-plane strain experienced in a VAN structure is given by the sum of the strain from both metal and dielectric's interfaces with the substrate. The average in-plane strain experienced by the VAN structure depends on the relative phase composition (i.e. molar or atomic ratio). A similar model has been proposed for the oxide-oxide systems which

discussed about the materials selection criteria, based on the lattice parameter, for obtaining an ordered VAN structure. During the initial nucleation and growth period, strain minimization plays a critical role due to its square dependence in the free energy term as compared to the surface energy minimization which has a linear dependence in the free energy term. Further, the energy difference between the competitive surfaces in different growth orientation is not much (~within 10-20%) as compared to the strain energy in different growth orientations.<sup>137</sup> Therefore, a growth orientation with a lower strain and higher surface energy is preferred over a growth orientation with a higher strain and a lower surface energy. Here, in addition to the linear strain composition model, areal strain compensation model is also proposed laying out the design criteria for fabricating a VAN structure.

### ***Linear strain compensation model***

Figure 1-26a shows the schematic of the lattice matching relationship between the metal and dielectric phases with the substrate. The in-plane lattice mismatch strain is calculated using:

$$f = 2 \frac{a_f - a_s}{a_f + a_s}$$

where  $a_f$  and  $a_s$  are lattice parameter of the film and the substrate, respectively. The model calculates the lattice mismatch along one dimension and works best for the cases when there is a cube on cube epitaxy with no rotation, with lattice parameters being equal in both the in-plane directions. Since the total in-plane strain in the nanocomposite depends on the phase composition, Figure 1-26b plots the metal and dielectric lattice parameter (on the left and right vertical axis) as a function of phase composition (on the X-axis) using the rule of mixtures with the STO substrate marked by a solid black line of the reported metal-dielectric VAN systems.<sup>32–35,37,41,42,104,110,111,138–</sup>

<sup>142</sup> Clearly the trendlines of all the reported VAN structures indicate the minimization of the effective in-plane strain as experienced by the nanocomposite. The lattice parameters of the metal and dielectric phases are plotted in Figure 1-26c. The plot can be divided into two regions based on the strain compensation. Region I (shaded in orange) is defined as the space where both the tensile and compressive strain acts on the two phases while region II (shaded in blue) defines the space where either compressive or tensile strain acts on both the phases. Further, several systems are marked (with a red star), indicating a highly spatially ordered VAN structure. Region I result in effective strain compensation and contains majority of the reported VAN structures. However,

when one of the phases undergoes a rotation or has a different crystal structure than the substrate, it results in different lattice parameter matching in the  $a$  and  $b$  directions, and linear strain model can only model one of the directions. In order to overcome this limitation, the areal strain compensation model is proposed.

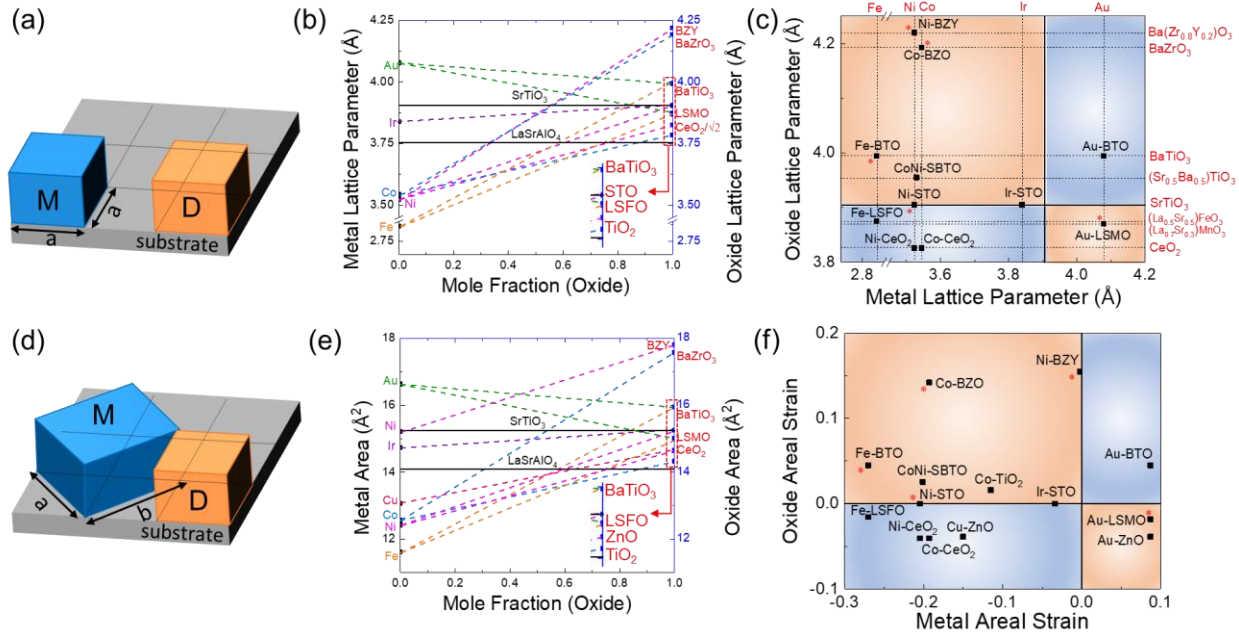


Figure 1-26: Linear and Areal strain compensation model. Schematic illustration of lattice matching relationship for the (a) linear and (d) areal strain compensation model. (b) In-plane lattice constant and (e) area for the metal and oxide phases as a function of oxide mole fraction. The dashed line joining the metal and oxide phases are the reported VAN systems and indicate the tunability of the in-plane strain on the substrate. Substrate are marked with a solid black line. (c) Plot showing the reported metal-oxide VAN systems plotted with their lattice parameters and (f) areal strain. The orange portions represent the region where both tensile and compressive strains are present while the blue shaded portion represent the region where either both tensile or compressive strain is present. The VAN systems marked with red star indicate highly spatially ordered systems.

### Areal strain compensation model

The areal strain compensation model considers the two-dimensional lattice matching between the phases and the substrate. As shown in Figure 1-26d, when one of the phases undergoes a rotation or has a different crystal structure, then strain is calculated using the projected area onto the substrate considering the in-plane matching between the phase and the substrate. The strain is calculated using:

$$f = 2 \frac{A_f - A_s}{A_f + A_s}$$

where  $A_f$  and  $A_s$  are the matching area of film and substrate, respectively. Area is calculated using the appropriate lattice matching relationship. For example, if the metallic phase is cubic and the oxide phase is hexagonal as in the case of Cu-ZnO, then it becomes hard the strain using linear model since Cu and ZnO grows along [001] and  $[11\bar{2}0]$  on STO [001] along the out-of-plane direction. Cu shows a cube-on-cube epitaxy on STO substrate while ZnO has different lattice parameters along the  $a$  and  $b$  directions as shown schematically in Figure 1-26c. The oxide strain can be calculated by comparing the oxide area with the corresponding substrate area. Similarly, matching in other orientations can also be calculated. In the case of cube-on-cube epitaxy relationships, the linear strain model and the areal strain model gives the same result however, the areal strain model provides an advantage when the epitaxy relationship occurs between different crystal structures.

Figure 1-26e plots the areal lattice parameter for both the metal and oxide phases as a function of oxide mole fraction. Clearly, we can see that all the trendlines work on minimizing the overall in-plane areal strain. Interestingly, the in-plane area strain of Ni (in Ni-BZY system) is calculated to be almost 0, compared to the non-zero strain calculated in the linear model, which is discussed in much more detail in the case studies in the following section. Figure 1-26f presents the reported metal-dielectric VAN systems, plotted as a function of metal and oxide areal strain. Similar to the linear strain compensation model the plot can be divided into 2 regions depending on the strain nature, i.e., tensile or compressive strain. We observe that most of the highly ordered VAN structure (marked with a red star) are present in region 1 where there is effective strain compensation. Based on these observations, the formation of self-assembled ordered VAN structures can be attributed to several key factors: (i) a close lattice match between the two phases and the substrate, (ii) presence of opposite strain nature, i.e., the structures are present in region I, (iii) Similar crystal structure of the two phases, and (iv) low solubility of the two phases.

The following section presents three case studies of the VAN structures, comparing the microstructure of the systems in region I and region II, having the same metallic phase but different dielectric phase. The VAN systems selected for comparison are marked in Figure 1-26f.

### 1.6.3 Case Studies

As discussed earlier, when the metallic and dielectric phase experience strain of the opposite nature, i.e., tensile strain on one phase and compressive strain on the other phase (region I), they present more ordered VAN structure as compared to when both the phases experience strain of the same nature, i.e., either both tensile or compressive strain. Figure 1-27 compares the microstructure of Co-CeO<sub>2</sub> and Co-BZO, both deposited on STO (001) substrate using PLD.<sup>33,35,111</sup> Co and CeO<sub>2</sub> experiences a compressive strain while BZO experience a tensile strain. Co crystallizes as either FCC or HCP structure while both CeO<sub>2</sub> and BZO have a cubic structure. In the case of Co-CeO<sub>2</sub> nanocomposite Co NWs are not perfectly aligned in the growth direction of [001] as seen in Figure 1-27a. The structure analyses using the HR-STEM further reveals that the misalignment is due to the HCP structure of Co NWs with their hexagonal *c* axis aligned along the <111> axis of the matrix as confirmed by Figure 1-27c1 and Figure 1-27c3. Although in some minor portions of the NWs, Co is present as a cubic structure (Figure 1-27c2). In contrast, Co-BZO shows primarily the FCC Co structure with growth along the [002] and [022] direction as confirmed by the plan-view HR-STEM image in Figure 1-27e. The cross-section HR-STEM image in Figure 1-27f-g shows the lattice matching relationship along the vertical interface between Co and BZO, with calculated *d* spacing of 1.82 Å and 2.12 Å for *d*<sub>Co (002)</sub> and *d*<sub>BZO (002)</sub>, respectively, showing the possibility of domain matching epitaxy and suggesting the presence of tensile strain in Co pillars. Although the Co pillar diameter is almost similar in both the systems (~5 nm), Co pillars present a more spatially ordered structure in BZO, with more aligned and continuous pillars. Therefore, effective strain compensation gives rise to a more continuous and ordered structure.

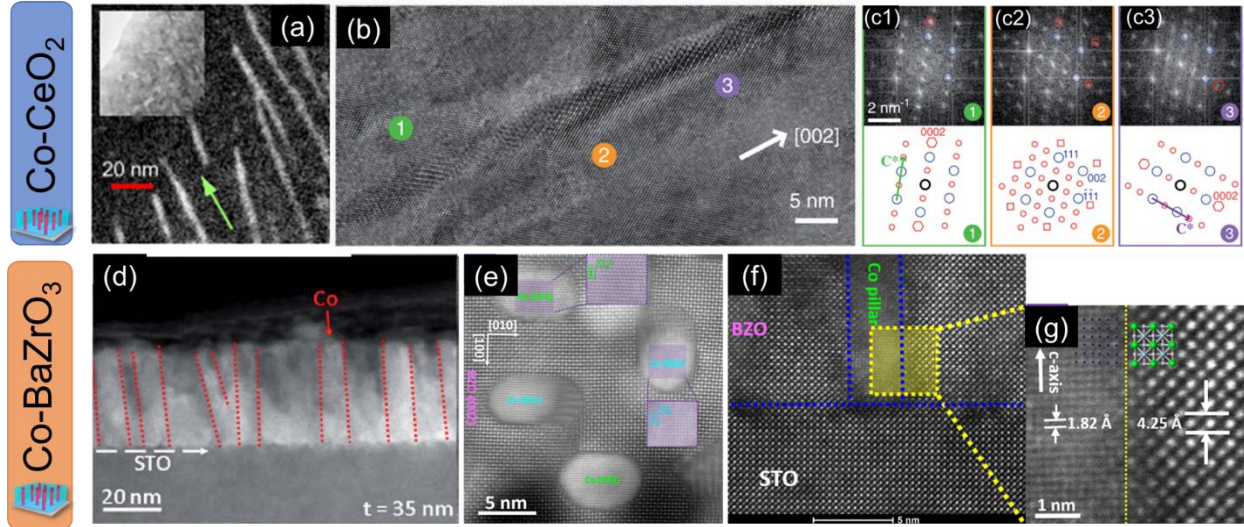


Figure 1-27: Case study I. (a) Cross-section EF-TEM image of the Co-CeO<sub>2</sub> showing the Co nanowires. (b) HR-TEM image of a Co nanowire and (c1)-(c3) the corresponding SAED patterns of the three regions marked in (b). (d) Cross-section STEM image of Co-BaZrO<sub>3</sub> nanocomposite. (e) HR-STEM plane-view image and (f) cross-section image. (g) shows an enlarged portion of the vertical interface between Co and BaZrO<sub>3</sub>.<sup>33,35,111</sup>

Figure 1-28 compares the microstructure of Ni-CeO<sub>2</sub> and Ni-BZY, deposited on STO (001) substrate.<sup>32,34</sup> Ni, CeO<sub>2</sub> and BZY have a cubic crystal structure, with Ni and CeO<sub>2</sub> experiencing a compressive strain and BZY having a tensile strain, placing the Ni-CeO<sub>2</sub> in region II and Ni-BZY system in region I. The XRD and HR-STEM analysis in Figure 1-28a-d indicate a cube-on-cube epitaxy of CeO<sub>2</sub> and Ni with both growing in the [001] out-of-plane direction. CeO<sub>2</sub> ( $a_{\text{CeO}_2} = 5.41 \text{ \AA}$ ) undergoes a 45° rotation to match with STO. Ni ( $a_{\text{Ni}} = 3.52 \text{ \AA}$ ) preferably grows along the [002] direction with some minor growth along the [022] direction, due to the low surface energy of the (002) orientation. In-plane domain matching epitaxy occurs between Ni and STO with  $10a_{\text{Ni}} \approx 9a_{\text{STO}}$ . The vertical strain is minimized by the domain matching epitaxy between CeO<sub>2</sub> and Ni since  $2a_{\text{CeO}_2} \approx 3a_{\text{Ni}}$ . However, Ni grows along the [111] out-of-plane direction in BZY matrix with lattice matching relationship given by Ni (011)//BZY (200) and Ni (110)//BZY (110), evidenced by the XRD and HR-STEM plan view images in Figure 1-28e-h. By maintaining such a relationship, Ni reduces its in-plane areal strain almost completely to 0, as shown in Figure 1-28d. In addition to the lowest surface energy of the Ni (111) orientation, the out-of-plane  $d$ -spacing ( $d_{\text{Ni}(111)} = 2.04 \text{ \AA}$ ) is closely matched with the  $d$ -spacing of BZY ( $d_{\text{BZY}(002)} = 2.11 \text{ \AA}$ ) orientation. Therefore, the difference in the growth orientation of Ni can be attributed to the combination of

both out-of-plane and in-plane strain minimization. The average Ni pillar diameter increases from  $\sim 4$  nm (in Ni-BZY) to  $\sim 7$  nm (in Ni-CeO<sub>2</sub>) and the cross-section STEM image shows a clear difference in the Ni pillar morphology. The Ni pillars are non-continuous and non-uniform in CeO<sub>2</sub> as compared to the almost vertically aligned pillars and spatially ordered pillars in the BZY matrix.

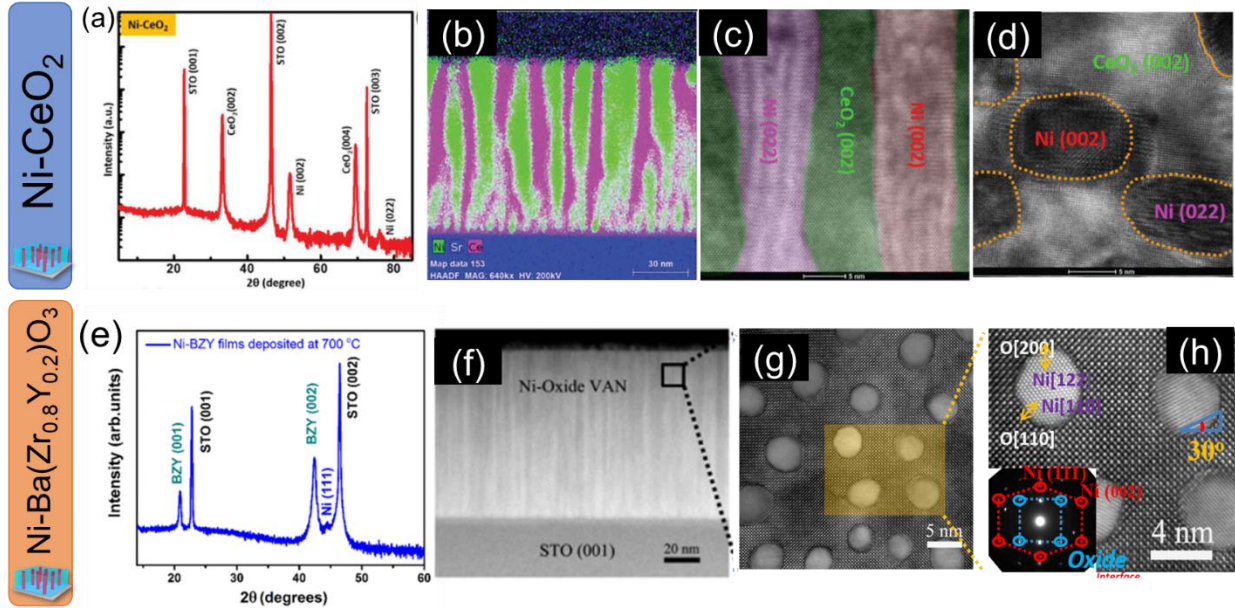


Figure 1-28: Case study II. X-ray diffraction of Ni-CeO<sub>2</sub> nanocomposite thin film, (b) Cross-section STEM-EDS map showing the elemental distribution, (c) HR-STEM cross-section image and (d) plan-view image showing the two different growth orientation of the Ni pillars. (e) X-ray diffraction of the Ni-Ba(Zr<sub>0.8</sub>Y<sub>0.2</sub>)O<sub>3</sub> nanocomposite thin film, (f) Cross-section STEM image, (g) Plan-view STEM image and (h) the corresponding HR-STEM image showing the Ni growth orientation.<sup>32,34</sup>

The last case study compares the Fe pillar structure embedded in (La<sub>0.5</sub>Sr<sub>0.5</sub>)FeO<sub>3</sub> and BTO, deposited on STO (001) substrate.<sup>139</sup> Fe and BTO crystallizes as a cubic structure while LSFO has tetragonal crystal structure. LSFO and Fe have a compressive strain while BTO has a tensile strain on the STO substrate. XRD plot in Figure 1-29a and Figure 1-29e shows the epitaxial growth of LSFO and BTO in the [001] direction. Although the Fe phase grows in the [110] out-of-plane direction, the morphology of the embedded Fe pillars shows much difference. Fe pillar diameter decreases from  $\sim 15$  nm in LSFO to  $\sim 5$  nm in BTO. Further, the microstructure changes from a less-ordered particle-like growth to a more ordered pillar-type growth. Such a change in microstructure can be attributed to the effective strain compensation along the lateral and vertical

interfaces between Fe and the dielectric matrix. Moreover, changing the growth kinetics such as the laser frequency and laser energy also tunes the size of the Fe pillars. Therefore, judicious selection of the metallic and the dielectric phases, based on the strain compensation model, offers enormous opportunities for tuning the microstructure of the metal-dielectric nanocomposites.

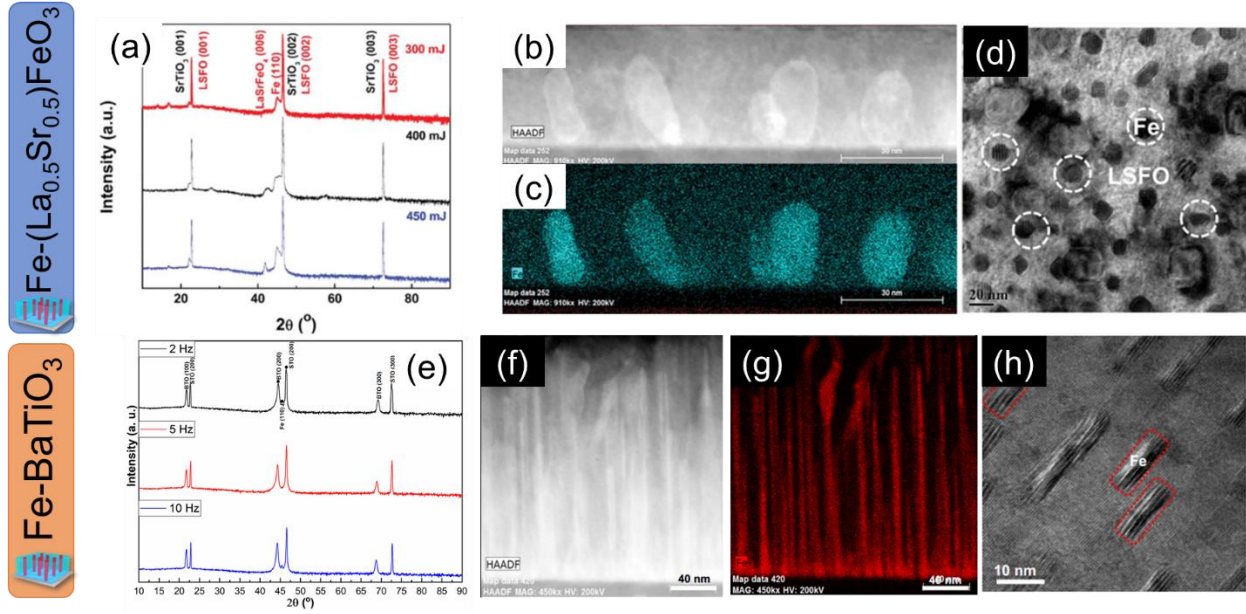


Figure 1-29: Case study III. X-ray diffraction of the Fe-(La<sub>0.5</sub>Sr<sub>0.5</sub>)FeO<sub>3</sub> nanocomposite thin film deposited with different laser energy. (b) Cross-section STEM image and (c) the corresponding Fe EDS map. (d) Plan-view TEM image showing the distribution of Fe pillars. (e) X-ray diffraction of the Fe-BaTiO<sub>3</sub> nanocomposite thin film deposited at different laser frequency. (f) Cross-section STEM image and (g) the corresponding Fe EDS map. (d) Plan-view TEM image showing the faceted structure of Fe pillars.<sup>139, 36</sup>

## 1.7 Research Motivation

As discussed above, both the particle-in-matrix and nanowire morphology, consisting of metal and dielectric materials, have been demonstrated for achieving improved physical and optical properties, such as ferroelectricity, ferromagnetism and negative refraction. Chapter III focuses on the Au-TiO<sub>2</sub> two phase nanocomposite as a particle-in-matrix morphology that has been achieved for efficient photocatalysis. However, due to the limited availability of structures in terms of crystallinity and morphology in the two-phase nanocomposites, a greater design flexibility and a structural complexity is needed for developing future integrated photonic and electronic devices.

One way of achieving this is by incorporating a third phase by careful selection of materials and functionalities through the three phase nanocomposite designs.

Chapter IV focuses on one such self-assembled ordered three phase nanocomposite Au-BaTiO<sub>3</sub>-ZnO that acts as a hyperbolic metamaterial in the visible and near-infrared wavelength regime. In addition, careful microstructural control presents enormous opportunities in tailoring the physical properties including the optical properties. Chapter V demonstrates a strong tunability in the microstructure of the self-assembled ordered three-phase Au-BaTiO<sub>3</sub>-ZnO nanocomposite along with its optical properties by varying the growth temperature, deposition frequency, template thickness, and the substrate. The change in growth parameter evolves the microstructure by tuning the Au and ZnO pillar geometry as well as the shape and size of the Au nanoparticle capping the ZnO nanowire. Further, thermal stability of metal-dielectric nanocomposites is important for designing practical devices for high temperature applications. Chapter VI explored the thermal stability of the self-assembled ordered three phase Au-BaTiO<sub>3</sub>-ZnO nanocomposite by *ex-situ* annealing in air and vacuum followed by *in-situ* heating in TEM in vacuum. Such *in-situ* heating in TEM provides a useful technique for the exploration of microstructure evolution and growth mechanisms at nanoscale and thermal stability of the multi-phase nanocomposites for refractory applications.

## 2. RESEARCH METHODOLOGY

### 2.1 Pulsed Laser Deposition

Pulsed laser deposition (PLD) is a physical vapor deposition (PVD) technique which is widely used for thin film depositions of a wide range of materials. The technique involves firing high power laser pulses to vaporize material from the target surface and deposit the film onto the substrate. Figure 2-1 shows the schematic of the PLD setup.<sup>143</sup> The setup consists of a high energy laser source which fires the laser pulses onto the target resulting in a plasma plume which consists of many species such as atoms, molecules, ions and particulates from the target. These species get deposited on the substrate which is usually kept at ~3-7 cm from the target in a high vacuum chamber. The adatoms crystallize at the substrate surface, which is kept at a high temperature (~400-800°C). The target carousel can have up to four to six targets which allow for an easy change of target in between the deposition without breaking the vacuum. More advanced PLD systems also allow for substrate rotation and target rasterization which help in more uniform thin film deposition.

There are several parameters that can be controlled using PLD. Among them are laser energy, laser frequency, substrate temperature, substrate-to-target distance, and background gas partial pressure. Increasing the laser energy and the substrate temperature provides more energy to the incoming adatoms for diffusion along the substrate surface, while increasing the laser frequency decreases the diffusion length. That substrate-to-target distance and the background gas partial pressure mainly controls the plasma plume shape which hits on the substrate. Usually for oxide growth, thin film deposition is done in an oxygen partial pressure. The thin film thickness can be easily controlled by the number of laser pulses.

In our experiment, all the films were deposited using a KrF laser with wavelength of 248 nm with a laser spot geometry of 3x1 mm. The laser beam was focused on the target at a 45° angle and the laser power density of 3 J/cm<sup>2</sup> was used for all the depositions. The laser frequency was varied from 1-10 Hz for the depositions. The composite targets were made using molar ratio calculation, powder mixing, pellet making and sintering. The chamber was pumped to below 10<sup>-6</sup> mbar, before the deposition. All the films were deposited in an oxygen background gas (20-200

mTorr). Substrate-to-target distance of 4.5 cm was used for all the depositions. The thin films were deposited on different single crystalline substrates including STO (001), MgO (001), and LAO (001).

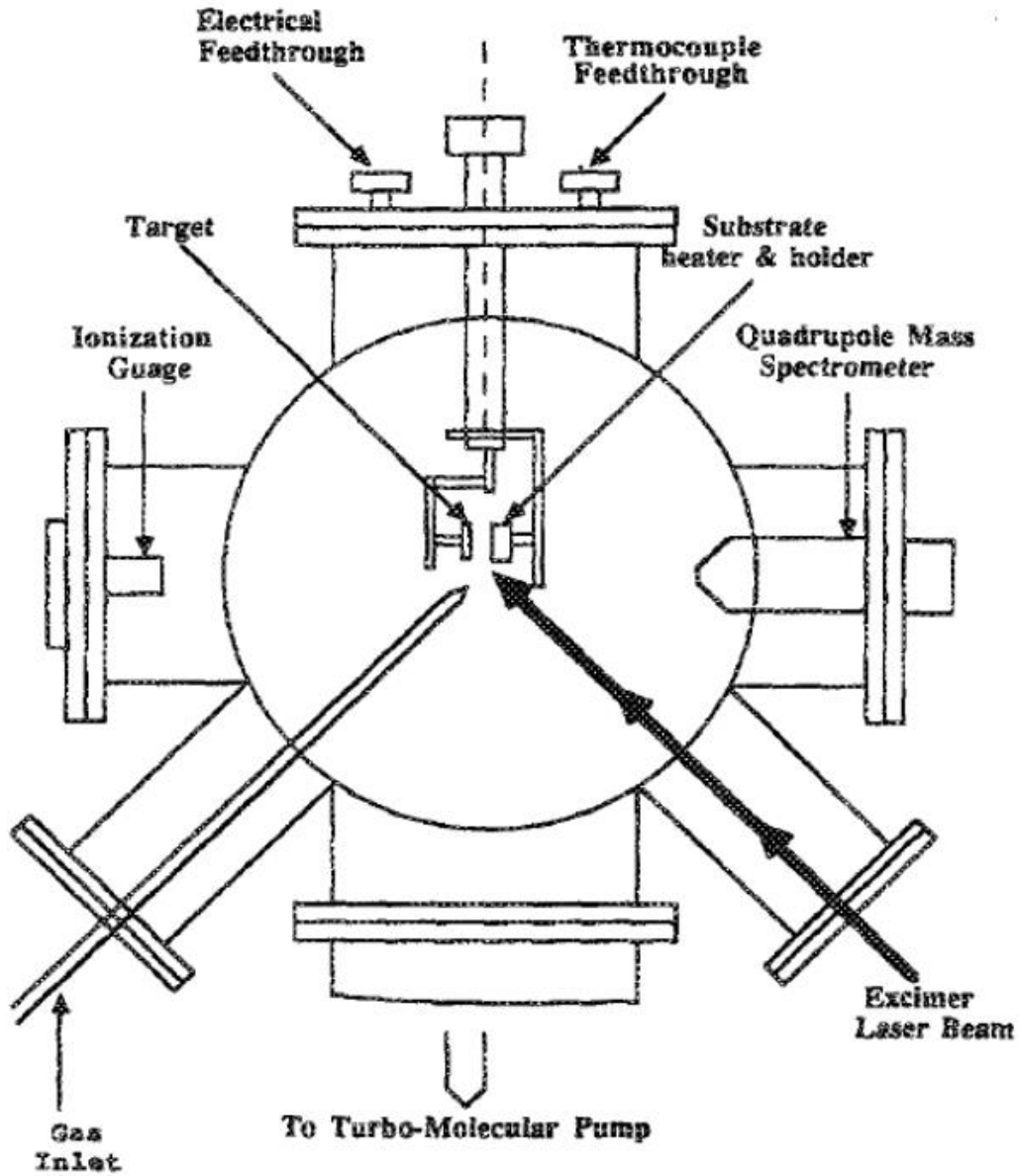


Figure 2-1. Schematic of the pulsed laser deposition system<sup>143</sup>

Compared to other PVD techniques such as e-beam deposition, evaporation and sputtering, PLD offer several advantages. First, it offers a good stoichiometric transfer from the target to the substrate which makes it an attractive technique for the deposition of complex oxides such as

YBCO. This is mainly because the plume that is generated from the target is instantly transferred to the substrate, thus minimizing the effects of different deposition rates of each component. Second, the growth of nanocomposite thin films can easily be achieved by simply changing the target composition. Third, since the target carousel can hold multiple targets, complex film architecture such as multilayer deposition can also be easily achieved by simply changing the target without breaking the vacuum. Last, PLD offers an easy control over film thickness, composition, and crystalline quality.

Despite its advantages, PLD also offers some disadvantages. First, since the plasma plume is highly forward directed, large area deposition using PLD is a challenge. Film parameters such as its thickness and composition can vary across the film, thus making PLD unsuitable for industrial applications. Second, the presence of big particulates in the target can sometimes get deposited on the substrate, thus degrading the film quality. Despite these disadvantages, PLD is widely used in research of complex oxides, nanocomposites and for obtaining high quality epitaxial thin films with novel functionalities.

## 2.2 Structural Characterization

### 2.2.1 X-Ray Diffraction

X-Ray Diffraction (XRD) is a nondestructive technique that is widely used for the crystal structure analysis. It can be used to identify crystal orientation, stress, chemical composition, and phase composition in a thin film or bulk sample. During the measurement the incident angle hits the sample surface resulting in a scattered beam. Diffraction occurs when the incoming radiation interacts with a crystal having an inter-planar spacing of the same magnitude as the incoming wavelength. Diffraction occurs when the following Bragg's law is satisfied:

$$n\lambda = 2d \sin \theta \quad (2.1)$$

where  $\lambda$  is the incident X-ray wavelength,  $d$  is the inter-planar spacing,  $n$  is an integral and  $\theta$  is the angle of incidence. When a particular set of incident angle and the inter-planar spacing satisfies the Bragg's law equation, then constructive interference happens, and the diffracted beam intensity can be detected as shown in Figure 2-2.<sup>144</sup> For other combinations of  $d$  and  $\theta$ , scattering occurs, and no diffracted beam intensity is detected by the detector. The lattice constant and the crystallite

size can be determined from the peak position and the full width half maximum (FWHM) of the peak respectively.

The XRD scans were carried using PANalytical Empyrean 2 with Cu K $\alpha$  radiation having a wavelength of 1.54 Å.

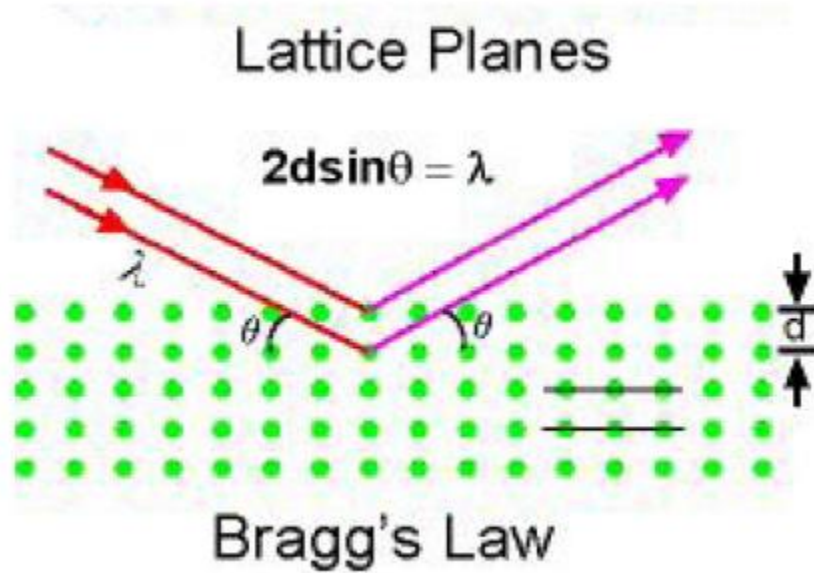


Figure 2-2. Illustration of the Bragg's law for lattice planes with inter-atomic spacing  $d$ <sup>144</sup>

### 2.2.2 Transmission Electron Microscopy

Transmission electron microscope (TEM) is a widely used technique for the structure characterization of materials which can provide important information regarding the microstructures, spatial phase distribution, and the crystallography of the material. In a TEM, electrons are generated by the electron gun which get accelerated by high voltage and get focused on the sample using magnetic lenses. Due to the very high operating voltage, the electrons are accelerated to very high speed. The relativistic wavelength of an electron is given by:

$$\lambda = \frac{h}{\sqrt{2meV(1+\frac{eV}{2mc^2})}} \quad (2.2)$$

where  $h$  is Planck's constant,  $m$  is the electron mass,  $e$  is the electron charge,  $c$  is the speed of light in vacuum, and  $V$  is the accelerating voltage.

The transmitted electrons contain the sample's information and can be focused to form either an image or a diffraction pattern using the objective lens. Figure 2-3 shows the basic

operation modes and the ray diagrams associated with the imaging and diffraction mode.<sup>145</sup> The objective lens forms a diffraction pattern in the back focal plane of the objective lens and an image in the image plane of the objective lens. Switching from the image mode (real space) to the diffraction mode (reciprocal space) can be easily achieved by changing the strength of the

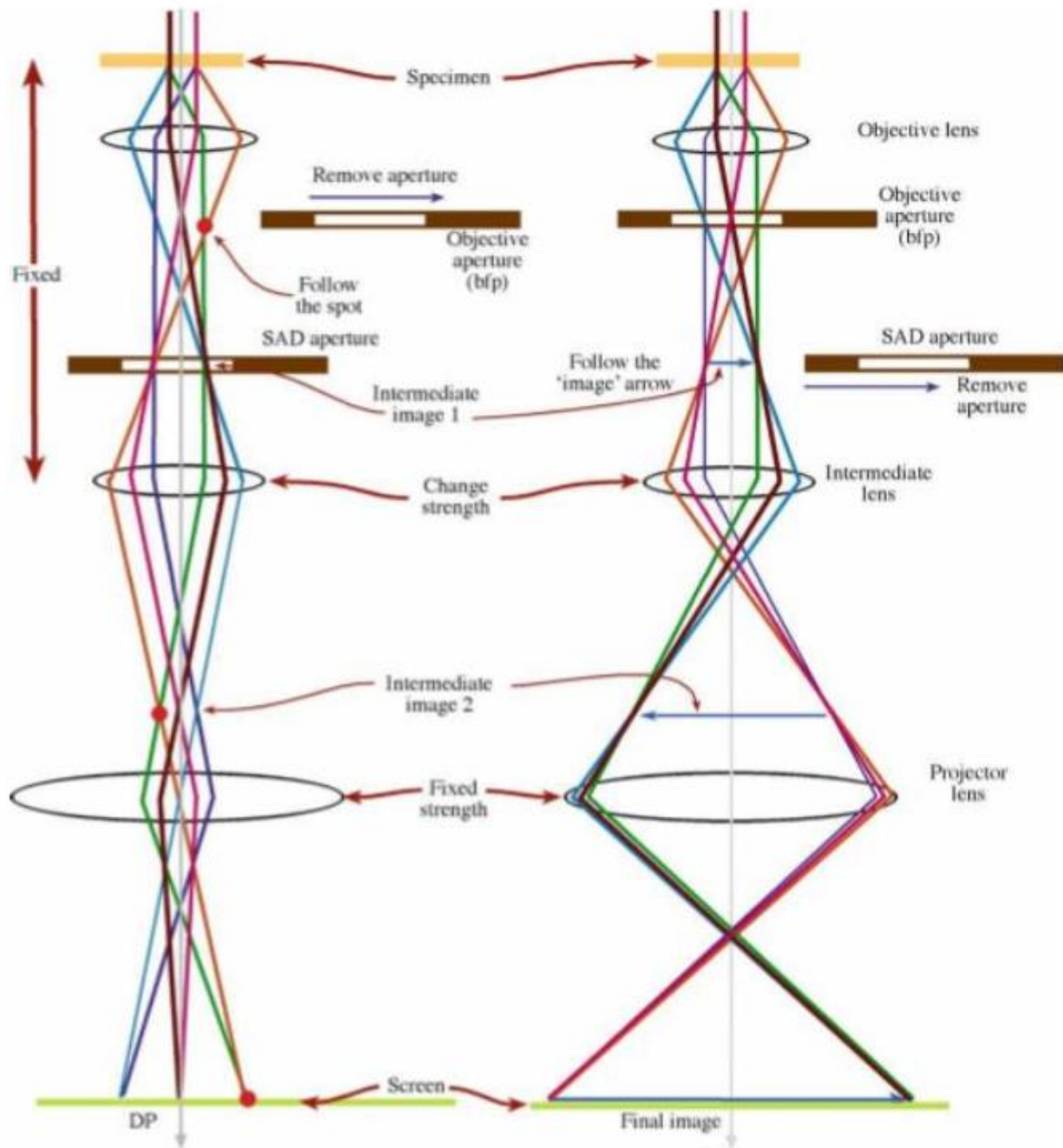


Figure 2-3. Ray diagrams for the two basic operation modes in TEM showing the diffraction mode (left) and the imaging mode (right)<sup>145</sup>

intermediate lens. In imaging mode, the objective aperture is placed at the back focal plane of the objective lens which can be used to achieve dark-field, bright-field and high-resolution images. While in the diffraction mode, a selected area electron diffraction (SAED) aperture is placed at the image plane of the objective lens, which can be used to select the region from which diffraction is obtained. In addition, more techniques such as high angle annular dark field (HAADF) scanning tunneling electron microscopy (STEM), energy dispersive spectroscopy (EDS), and electron energy loss spectroscopy (EELS) can also be performed in TEM to obtain more chemical and microstructural information about the sample.

TEM and STEM characterizations were performed using FEI Talos 200X with a point-to-point resolution of 1.6 Å. TEM samples for prepared by manual grinding and polishing followed by ion milling using Precision Ion Polishing System (PIPS 691, Gatan), to obtain a thin area with a thickness below 100 nm around the hole.

### **2.2.3 Atomic Force Microscopy**

Atomic Force Microscopy (AFM) is scanning probe microscopy technique, which is widely used for characterizing the surface morphology and topography. It takes advantage of the interaction forces, including the van-der Waals forces, dipole-dipole interactions, electrostatic interactions and others, between the tip and surface to map out the morphology. Figure 2-4 shows the setup of an AFM schematically.<sup>146</sup> While scanning the surface, a constant force is maintained between the tip and surface through the feedback circuit. Change in the surface morphology causes the tip deflection and rotation, which can be measured by the position of the laser spot on the photodetector.

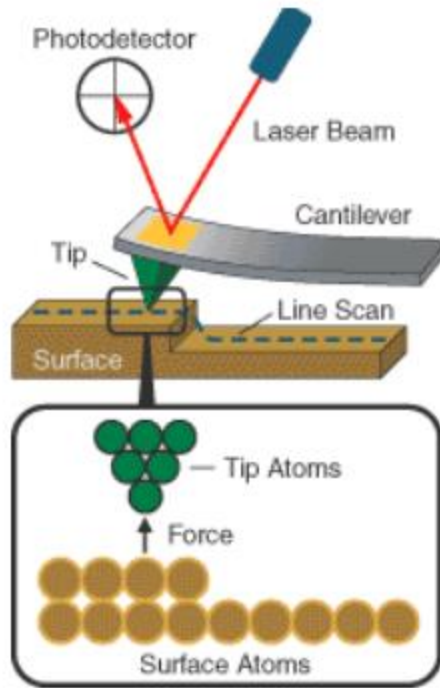


Figure 2-4. Schematic set-up for atomic force microscope<sup>146</sup>

In addition to detect surface morphology, AFM can also be integrated to measure other functionalities such as piezoresponse, magnetic response, nanomechanical behavior and conductive response. Piezoresponse Force Microscopy (PFM) has been widely used to map the piezoelectric/ferroelectric domain structure, phase and amplitude structure. Figure 2-5a shows the schematic of the PFM setup.<sup>147</sup> The measurement is done with a conductive tip which is brought in contact with a sample surface. The sample surface is deformed using the AC bias (converse piezoelectric effect) and the resulting piezoresponse is detected through a photodiode detector which is further demodulated using a lock-in amplifier. The AC frequency must be set high enough so that it is possible to distinguish between the piezoresponse and the surface height variations while scanning, i.e., the time constant of the feedback-loop should be greater than  $1/f$ . Domains with opposite phase causes opposite deflection in the tip, thus mapping out the  $180^\circ$  phase and same amplitude as shown in Figure 2-5b.<sup>147</sup>

AFM and PFM characterizations were performed using Bruker Icon. For PFM measurements, a conductive tip with Pt/Ir coating was used (Bruker SCM-PIT). The deflection sensitivity was calibrated on the thin film sample before performing PFM to convert voltage measured on the

photodiode detector to nanometers of motion. This was achieved by measuring the slope of the force curve of photodetector signal vs. piezo movement. Further,  $d_{33}$  was calibrated using a reference PVDF sample.

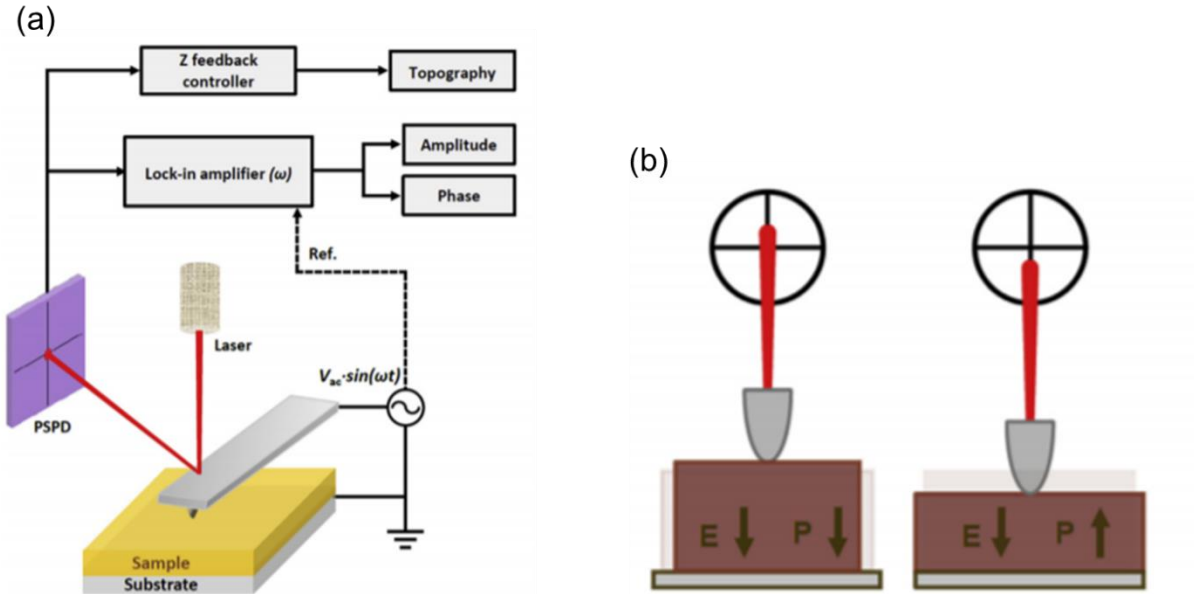


Figure 2-5. Schematic setup of the PFM<sup>147</sup>

## 2.3 Optical Characterization

### 2.3.1 UV-Vis-NIR Spectroscopy

Ultraviolet-visible-near-infrared (UV-Vis-NIR) spectroscopy is used to measure the optical properties of materials. It can measure the transmittance, reflectance and absorbance of the material from ultraviolet to near-infrared wavelength regime. Figure 2-6 shows the schematic setup of the instrument.<sup>148</sup> The measurement follows the Beer-Lambert law which states that the decreasing absorption of light is proportional to the absorptivity of the material. Three different detectors namely: (i) Photomultiplier tube (PMT), (ii) Indium Gallium Arsenide (InGaAs), and (iii) Lead Sulphide (PbS) Detectors are used for the light detection in different wavelength regimes. PMT detector detects the light from 200 nm to 860 nm, InGaAs detector detects the light from 860 nm to 1800 nm and the PbS detector detects the light from 1800 nm to 2500 nm. The hydrogen and tungsten filament lamps are used as a source for UV (200-375 nm) and visible (350-2500 nm)

light, which is then split into its component wavelength through a monochromator. A depolarizer is further used to depolarize the light after the light is passed through the sample and detected.

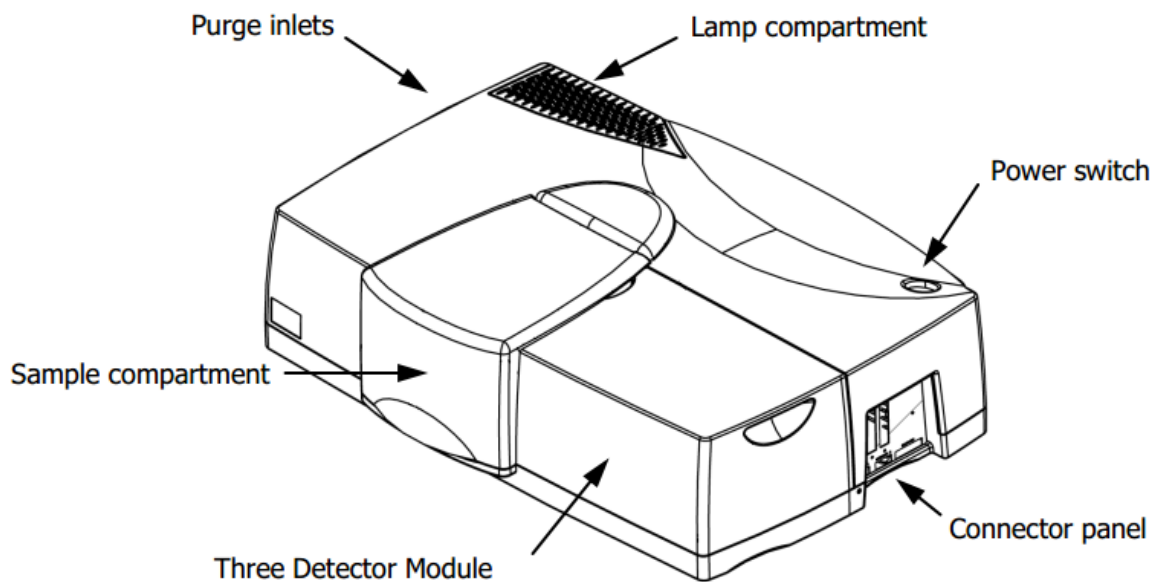


Figure 2-6. Setup of the UV-Vis-NIR spectrophotometer<sup>148</sup>

The thin film samples are polished on the back side of the substrate for transmission measurement while they are roughened on the back side for reflectivity measurement. The instrument used for the characterization was PerkinElmer Lambda 1050.

### 2.3.2 Ellipsometer

Ellipsometer is a non-destructive optical characterization technique which is used to measure the dielectric properties of thin films. It detects the change in polarization of light after the light interacts with the sample. Figure 2-7 shows the schematic setup of the ellipsometer. A linearly polarized light hits on the sample surface which becomes elliptically polarized after interaction with the sample. The measurement is repeated at several angles of incidence for better accuracy. The changes in polarization is measured using ellipsometer parameters:  $\psi$  and  $\Delta$ , related by the following equation:

$$\frac{r_p}{r_s} = \tan \psi e^{i\Delta} \quad (2.3)$$

where  $r_p$  and  $r_s$  are the reflection coefficient for the p-polarization and s-polarization light, respectively. Since ellipsometer measures the polarization change ratio, it provides very accurate information without depending on absolute intensity values.

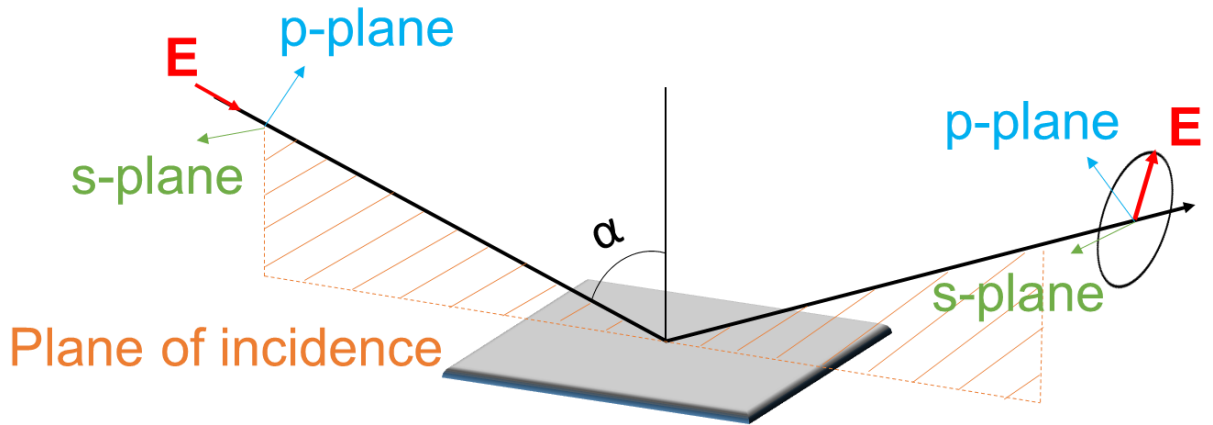


Figure 2-7. Schematic setup of the ellipsometer

The measured ellipsometer parameters are then fitted with an appropriate model to get the dielectric constants and refractive index. The thickness of the thin film samples was provided as an input to the model after calculating it from the cross-section TEM images. A uniaxial anisotropic model was used for the vertically aligned nanocomposites while an isotropic model was used for the particle in matrix nanocomposite. The metal and dielectric optical constants were modeled with the use of general oscillator models.

The ellipsometer measurements were performed using JA Woollam RC2. The thin film samples were roughened on the back side of the substrate to minimize the back reflection. The measurements were performed at three angles for better accuracy of the model.

### **3. TAILORABLE AU NANOPARTICLES EMBEDDED IN EPITAXIAL TiO<sub>2</sub> THIN FILMS FOR TUNABLE OPTICAL PROPERTIES**

This chapter is reprinted with permission from “Tailorable Au nanoparticles embedded in epitaxial TiO<sub>2</sub> thin films for tunable optical properties” by S. Misra, et al., ACS Applied Materials & Interfaces, 2018, 10, 32895-32902. © 2018 American Chemical Society

#### **3.1 Overview**

The unique property of plasmonic materials to localize light into deep sub-wavelength regime has greatly driven various applications in the field of photovoltaics, sensors and photocatalysis. Here, we demonstrate a one-step growth of oxide-metal hybrid thin film incorporating well dispersed gold (Au) nanoparticles (NPs) with tailorable particle shape and diameters (ranging from 2 to 20 nm) embedded in highly epitaxial TiO<sub>2</sub> matrix, deposited using pulsed laser deposition. Incorporation of Au NPs reduces the band gap of TiO<sub>2</sub> and enhances light absorption in the visible regime owing to the excitation of localized surface plasmons. Optical properties including the plasmonic response and permittivity, and photocatalytic activities of the Au-TiO<sub>2</sub> hybrid materials are effectively tuned as a function of the Au NP sizes. Such optical property tuning is well captured using full field simulations and effective medium theory for better understanding of the physical phenomena. The tailorable shape and size of Au NPs embedded in TiO<sub>2</sub> matrix present a novel oxide-metal hybrid materials platform for optical property tuning and highly efficient plasmonic properties for future oxide-based photocatalytic sensors and devices.

#### **3.2 Introduction**

Titanium dioxide (TiO<sub>2</sub>), a wide band-gap semiconductor (~3 eV for rutile and ~3.2 eV for anatase), has been extensively studied for its photocatalytic properties following the discovery of the Fujishima-Honda effect in 1972.<sup>48</sup> Since this discovery, TiO<sub>2</sub> has been proposed to be used in the areas of solar cells, water-splitting, degradation of pollutants and organic molecules, water purification, etc.<sup>49–52</sup> Towards the practical applications of TiO<sub>2</sub> as photocatalyst, its wide band gap has limited the usage in the ultraviolet regime, which constitutes ~5% of the solar electromagnetic spectrum.<sup>60</sup> Much efforts have been devoted to increase its efficiency in the visible regime by incorporating plasmonic nanostructures in TiO<sub>2</sub>.<sup>79,149–152</sup> For example, the integration

of noble metal nanoparticles (NPs) in a semiconductor has attracted much attention because of the strong absorption of light in the visible regime due to the resonant oscillation of surface conduction electrons excited by light, known as localized surface plasmon resonance (SPR). The SPR effect has been efficiently exploited in various applications such as photocatalysis and photovoltaics.<sup>80,82</sup> To further enhance the absorption efficiency of solar spectrum, noble metal based plasmonic structures can be further nanoengineered to achieve extreme control over light at nanoscale. For example, plasmonic structures have the ability to enhance low-intensity light by concentrating light over a small area. More recent applications of nanoscale plasmonic materials are in quantum optics, cloaks, water purification, solar distillation and reconfigurable metamaterials.<sup>153–157</sup> Among all the plasmonic materials, Au is one of the most promising and widely used materials because of its biocompatibility, high stability and excellent quality factor.<sup>75</sup> It allows the nanocomposite structure to harvest sub-bandgap photons, thus, increasing its absorption range.

Most of the metal integrations focus on surface incorporation by various methods such as evaporation,<sup>149,158,159</sup> photocatalytic reduction,<sup>79</sup> chemical reduction<sup>160</sup>, colloid photodeposition (CPH)<sup>161</sup> and facile adsorption<sup>162</sup>. Incorporating the metal nanostructures within an oxide matrix poses significant challenges due to potential inter-diffusion, oxidation and structure instability. For example, most of the metals readily diffuses in oxide matrix. Very recently, several successful demonstrations on the growth of epitaxial metal-oxide systems have opened the possibilities of such hybrid materials platform with the two phases deposited simultaneously using pulsed laser deposition (PLD).<sup>35,41,132</sup>

In this work, we fabricated a new nanostructure with Au NPs embedded in TiO<sub>2</sub> matrix grown on STO (001) using PLD as illustrated in the embedded schematics in Figure 3-1. The advantages of PLD include good stoichiometry control, flexibility in co-growing two-phase nanocomposites, and relatively low contamination levels.<sup>6,23,163</sup> Moreover, being a non-equilibrium process, PLD is effective in fabricating thin films with complex stoichiometry and producing metastable phases such as anatase phase (instead of the bulk thermodynamically stable rutile phase) which has been reported as a better photocatalyst than rutile.<sup>164</sup> However, very limited studies have been conducted regarding plasmonic noble metal NPs embedded in photocatalysts using PLD and are mostly based on nanocrystalline TiO<sub>2</sub> thin films.<sup>165,166</sup> Here we demonstrate the ability to incorporate Au nanoparticles uniformly and epitaxially in TiO<sub>2</sub> matrix. More interestingly, the size, shape and distribution of Au NPs can be effectively tailored to tune the

plasmonic properties of the Au NPs and the photocatalytic properties of TiO<sub>2</sub>. This straightforward approach is demonstrated by fabricating a multilayer stack of Au-TiO<sub>2</sub> with distinct sizes of Au NPs by varying the substrate temperature. In addition, effective medium approximation (EMA) coupled with spectroscopic ellipsometry can be used to estimate the Au NP size effect on the effective permittivity of Au-TiO<sub>2</sub> nanocomposite.

### 3.3 Results and Discussion

To study the deposition temperature effect on the size and shape dependence of Au NPs embedded in TiO<sub>2</sub>, high-angle annular dark-field scanning transmission electron microscopy (HAADF-STEM) studies were performed on all the samples deposited at 300 °C, 500 °C, 700 °C and 3 mixed temperatures. Figure 3-1 and Figure 3-2 (in Supporting Information) shows the cross-sectional STEM images of TiO<sub>2</sub> and Au-TiO<sub>2</sub> thin films on STO (001) and MgO (001), respectively. The STEM imaging under HAADF condition is also called Z-contrast where the image contrast is roughly proportional to  $Z^2$ .<sup>167</sup> Such composition based contrast difference in STEM is ideal for microstructural analysis of 2-phase nanocomposites. STEM image clearly shows the Au NPs uniformly embedded in TiO<sub>2</sub> matrix where Au has a brighter contrast than TiO<sub>2</sub> because of its higher atomic number (Z) (Figure 3-1). The average Au NP size decreases as the substrate temperature reduces. The average Au NP size decreases from 16.5±2.8 nm at 700 °C to 4.7±1.1 nm at 500 °C and 1.6±0.3 nm at 300 °C as shown in Figure 3-3. The particle size was measured along the major and minor axis using ImageJ and the error bar signifies the ±1 standard deviation of the normal distribution. The same trend is also observed for the samples on MgO (001) substrates (Figure 3-2), i.e., the particle size decreases from ~9 nm at 700 °C to ~4 nm at 500 °C and ~2 nm at 300 °C. Higher growth temperature increases the surface mobility (i.e., surface diffusivity) of the Au ad-atoms which leads to larger Au growth islands, e.g., larger Au nanoparticles in the TiO<sub>2</sub> matrix for the case of the 700°C sample. In comparison, decreasing the temperature to 500 °C and 300 °C decreases the surface mobility of Au NPs and thus leads to smaller Au NPs formation. Interestingly, the particle shape also changes with the deposition temperature to minimize the overall interfacial energy. At 700 °C, well faceted large Au nanoparticles are observed (growing along the (002) out-of-plane direction). The particle shape changes to elliptical and spherical for samples deposited at 500 °C and 300 °C, respectively, shown

by the presence of a larger difference in major and minor axis in Figure 3-3b and Figure 3-3c. In addition, the particles show more uniform distribution in the matrix for both cases. Figure 3-1d shows the film grown at three different temperatures consequently that clearly illustrates the ability to easily tune the sizes and distribution of Au NPs via the deposition temperature control. Another notable feature observed in the STEM images is the ability of the Au NPs to self-align in order to form pillars. At 500 °C, the tendency to form nanopillar-like structures from the vertically aligned nanoparticles is clear as indicated by the circled areas. The ability of Au particles to align as nanopillars suggests the possible strain driven alignment of Au NPs in TiO<sub>2</sub> matrix. Overall the growth temperature plays a critical role in determining the particle shape and size. For all the samples, a seed layer of Au NPs is nucleated near the film-substrate interface to assist the initial nucleation and growth of the Au-TiO<sub>2</sub> nanocomposite structure.

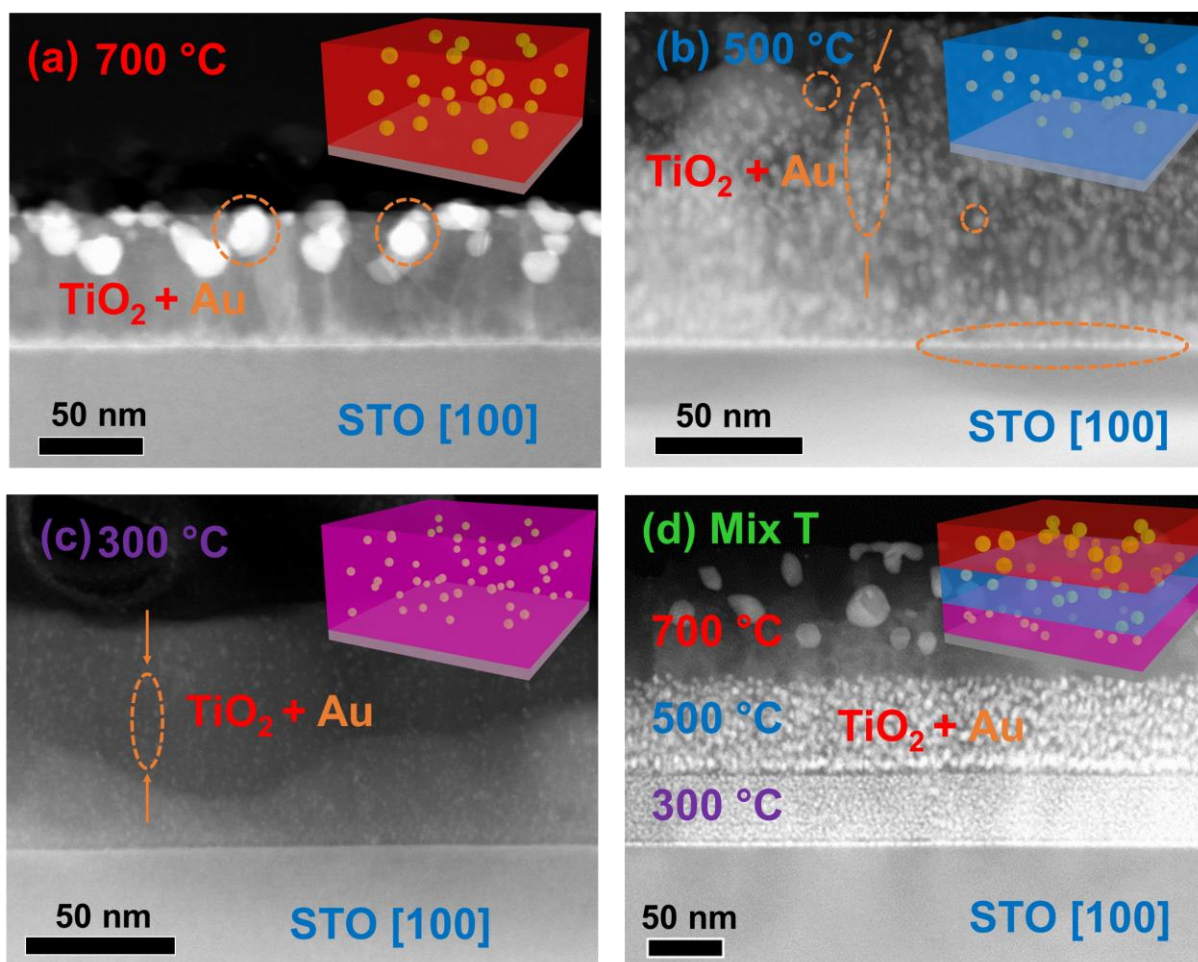


Figure 3-1. Cross-sectional STEM images showing Au NPs embedded in epitaxial TiO<sub>2</sub> thin film for growth temperature of (a) 700 °C, (b) 500 °C, (c) 300 °C and (d) mixed temperature.

The XRD  $\theta$ - $2\theta$  scans of TiO<sub>2</sub> films (Figure 3-5) confirm the highly textured growth of anatase TiO<sub>2</sub> along (004) direction for all the cases. As opposed to the more thermodynamically stable rutile phase, the growth of metastable anatase phase results in the lowering of the overall free energy by forming a semi-coherent interface and is the preferred phase to form on STO because of better epitaxy matching.<sup>1</sup> Au peaks show the presence of two major orientations of (002) and (111) and the orientation preference varies as a function of temperature, i.e., (002) for the 700 °C one and (111) for the 500 °C one and the 3-temperature one, as shown in Figure 3-5c. A narrow full-width half maximum (FWHM) of the rocking curve for the (004) TiO<sub>2</sub> peak indicates the high epitaxial and crystalline quality of the film (Figure 3-6). While the TiO<sub>2</sub> peak completely disappears for the 300 °C sample implying that the crystallinity of the film reduces at lower growth temperatures. Moreover, the XRD  $\theta$ - $2\theta$  scans (Figure 3-5) and the selected area electron diffraction (SAED) pattern (Figure 3-4) confirm the epitaxial growth of TiO<sub>2</sub> and Au NPs on STO evidenced by their distinguished diffraction dots. The growth orientations of TiO<sub>2</sub> and Au are determined to be Au (002) // TiO<sub>2</sub> (004) // STO (002) and Au (200) // TiO<sub>2</sub> (200) // STO (200). Hence, the growth temperature plays a critical role in determining the film crystallinity and the Au NP sizes.

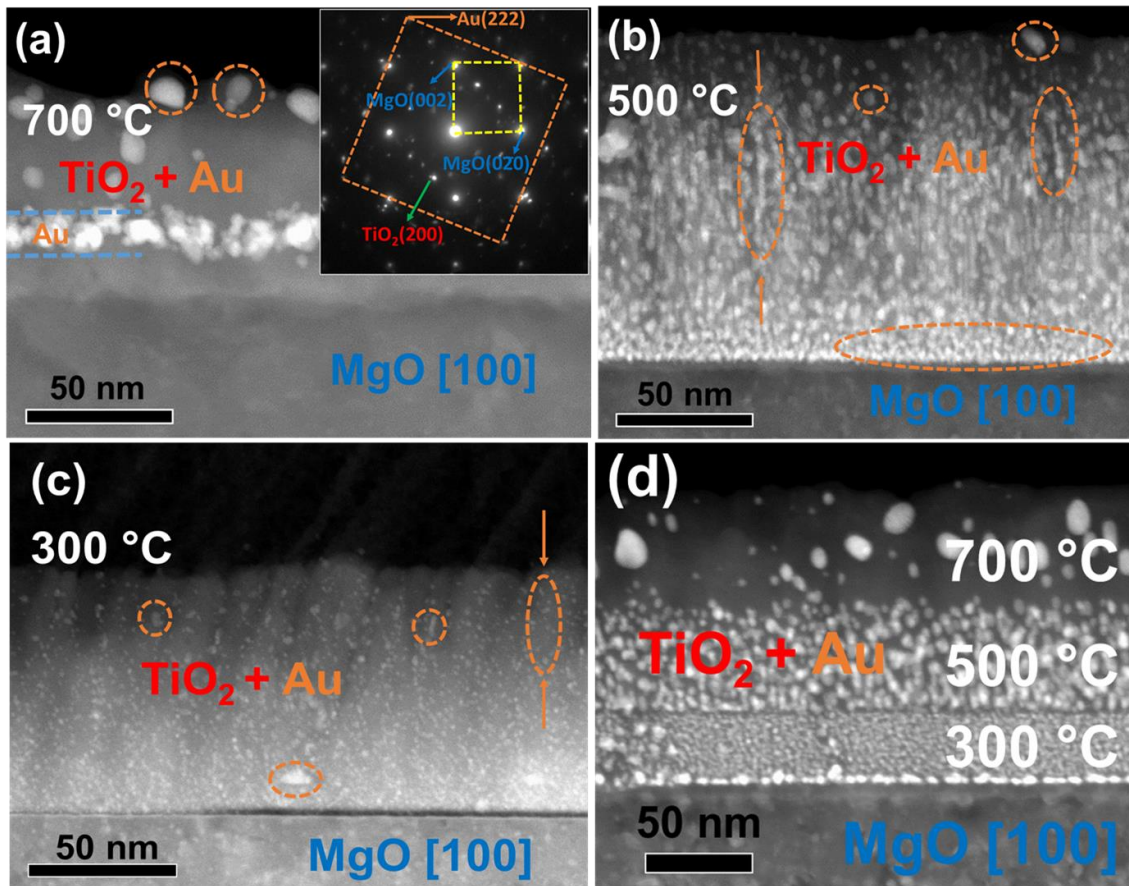


Figure 3-2. STEM images of Au-TiO<sub>2</sub> nanocomposite at (a) 700 °C, (b) 500 °C, (c) 300 °C and (d) mixed temperatures

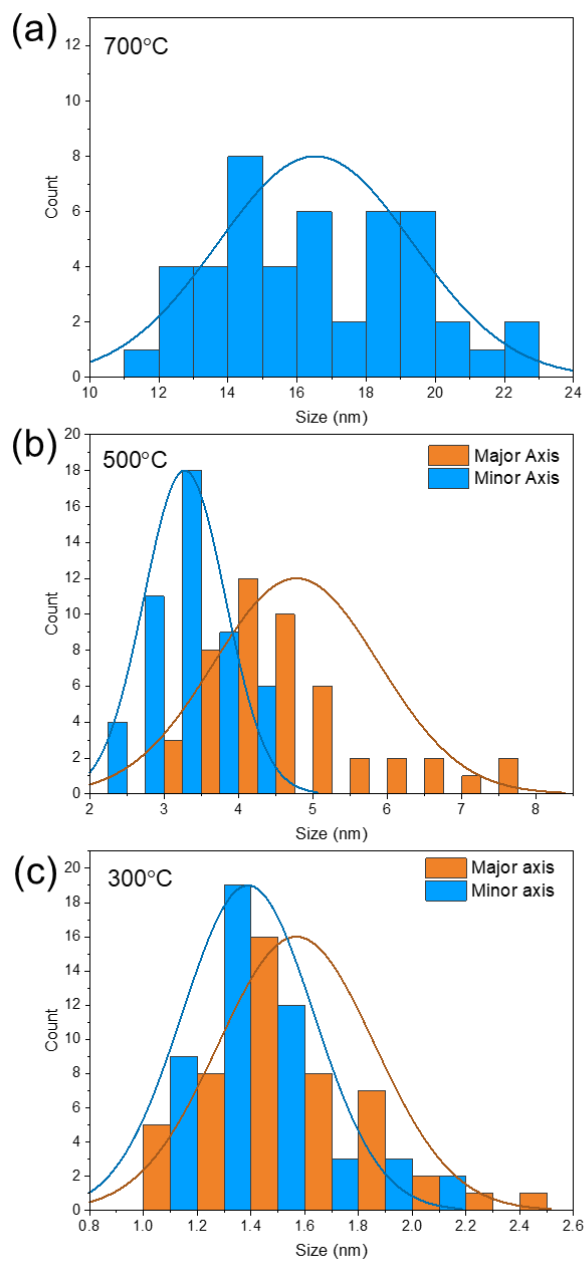


Figure 3-3. Statistics of the Au NP size distribution as a function of deposition temperature

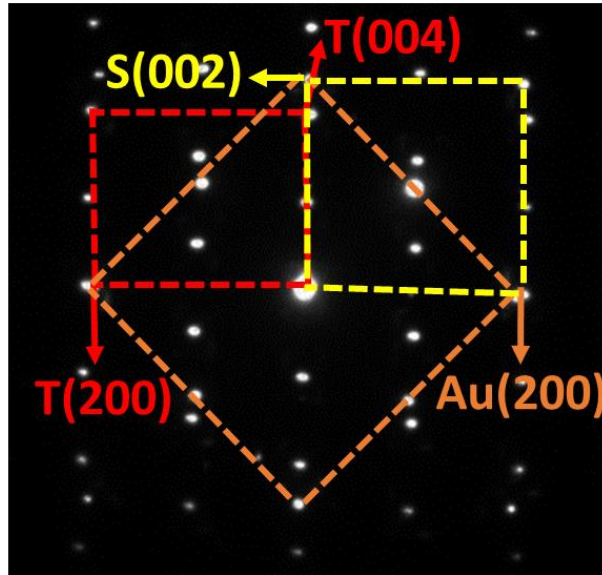


Figure 3-4. SAED of Au-TiO<sub>2</sub> nanocomposite for the growth temperature of 700 °C

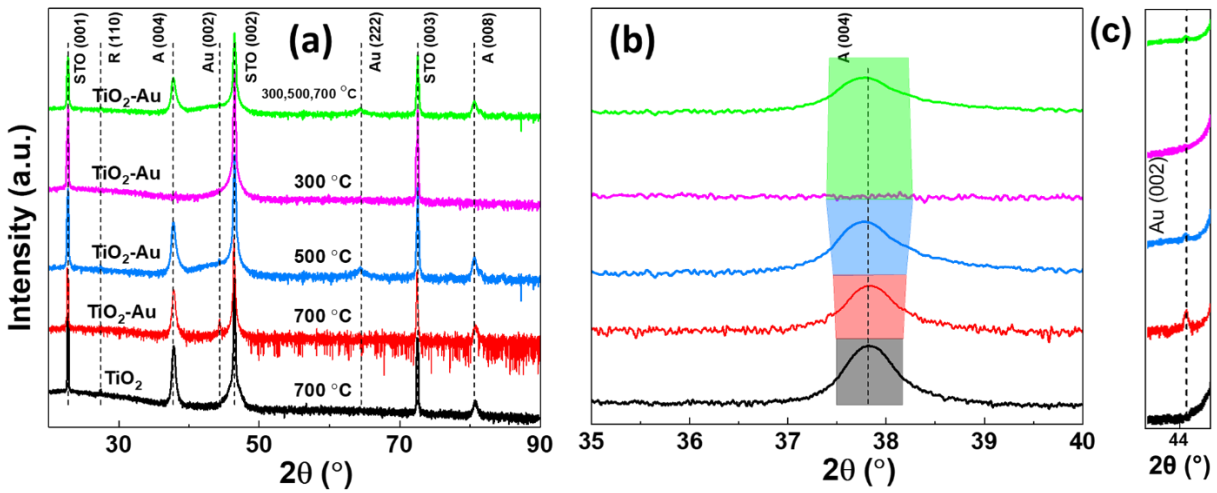


Figure 3-5. (a) XRD patterns of Au-TiO<sub>2</sub> nanocomposite at different growth temperature and (b) the variation in FWHM of TiO<sub>2</sub> (004) peak, (c) Au (002) peak.

An important characteristic of the Au-TiO<sub>2</sub> nanocomposite thin films is their highly tunable optical properties. The optical response of nanocomposites varies greatly with the Au NPs' size, shape and density. All the films on MgO substrates were characterized by optical transmittance measurements at the normal incident angle. Figure 3-7a shows the UV-Vis-NIR transmittance spectra of the films grown at different temperatures. The spectra were normalized between 0 and 1 while the un-normalized transmission spectra is shown in Figure 3-8a. First, all the samples present an obvious absorption edge around 350 nm which is related to the bandgap of the TiO<sub>2</sub> films. Specifically, the absorption edge of TiO<sub>2</sub> presents an obvious red-shift from 380 nm (pure TiO<sub>2</sub>) to as high as 460 nm (grown at mix temperature) in the visible regime because of the presence of Au NPs. A detailed bandgap calculation using the Tauc plot yields the plot in Figure 3-7b where the band gap of TiO<sub>2</sub> varies from 3.25 eV (grown at 700 °C, closer to its bulk value of 3.2 eV) to 2.91 eV (grown at 300 °C). Such obvious E<sub>g</sub> reduction is attributed to possible TiO<sub>2</sub> film stoichiometry variation due to the Au inclusions as well as the interface effects at the

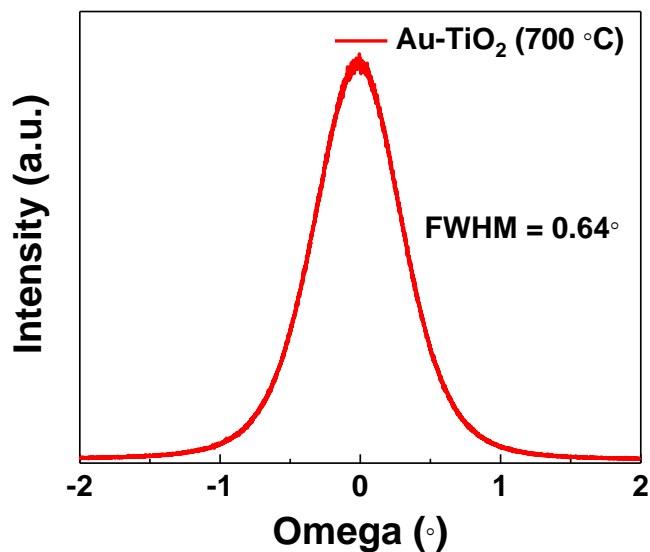


Figure 3-6. Rocking curve for the (004) TiO<sub>2</sub> peak indicating the FWHM of 0.64

Au-TiO<sub>2</sub> interfaces, which will be discussed in more detail later. It has been reported that the variation in oxygen stoichiometry could change the conduction band of oxide semiconductors and thus leads to the bandgap variation.<sup>168,169</sup> In this work, we have confirmed that the Au-NP incorporation actually results in more stoichiometric TiO<sub>2</sub> (Ti:O ratio of 1:2) using XPS analysis,

and considered this as one of the possible reasons for the bandgap tuning. In addition, interface based strain tuning could also cause tuning in bandgaps as shown by others.<sup>170</sup> Second, all the Au-TiO<sub>2</sub> nanocomposite films present an obvious plasmonic absorption peak and the peak position shifts systematically. We recall that the Au NPs' size varies from ~17 nm (700 °C) to 2 nm (300 °C). Such large tunability in Au NP size results in the large shift in the plasmonic absorption peak from 578 nm (500 °C sample) to 622 nm (700 °C sample). Note that the plasmonic absorption for the sample grown at 300 °C is relatively weak and broad and thus there is no clear SPR peak assigned. The 500 °C sample shows relatively higher absorbance than the 300 °C and 700 °C sample, due to the presence of thicker film. The average films thickness of the TiO<sub>2</sub> and Au-TiO<sub>2</sub> nanocomposite at 700°C, 500°C, and 300°C are ~60nm, ~65nm, ~115nm, and ~85nm, respectively. In addition, the absorption coefficient was calculated using the unnormalized spectra using the formula  $\frac{\log(T)}{t}$ , where t and T are the thickness and transmission of the samples. The calculated absorption coefficient is shown in Figure 3-8b. The absorption coefficient of both the 700°C and 500°C is similar in the near-infrared wavelength regime. More interestingly, the film grown under the mixed temperatures of 300 °C, 500 °C and 700 °C shows the maximum absorption of light over a very broad range of spectrum from ~1000 nm to 480 nm which is attributed to the various Au NPs sizes introduced by the three different growth temperatures. Such systematic SPR peak shifting for the Au-TiO<sub>2</sub> samples is believed to be related to the tunable Au NP sizes which leads to the enhanced plasmonic absorption at specific wavelengths.

Furthermore, the anisotropic optical properties of the Au-TiO<sub>2</sub> film deposited under mixed temperatures have been explored using angular dependent transmittance measurements. A schematic of the setup is shown in Figure 3-9a. The incident depolarized light strikes the sample at various incidence angles and the subsequent transmission is recorded. Figure 3-9 summarizes the angular dependent transmittance and reflectivity results of samples grown at mixed temperatures. The plasmonic resonance peak shows a red shift from 579 nm to 592 nm as the incident angle decreases, which is due to the anisotropic nature of Au NPs (see Figure 3-10b). At higher angles, the light in higher wavelength regime is required for the plasmonic resonance of Au NPs. Moreover, varying the transmittance angle from 20° to -20° increases the absorption by 3% (Figure 3-9c). Hence, angular measurement provides a direct measure of the anisotropy nature in the material and confirms the shape dependence of the plasmonic response. It is observed that transmittance decreases at higher angles in all the samples. This is because at higher angles, the

incident and reflected wave can destructively interfere more easily thus decrease the transmission (and increase the reflection).

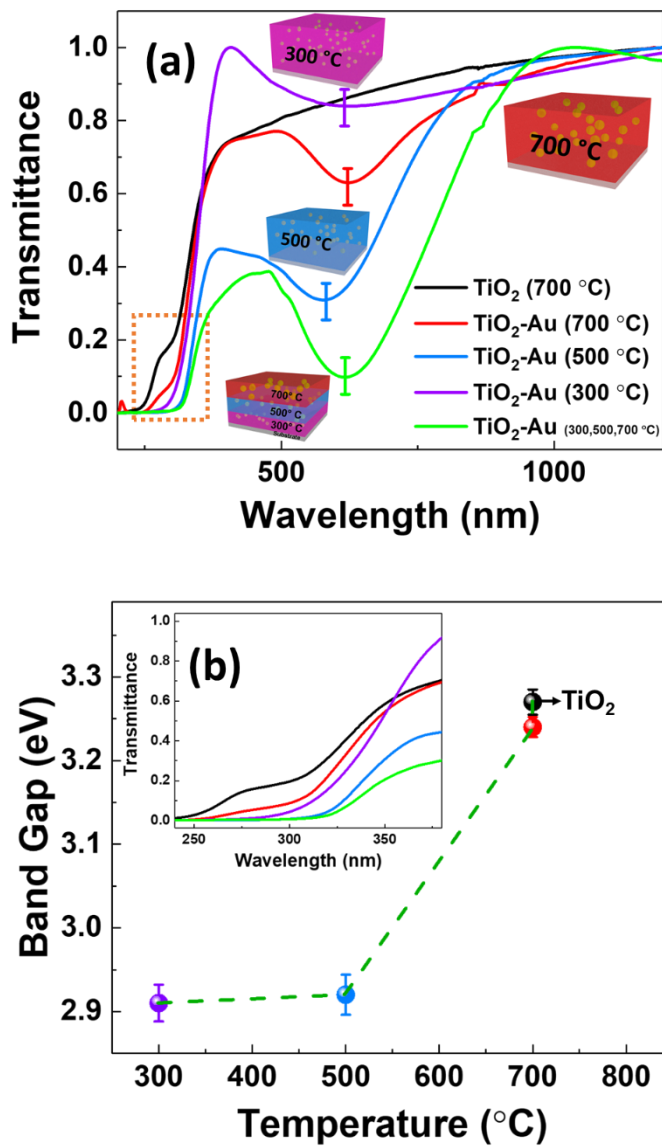


Figure 3-7. (a) Normalized transmittance spectra of the  $\text{TiO}_2$  and Au- $\text{TiO}_2$  nanocomposite films for varied growth temperature and (b) their corresponding band gap calculated using Tauc plot. Marked region in (a) is shown as an inset in (b).

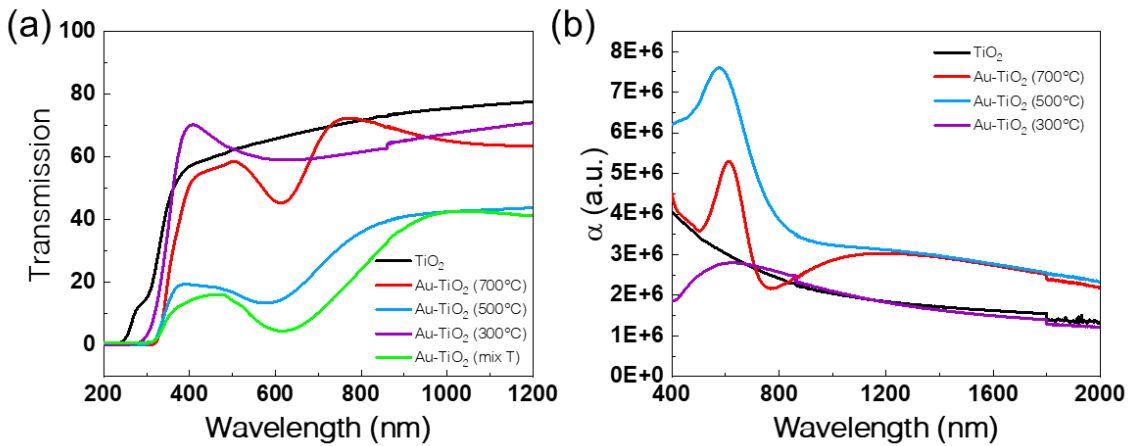


Figure 3-8. (a) Unnormalized transmittance spectra of the TiO<sub>2</sub> and Au-TiO<sub>2</sub> nanocomposite films for varied growth temperature, and (b) the absorption coefficient

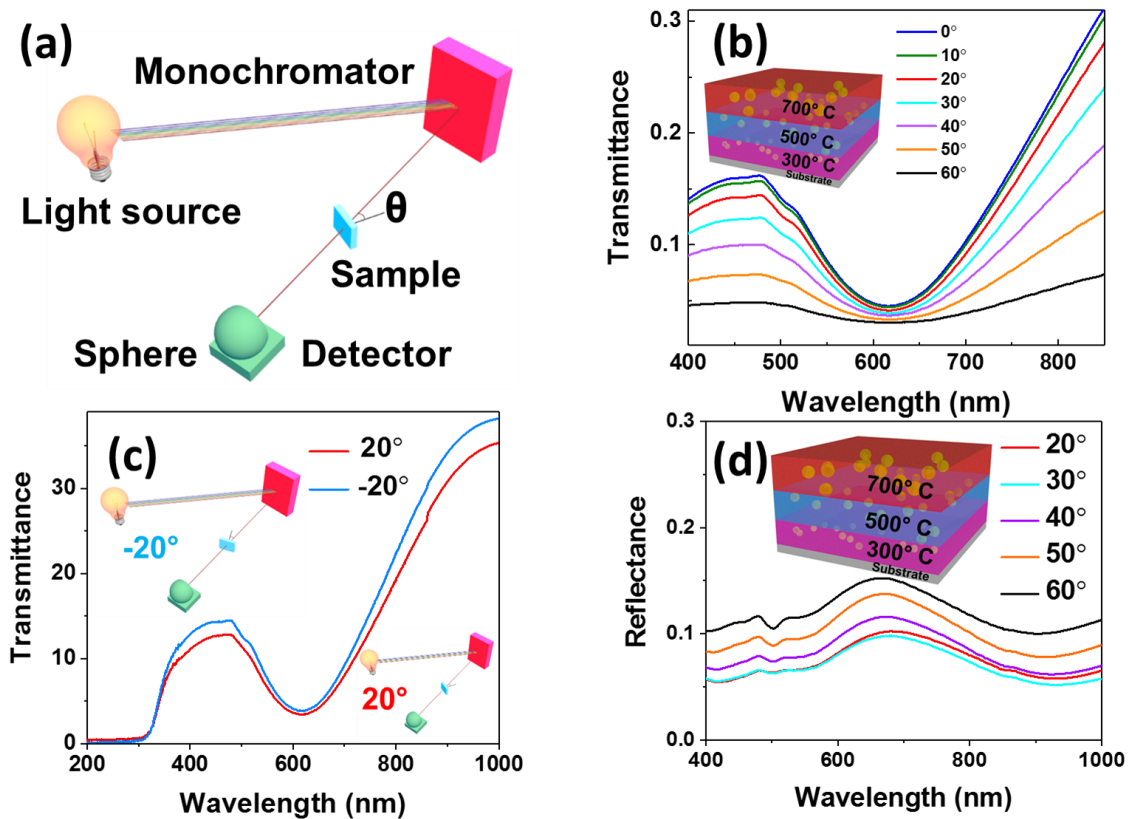


Figure 3-9. (a) Experimental setup used to measure the angular dependent transmission and reflection, (b) transmission spectra for the sample grown at mixed temperature at varying angles, (c) transmittance at 20° and -20° and (d) reflectance at varying angles

To gain a better understanding of the optical properties, the optical response in the nanocomposite system was modeled using the COMSOL Multiphysics 5.3. Figure 3-11a shows the cross-section STEM image of Au-TiO<sub>2</sub> sample grown at 700 °C which was used to approximate the simulated geometry shown in Figure 3-11b. Experimental and calculated absorption spectra show a reasonable match as shown in Figure 3-11c and Figure 3-11d, respectively. The absorption spectra show two major peaks at regimes near 580 nm and 710 nm, observed in both simulated and experimental spectra. Figure 3-11e and Figure 3-11f maps the absorption of Au NPs at 585 nm and 710 nm, respectively. Based on the calculation, it is observed that the peak near 580 nm is caused by Au NPs themselves while the peak near 710 nm corresponds to the sharp corners and inter-particle coupling of Au NPs. Figure 3-11d shows the absorption (W/m) in Au NPs from the surface of Au NPs and from the bulk Au NPs. It again shows that the surface (coupling) effect becomes more prominent at higher wavelengths as the bulk absorption decreases at higher wavelengths. The difference between the experimental and simulation spectrum could be due to that the simulation was based on the geometry from a small region while the experimental data was collected from a large area of the samples.

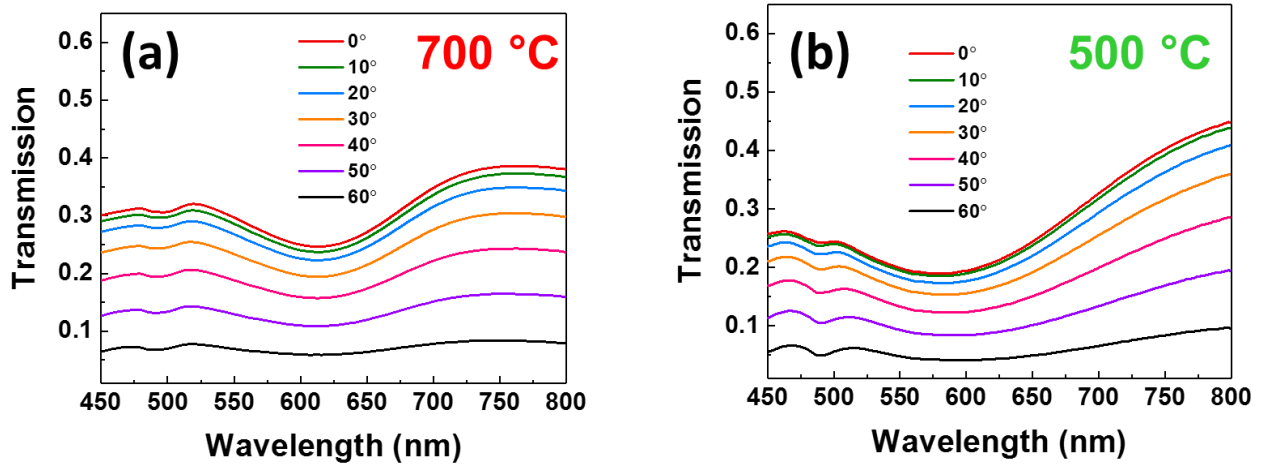


Figure 3-10. Angular dependent transmittance spectra for the Au-TiO<sub>2</sub> sample grown at (a) 700 °C and (b) 500 °C

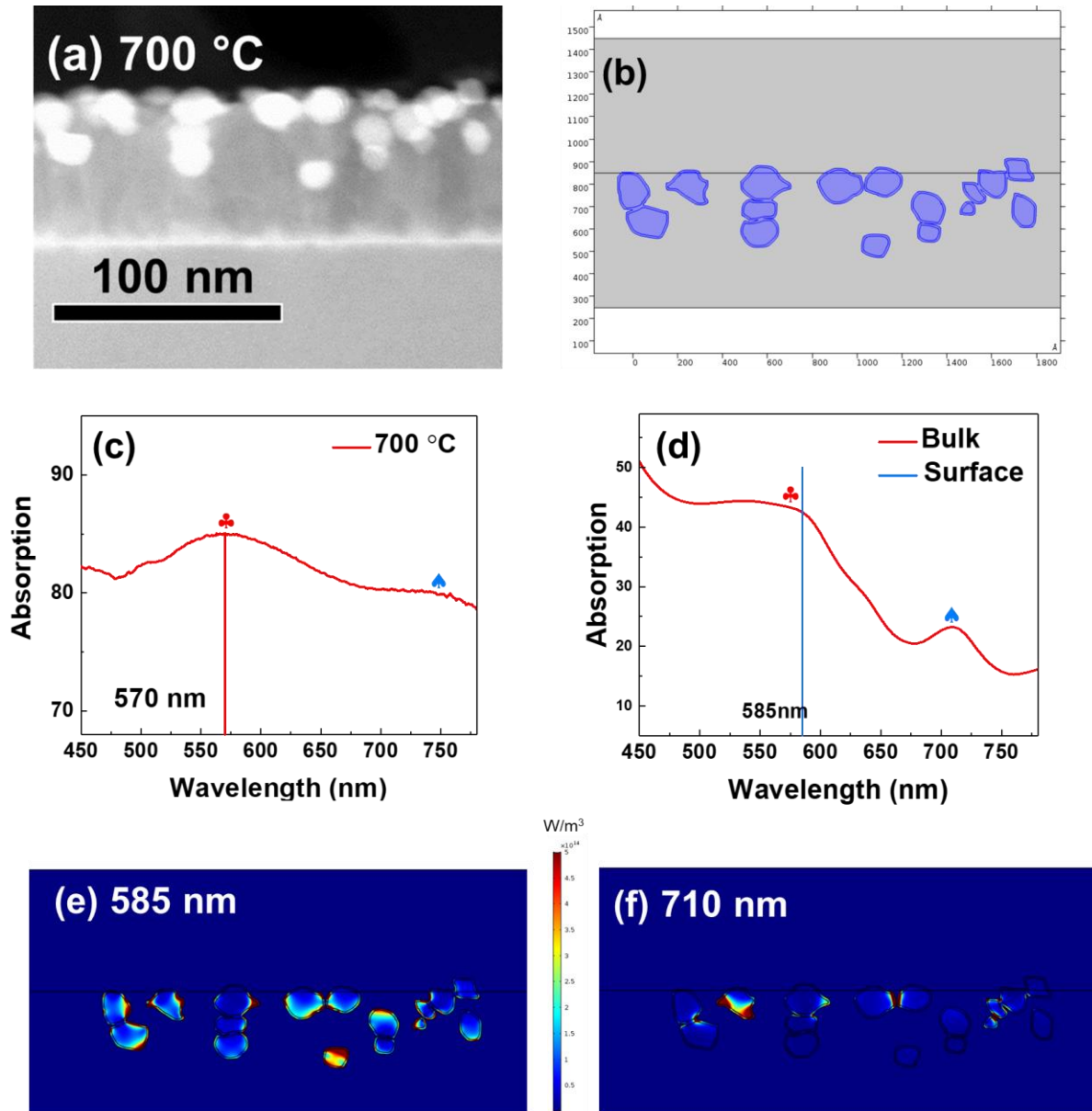


Figure 3-11. (a) Cross-sectional STEM image of the Au-TiO<sub>2</sub> film grown on STO (001) at 700 °C, (b) approximate geometry used to simulate the absorption spectra, (c) Experimental absorption spectra and (d) calculated absorption spectra showing the surface and bulk contribution of Au NPs, (e) absorption map corresponding to incident illumination at 585 nm and (f) 710 nm.

Au NPs introduced during the growth of TiO<sub>2</sub> thin films have major impacts on the overall optical response of the hybrid materials. One of the possible reasons for such strong effects is the possible impact on the overall stoichiometry of TiO<sub>2</sub> matrix. Thus, a detailed study on the film

composition and oxidation states of the elements were studied using XPS. Survey spectra showed the presence of Ti, Au, O and C. High-resolution XPS spectra of Ti 2p and Au 4f core levels for

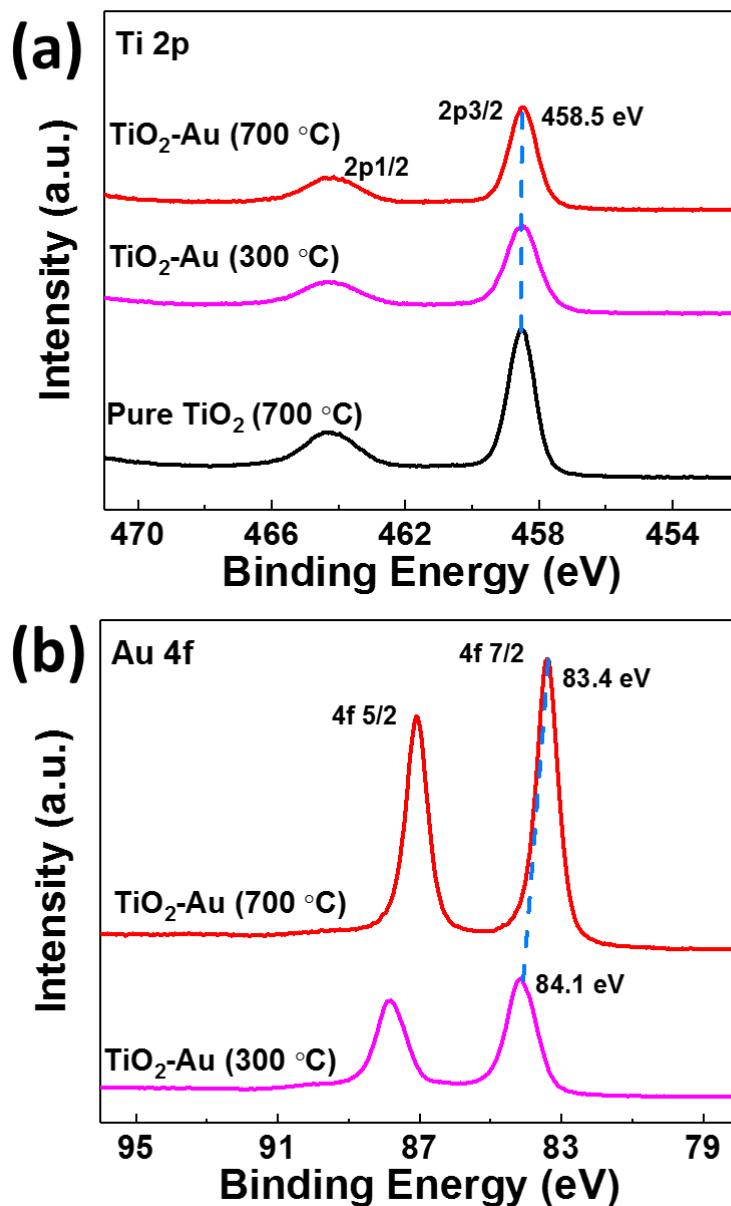


Figure 3-12. High resolution XPS spectra of (a) Ti 2p and (b) Au 4f of Au-TiO<sub>2</sub> nanocomposite thin film.

pure TiO<sub>2</sub> grown at 700 °C and Au-TiO<sub>2</sub> films grown at 300 °C and 700 °C are shown in Figure 3-12. The Ti 2p<sub>3/2</sub> and Ti 2p<sub>1/2</sub> peaks have binding energies of 458.5 eV and 464.3 eV, respectively, with a spin-orbital splitting 5.8 eV. According to the Ti 2p peak positions, Ti chemical state can

be unambiguously assigned to  $Ti^{4+}$  state: these values are consistent with those reported for  $TiO_2$  films.<sup>166,171</sup> The Au 4f<sub>7/2</sub> and Au 4f<sub>5/2</sub> peaks have binding energies of approximately 84.1 and 87.8 eV, respectively, at 300 °C with a spin-orbital splitting of 3.7 eV. The Au 4f peak position and shape correspond to the metallic gold  $Au^0$ . The low binding energy shift of the Au 4f<sub>7/2</sub> peak from 84.1 eV to 83.4 eV is observed as the growth temperature increases from 300 °C to 700 °C. This shift can be explained by the charge transfer from titania to Au NPs ( $Au^{n+} + ne' \leftrightarrow Au^0$ ).<sup>79</sup> Interestingly, the interfacial charge transfer in the case of Au- $TiO_2$  sample grown at 700 °C is more than that of the sample grown at 300 °C. The binding energy of Au increases with the decreasing particle size. Atomic percentage calculated based on the XPS results show that  $TiO_2$ -Au has a closer stoichiometric ratio (atomic ratio of Ti:O) to be 1:2 as shown in Table 3-1. The O/Ti ratio for all the samples was calculated using the survey spectra of XPS in CasaXPS software. The highest intensity peaks for all the elements were chosen and area under the curve was calculated by subtracting the background, separately for different elements. All the peak positions were calculated with reference to the C1s peak being at 284.8 eV. The Au NPs preferentially nucleate near the oxygen vacancies ( $O_o \leftrightarrow V_o^- + \frac{1}{2}O_2 + 2e'$ ), which results in the reduction in the amount of oxygen vacancies.<sup>172-175</sup>

Table 3-1. Quantitative analysis of the XPS spectrum

Sample	Au 4f% (±SD)	C 1s% (±SD)	O 1s%(±SD)	Ti 2p% (±SD)	C-C%	C-O%	O-C-O%	O/Ti (±SD)
$TiO_2$ (700°C)	0	17.04(±0.27)	56.71(±0.25)	25.5(±0.08)	12.31	2.71	2.02	1.96(±0.004)
Au- $TiO_2$ (700°C)	6.17(±0.02)	21.15(±0.33)	50.35(±0.27)	22.33(±0.12)	16.90	2.63	1.62	1.99(±0.001)
Au- $TiO_2$ (300°C)	10.73(±0.03)	22.84(±0.44)	45.54(±0.25)	20.89(±0.14)	19.40	2.75	0.70	1.98(±0.001)

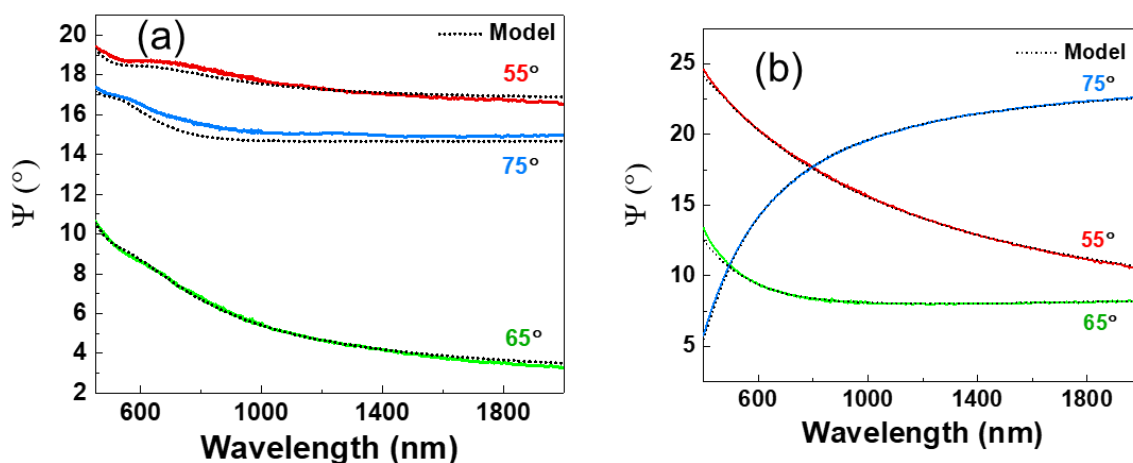


Figure 3-13. Experimental (solid) and fitted (dot) components of the ellipsometric parameter Psi ( $\psi$ ) for the (a) Au-TiO<sub>2</sub> sample deposited at 300 °C and (b) TiO<sub>2</sub> deposited at 700 °C.

Tunability of the optical properties with and without Au addition was evaluated based on the spectroscopic ellipsometry measurement. The data fittings were performed assuming isotropic response ( $\epsilon_{[001]} = \epsilon_{[010]} = \epsilon_{[100]}$ ) through the use of general oscillator models to enforce the Kramers-Kronig consistency. Figure 3-14a shows the ellipsometer parameter  $\psi$  fitted using an appropriate model to calculate the dielectric permittivity (see Methods section). The dielectric complex function, i.e., permittivity real part  $\epsilon'$  and imaginary part  $\epsilon''$  of the TiO<sub>2</sub> and Au-TiO<sub>2</sub> nanocomposite are plotted in Figure 3-14b. The optical constants calculated from Maxwell Garnett EMA closely matches with the constants obtained by the ellipsometry model fitting shown in Figure 3-14b. The additional broadening may be due to anisotropic nature or the size variation of the Au NPs. It is interesting to note that the permittivity of TiO<sub>2</sub> sample deposited at 300 °C is the same as the TiO<sub>2</sub> sample deposited at 700 °C. Therefore, significant effects on tuning the overall permittivity of the Au-TiO<sub>2</sub> nanocomposite comes primarily from the Au NPs and the TiO<sub>2</sub> crystallinity plays a minor in tailoring the properties. The effects of the Au NPs on the overall TiO<sub>2</sub> photocatalytic properties were further characterized by photodegradation of methylene blue (MB) dye with an initial concentration of 10 mg/L. Figure 3-14c shows a typical measurement of MB degradation over time. The normalized absorbance of pure MB, pure TiO<sub>2</sub>, Au-TiO<sub>2</sub> grown at 300 °C, 500 °C, 700 °C and mix temperature is plotted in Figure 3-14d. Interestingly, the experimental results demonstrate that the Au-TiO<sub>2</sub> grown at 500 °C has the highest photodegradation rate among all the five samples. The increased photoactivity of the 500 °C

sample can be attributed to the lower bandgap of TiO<sub>2</sub> ~2.9 eV (see Figure 3-7b) and higher plasmonic absorption over a broader wavelength range as compared to the 300 °C and 700 °C sample (see Figure 3-7a). Since photodegradation is mainly a surface phenomenon with charge transfer taking up to a few nanometers<sup>164</sup>, the relative different thicknesses of the film can be disregarded. In addition, effective interfacial charge transfer across the Au/TiO<sub>2</sub> interface for the films deposited at higher temperature (as shown by XPS) also contributes to the increased photocatalytic activity. Thus, these results directly correlate the size dependence of Au NPs with their photocatalytic activity and demonstrate potential in designing photocatalytic devices with higher efficiencies. Different Au NP sizes have resulted in the obvious tuning of the absorption peak and the band gap of TiO<sub>2</sub> as shown earlier. Therefore, we believe that the obvious tuning effects on permittivity and catalytic properties observed in the Au-TiO<sub>2</sub> samples comes primarily from the Au NPs particle size.

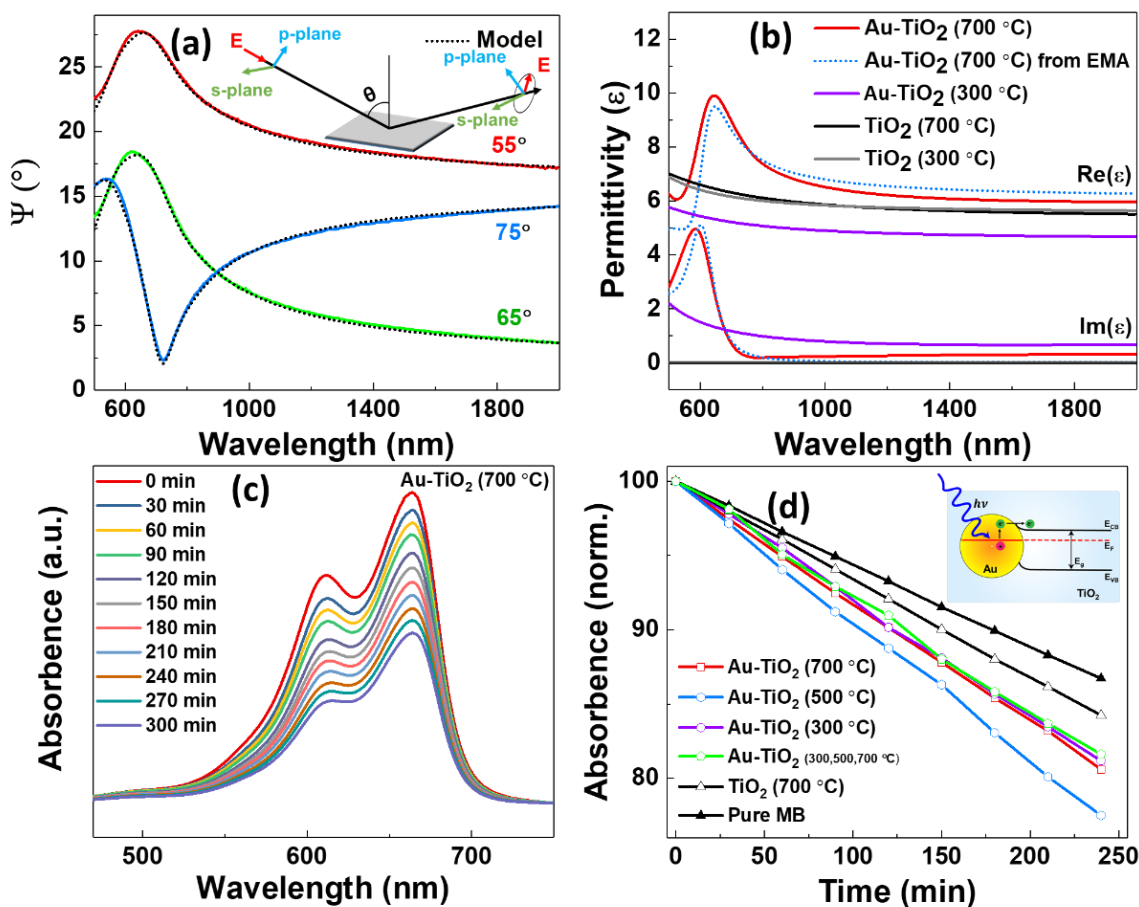


Figure 3-14. (a) Experimental (solid) and fitted (dot) components of the ellipsometric parameter  $\Psi$  ( $\psi$ ) for the  $\text{TiO}_2$ -Au sample deposited at  $700\text{ }^\circ\text{C}$ . Inset shows the ellipsometer measurement setup. The ellipsometer parameters  $\psi$  and  $\Delta$  (not shown here) were measured at different angles to improve the accuracy of the fitted model (b) Real and imaginary part of the permittivity for the  $\text{TiO}_2$  and  $\text{TiO}_2$ -Au sample deposited at  $700\text{ }^\circ\text{C}$  and  $300\text{ }^\circ\text{C}$ , (c) Absorption spectra for methylene blue for different irradiation times with the  $\text{Au-TiO}_2$  film grown at  $500\text{ }^\circ\text{C}$  and (d) normalized absorbance plotted against the irradiation time for the three different films along with the reference MB solution. Inset shows the mechanism of plasmon-induced charge transfer. Electrons near the Au Fermi level are excited to surface plasmon state and get transferred to  $\text{TiO}_2$  conduction band where the electron-driven hydrogen evolution half-reaction takes place.

There are several key features that this novel structure provides over other previously reported  $\text{Au-TiO}_2$  systems.<sup>149,150,158,176-178</sup> First, the fully embedded Au NPs inside the  $\text{TiO}_2$  matrix present efficient charge transfer to the semiconductor matrix as compared to other surface Au NPs cases.<sup>159</sup> This is attributed to the increased interfacial area available for electron injection. Second, the shape, size and density of Au NPs can be tailored and achieved by using a one-step growth

method. Controlling the shape and size of NPs is important for tailoring their plasmonic response and for further exploring the size dependence on charge injection efficiency.<sup>159</sup> A highly uniform size distribution of Au NPs can also be achieved. In addition, very small Au NPs, as fine as 2 nm, can be achieved, which is much less than the mean free path of electron-electron scattering (~30 nm for a 2 eV electron) and ideal for the electron to reach the interface.<sup>159</sup> Third, the optical permittivity and the catalytic properties of the Au-TiO<sub>2</sub> nanocomposites can be effectively tuned by varying the Au NP size as measured using ellipsometry and photodegradation experiments. Fourth, the co-growth method provides flexibility in morphology control (in terms of crystallinity, purity and composition) over other methods previously employed to fabricate Au-TiO<sub>2</sub> nanocomposites.<sup>165,166</sup> It is possible to adopt this approach for incorporating other plasmonic nanostructures in oxide matrix for enhanced optical, electrochemical and photocatalytic properties. Incorporation of Au particles increases the solar energy harvesting range to as high as 1000 nm (compared to bare TiO<sub>2</sub> which is active below 390 nm) allowing applications as photocatalysis and light concentrators.<sup>74</sup> The one-step PLD process employed here offers easy control of the volume fraction of Au NPs which provide new opportunities to manipulate light-matter interaction over a wide range of wavelength.

### 3.4 Conclusion

In summary, we have demonstrated a one-step PLD deposition technique to deposit highly textured metastable anatase TiO<sub>2</sub>-Au nanocomposite thin films with highly tailorable shape and size of Au NPs by varying the growth temperature. Incorporation of Au NPs effectively tunes the band gap of TiO<sub>2</sub>. The shape and size tuning of Au NPs increases the absorption efficiency over a broad optical spectrum. The absorption spectra have mainly two components: one arises from Au NPs at its resonant wavelength and the other results from coupling between Au NPs seen at longer wavelengths. In addition, results confirm that the binding energy of Au increases with decreasing NP size and incorporation of Au helps to improve the stoichiometry of TiO<sub>2</sub>. Photodegradation results conclude that the synergistic impact of lowering of the TiO<sub>2</sub> bandgap along with the plasmonic absorption of Au NPs play a significant role in determining the photoactivity of the thin films. This controlled fabrication of TiO<sub>2</sub>-Au nanocomposite thin films presents new opportunities

to fabricate nanoscale metamaterials and control photon-matter interaction at nanoscale, which can find useful applications as photocatalysis and photovoltaics.

### 3.5 Experimental Section

**Thin Film Growth.** Au-TiO<sub>2</sub> films were fabricated using a TiO<sub>2</sub>- Au target prepared by conventional solid-state sintering process in air at 1000 °C for 3 hours. Both pure TiO<sub>2</sub> and Au-TiO<sub>2</sub> thin films were deposited on single-crystal STO (001) substrates using a PLD system (with a KrF excimer laser, Lambda Physik Compex Pro 205,  $\lambda = 248$  nm). The laser beam was focused on the target surface at a 45° angle of incidence to obtain an energy density of approximately 3 J/cm<sup>2</sup>. The base pressure of the chamber was  $1 \times 10^{-6}$  Torr or lower before deposition. The Au-TiO<sub>2</sub> samples were deposited with the temperature ranging from 300 °C to 700 °C and a laser frequency of 5 Hz. To avoid oxygen deficiencies in the films and potential oxidation of Au, an intermediate O<sub>2</sub> partial pressure of 20 mTorr was maintained during the depositions. The samples were cooled to room temperature under 100 Torr O<sub>2</sub> after the deposition.

**Structural, Optical and Surface Characterization.** Structural characterization of the samples was carried out using X-Ray Diffraction (XRD) and Transmission Electron Microscopy (TEM). XRD 2-theta scans were recorded using PANalytical Empyrean 2 with Cu K <sub>$\alpha$</sub>  radiation and the TEM/STEM images and selected area electron diffraction (SAED) patterns were acquired using FEI TALOS 200X. The TEM samples were prepared by cutting and manual grinding followed by dimpling and ion-polishing (precision ion polishing system (PIPS II)). Optical characterization was carried using UV-Vis-NIR absorption spectrophotometer (Perkin Elmer Lambda 1050). The angular dependent transmission/reflectivity measurements were performed using Total Automated Measurement System (TAMS). Incident angle was varied from 10° to 60°. Full wave simulations were carried out using COMSOL Multiphysics 5.3 to fit the optical measurement results. The chemical composition of the TiO<sub>2</sub>-Au films was investigated using X-ray photoelectron spectroscopy (XPS) system (Kratos Axis Ultra DLD) with monochromatic Al K <sub>$\alpha$</sub>  radiation (1486.6 eV).

**Photocatalytic activity measurement.** The photocatalytic activity of different samples was evaluated using photodegradation of methylene blue (MB) dye under solar light using a Newport 300W Xenon arc lamp (Model 66902) equipped with an AM1.5G filter with an intensity of 54

mW/cm<sup>2</sup>. The 10 x 5 mm samples were suspended within the quartz cuvettes in a MB solution. After regular intervals, the samples were measured with UV-Vis spectrometer. The peak area was used to estimate the concentration of MB shown in Figure 3-13.

**Permittivity Measurements.** The permittivity of the TiO<sub>2</sub> and Au-TiO<sub>2</sub> nanocomposite was evaluated using spectroscopic ellipsometry (JA Woollam RC2). The incident angle was varied from 55° to 75° with a step size of 10°. The ellipsometer parameters  $\psi$  and  $\Delta$  are related by the equation:  $r_p/r_s = \tan(\psi)e^{i\Delta}$ , where  $r_p$  and  $r_s$  are the reflection coefficient for the p-polarization and s-polarization light, respectively. The parameters  $\psi$  and  $\Delta$  were fitted using an appropriate model to calculate the dielectric permittivity. The  $\psi$  and  $\Delta$  are measured at different angles to improve the accuracy of the fitted model. The calculations were carried out using the ellipsometry software CompleteEASE. A Cauchy model was used to fit the anatase TiO<sub>2</sub>. A general oscillator layer consisting of one Tauc-Lorentz oscillator and one Lorentz oscillator was used to fit the Au-TiO<sub>2</sub> nanocomposite. The fitted models are shown in Figure 3-13.

## 4. SELF-ASSEMBLED ORDERED THREE-PHASE Au-BaTiO<sub>3</sub>-ZnO VERTICALLY ALIGNED NANOCOMPOSITES ACHIEVED BY A TEMPLATING METHOD

This chapter is reprinted with permission from “Self-assembled ordered three-phase Au-BaTiO<sub>3</sub>-ZnO vertically aligned nanocomposites achieved by a templating method” by S. Misra, et al., *Advanced Materials*, 2018, 1806529. © 2018 WILEY-VCH Verlag GmbH & Co. KGaA

### 4.1 Overview

Complex multi-phase nanocomposite designs present enormous opportunities for developing next generation integrated photonic and electronic devices. Here, we demonstrate a unique three-phase nanostructure combining a ferroelectric BaTiO<sub>3</sub>, a wide band-gap semiconductor of ZnO and plasmonic metal of Au towards multifunctionalities. By a novel two-step templated growth, a highly ordered Au-BaTiO<sub>3</sub>-ZnO nanocomposite in a unique “*nanoman*”-like form, i.e., self-assembled ZnO nanopillars and Au nanopillars in BaTiO<sub>3</sub> matrix, has been realized, and is very different from the random three-phase ones with randomly arranged Au nanoparticles and ZnO nanopillars in BaTiO<sub>3</sub> matrix. The ordered three-phase “*nanoman*”-like structure provides unique functionalities such as obvious hyperbolic dispersion in the visible and near infrared regime enabled by the highly anisotropic nanostructures compared to other random structures. Such self-assembled and ordered three-phase nanocomposite is obtained through a combination of Vapor-Liquid-Solid (VLS) and two-phase epitaxy growth mechanisms. The study opens up new possibilities in the design, growth and application of multi-phase structures and provides a new approach to engineer the ordering of complex nanocomposite systems with unprecedented control over electron-light-matter interaction at nanoscale.

### 4.2 Introduction

Complex functional oxide materials have received much interests for both the discovery of new material systems and the control of physical properties and multifunctionalities towards emerging technological developments of metamaterials,<sup>85</sup> spintronics,<sup>179</sup> multiferroics,<sup>13</sup> and quantum systems.<sup>180</sup> Several two-phase nanocomposite systems, exhibiting multilayer or nanowire morphology, have been demonstrated for achieving enhanced physical properties, including

enhanced ferroelectricity,<sup>27</sup> ferromagnetism,<sup>181</sup> magnetoresistance<sup>182</sup> and exotic optical properties such as optical magnetism,<sup>87</sup> negative refraction,<sup>88</sup> and hyperbolic dispersion.<sup>89</sup> For example, hyperbolic metamaterials, having ordered and anisotropic metal-dielectric nanocomposite design, support the propagation of high wavevectors.<sup>90</sup> Since very few naturally hyperbolic materials exist, this artificially engineered nanocomposite approach provides a multi-functional platform to realize such materials with applications in sub-diffraction imaging,<sup>84</sup> sensing,<sup>183</sup> waveguiding<sup>184</sup> and an opportunity to achieve coupled electric, magnetic and optical responses. However, due to the availability of a limited range of structures in terms of crystallinity and morphology, a greater design flexibility and a structural complexity along with versatile growth techniques are needed for developing next generation integrated photonic and electronic devices. This can be achieved by incorporating a third phase through the three phase nanocomposite designs by judicious selection of materials and functionalities.

Besides material selection, the spatial ordering of the phases has great impacts on the overall functionalities of nanocomposite materials. Previous efforts to grow ordered ceramic-metal nanocomposites have focused on applying patterning techniques such as anodized alumina oxide (AAO) templates,<sup>79</sup> e-beam lithography,<sup>44</sup> focused ion beam (FIB),<sup>185</sup> and substrate nanotemplating.<sup>22</sup> In contrast, a self-assembly approach for fabricating such ordered oxide-metal nanocomposites prove cost-effective and overcome the resolution limitation and complex fabrication steps. Controlled synthesis of such self-assembled complex hybrid nanostructures with desired ordering and epitaxial quality remains a challenge. Specifically, large difference in surface energy, growth kinetics, and high tendency of oxidation and inter-diffusion between vastly different phases remain as major challenges and further impose difficulties in ordering control. Despite the recent success of the self-assembled epitaxial 2-phase oxide-metal nanocomposite growths,<sup>7,35,40,41,132,139,186</sup> achieving spatial ordering in nanoscale hybrid materials is still a great challenge and such success is very limited.<sup>22,187</sup>

In this work, we introduce a new design with highly epitaxial ordered three phase thin film (i.e., Au-BaTiO<sub>3</sub>-ZnO), for the first time, taking advantage of the Vapor-Liquid-Solid (VLS) mechanism through a templating method using pulsed laser deposition, a physical vapor deposition (PVD) tool. Instead of a randomly arranged three-phase nanostructure (Figure 4-1b), such three-phase ordering is achieved via a combined self-assembly and templating method as illustrated in the schematic drawings in Figure 4-1c. BaTiO<sub>3</sub> (BTO), a perovskite oxide with both ferroelectric

and non-linear optical properties, and ZnO, a direct wide band-gap semiconductor, allow the possibility of BTO:ZnO vertically aligned nanocomposite (VAN) structure because of their phase immiscibility (evidenced by the BaO-TiO<sub>2</sub>-ZnO ternary phase diagram<sup>188</sup>) and chemical compatibility as shown in Figure 4-1a. Being motivated by the ordered growth of ZnO nanowires (NW) via VLS growth mechanisms, the vertically aligned Au nanopillars embedded in the template layer of Au-BTO act as the seeds for catalyzing ZnO NW growth and allows the highly ordered spatial control of ZnO nanostructures as illustrated in Figure 4-1c. More interestingly, the ordered Au-BTO-ZnO three-phase metamaterials allow a high degree of optical and electrical property tunabilities, including the hyperbolic dispersion in the visible and near infrared regime, in addition to the very strong ferroelectric/piezoelectric properties. The properties are compared with the random three-phase nanocomposite structures to explore the power of structural ordering in functionality tuning towards future three-phase hybrid metamaterial designs.

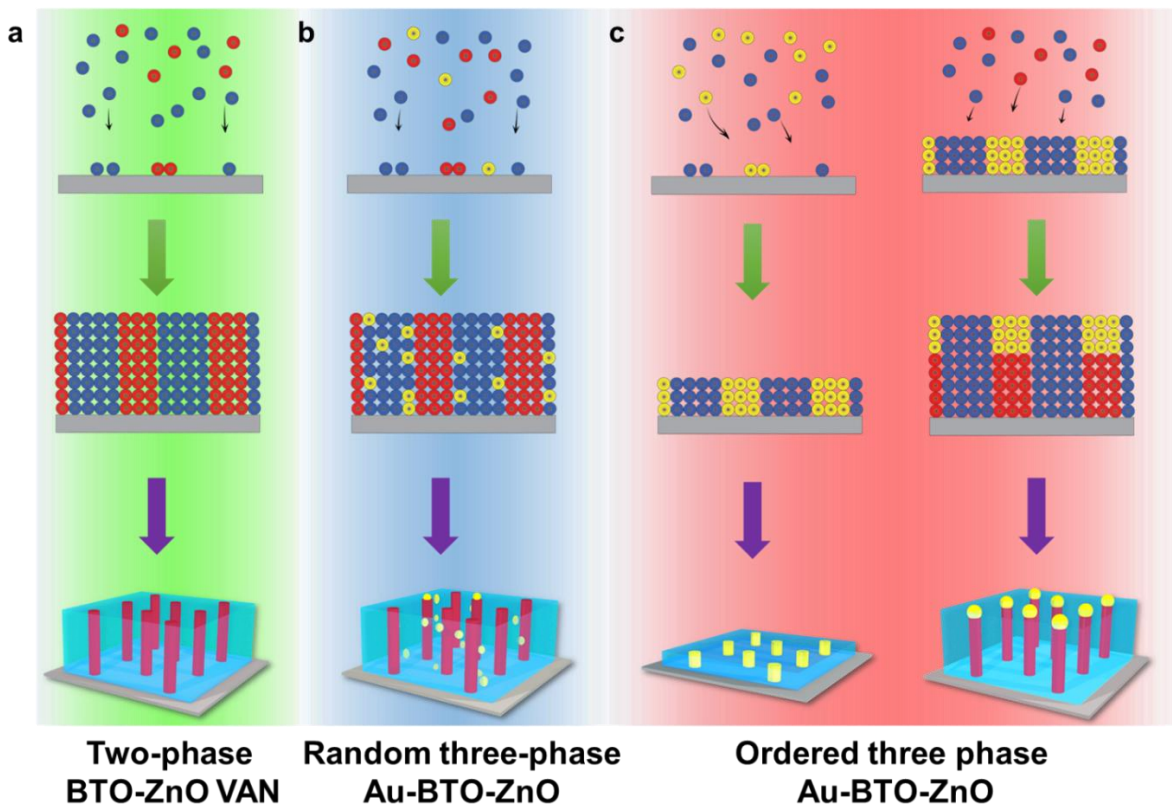


Figure 4-1. Growth mechanism schematic of (a) two-phase BTO-ZnO vertically aligned nanocomposite (VAN), (b) random three-phase Au-BTO-ZnO, and (c) ordered three-phase Au-BTO-ZnO. In (a), regions of BTO and ZnO get nucleated side each other giving rise to a self-assembled BTO-ZnO VAN. (b) shows three separate regions of nucleation for Au, BTO and ZnO. (c) shows the two-step growth of ordered three phase nanocomposite. Au NPs are capped at the end of ZnO pillars giving rise to the ordered three-phase *'nanoman'* structure.

### 4.3 Results and Discussion

The microstructure and three-phase morphologies are compared between the random and highly ordered nanocomposites using X-ray diffractometry (XRD), high-angle annular dark-field scanning transmission electron microscopy (HAADF-STEM) and electron diffraction. Figure 4-2 shows a collection of TEM/STEM/EDS (energy-dispersive X-ray spectroscopy) mapping for both plan view and cross-section samples of the random three-phase nanocomposite. The expected morphology is shown in Figure 4-2a. The EDS elemental map of Au, Zn and Ba from the plan-

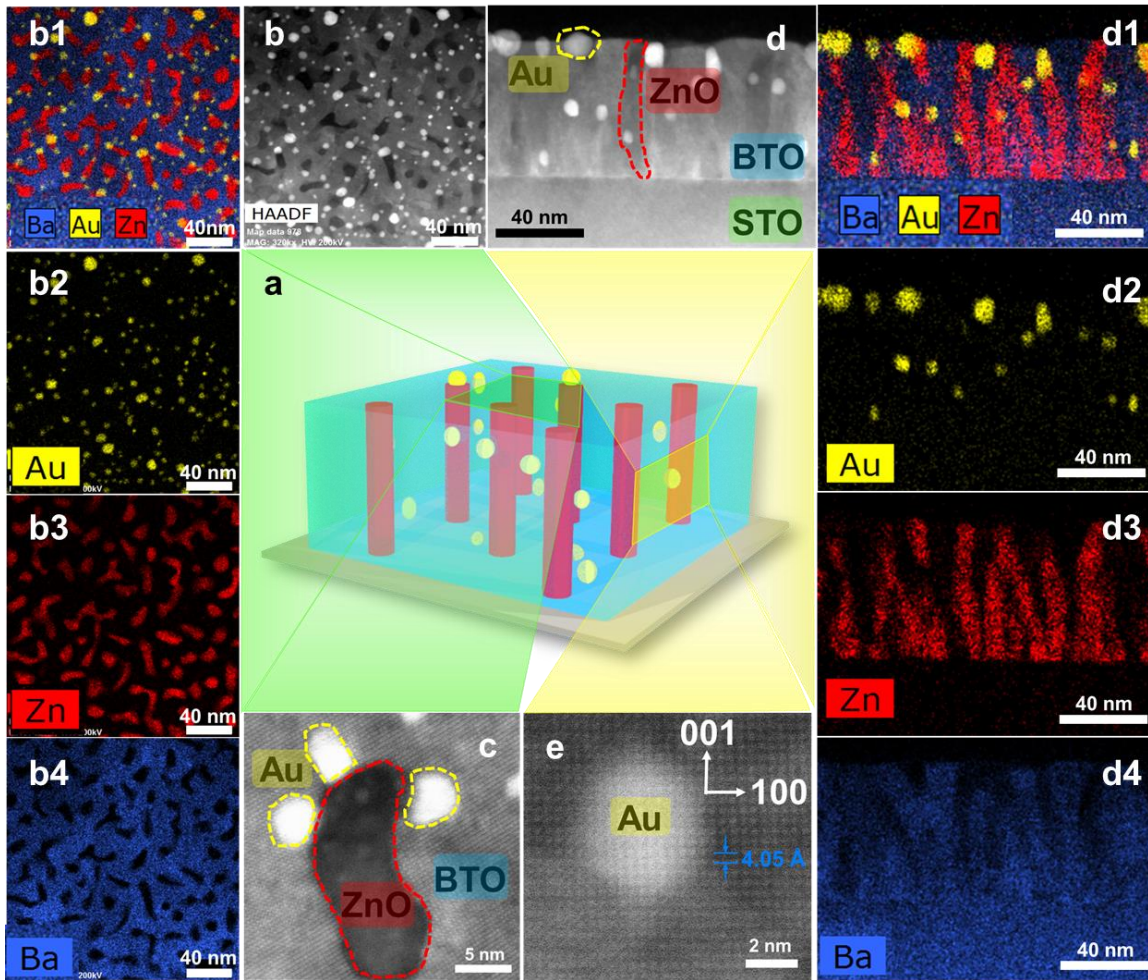


Figure 4-2. Microstructure study of the random three-phase Au-BTO-ZnO nanocomposite. (a) 3D schematic illustration of the random three-phase Au-BTO-ZnO nanocomposite, (b) plan-view scanning transmission electron microscopy (STEM) image with the corresponding EDS mapping showing distribution of the phases, (c) atomic-scale high resolution STEM (HRSTEM) plan-view image showing the three phases, (d) cross-sectional STEM image with the corresponding EDS mapping, and (e) HRSTEM image showing the lattice spacing and growth direction of BTO.

view sample (in Figure 4-2b) shows a clear and sharp interface between the three phases which suggests that all the phases grow separately without any obvious inter-diffusion (Figure 4-6a-c). Clearly, random random distribution of Au NPs embedded within the columnar VAN structure of BTO-ZnO can be observed in Figure 4-2c. The cross-sectional STEM study along with its corresponding EDS mapping shown in Figure 4-2d shows the vertical ZnO pillars and Au NPs with an average diameter of ~6 nm distributed in the BTO matrix. The corresponding selected area electron diffraction pattern (SAED) shown in Figure 4-3a indicates the highly epitaxial growth of

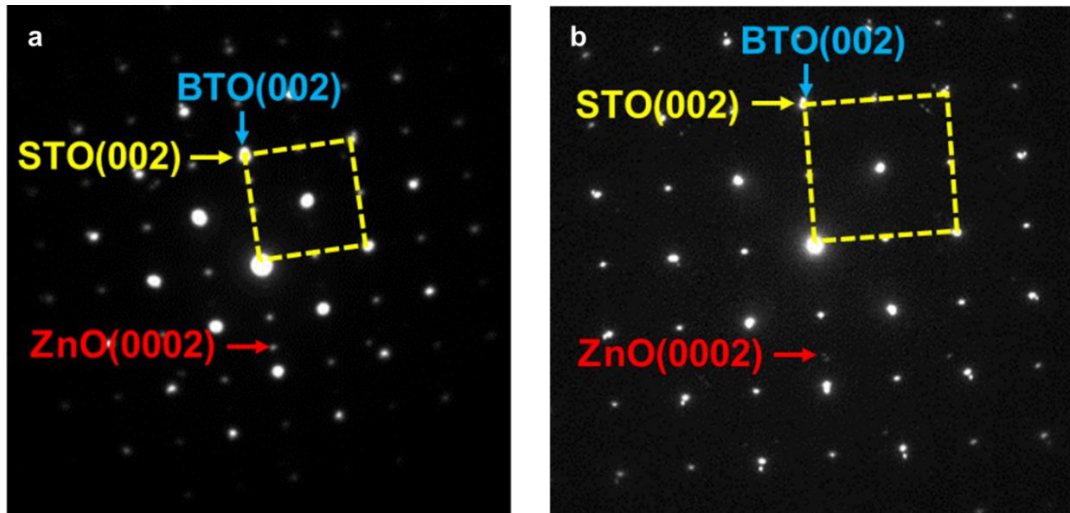


Figure 4-3. SAED of (a) random and (b) ordered three phase Au-BTO-ZnO nanocomposite

the nanocomposite. From the cross-sectional and plan-view high resolution STEM images shown in Figure 4-2c and Figure 4-2e along with SAED pattern taken in the [100] zone axis, the growth direction of the nanocomposite can be identified as BTO(002)//ZnO(0002)//Au(111)//STO(002) and BTO[002]//ZnO[0002]//Au[111]//STO[002]. These results are well consistent with the XRD results in Figure 4-4.

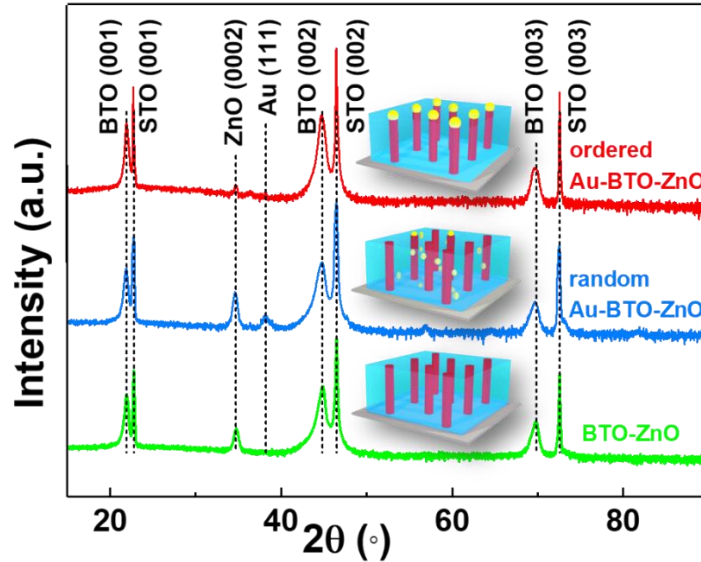


Figure 4-4. XRD  $\theta$ - $2\theta$  scan of the three different nanocomposite designs deposited on SrTiO<sub>3</sub> (001)

Figure 4-5 presents the microstructure and phase distribution of the ordered three-phase structure with the schematic of the expected morphology shown in Figure 4-5a. The highly ordered structure is evident from both the plan-view and cross-section STEM images shown in Figure 4-5b and Figure 4-5c, respectively. The auto-correlation map shown in Figure 4-7 shows the preferred ordering of the ZnO phase. Figure 4-5b1-b4 shows the elemental EDS mapping of the plan-view sample showing clear and sharp interfaces between the three phases and confirming no obvious inter-diffusion between the phases (Figure 4-6d-f). Figure 4-5c displays the phase distribution in cross-section where a clear separation of three-phases is evident by the unique ‘*nanoman*’ structure. The average diameter of both the ZnO and Au nanopillars is about 6 nm. Evidently, Au NPs are capped at the end of ZnO NWs which is characteristic of the VLS growth mechanism.

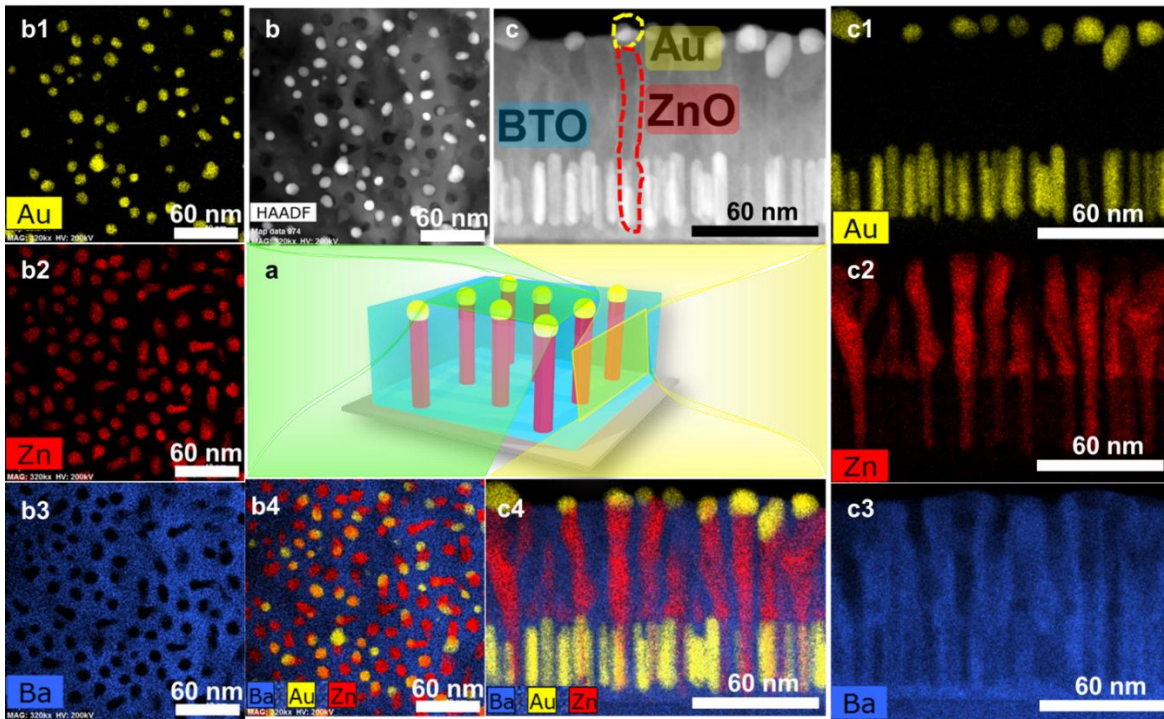


Figure 4-5. Microstructure study of the ordered three-phase Au-BTO-ZnO nanocomposite. (a) 3D schematic illustration of the ordered three-phase Au-BTO-ZnO nanocomposite, (b) plan-view STEM image with the corresponding EDS mapping showing distribution of the phases, and (c) cross-sectional STEM image with the corresponding EDS mapping

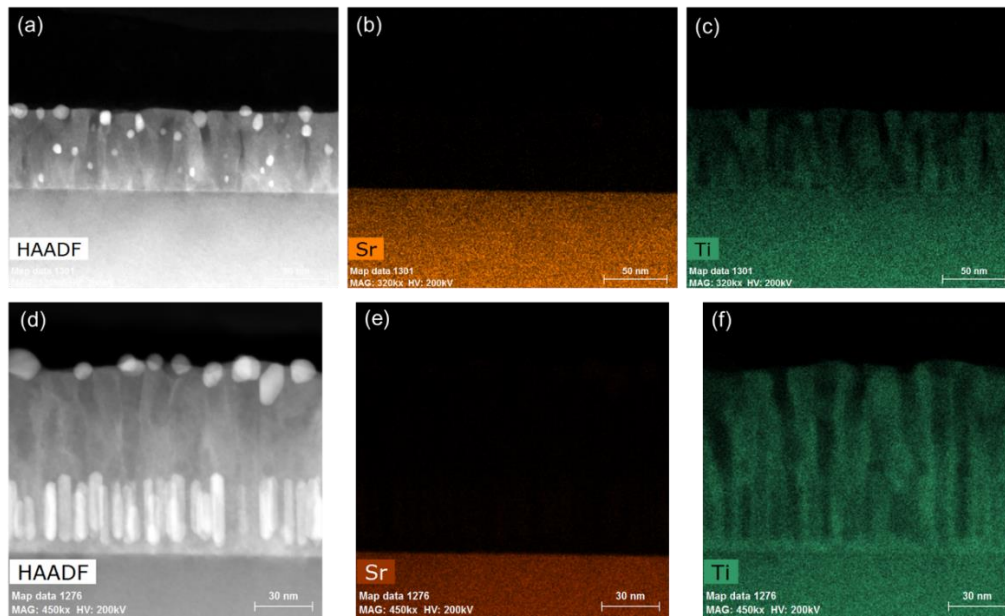


Figure 4-6. EDS elemental maps for Sr and Ti for both random and ordered three-phase nanocomposite

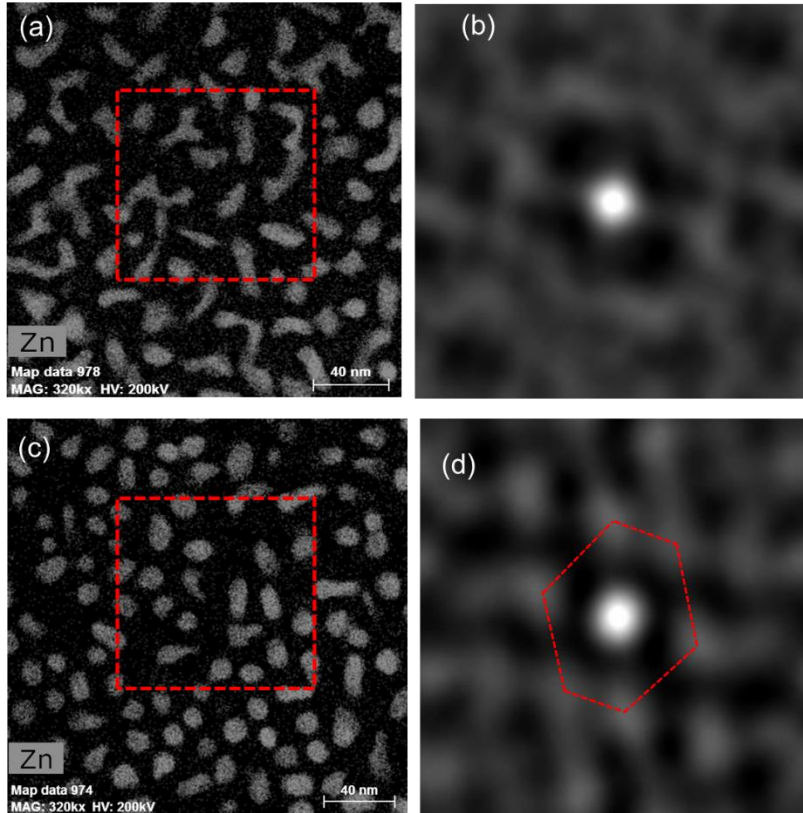


Figure 4-7. Auto-correlation maps for (a-b) random and (c-d) ordered three-phase nanocomposite

In the past, VLS mechanism has also been widely explored for the growth of ZnO NWs using chemical vapor deposition (CVD) growth techniques.<sup>191,192</sup> Complications arise for the oxide NW growth since most oxides have a high melting point and achieving ordered and orientation-controlled NW synthesis is challenging. In the conventional VLS mechanism (Figure 4-9), the substrate is patterned with the isolated catalyst nanoclusters for the subsequent NW growth. The choice of catalyst is dependent on the choice of NW material. For example, metals such as Au, Fe, Al, Cu, Ni, Sn, Fe and Ag have been selected for the growth of Si, ZnO, GaN, ITO and GaAs NW.<sup>191–198</sup> Specifically, the Zn vapor reacts with the Au catalyst to form a lower melting point liquid eutectic alloy shown in Figure 4-8a. Once this eutectic alloy droplet become supersaturated, crystalline ZnO is formed.<sup>189,190,199–201</sup> Different from the conventional VLS growth, the ordered three-phase ‘*nanoman*’ structure uses the Au pillars in the BTO-Au nanocomposite as the catalysts for the growth of ZnO nanopillars in BTO matrix. This allows the growth of perfect vertically aligned ZnO nanowires nucleated preferentially on top of Au nanopillars through the VLS mechanism schematically presented in Figure 4-8b. It is observed that BTO phase in the upper

BTO-ZnO layer coherently grows on top of the BTO phase in the lower Au-BTO layer due to matching interfacial energy and perfect lattice matching. Subsequent incoming flux of BTO and ZnO adatoms constrains the ZnO to grow on top of Au nanopillars which catalyzes the further unidirectional growth of ZnO NW by forming a low temperature eutectic alloy through the VLS mechanism. As a result, ZnO NW precipitate at the solid-liquid interface while growing epitaxially on STO (001) substrate.

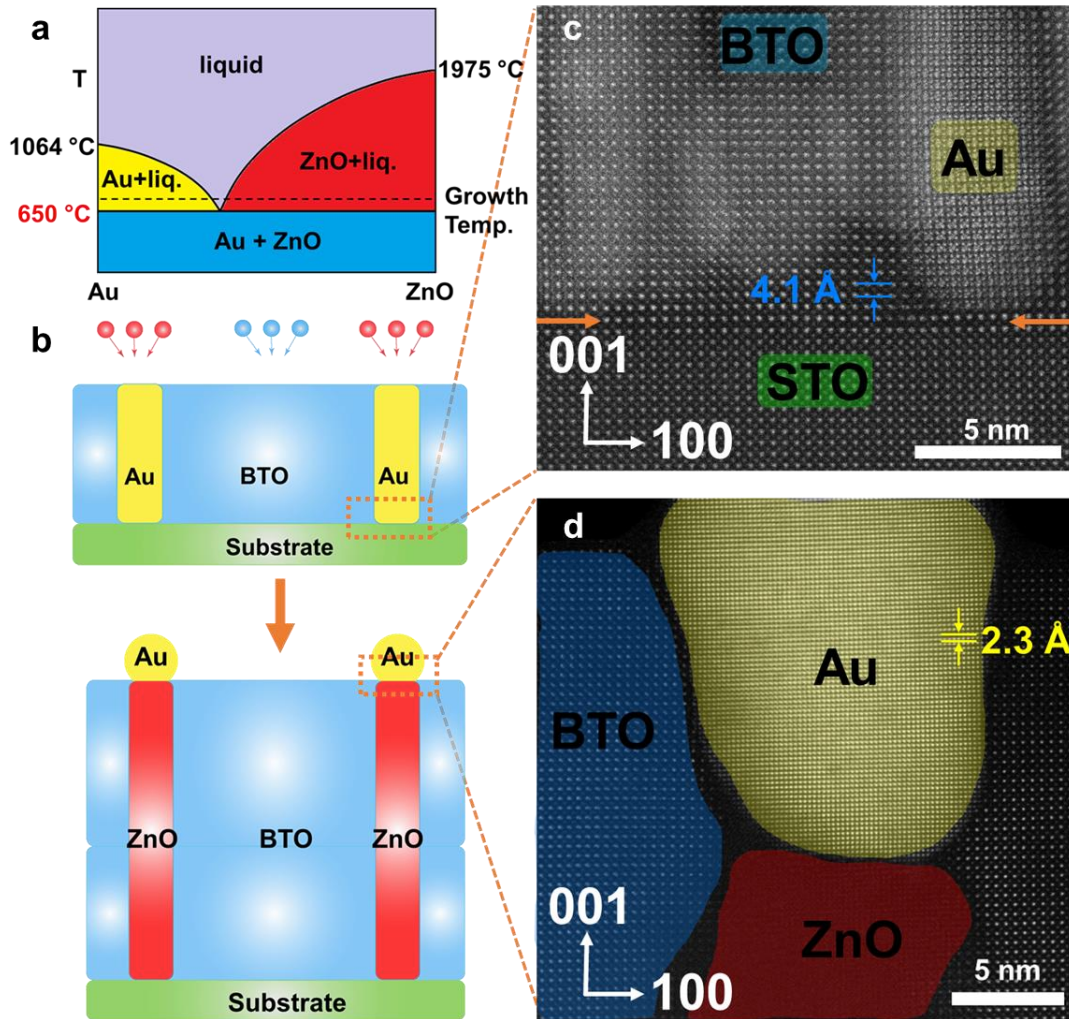


Figure 4-8. (a) Phase diagram of Au and ZnO showing the eutectic temperature at 650°C.<sup>189,190</sup> The growth temperature used for the deposition was 700°C. (b) 2-step growth process employing the EAVLS mechanism enabling the growth of ordered vertically aligned three-phase nanocomposite, (c) atomic-scale HRSTEM cross-section image showing the templated Au-BTO and STO epitaxial interface before the growth of second layer, and (d) atomic-scale HRSTEM image showing the Au NP capping the ZnO NW and surrounded by the BTO matrix indicative of the VLS mechanism.

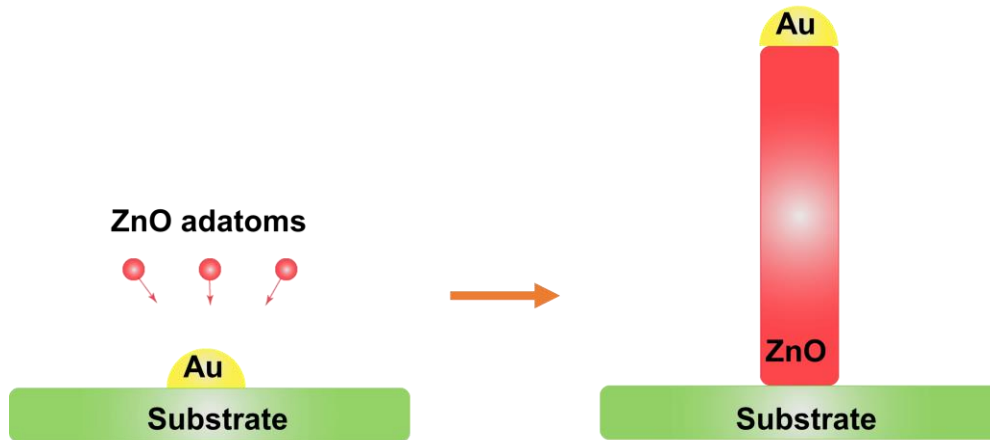


Figure 4-9. Conventional VLS mechanism enabling the growth of crystalline ZnO NW using Au NPs as catalysts.

High-resolution cross-sectional STEM image of the templated Au-BTO film and STO (001) substrate shown in Figure 4-8c presents a fully coherent interface and confirms the epitaxial growth of Au nanopillars throughout their length with a sharp interface with BTO. Figure 4-8d shows the atomic-scale HRSTEM image after the two-step growth showing the Au NP capping the ZnO NW indicative of the VLS mechanism. Au pillars and NPs grow along the [111] direction to minimize its interfacial free energy and the  $d$ -spacing of the (111) planes is  $2.3\text{\AA}$ . The lattice parameters, estimated to be  $\sim 4.0\text{\AA}$  for Au and  $4.1\text{\AA}$  for BTO, are consistent with the XRD measurements in Figure 4-4 (Supporting Information). The epitaxial matching relationships of the nanocomposite can be identified as  $\text{BTO}(002)//\text{ZnO}(0002)//\text{Au}(111)//\text{STO}(002)$  and  $\text{BTO}[002]//\text{ZnO}[0002]//\text{Au}[111]//\text{STO}[002]$  from the high-resolution STEM images and the corresponding SAED of the area, taken in the  $\langle 001 \rangle$  zone axis (Figure 4-3b, Supporting Information). Thus, by a template-assisted growth method, the ordered growth of three-phase nanocomposites has been demonstrated.

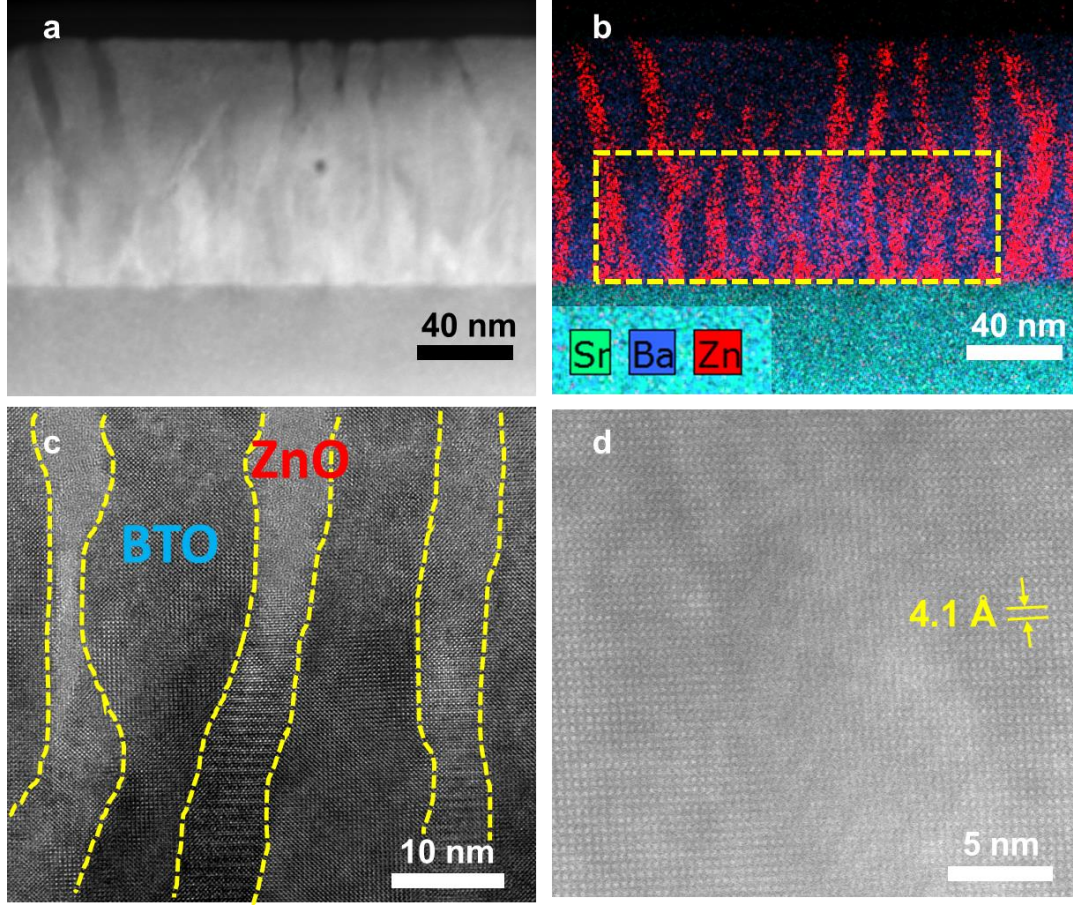


Figure 4-10. (a) STEM image of the BTO-ZnO two phase nanocomposite, (b) composition EDS mapping showing the VAN structure, (c) HRTEM image showing the phase contrast between BTO and ZnO, and (d) HRSTEM image showing the inter-planar spacing of BTO to be 4.1 Å

Regarding the growth mechanism, the driving force for the ZnO NW growth,  $\Delta\mu_{ZnO}$  is given by:

$$\Delta\mu_{ZnO} = \mu_{ZnO/Au-ZnO}^l(NW) - \mu_{ZnO}^s(NW) \quad (4.1)$$

where  $\mu_{ZnO/Au-ZnO}^l(NW)$  is the potential of supersaturated ZnO in the Au-ZnO eutectic liquid droplet and  $\mu_{ZnO}^s(NW)$  is the potential of the solid ZnO NW.  $\Delta\mu_{ZnO}$  must be greater than the critical energy for nucleation in order to maintain the nanowire growth. A smaller NW diameter results in a smaller  $\Delta\mu_{ZnO}$  due to the Gibbs-Thomson effect and will stop the further NW growth. This results in a uniform distribution of ZnO NW diameter growing inside Au-BTO matrix. Due to the high density of Au nanopillars, it is observed that only  $\approx 50\%$  of Au nanopillars undergo VLS mechanism, thus producing a mix of Au particles and pillars in the matrix. Therefore, such

epitaxy assisted VLS mechanism enables the vertical ordered growth of ZnO and helps create both Au particles and pillars embedded in a two-dielectric medium of BTO and ZnO with all the three phases growing epitaxially on STO (001) substrate.

Figure 4-11a shows the UV-Vis-NIR transmittance spectra at normal incidence for the random and ordered three-phase nanocomposite designs compared with the two-phase BTO-ZnO one, all on MgO (001) substrates. The random and ordered nanocomposite structures present a distinct plasmonic absorption peak at 597 nm and 589 nm, respectively. Because of the minor thickness variation in the samples (less than 10%), the impact of sample thickness variation on the transmittance intensity is minimal (Figure 4-12). More importantly, the plasmonic absorption peak is mainly determined by the morphology of the Au nanoparticles (NPs) and pillars and thus will not be affected by the thickness variation. The random Au-BTO-ZnO nanocomposite (~105 nm) has a range of Au NPs embedded inside it, therefore, it exhibits a wide range of plasmonic absorption as compared to the ordered Au-BTO-ZnO (~95 nm) which has a more uniform particle size distribution at normal incidence. Clearly, the absorption edge shows a blue-shift from 380 nm to 350 nm for the random and ordered nanocomposites. This blue-shift in the absorption edge can be attributed to the increase in the compressive strain of BTO out-of-plane.<sup>202</sup> The out-of-plane phase switching image for the ordered three-phase '*nanoman*' structure in Figure 4-11b further confirms the ferroelectric response. Specifically, the 5x5  $\mu\text{m}^2$  square box domain pattern was first written by scanning the piezo-responsive force microscopy (PFM) tip with +5V tip bias and followed by a 2x2  $\mu\text{m}^2$  central area scan with a -5V tip bias. The distinct

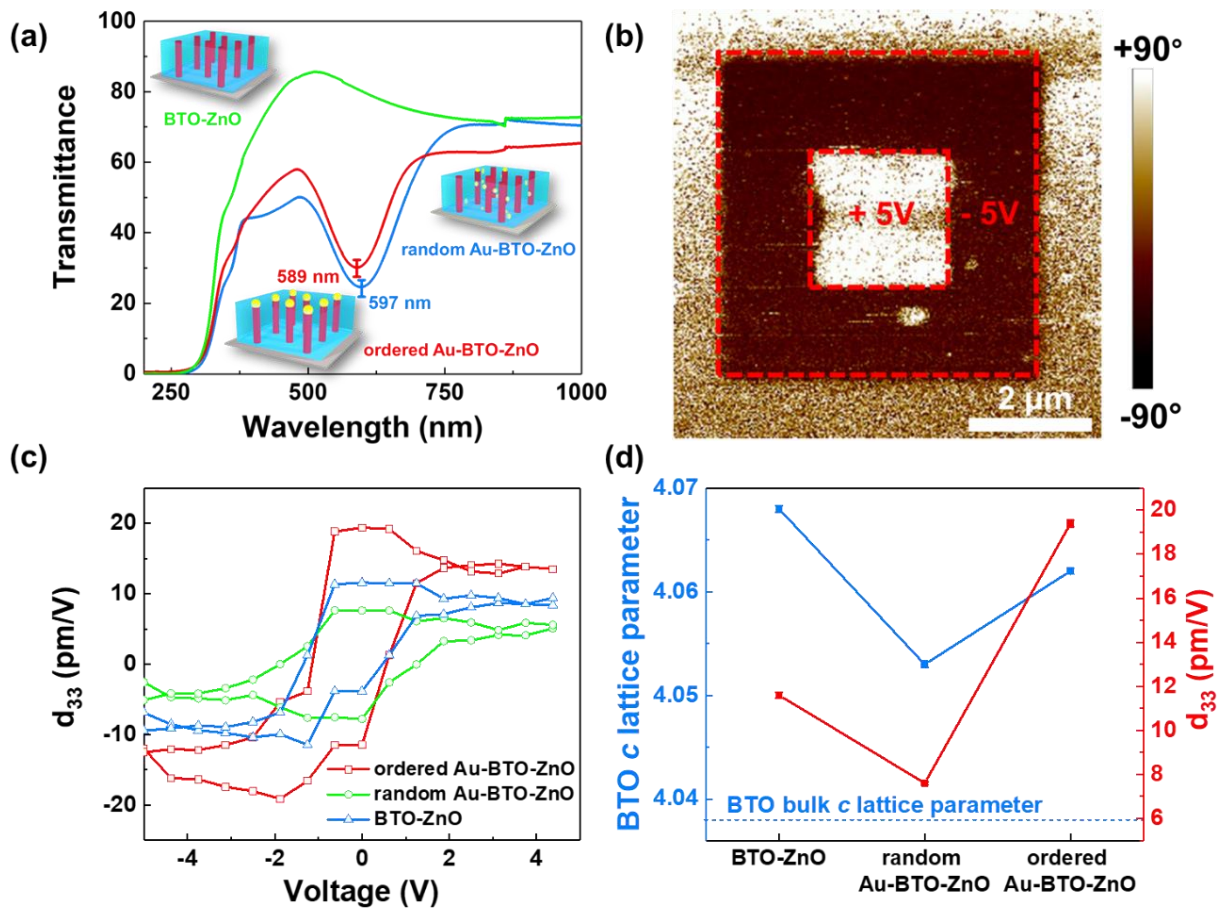


Figure 4-11. Nanocomposite multifunctionalities. (a) The optical transmission spectra for the three different nanocomposite design, (b) PFM out-of-plane phase map for the ordered three-phase nanocomposite obtained after poling with +5V (bright contrast) and -5V (dark contrast) over an area of  $5 \times 5 \mu\text{m}^2$ , (c) piezoelectric coefficient  $d_{33}$ -voltage ( $d_{33}$ -V) curves for the three different nanocomposite designs confirming their switchable and ferroelectric behavior, and (d) comparison of the BTO  $c$  lattice parameter (calculated using XRD) and its corresponding piezoelectric coefficient ( $d_{33}$ ).

image contrast in the phase image clearly shows the domain switching capability indicating the ferroelectric nature of the three-phase ‘nanoman’ structure. The piezoelectric coefficient  $d_{33}$ -voltage ( $d_{33}$ -V) curves can be obtained from the corresponding displacement-voltage ( $D$ -V) “butterfly” loops from the following equation:

$$d_{33} = \frac{D - D_i}{V - V_i} \quad (4.2)$$

where  $D_i$  and  $V_i$  are the piezoelectric deformation and applied voltage at the point of intersection, respectively.<sup>203</sup> The piezoelectric hysteresis loop ( $d_{33}$ -V) shown in Figure 4-11c confirms the

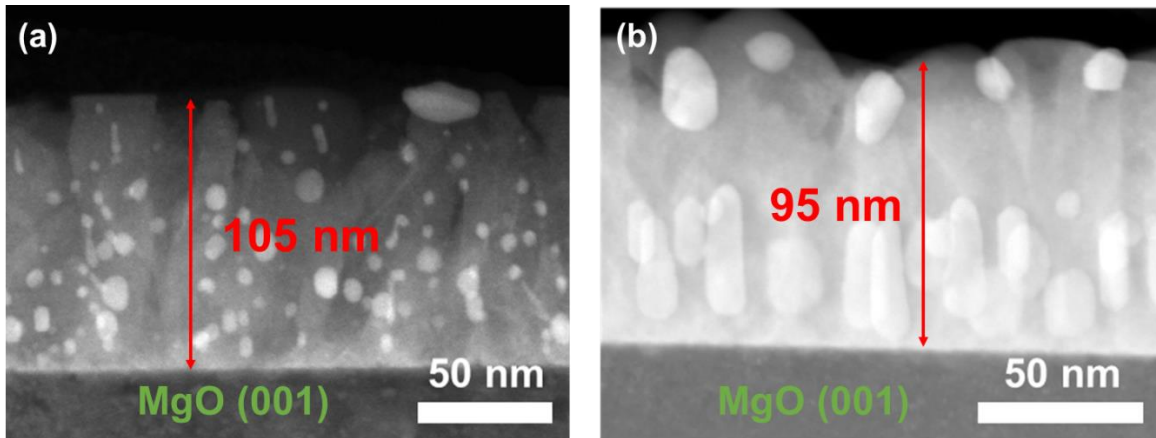


Figure 4-12. (a) random and (b) ordered three phase Au-BTO-ZnO nanocomposite deposited on MgO (001) substrate used for the optical transmittance measurements.

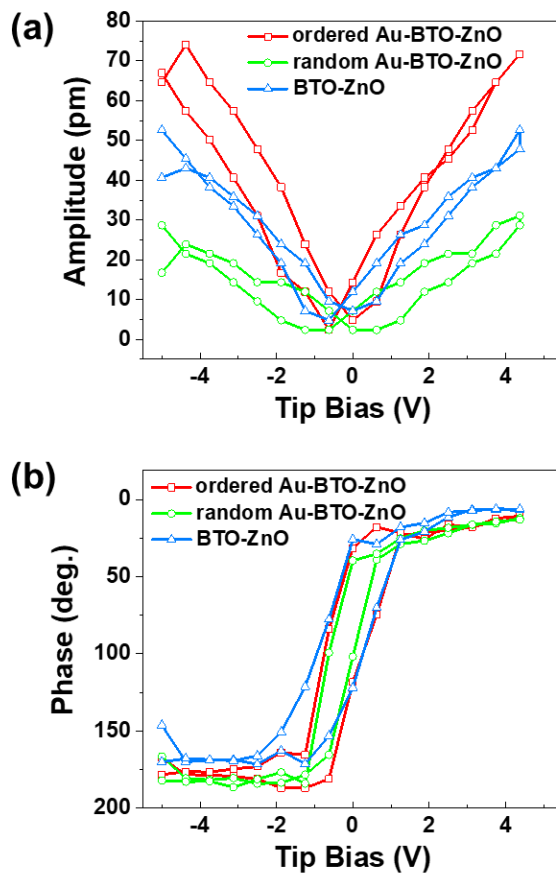


Figure 4-13. a) PFM amplitude and (b) phase hysteresis loops for all the three nanocomposite designs

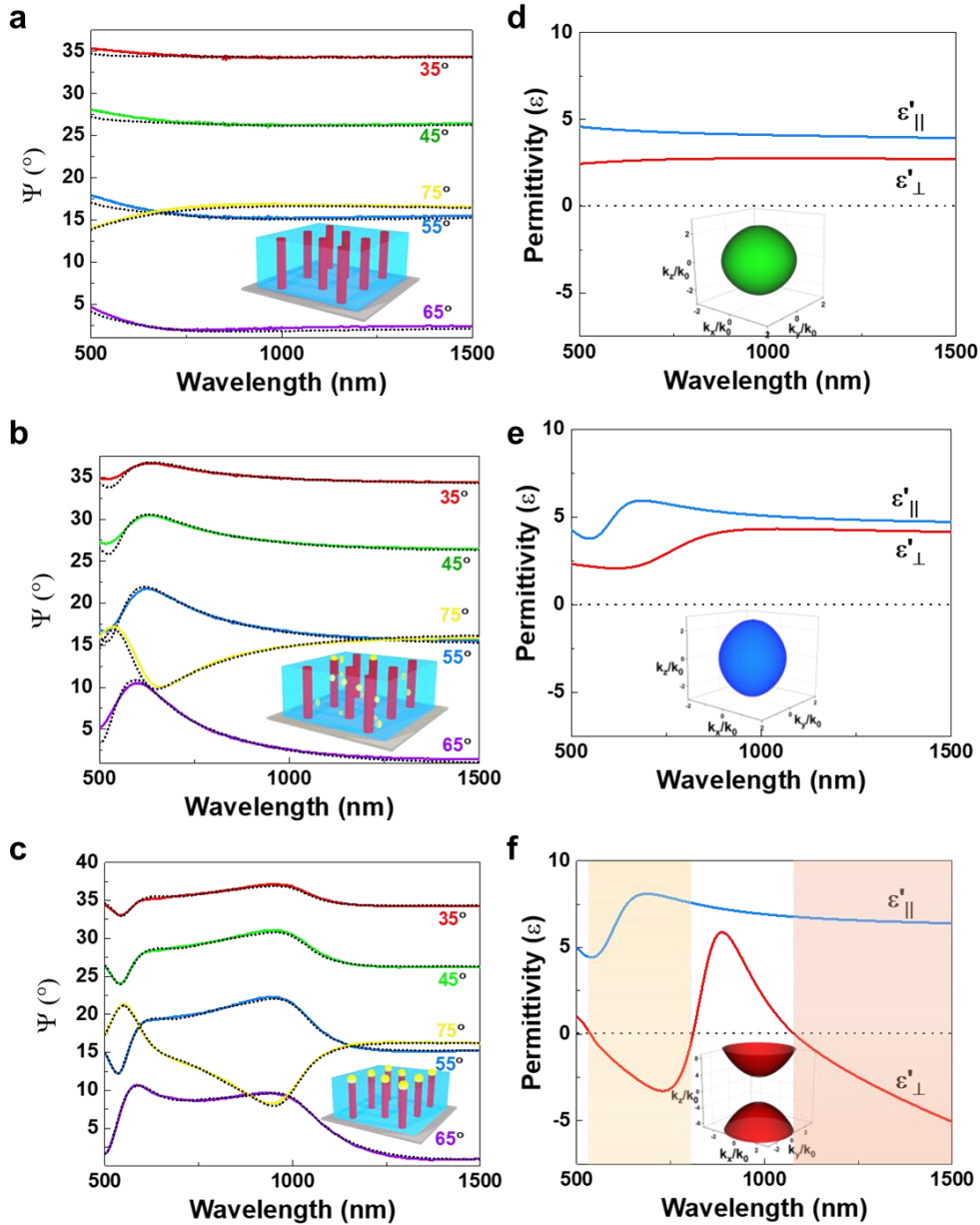


Figure 4-14. Nanocomposite optical properties. (a)-(c) Experimental (solid) and fitted (dot) components of the ellipsometric parameter  $\psi$  for the three different nanocomposite designs. The ellipsometer parameters  $\psi$  and  $\Delta$  (not shown here) were measured at different angles to improve the accuracy of the fitted model. (d)-(f) Corresponding real part of the in-plane and out-of-plane permittivity. Inset shows their corresponding iso-frequency curves (at 650 nm) where  $k_0 = \omega^2/c^2$  is the wavenumber in vacuum,  $k_x$ ,  $k_y$  and  $k_z$  are the [100], [010], and [001] components of the wave vector, respectively. (d) and (e) shows an ellipsoidal surface while (f) shows a hyperbolic response in the visible and near-infrared regime.

switchable and ferroelectric behavior for all the different designs of the nanocomposite. Figure 4-13 compares the PFM phase and amplitude for all the samples. Figure 4-11d plots the  $d_{33}$  and the out-of-plane  $c$  lattice parameter for BTO as calculated by  $\theta$ - $2\theta$  plot in XRD.  $d_{33}$  (pm/V) is calculated from the slope of the  $D$ - $V$  “butterfly” loop. The random three-phase nanocomposite shows the lowest  $d_{33}$  coefficient of 7.6 pm/V which is due to its small out-of-plane strain. However, the three-phase ‘*nanoman*’ structure shows the highest  $d_{33}$  piezoelectric coefficient of 19.4 pm/V. The tetragonal distortion of BTO is responsible for tuning the  $d_{33}$  piezoelectric coefficient since the out-of-plane  $c$  lattice parameter of BTO (calculated from XRD) follows a similar trend as their corresponding  $d_{33}$  coefficient, shown in Figure 4-11d.

The optical properties depend closely on the microstructure of the material including the morphology and ordering of the phases. The angular dependent ellipsometry data of the random and ordered three-phase nanocomposites were measured and compared with that of the two-phase BTO-ZnO sample in Figure 4-14a-c. To demonstrate the anisotropic nature of these vertically aligned nanocomposites, the permittivity in-plane ( $\epsilon_{\parallel}$ ) and out-of-plane ( $\epsilon_{\perp}$ ) was modeled by fitting the angular dependent spectroscopic ellipsometry data through the use of general oscillator models to enforce the Kramers-Kronig consistency (see Methods section) plotted in Figure 4-14d-f. The two-phase BTO-ZnO sample shows normal dispersion curves characteristic of a dielectric because of the absence of metallic phase. There is a minor difference in permittivity in-plane ( $\epsilon_{\parallel}$ ) and out-of-plane ( $\epsilon_{\perp}$ ) in Figure 4-14d. The deviation of relative permittivity of BTO from the bulk value is due to the strained state of BTO and the incorporation of secondary phases including ZnO and Au. Interestingly, the permittivity of the random and ordered three-phase nanocomposites shows a pronounced difference despite the similarity in their transmission spectrum (Figure 4-11a). The in-plane permittivity component ( $\epsilon'_{\parallel}$ ) of both the random and ordered three-phase nanocomposite design possess similar features such as an absorption peak near 600 nm because of the plasmonic absorption by Au (Figure 4-15). Their out-of-plane permittivity components ( $\epsilon'_{\perp}$ ) are drastically different (Figure 4-14e,f). The ordered ‘*nanoman*’ structure possesses negative permittivity ( $\epsilon'_{\perp}$ ) and shows the epsilon near zero (ENZ) regime in the visible and near-infrared regime. This is mainly due to the highly anisotropic nature of the ordered ‘*nanoman*’ structure with highly ordered ZnO nanopillars and Au nanopillars in the systems. The in-plane and out-of-plane real and imaginary part of the refractive index are also compared and plotted in Figure 4-17 for the three nanocomposites.

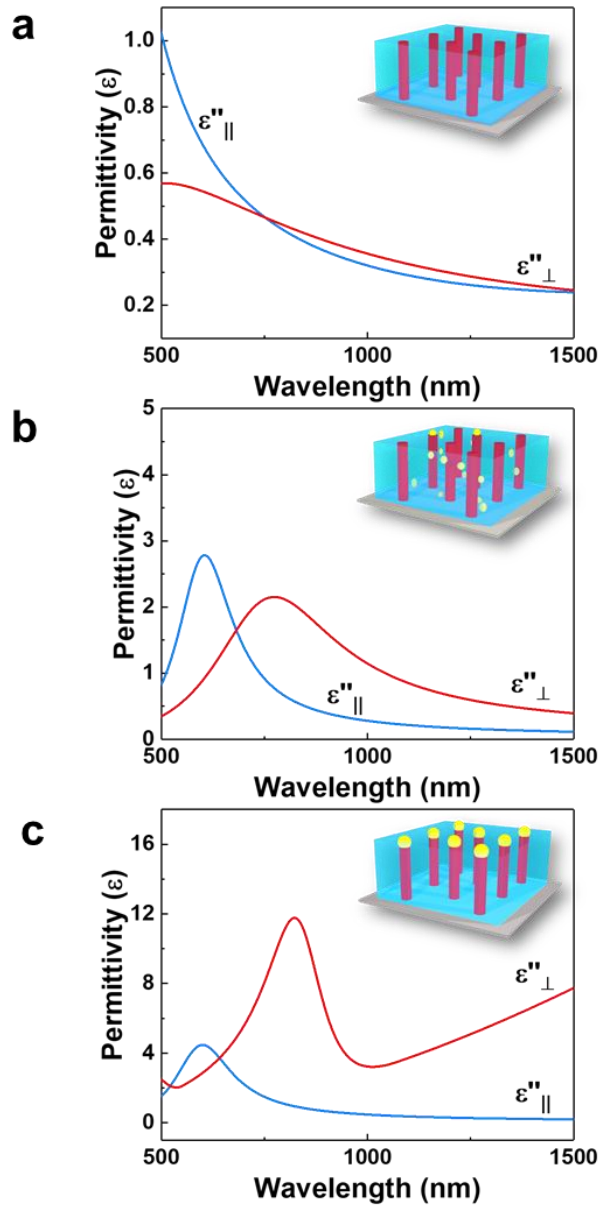


Figure 4-15. In-plane and out-of-plane imaginary permittivity for (a) two phase BTO-ZnO nanocomposite, (b) random three-phase Au-BTO-ZnO nanocomposite, and (c) ordered three-phase Au-BTO-ZnO nanocomposite

The nature of this enhanced optical anisotropy can be better visualized by plotting the optical iso-frequency surfaces. The iso-frequency curve for the electromagnetic wave ( $k$ -wavevector) propagation in a uniaxially anisotropic material is given by the dispersion relation:

$$\frac{k_x^2 + k_y^2}{\epsilon_{\perp}} + \frac{k_z^2}{\epsilon_{\parallel}} = \frac{\omega^2}{c^2} \quad (4.3)$$

where  $\omega$  and  $c$  are the frequency and the speed of light, respectively. The iso-frequency k-space surface at a wavelength of 650 nm is plotted as an insert in Figure 4-14d-f. The two phase BTO-ZnO and the three-phase random Au-BTO-ZnO exhibit a closed ellipsoidal iso-frequency surface. However, due to the extreme anisotropy in the ordered ‘*nanoman*’ structure, its iso-frequency surface becomes a hyperbola with two sheets and thus, can be classified as a class 1 hyperbolic material. Figure 4-18 shows the permittivity of the single layer Au-BTO film which was used as a buffer layer as a reference. The out-of-plane permittivity ( $\epsilon'_{\perp}$ ) in Au-BTO shows a monotonous decrease in the near infrared regime. Clearly the three-phase nanocomposite results in capping of the ZnO NWs with Au NPs making the ‘*nanoman*’ structure hyperbolic even in the visible regime. Thus, ordering in the nanocomposite dramatically changes the iso-frequency surface from a closed ellipsoid to an open hyperboloid in the visible regime. Such hyperbolic dispersion can support the propagation of evanescent waves (high- $k$  waves) and an enhanced photonic density of states and can be used for a range of exciting applications such as far-field sub-diffraction imaging (hyperlenses) and optical sensing in the visible and near infrared regime.

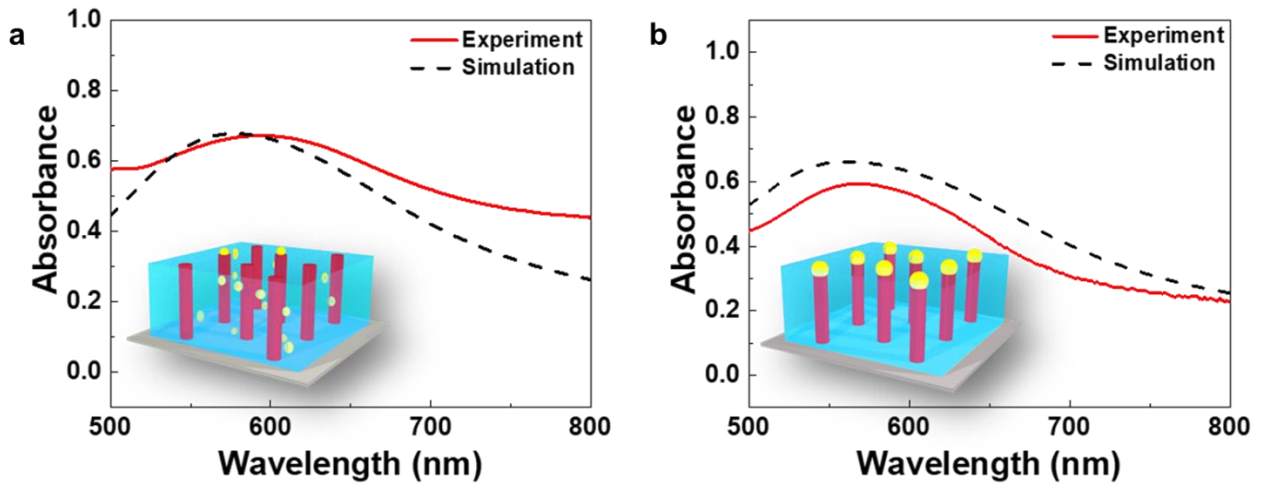


Figure 4-16. Experimental and calculated absorption for (a) random and (b) ordered three phase nanocomposite.

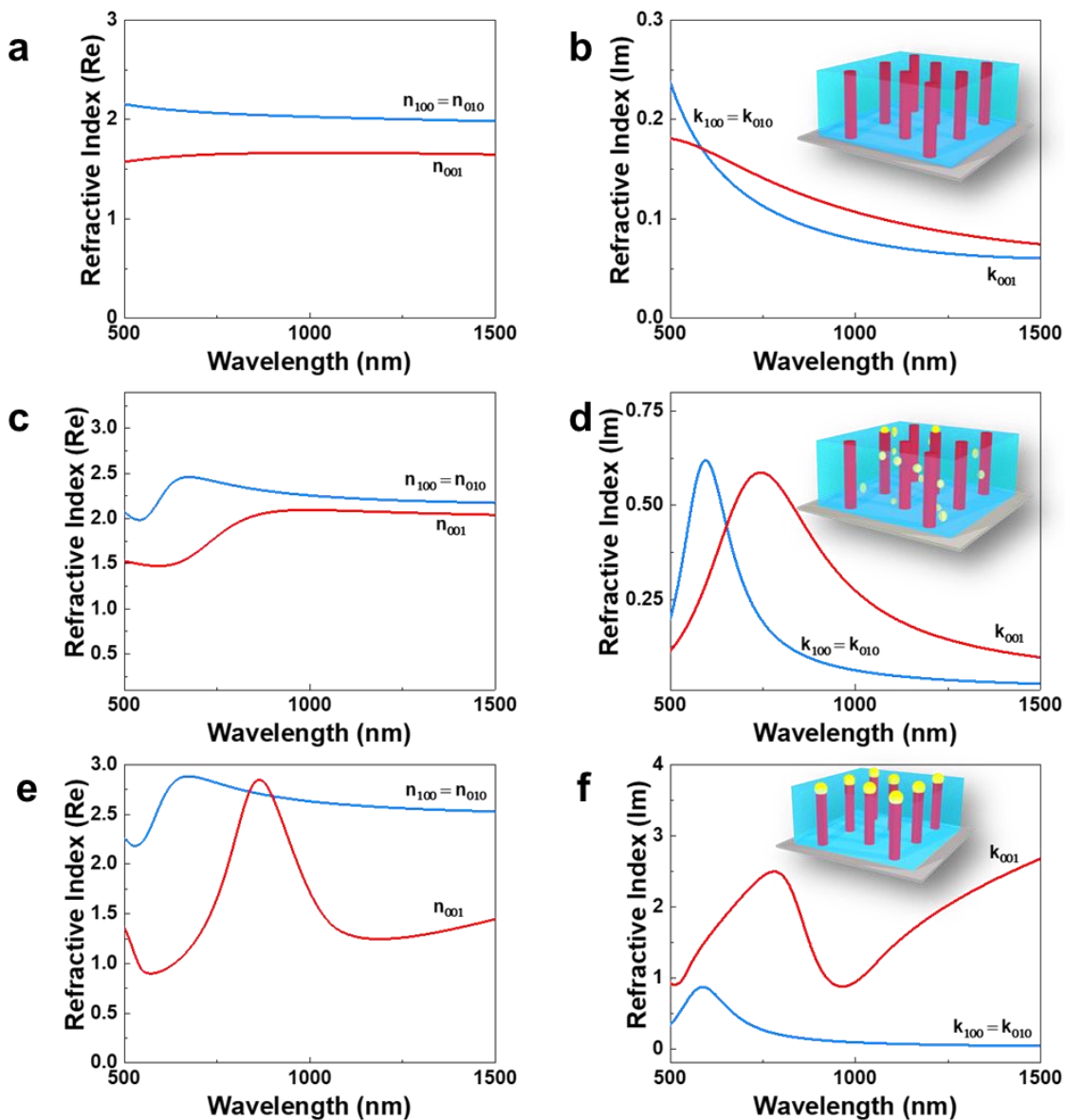


Figure 4-17. Real ( $n$ ) and imaginary ( $k$ ) part of the refractive index for (a)-(b) two-phase nanocomposite, (c)-(d) random three-phase nanocomposite, and (e)-(f) ordered three-phase nanocomposite.

The three-phase ordered nanocomposites enabled by the combined templated method and the VLS mechanisms offer great opportunities for order nanocomposite designs and provides a wide range of material selection and functionality combinations. By using the self-assembled Au-BTO film (with  $\sim 10$  nm Au pillar diameter) as the buffer layer, helps overcome the resolution limitation of conventional VLS mechanism which relies on direct Au deposition control forming equilibrium Au clusters or the optical lithography resolution by patterning the substrate with Au

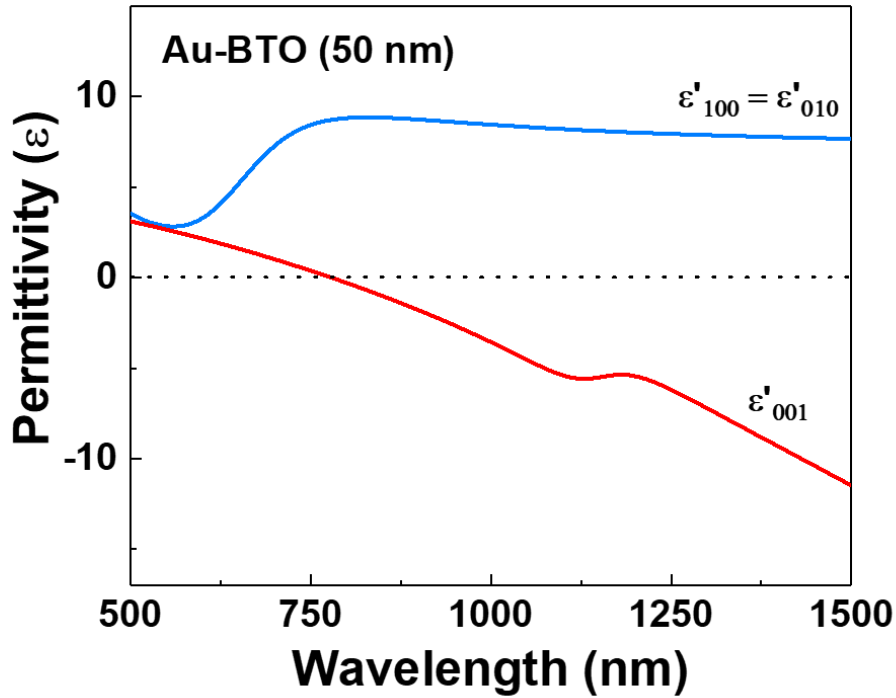


Figure 4-18. Real and imaginary part of the permittivity for Au-BTO film of 50 nm thickness deposited on SrTiO<sub>3</sub> (001) substrate.

structures for ordered ZnO NW growth.<sup>191,201,204</sup> The ordered growth provides obvious advantages over the random growth as demonstrated by the high degree of anisotropic optical properties, such as strong hyperbolic properties. Besides the ferroelectric properties, non-linear and anisotropic optical properties, these ordered three-phase materials could find applications in photocatalyst designs, gas sensors, high density magnetic storage and spintronic devices, by combining magnetic, electrical and optical properties of three phases. As a demonstration, a successful growth of another multi-phase nanocomposite of Au-BTO/LSMO-CuO system has been demonstrated via the VLS and template method as shown in Figure 4-19. It is clear that this complex system combined magnetoresistive<sup>30</sup> and hyperbolic properties enabled by the novel approach combining ordered templating method and VLS mechanisms.

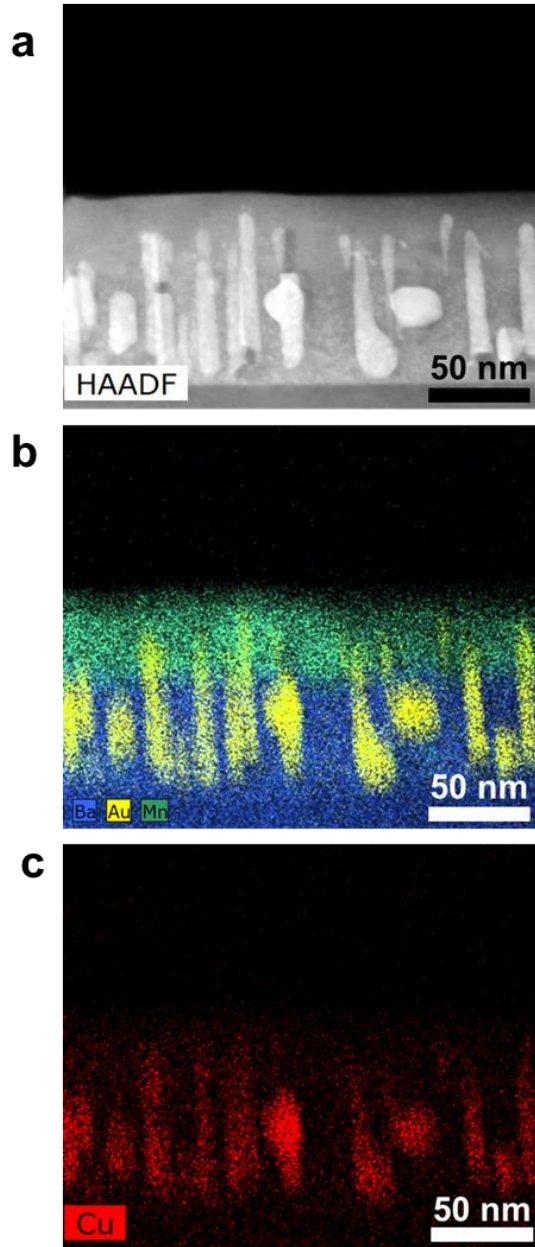


Figure 4-19. (a) STEM image and (b)-(c) EDS map showing phase distribution of the elements.

#### 4.4 Conclusion

Three different nanocomposite designs, namely, two phase BTO-ZnO VAN, random and ordered three-phase Au-BTO-ZnO nanostructures have been demonstrated. A new growth paradigm of three-phase nanocomposite with high degree of ordering has been demonstrated by the combined templating and VLS mechanism. This approach provides an alternative to the top-down fabrication approach for the growth of complex nanoscale metamaterials. Ellipsometry

measurements confirms the obvious effect of ordering on its optical properties showing highly anisotropic permittivity in visible and near infrared regime. The three-phase ordered microstructure tunes the iso-frequency curve from ellipsoidal to hyperbolic providing additional degree of freedom to control light-matter interaction at the nanoscale. Such ordered three-phase nanocomposite process enabled by the template assisted VLS growth method provides enormous opportunities in future metamaterials designs towards optical, electrical and magnetic property tuning.

#### 4.5 Experimental Section

*Composite Film Growth.* Two phase BTO-ZnO films were fabricated using a composite BTO-ZnO (1:1) target. A Au-BTO-ZnO composite target was used to deposit the random three phase nanocomposite while a Au-BTO (1:1) composite target was used to deposit a template layer for the subsequent BTO-ZnO deposition. All the thin films were deposited on single-crystal STO (001) substrates using pulsed laser deposition (PLD) (with a KrF excimer laser, Lambda Physik Compex Pro 205,  $\lambda = 248$  nm). The substrate temperature was kept at 700 °C and an intermediate oxygen pressure of 40 mTorr was maintained during the deposition. Laser frequency of 2 Hz was used, and all the films were cooled at 10 °C min<sup>-1</sup> under 200 Torr O<sub>2</sub> following the deposition.

*Structural and Optical Characterization.* The crystallinity and microstructure of the films were investigated by XRD (PANalytical Empyrean XRD), TEM and high-resolution STEM (FEI TALOS 200X operated at 200kV). TEM samples were prepared using the standard manual grinding and thinning process followed by dimpling and ion milling using precision ion polishing system (PIPS II, Gatan). Transmission measurements were obtained using UV-Vis-NIR absorption spectrophotometer (Perkin Elmer Lambda 1050) at normal incidence. The angular dependent transmission/reflectivity measurements were performed using Total Automated Measurement System (TAMS).

*Permittivity Measurements.* The effective refractive index and optical dielectric permittivity of the films was evaluated using spectroscopic ellipsometry (JA Woollam RC2). The ellipsometer parameters  $\psi$  and  $\Delta$ , related by the equation:  $r_p/r_s = \tan(\psi)e^{i\Delta}$  (where  $r_p$  and  $r_s$  are the reflection coefficient for the p-polarization and s-polarization light, respectively) were fitted using appropriate models using the CompleteEASE software. The incident angle was varied from 35° to 75° with a step size of 10°. The  $\psi$  and  $\Delta$  are measured at different angles to improve the accuracy

of the fitted model. All the samples were assumed to be anisotropic since the second phase is grown as a vertically aligned nanopillar. The in-plane permittivity of the uniaxial model was modeled using a Tauc-Lorentz oscillator and a Lorentz oscillator. The permittivity along the  $z$  direction was built using two Tauc-Lorentz oscillators. In addition, a Drude oscillator was used in case of the '*nanoman*' structure for the out-of-plane permittivity. Mean squared error (MSE) of all the fits was around 5. The fitted models are shown in Figure 4-14a-c. The thickness of the films was measured using the STEM images and input in the model. The experimental and simulated transmission spectra are shown in Figure 4-16.

## **5. MORPHOLOGICAL CONTROL OF THE SELF-ASSEMBLED THREE-PHASE Au-BaTiO<sub>3</sub>-ZnO METAMATERIAL FOR TUNABLE OPTICAL PROPERTIES**

### **5.1 Overview**

Microstructural control in metal-dielectric nanocomposites presents enormous opportunities in tailoring the physical properties including the magnetic and optical properties. Here, we demonstrate a strong tunability in the microstructure of the self-assembled ordered three-phase Au-BaTiO<sub>3</sub>-ZnO nanocomposite along with its optical properties, grown by a pulsed laser deposition method. Varying the growth temperature, deposition frequency and template thickness evolves the microstructure by tuning the Au and ZnO pillar geometry as well as the shape and size of the Au nanoparticle capping the ZnO nanowire. The three-phase nanocomposite exhibits enhanced non-linear optical properties (demonstrated by the Second Harmonic Generation (SHG)) and shows hyperbolic dispersion in the visible and near-infrared wavelength regime whose Epsilon-Near-Zero (ENZ) wavelength can be tuned by changing the deposition parameters, all attributed to their anisotropic microstructure evolution. This study provides opportunity in the microstructure and optical property tuning that can also be explored in other two-phase and three-phase nanocomposite systems.

### **5.2 Introduction**

Metal-dielectric nanocomposites have been shown to exhibit a variety of physical properties and multifunctionalities towards the development of magnetic storage devices, photocatalysts, waveguides, smart windows, batteries, and optical metamaterials.<sup>37,39,40,105,109,111,135</sup> The anisotropic nature of these nanocomposites is usually achieved by fabricating them in either multilayer or nanowire morphology using the two-phase nanocomposite approach.<sup>33,34,41,96,109,141</sup> The metallic phase embedded inside the oxide matrix as a vertical pillar or alternatively stacked in a multilayer design show very strong anisotropic physical properties, ideal for applications such as sub-diffraction imaging, negative refraction and optical magnetism.<sup>87,91,205,206</sup> However, a greater structural complexity and design flexibility is needed in order to achieve more functionality for developing next generation integrated electronic and photonic devices. This is achieved

through the three-phase nanocomposite design by combining a third phase through a careful selection of materials and functionalities.

Incorporating a third phase within the two-phase nanocomposite poses a significant challenge due to potential interdiffusion, structure instability and complex phase interaction. Recently, a successful demonstration of self-assembled ordered Au-BaTiO<sub>3</sub>-ZnO with coupled functionalities including ferroelectric and hyperbolic dispersion in the visible and near-infrared wavelength regime has opened the possibility of designing epitaxial three-phase nanocomposite using pulsed laser deposition (PLD).<sup>106</sup> The nanocomposite acts as a hyperbolic metamaterial for the wavelengths longer than the epsilon-near-zero (ENZ) wavelength due to its uniaxial anisotropy, behaving as a metal in one direction ( $\epsilon_z < 0$ ) and dielectric in the other direction ( $\epsilon_x = \epsilon_y > 0$ ). Such hyperbolic metamaterials support the propagation of high wavevectors which provide a multifunctional platform for realizing subdiffraction-limited imaging, nanolithography, and ultrasensitive optical sensing devices.<sup>85,90,205,207-209</sup> In addition, tuning the effective electromagnetic response of the hyperbolic metamaterials by changing the ENZ wavelength is technologically important for realizing nonlinear material response in different wavelength regimes.<sup>92,93</sup> ENZ wavelength can be usually tuned by controlling the deposition parameters, post-annealing, dopant concentration, and varying the periodicity and width of the metallic phase.<sup>94,95</sup> Recent studies on tunable hyperbolic metamaterials, including Au-BaTiO<sub>3</sub> (Au-BTO) and Au-ZnO have focused on tuning the ENZ wavelength by varying the geometry and deposition conditions such as oxygen partial pressure and deposition frequency.<sup>43,96</sup> In these studies, careful microstructural control modulates the free electron density in the out-of-plane direction, thereby tuning the hyperbolic dispersion characteristic of the metal-dielectric nanocomposites.

In this work, we demonstrate the tunable morphology of the Au-BaTiO<sub>3</sub>-ZnO three-phase nanocomposite, achieved by varying the deposition parameters using a two-step PLD process. Different deposition parameters, including the growth temperature, template thickness, deposition frequency and the underlying substrate, were varied which gave rise to distinct microstructure. Varying these parameters help in the understanding of the growth mechanism, driven by thermodynamics and growth kinetics of the self-assembled three-phase nanocomposite. The three-phase metamaterials show a high degree of tunability in their anisotropic optical dielectric permittivity, specifically the ENZ wavelength in the visible and near-infrared wavelength regime, which is correlated to their corresponding microstructure. Controlling the deposition parameters

offer an interesting approach to tune the microstructure and light-matter interaction at the nanoscale.

### 5.3 Results and Discussion

All the samples were deposited using a two-step templating growth method (see Experimental details). Figure 1 shows a collection of X-ray diffraction (XRD) graphs for the three-phase Au-BTO-ZnO as a function of temperature, template thickness and frequency to determine the growth orientation and strain relaxation in the films on single-crystalline SrTiO<sub>3</sub> (STO) (001) substrates. Figure 5-1a shows the temperature dependent XRD graphs. The samples were deposited at four different temperatures: 400 °C, 500 °C, 600 °C and 700 °C. BTO grows along the [001] out-of-plane direction and ZnO is textured along [0002] direction. The BTO (002) peak shows a splitting which correspond to the different strain state in the BTO. Both the BTO and ZnO peaks completely disappear at 400 °C, implying that the crystallinity of the film reduces at lower growth temperature. Figure 5-1b shows the XRD plot as a function of the bottom Au-BTO template layer. The template thickness was varied from 20 nm to 60 nm. Interestingly, the peak splitting in BTO can be attributed to the lower (Au-BTO) and upper (BTO-ZnO) layer respectively. The bottom BTO layer is constrained by the STO substrate and experiences tensile strain in the out-of-plane direction. However, the upper BTO layer, being constrained by the lower BTO layer, becomes slightly relaxed in the out-of-plane direction as compared to lower BTO layer. Therefore, the two-step deposition causes the peak splitting in the BTO peak. In addition, the 60 nm sample shows the presence of Au (111) peak, due to the presence of relatively long Au pillars.

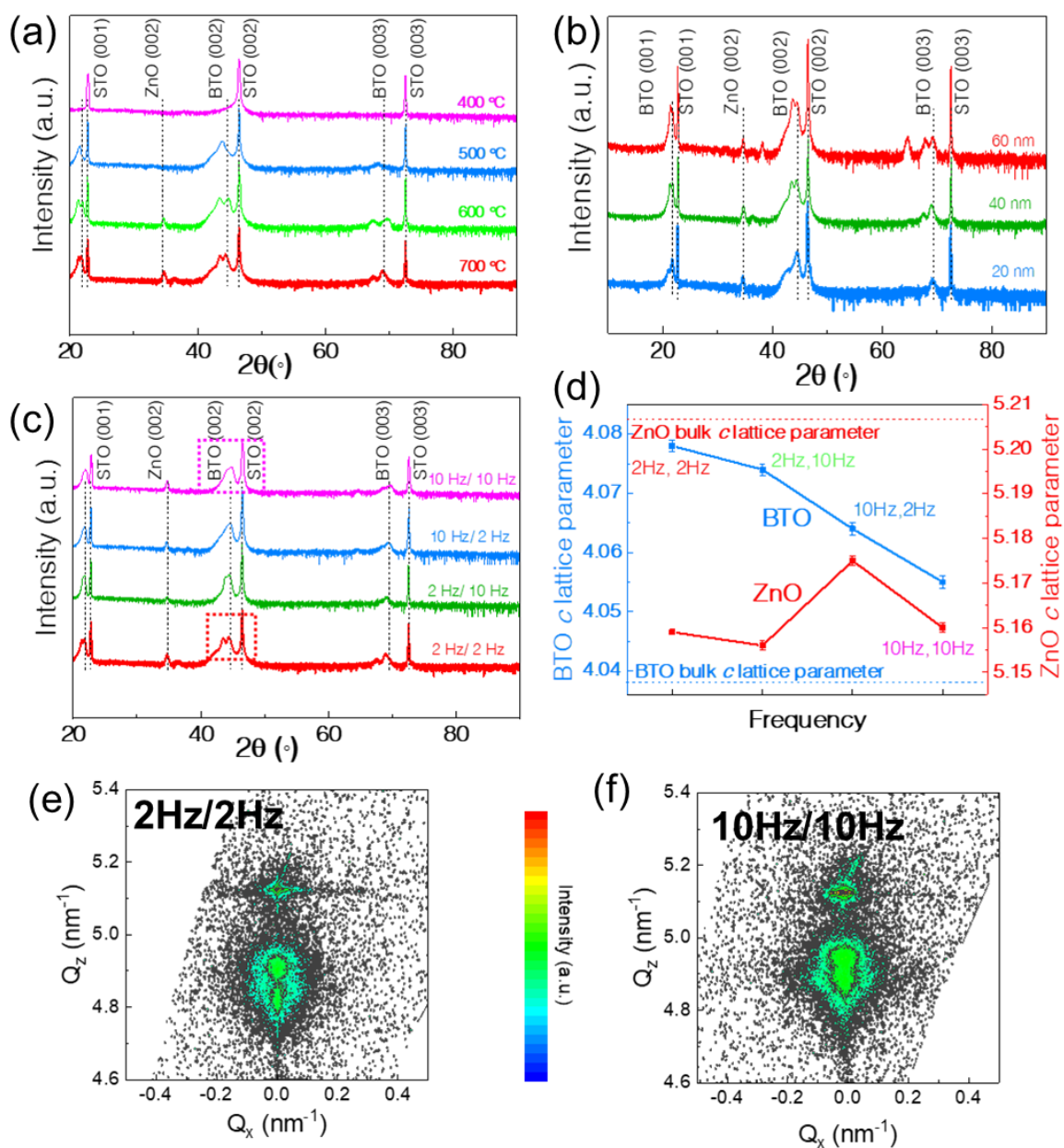


Figure 5-1. X-ray diffraction of the ordered three-phase Au-BaTiO<sub>3</sub>-ZnO nanocomposite thin films. XRD plots as a function of (a) temperature, (b) Au-BaTiO<sub>3</sub> template thickness and (c) deposition frequency. (d)  $c$  lattice parameter of BaTiO<sub>3</sub> and ZnO plotted as a function of deposition frequency. (e)-(f) Reciprocal space maps (RSM) around the SrTiO<sub>3</sub> (002) peak for the 2 Hz/2 Hz and 10 Hz/10 Hz samples, respectively.

Figure 5-1c presents the frequency dependent XRD plots. The nomenclature ‘x Hz/y Hz’ refers to the Au-BTO layer being deposited at x Hz and the BTO-ZnO layer being deposited at y Hz. Evidently, when both the layers are deposited at lower frequencies (2 Hz/2 Hz), there is a clear

peak splitting in BTO, which is not shown when depositing only the template layer of Au-BTO (Figure 5-2). Since the diffusion length is roughly given by:  $x \sim \sqrt{2Dt}$ , the adatoms can diffuse to a longer length to find the equilibrium position, thus forming a complete coherent interface with STO, which will be discussed later. As a result, the bottom BTO adatoms experience more strain due to the longer diffusion time. In contrast, the peak splitting becomes less obvious as the two layers are deposited at higher frequencies due to the formation of semi-coherent interface as discussed later. The  $c$  lattice parameter of BTO and ZnO is presented in Figure 5-1d with the bulk  $c$  lattice parameter marked with a dotted line. Clearly, the BTO phase experiences a tensile strain while the ZnO phase experiences a compressive strain in the out-of-plane direction. The BTO strain gets relaxed as the frequency of deposition is increased due to the formation of dislocations at the interface with the underlying substrate. The epitaxial quality of the samples deposited at extreme frequencies was further compared using reciprocal space mapping (RSM). Figure 5-1e and Figure 5-1f shows the RSMs near substrate STO (002) peak for the 2Hz/2Hz sample and 10Hz/10Hz sample, respectively. The distinct diffraction spots of BTO confirm the high epitaxial of the thin films on STO (001) substrate. The BTO (002) peak for the 2Hz/2Hz sample shows a peak splitting and is slightly shifted upward along the Qz direction as compared to the 10Hz/10Hz sample. The  $c$  lattice parameter of the BTO layer deposited on top of STO deposited at 2Hz and 10Hz is 4.14Å and 4.07Å, respectively as calculated from the RSM. It confirms that the template layer is more strained in-plane at lower frequencies compared to higher frequencies. The  $c$  lattice parameter of the upper BTO layer deposited at 2Hz and 10Hz is 4.07Å and 4.04Å, respectively. This is consistent with the observations in Figure 1c and correspond to the different strain states of the two BTO layers present in the film. In addition, no obvious degradation of the film quality was observed on changing the frequency.

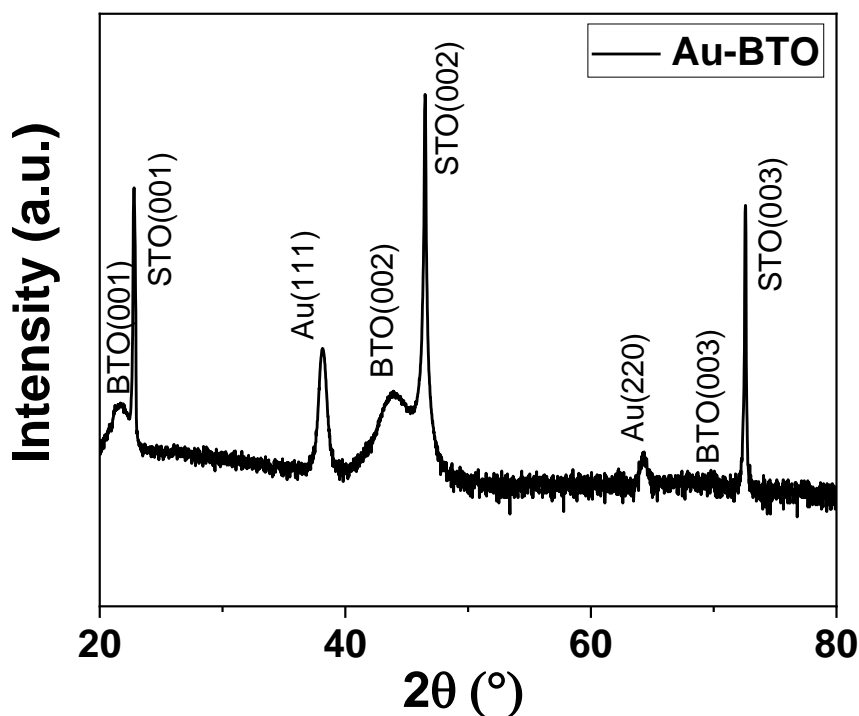


Figure 5-2. X-ray Diffraction graph of Au-BTO thin film showing no peak splitting in BTO

Figure 5-3a-c shows a collection of EDS elemental maps for the sample deposited at 700 °C, 600 °C, and 500 °C, respectively. The temperature dependent microstructure evolution requires the knowledge of the Au-ZnO phase diagram. The bulk Au-Zn phase diagram is well known<sup>210</sup> and forms a eutectic solution at 683 °C at 33.5 at.% Zn giving  $L \rightarrow Au + AuZn$ . AuZn is a congruently melting intermetallic at 753 °C and 50 at. % Zn. Assuming that the miscibility of ZnO in Au-Zn intermetallic is almost negligible just like pure Au and Zn are immiscible in ZnO, there must exist a pseudo-binary eutectic system between Au and ZnO. The eutectic point should exist on the Au rich side of the phase diagram since Au and ZnO, forming the eutectic liquid, are almost immiscible with ZnO having a higher melting point (1975 °C) than Au (1064 °C).<sup>189</sup> Similar pseudo-binary systems such as Au-GaAs, Ge-GaSb, Al-Mg<sub>2</sub>Si, etc. have been reported earlier.<sup>194,211,212</sup> Figure 5-3b and Figure 5-3c show the presence of Au NPs at the tip of ZnO NWs which is indicative of the VLS mechanism. Above 600 °C, Au and ZnO form a low melting point eutectic solution which gets supersaturated from the incoming flux of ZnO adatoms to give rise to the uniaxial growth of ZnO nanowires. Clearly, the growth temperatures at 600 °C and 700 °C

shows the presence of VLS mechanism, enabling the formation of the eutectic solution while the VLS mechanism is absent at 500 °C. Therefore, the growth temperature must be at least above 600 °C for the VLS mechanism to take place.

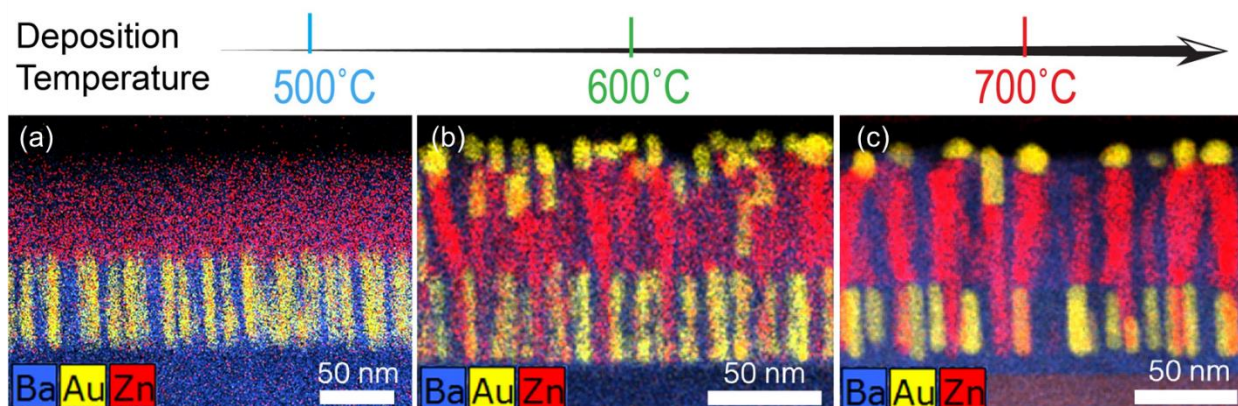


Figure 5-3. Cross-sectional EDS elemental maps as function of substrate, varied from (a) LAO, (b) STO, and (c) MgO

The effect of growth kinetics on the overall morphology was studied by varying the deposition frequency. Figure 5-4a-d shows a set of EDS maps as a function of frequency, i.e., 2 Hz/2 Hz, 2 Hz/10 Hz, 10 Hz/2 Hz and, 10 Hz/10 Hz, respectively. Clearly, all the samples show the presence of Au NP capping the ZnO NW. The EDS elemental map shows the clear and sharp interfaces between Au, BTO, and ZnO suggesting that all the three phases grow separately without any obvious inter-diffusion. The interface between BTO and STO remains largely coherent as seen from the HR-STEM images and their corresponding Fourier-filtered images (Figure 5-5) at 2Hz and 10Hz. However, formation of dislocation can be seen in the sample deposited at 10Hz, resulting in strain relaxation, as observed from the XRD plots earlier. In addition, the deposition kinetics play a key role in determining the Au pillar diameter, ZnO pillar diameter and the shape of Au NP. The Au pillar diameter varies from ~7.5 nm at 2Hz to ~10 nm at 10Hz. The diameter was averaged over several Au pillars at three different locations as shown in Figure 5-6. In addition, the aspect ratio (length/height) of the Au NP capping the ZnO NW decreases from ~1.2 at low frequencies (2Hz/2Hz sample) to ~0.8 at high frequencies (10Hz/10Hz sample). This is due to the different growth kinetics at low and high frequency. At 2Hz, the Au adatoms have a longer diffusion length to nucleate and grow, giving rise to narrower Au pillars with less inter-pillar

spacing as compared to the Au adatoms grown at 10Hz with wider diameter and more inter-pillar spacing. The diameter of both ZnO and Au pillars is around  $\sim 7.5$  nm and show a good match when both are deposited at 2Hz. The ZnO pillar diameter decreases from  $\sim 7.6$  nm at 2Hz to  $\sim 5.7$  nm at 10Hz. The large mismatch of Au and ZnO pillar diameter at 10Hz makes the Au NP aspect ratio  $< 1$ . Therefore, the relative matching of the ZnO and Au pillar diameter makes it easier for Au-ZnO system to undergo VLS mechanism at 2Hz, which also determines the aspect ratio of the Au NP capping the ZnO nanowire.

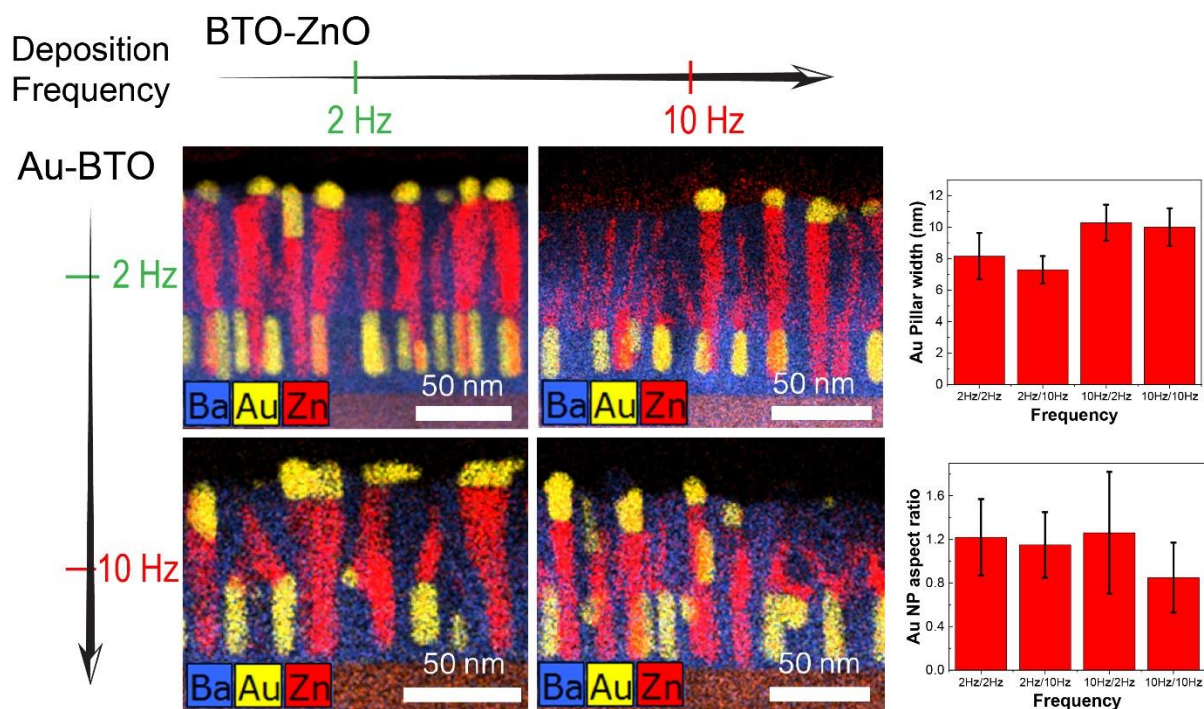


Figure 5-4. (a)-(d) Cross-sectional EDS elemental maps as function of deposition frequency of Au-BaTiO<sub>3</sub> template layer and BaTiO<sub>3</sub>-ZnO layer. (e) Plot of the Au pillar width and (f) Au nanoparticle aspect ratio as a function of frequency.

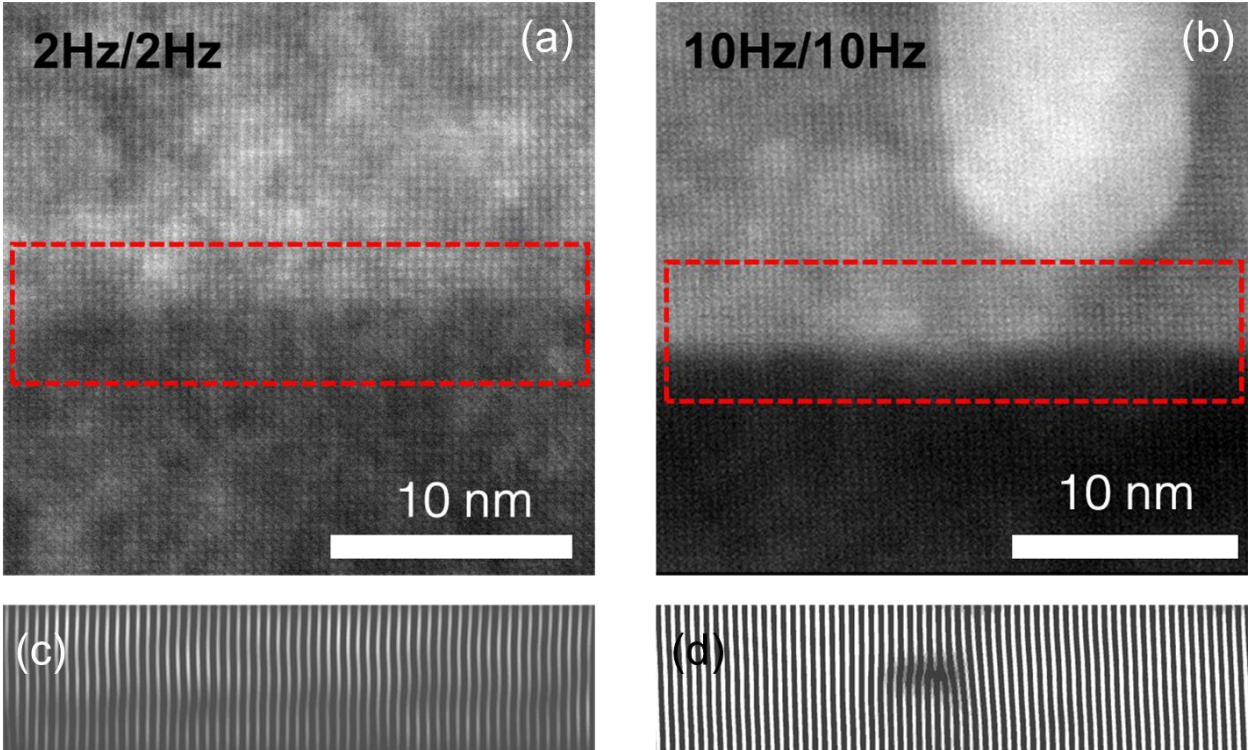


Figure 5-5. HR-STEM image of the BaTiO<sub>3</sub>-SrTiO<sub>3</sub> interface of three-phase Au-BaTiO<sub>3</sub>-ZnO sample deposited at (a) 2Hz/2Hz and (b) 10Hz/10Hz and their corresponding Fourier transform images in (c) and (d) respectively.

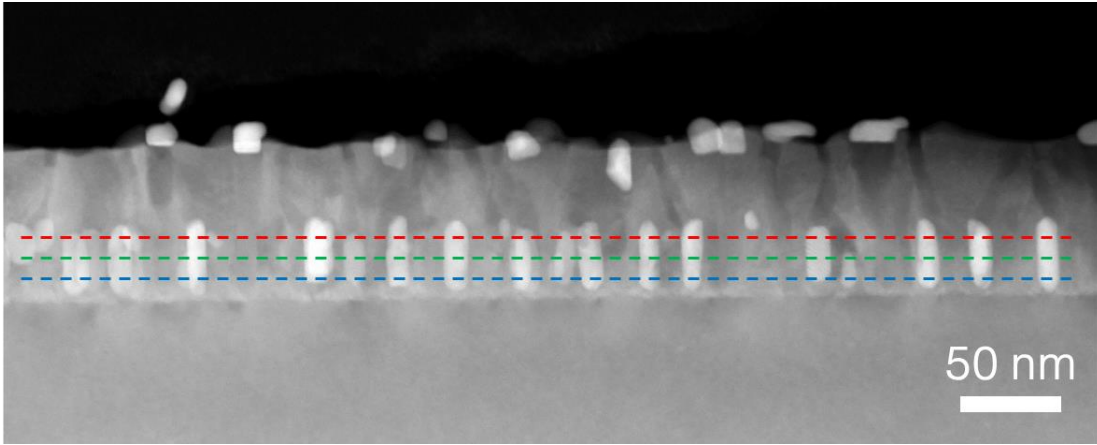


Figure 5-6. STEM image showing the lines used for calculating the Au pillar diameter.

The effect of Au-BTO template geometry on the overall morphology was studied by varying the template thickness. Figure 5-7a-c presents the STEM-EDS images for the 20 nm, 40 nm, and 60 nm Au-BTO template thickness, showing the elemental distribution of Au, BTO and

ZnO phases. All the samples show the presence of Au NP capping the ZnO NW, evident of the VLS mechanism. However, as the template thickness is increased from 20 nm to 60 nm, lesser number of Au pillars undergo the VLS mechanism. Figure 5-7d-f shows the EDS mapping of the ZnO phase for the three different template thickness. Clearly, the number of ZnO pillars penetrating inside the Au-BTO template layer decreases as the template layer increase. This is due to the relative concentration of Au and ZnO during the deposition. At 20 nm template thickness, there is sufficient concentration of ZnO present to undergo the VLS mechanism with Au pillars. However, as the template thickness is increased, some of the ZnO pillars, although being deposited on top of Au pillars, do not have enough concentration at the Au-ZnO interface to undergo the VLS mechanism with Au. Therefore, tuning the template thickness plays an important role in determining the final morphology of the three-phase nanocomposite.

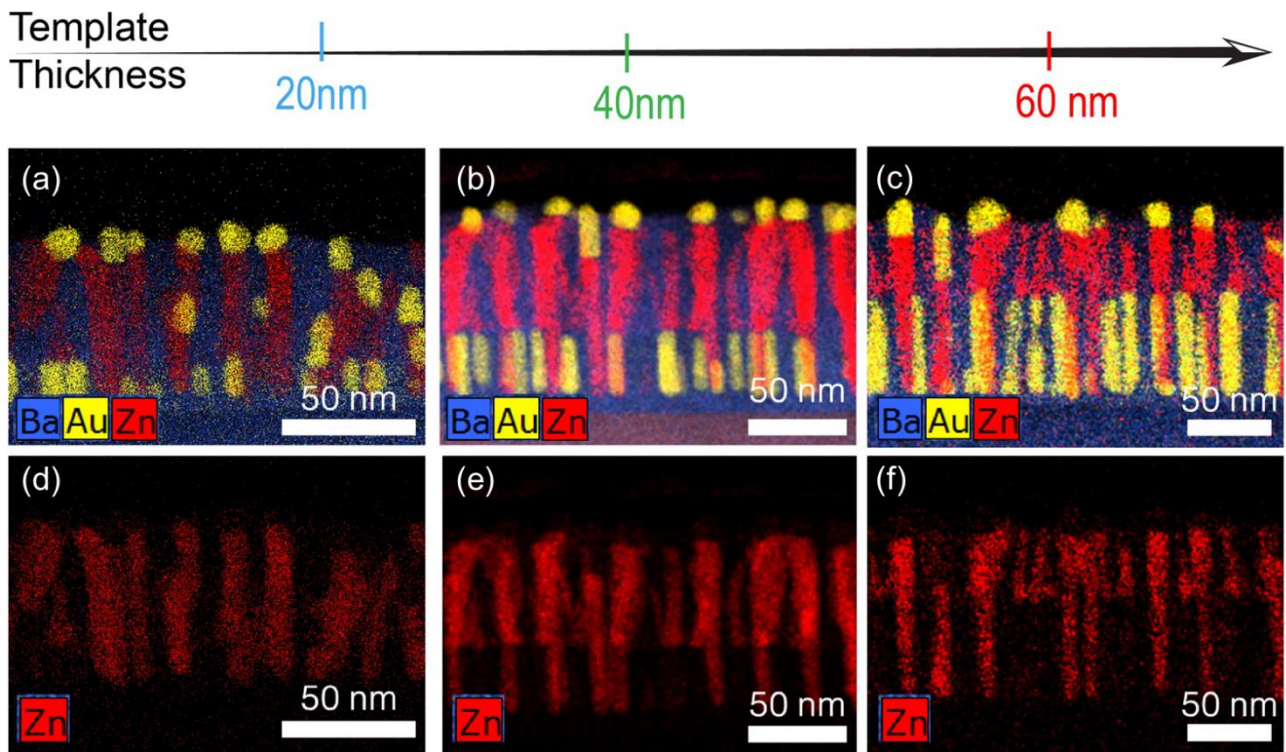


Figure 5-7. Cross-sectional EDS elemental maps as function of Au-BaTiO<sub>3</sub> template thickness, varied from (a) 20 nm, (b) 40 nm, and (c) 60 nm and their corresponding Zn EDS map in (d)-(f).

The effect of strain on the morphology of the three-phase nanocomposite was studied by depositing the films at three different substrates: LAO (001), STO (001), and MgO (001) having a

lattice parameter of 3.79Å, 3.91Å, and 4.21Å respectively. All the three substrates have slightly different lattice parameter which results in different strain state. All the samples were deposited at 700°C at 40mTorr oxygen partial pressure with 10Hz/2Hz frequency. Figure 5-8 shows the X-ray diffraction for all the samples. Clearly, BTO shows a highly crystalline and textured (00l) growth. BTO phase experiences a tensile strain of ~0.50% on STO while it sustains a compressive strain of ~0.50% on both LAO and MgO substrates. Figure 5-9 compares the microstructure of the three different samples. Overall, the morphology undergoes a change by changing the substrate. The Au pillar diameter varies from ~13 nm (MgO substrate) to ~9 nm (STO substrate) to ~7.5 nm (LAO substrate). The ZnO pillar diameter at 2Hz is ~8 nm which matches reasonably well with the Au pillar diameter on STO and LAO substrate. However, there is a large mismatch between the Au and ZnO pillar diameter on MgO, hence, very few pillars undergo VLS mechanism resulting in the formation of Au NP on the film surface. In contrast, relatively more Au pillars undergo VLS mechanism on STO and LAO substrate due to the similar pillar diameter of Au and ZnO.

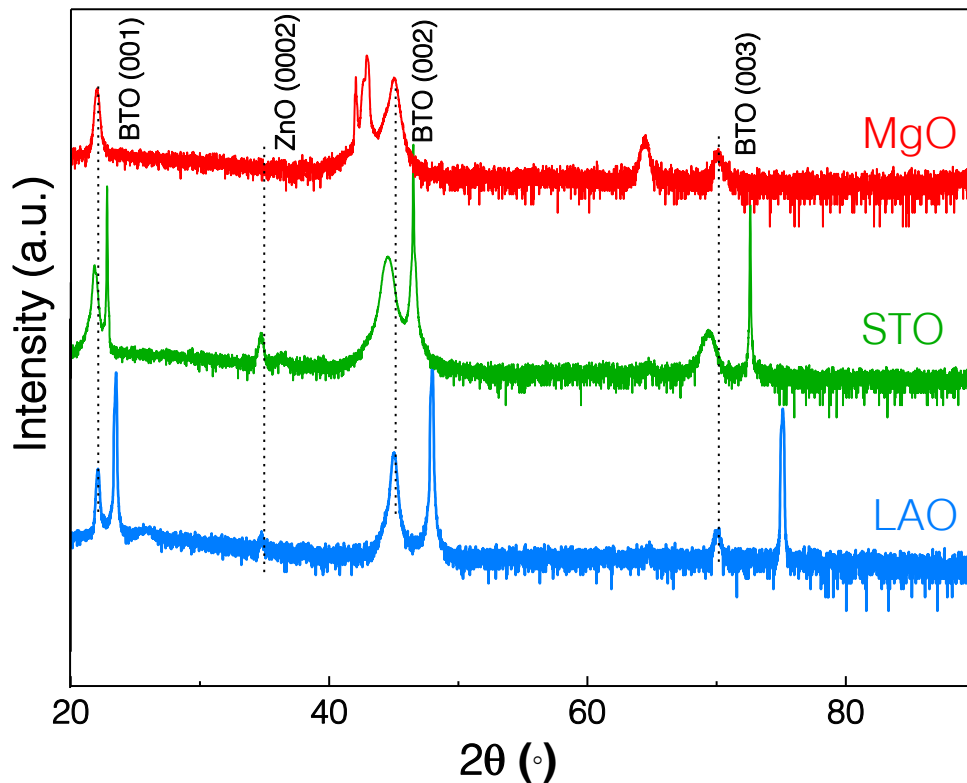


Figure 5-8. X-ray diffraction of the three-phase Au-BaTiO<sub>3</sub>-ZnO deposited on MgO, STO and LAO

The nonlinear response of the ordered three phase sample was measured using the second harmonic generation (SHG). Figure 5-10a and Figure 5-10b presents a polar plot showing the measured SHG intensity as a function of incident light polarization angle with output polarization fixed at  $0^\circ$  (P-out) and  $90^\circ$  (S-out), respectively. An angle resolution of  $2^\circ$  ( $1^\circ$  for the half wave-plate) was used to scan the input polarization. The SHG intensity of BTO is also plotted for comparison. Clearly, the second order non-linearity of the ordered three phase Au-BTO-ZnO gets enhanced by up to one order of magnitude for both  $0^\circ$  and  $90^\circ$  output polarization as compared to the pure BTO film. This enhancement can be attributed to two factors: (i) increased strain state of BTO, and (ii) the interface between Au and BTO. The presence of Au and ZnO, growing vertically in the BTO matrix, results in a higher strained state of BTO up to a greater thickness. In addition, the SHG signal also arises due to the surface nonlinearity at the metal-dielectric interface (Au-BTO interface in this case) as has been observed before.<sup>213,214</sup>

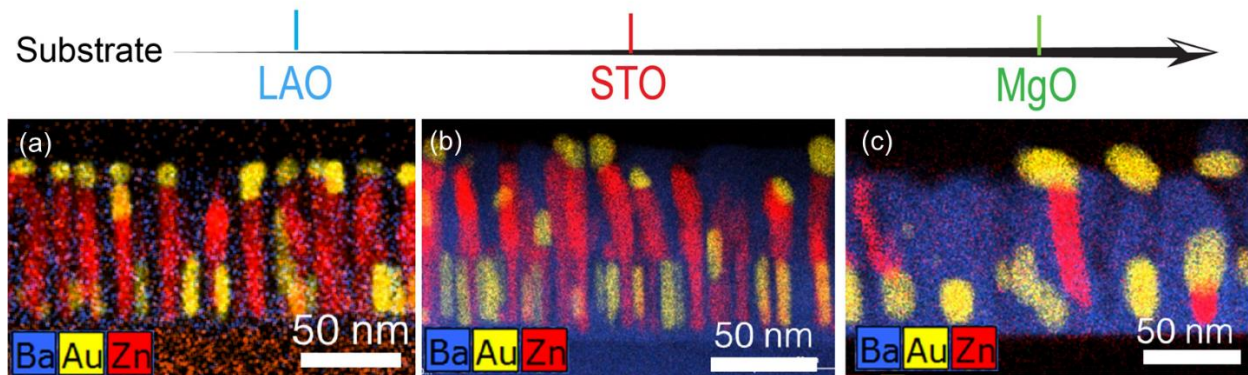


Figure 5-9. Cross-sectional EDS elemental maps of the three-phase Au-BaTiO<sub>3</sub>-ZnO nanocomposite thin films, deposited at (a) 500°C, (b) 600°C, and (c) 700°C.

The optical properties depend closely on the deposition parameters and the corresponding microstructure. Figure 5-10c and Figure 5-10d shows the optical dielectric permittivity as function of frequency and template thickness, respectively, measured using an angular dependent spectroscopic ellipsometer. Due to the anisotropic nature of the nanocomposites, the permittivity was modeled using an in-plane and out-of-plane permittivity component using the general oscillator models to make them Kramers-Kronig consistent. Figure 5-10c compares the dielectric permittivity for the 2Hz/2Hz and 10Hz/10Hz sample. The in-plane permittivity follows similar trends and remains positive throughout the wavelength regime. However, the out-of-plane

permittivity increases in the visible wavelength regime on increasing the frequency from 2Hz to 10Hz. In addition, the epsilon-near zero (ENZ) wavelength shows a red-shift from 895 nm to 927 nm as the frequency is increased from 2Hz to 10Hz. This can be attributed to the lower free electron density in the 10Hz sample. Figure 5-10d compares the dielectric permittivity for the 20 nm and 60 nm template thickness. Again, the in-plane permittivity for both the samples show similar trends and remains positive throughout the wavelength regime. Interestingly, the out-of-plane permittivity shows a clear red-shift in the ENZ wavelength from 678 nm to 995 nm as the template thickness is increased, implying that the sample with the thinner template is more metallic. Owing to the higher free electron density, the 20 nm template thickness sample shows a red-shift in the ENZ wavelength. The 20 nm sample also exhibits negative out-of-plane permittivity in the visible wavelength regime due to presence of a greater amount of Au NP as compared to the 60 nm sample. Therefore, by tuning the template geometry as well as the deposition kinetics, the optical response of the three-phase nanocomposite can be successfully tuned.

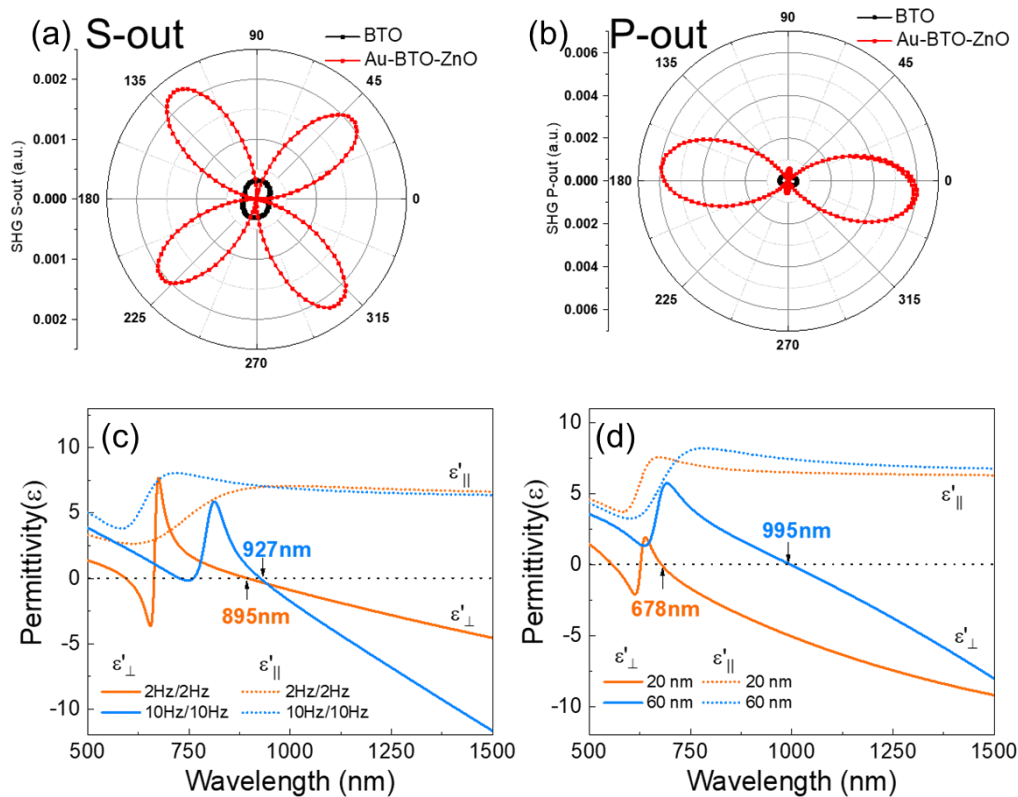


Figure 5-10. Polar plot of the measured SHG intensity as a function of incident polarization angle with output polarization fixed at (a)  $90^{\circ}$  (S-out) and (b)  $0^{\circ}$  (P-out). Real part of the in-plane ( $\epsilon'_{\parallel}$ ) and out-of-plane ( $\epsilon'_{\perp}$ ) permittivity as a function of (c) frequency and (d) Au-BaTiO<sub>3</sub> template thickness.

Tuning the deposition parameters such as growth temperature, deposition frequency and template thickness provides extra degree of freedom to tune the microstructure and its corresponding optical properties. Such study helps understand the diffusion kinetics during the growth process. In addition, microstructure evolution tunes the ENZ wavelength which is important for achieving nonlinear material response in different wavelength regimes. This study provides an opportunity to tune the microstructure and physical properties of other two-phase and three-phase metal-dielectric nanocomposite systems.

#### 5.4 Conclusion

In summary, the morphology tuning of the three-phase nanocomposite by varying the deposition frequency and template thickness has presented as an effective approach in achieving tunable microstructure and properties. The growth temperature above 600°C shows the presence of Au NP capping the ZnO NW, indicative of the VLS mechanism. Increasing the template thickness decreases the number of ZnO pillars undergoing the VLS mechanism. Varying the frequency of the Au-BTO template and BTO-ZnO layer results in microstructure evolution, which is mainly driven by the relative matching of the Au and ZnO pillar diameter. Such microstructure evolution in these hyperbolic metamaterials tunes the free electron density in the out-of-plane direction, thereby tuning the ENZ wavelength in the Z-direction. This study provides the opportunities in the design and tuning of the three-phase nanocomposite microstructure and achieving physical property tunability.

#### 5.5 Experimental Details

*Thin Film Growth:* The self-assembled three-phase Au-BTO-ZnO nanocomposite thin films was deposited using a two-step growth using a Au-BTO buffer layer as a template as shown previously.<sup>106</sup> The thin films were deposited on STO (001), MgO (001), LAO (001) single-crystal substrates using pulsed laser deposition (PLD) (with a KrF excimer laser, Lambda Physik Compex Pro 205,  $\lambda = 248$  nm). All the films were deposited at 40 mTorr oxygen pressure with varying deposition temperature and frequency.

*Structural and Optical Characterization:* The microstructure of the films were characterized using XRD (PANalytical Empyrean XRD), and high-resolution STEM (FEI TALOS 200X operated at

200 kV). Cross-section TEM samples were prepared using the manual grinding, polishing and thinning process followed by dimpling and ion milling using precision ion polishing system (PIPS II, Gatan). The SHG measurements were carried out using a home-built system with an amplified Ti:sapphire laser. The dielectric permittivity of the films was measured using spectroscopic ellipsometer (JA Woollam RC2).

## **6. STABILITY STUDY OF SELF-ASSEMBLED ORDERED THREE PHASE Au-BaTiO<sub>3</sub>-ZnO BY IN-SITU HEATING IN TRANSMISSION ELECTRON MICROSCOPY**

### **6.1 Overview**

Thermal stability of metal-dielectric nanocomposites is important for designing practical devices for high temperature applications. Here, we study the thermal stability of the self-assembled ordered three phase Au-BaTiO<sub>3</sub>-ZnO nanocomposite by ex situ annealing in air and vacuum followed by in situ heating in TEM in vacuum. The study reveals that changing the annealing environment greatly changes the microstructure and the associated dominant mechanism. Au nanoparticles show coarsening upon air annealing while Au and Zn either form a solid solution, with Zn atomic percentage less than 10% or undergo reverse Vapor-Liquid-Solid (VLS) mechanism upon vacuum annealing. The distinct microstructure obtained also show different permittivity response in the visible and near-infrared regime, while retaining their hyperbolic dispersion characteristic enabled by their highly anisotropic structures. Such in situ heating in TEM provides a useful technique for the exploration of microstructure evolution and growth mechanisms at nanoscale and thermal stability of the multi-phase nanocomposites for refractory applications.

### **6.2 Introduction**

Metamaterials offer extensive opportunities for engineering the light-matter interaction, ideal for achieving exotic optical properties including optical magnetism,<sup>87</sup> negative refraction,<sup>88</sup> and hyperbolic dispersion<sup>89</sup> which have potential applications in the field of optical computing, cloaking and sub-diffraction imaging. One such class of metamaterials is hyperbolic metamaterial (HMM), which have a highly anisotropic structure, composed of metal and dielectric units, and support the propagation of high wavevectors.<sup>90,91</sup> Recently, several two-phase metal-dielectric self-assembled nanocomposites, as vertically aligned or in a layer-by-layer stacking have been shown to exhibit hyperbolic dispersion.<sup>7,41,42</sup> Since the two-phase nanocomposite structure has limited morphological control, a greater design flexibility can be achieved by incorporating a third phase through the three-phase nanocomposite design. The three phase nanocomposites offer great

opportunities for a wide range of material selection and functionality coupling for developing next generation integrated electronic and photonic devices.<sup>106,215</sup> A careful selection of materials and functionalities can further help in the spatial ordering of the three phases which is essential for metamaterial properties.

Recently, a self-assembled Au-BaTiO<sub>3</sub>-ZnO ordered three-phase nanocomposite has been demonstrated as a hyperbolic metamaterial in the visible and near-infrared wavelength regime.<sup>106</sup> However, it is important to study the thermal stability of such structures for refractory applications. Largely, the thermal stability study of metal-dielectric hyperbolic metamaterials is lacking and exploring thermally stable HMM systems is critical. With increasing temperatures, different physical processes become active such as enhanced diffusion, increased solid solubility, phase change and crystallinity change. Interestingly, the heating environment, such as oxidizing or reducing environment, also plays a key role in determining the growth thermodynamics and tune the physical properties.<sup>216-219</sup> For example, enhanced transmission and widening of the optical band gap has been observed in Cu<sub>2</sub>O thin films after air annealing due to the reduction of the impurity scattering.<sup>220</sup> However, most of the studies have focused the annealing effects on single phase thin films.<sup>221-226</sup> Therefore, exploring the complex phase interactions, phase change, growth mechanisms and thermal stability, upon changing the annealing environment, is extremely interesting in the self-assembled three phase nanocomposite structure.

In this work, thermal stability studies were performed on the ordered three phase Au-BaTiO<sub>3</sub>-ZnO sample by *ex-situ* annealing it in air and vacuum environment and *in-situ* annealing it in TEM to investigate the microstructural change. BaTiO<sub>3</sub> (BTO) matrix serves as a highly thermally stable matrix<sup>227</sup> whereas Au and ZnO undergo microstructural changes at elevated temperatures. The heating profiles used for air and vacuum annealing is illustrated in Figure 6-1 which allowed the exploration of growth mechanism. The samples were heated to 650°C *ex-situ* in air and vacuum for 1 hr. Interestingly, changing the annealing environment activates a different growth mechanism, leading to the formation of very distinct microstructures. The sample was also heated *in-situ* in TEM in vacuum to study the interfacial effects between Au and ZnO. The optical properties of all the three samples are also compared which are correlated to their microstructures. Changing the annealing environment provides an interesting approach to achieve microstructure and property tuning in oxide-metal nanocomposite systems.

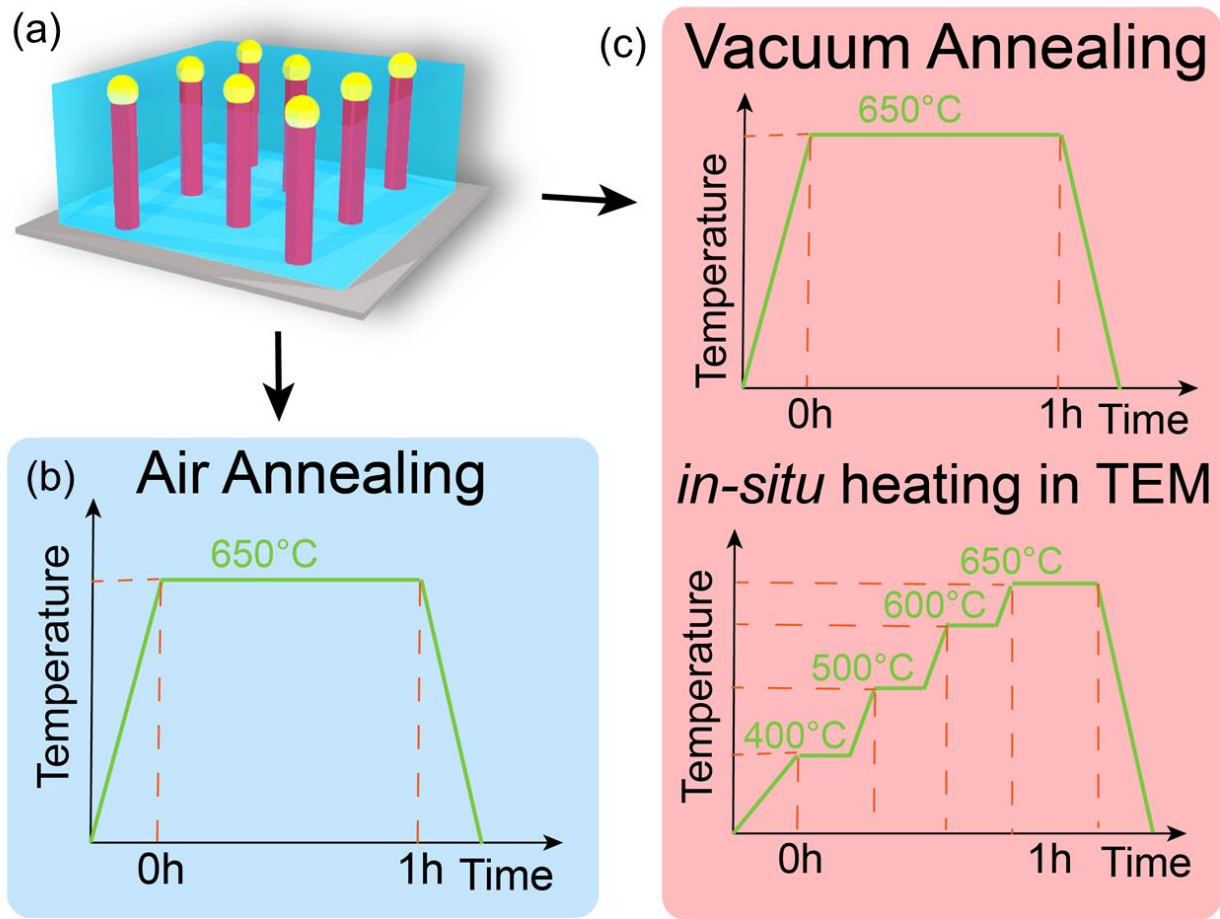


Figure 6-1. Schematic illustration of the (a) ordered three-phase Au-BaTiO<sub>3</sub>-ZnO nanocomposite. Heating profiles showing the (b) *ex-situ* annealing in air, (c) in vacuum, and during *in-situ* heating in TEM to investigate the thermal stability of the nanocomposite thin film.

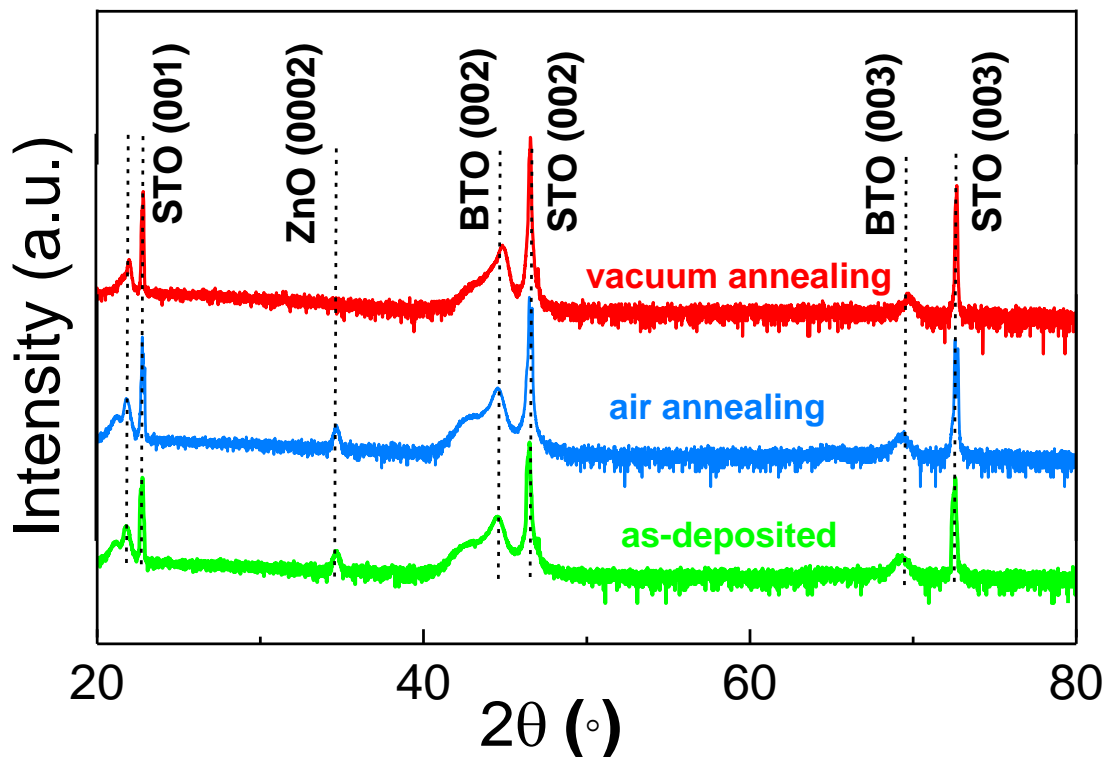


Figure 6-2. X-ray Diffraction. XRD plots of the as-deposited, air annealed and vacuum annealed three-phase Au-BaTiO<sub>3</sub>-ZnO nanocomposite.

### 6.3 Results and Discussion

To study the thermal stability of the three-phase nanocomposite, the sample was annealed at 650°C separately in air and in vacuum for 1 hr. The X-ray diffraction (XRD)  $\theta$ - $2\theta$  scans (Figure 6-2) of all the three-phase samples show that the BTO phase remains textured in the [001] direction. The splitting in the BTO peak arises from the two different BTO layers, present in the Au-BTO and BTO-ZnO films, respectively, and can be attributed to the lattice parameter relaxation in the two layers. The BTO present in the upper BTO-ZnO layer undergoes strain relaxation since it gets deposited onto BTO, instead of STO, as the effective substrate. However, upon annealing the sample in vacuum, the ZnO (0002) peak disappears. To further confirm the absence of the ZnO phase upon vacuum annealing, Raman spectroscopy was done on the samples after annealing them in air and vacuum. The Raman signal exhibited by the ZnO is relatively weak due to its very small diameter (~7.6 nm). The Raman shift presented in Figure 6-3 shows that the two samples share

similar features overall. However, the absence of the ZnO peak at  $414\text{ cm}^{-1}$  and  $\sim 1100\text{ cm}^{-1}$  after vacuum annealing confirms that the ZnO phase is absent.

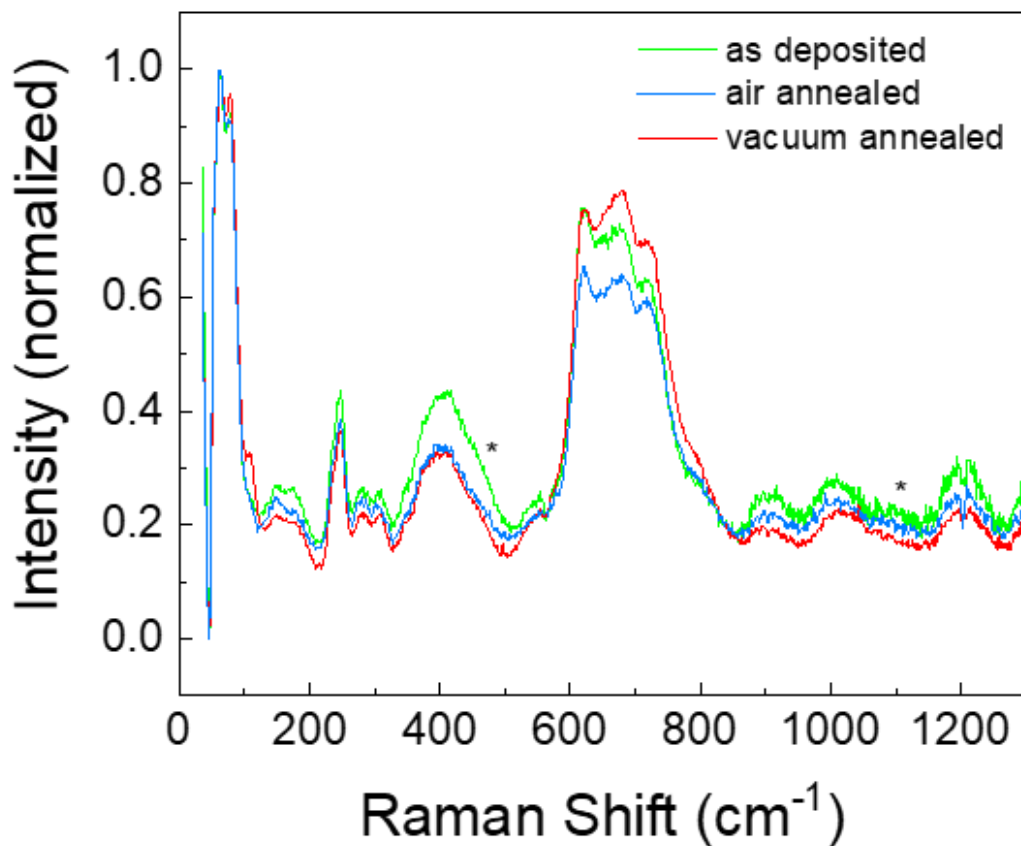


Figure 6-3. Raman Spectroscopy of the as-deposited, air annealed and vacuum annealed three-phase Au-BaTiO<sub>3</sub>-ZnO nanocomposite.

To gain a better understanding of the growth mechanism, scanning transmission electron microscopy (STEM) was performed on the samples. Figure 6-4 compares the sample morphology of the as-deposited sample and after annealing it in air and vacuum for 1hr. The microstructure of the as-deposited sample (shown in Figure 6-4a) is similar to the one that has been reported earlier.<sup>106</sup> It shows the presence of Au NPs capping the ZnO nanowires, embedded inside the BTO matrix. Figure 6-4b shows the microstructure and phase distribution after annealing the sample in air at 650°C for 1hr. Overall, the morphology looks quite similar with Au and ZnO pillars arranged in an ordered fashion. The length and diameter of the Au and ZnO pillars are approximately the

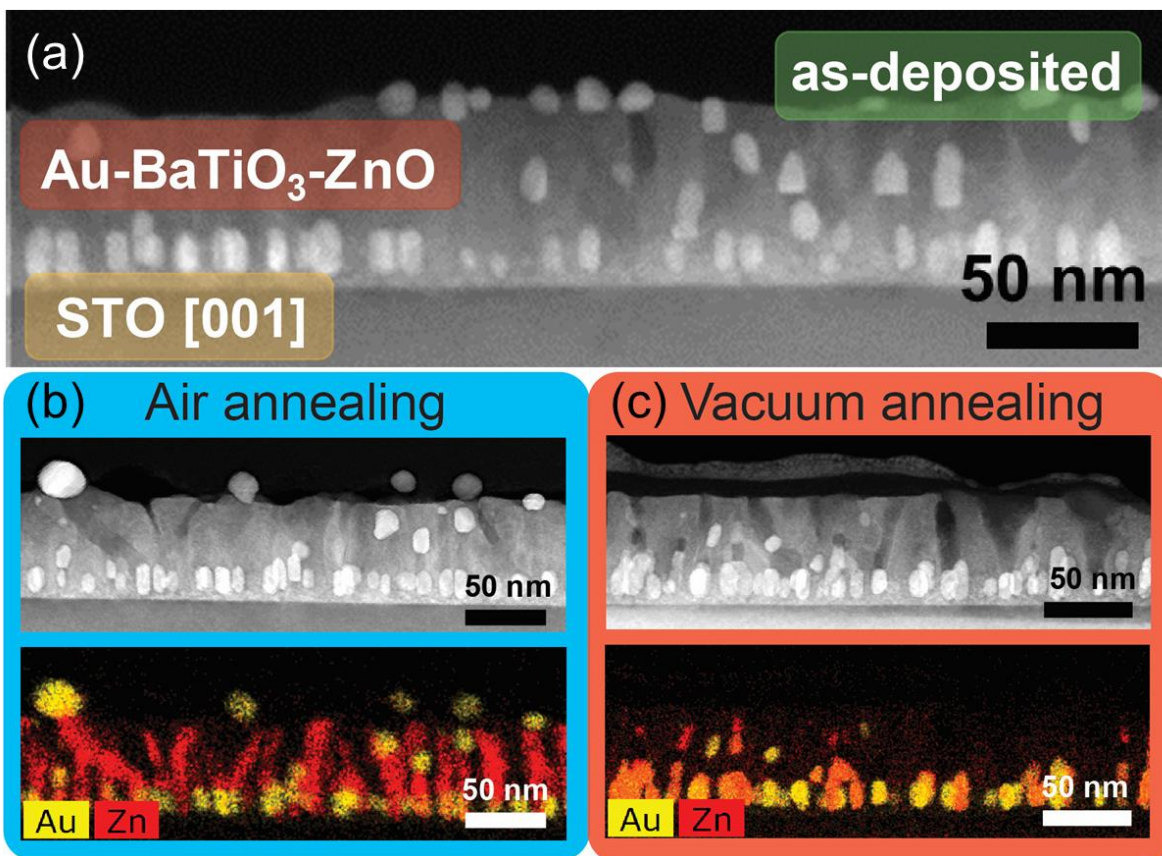


Figure 6-4. *Ex-situ* annealing of the ordered three-phase Au-BaTiO<sub>3</sub>-ZnO nanocomposite. (a) Cross-sectional STEM image of the as-deposited Au-BaTiO<sub>3</sub>-ZnO nanocomposite, Cross-sectional STEM image and the corresponding EDS map after *ex-situ* annealing in (b) air and (c) vacuum

same ( $\sim 7.2$  nm and  $\sim 7.6$  nm, respectively). However, the size of the Au NPs capping the ZnO NWs is very different. The size of the Au NPs increases from  $\sim 10$  nm to  $\sim 16$  nm after post-growth annealing in air. Besides, the number of Au NPs capping the ZnO NWs significantly reduces after annealing. Such increase in the size of the Au NPs size suggests the diffusion of Au from smaller particles to the larger ones (Ostwald ripening) along the BTO surface to reduce the total particle surface area. During the post-growth anneal, coarsening of the Au NPs make the particles transition from a faceted shape to a round shape. In contrast, the particles embedded inside the BTO matrix do not undergo Ostwald ripening, maintain their shape and size and are thermally stable during the annealing process. These results confirm that Au can diffuse from one catalyst NP to another NP during equilibrium conditions by migrating along the BTO surface. Further investigation was done by annealing the sample at  $650^{\circ}\text{C}$  in vacuum for 1hr. Figure 6-4c shows

the microstructure and phase distribution after doing vacuum annealing. Surprisingly, the morphology looks completely

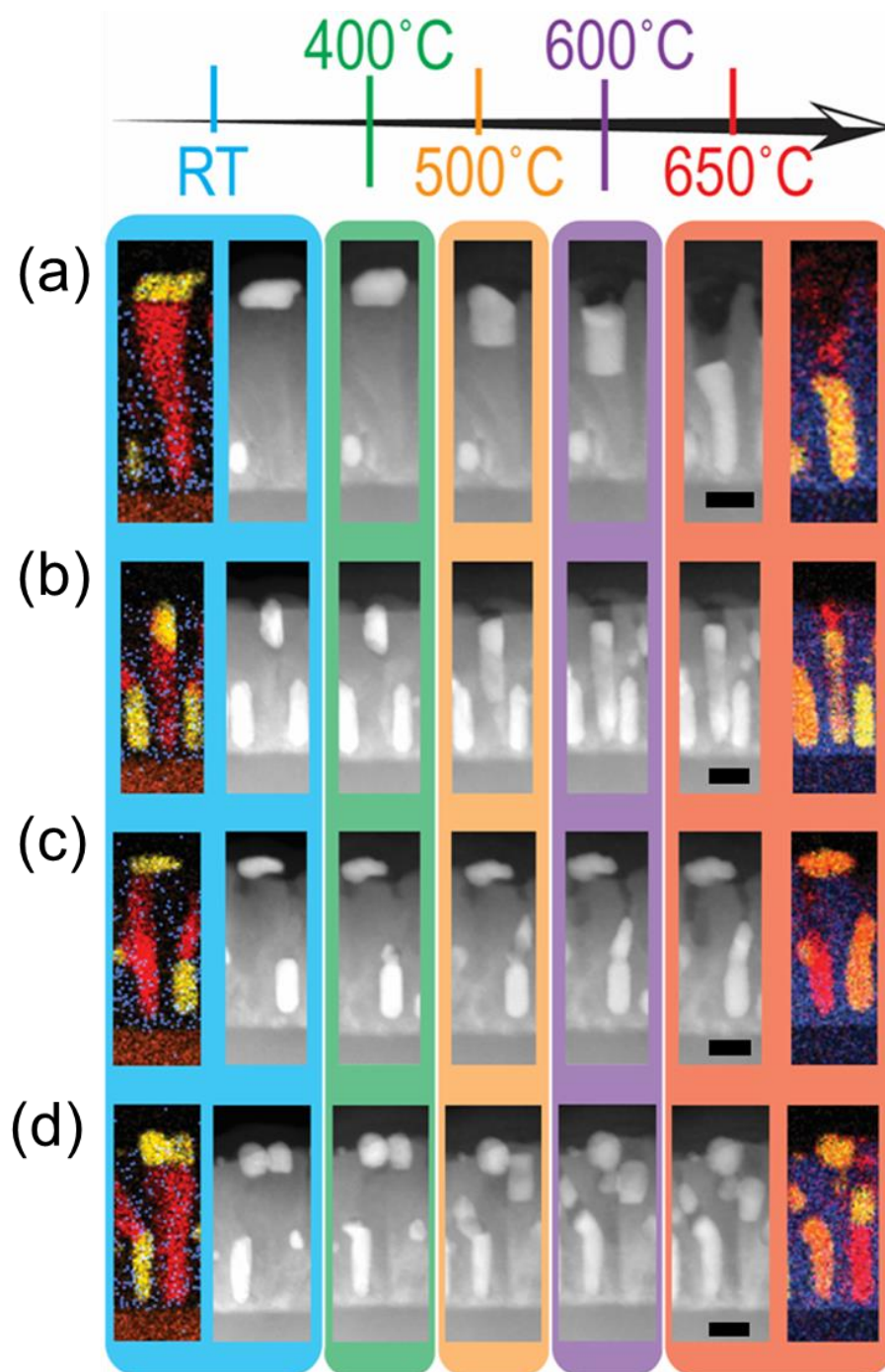


Figure 6-5. *In-situ* heating of Au-BaTiO<sub>3</sub>-ZnO in TEM. Cross-sectional STEM image along with the initial and final EDS map during the *in-situ* heating in TEM from room temperature (RT) to 650°C of the (a)-(d) four selected regions. Scale bar corresponds to 20 nm

different on changing the annealing environment. The Au NPs present at the surface reduces significantly after vacuum annealing. EDS mapping also shows the alloying between Au and Zn to form a AuZn solid solution. The oxygen partial pressure required to reduce bulk ZnO to Zn at 650°C is  $10^{-25}$  torr, as calculated from the Ellingham diagram.<sup>172</sup> However, the pressure in furnace and column pressure in TEM was maintained at  $10^{-6}$  torr and  $10^{-10}$  torr before annealing, respectively. The oxygen partial pressure required for the dissociation of bulk ZnO (above 750°C) has been reported previously as<sup>228</sup>:  $\log P_{O_2}(Torr) = -\frac{13500}{T} + 8.01$ , which gives oxygen partial pressure of  $10^{-5}$  torr at 750°C. It is likely that the ZnO NW still gets reduced to Zn by annealing in vacuum due to the reducing environment created by the low oxygen partial pressure, high temperature, oxygen vacancies, nanostructure formation and impurity carbon as has been reported before.<sup>228-233</sup> Reducing environment increases the oxygen vacancies in ZnO<sub>x</sub>, thereby reducing the interfacial energy of Au/ZnO<sub>x</sub> due to the miscibility of Au and Zn. Interestingly, Au and Zn forms a solid solution, evident from the EDS mapping showing the elemental distribution in Figure 6-4d. The phase composition of the AuZn solid solution is discussed in more detail later. Clearly, oxygen pressure plays a critical role in determining the final morphology of the three-phase Au-BTO-ZnO nanocomposite.

In order to gain a further understanding of the growth mechanism of the ordered three phase nanocomposite, the thermal stability of the film was investigated using in situ heating in TEM in vacuum. In situ heating in TEM was done on a cross-section TEM sample from room temperature (RT) to 650°C and the corresponding STEM images were recorded at RT, 400°C, 500°C, 600°C and 650°C. Figure 6-5 shows the transformation in four selected Au NPs and pillars which highlight the different aspects of the mechanism at five different temperatures. Figure 6-5a shows a Au NP capping a ZnO NW, having a faceted surface at room temperature. Upon increasing the temperature to 400°C, the particle starts to have a smoothly curved surface. The curvature of Au-ZnO interface remains as flat as possible. The instability arises from the curved surface near the edge of the ZnO NW. Due to the Gibbs-Thomson effect, the solubility of Au in ZnO at this curved surface is greater as compared to the flat surface (Figure 6-6). Therefore, the Au NP shape starts changing from the corner of the Au-Zn interface. Overall, the particle remains relatively stable till 400°C. Increasing the temperature to 500°C, increases the diffusion rate of Au into ZnO and they become a liquid alloy phase. The existence of such eutectic liquid alloy phase below the bulk eutectic temperature is attributed to the nanoscale size effects due to the Gibbs-Thomson effect.

Further increasing the temperature to 600°C and 650°C, causes the liquid phase alloy to diffuse through ZnO phase present below it. It is also possible that the VLS mechanism happens reversibly, specifically, by precipitating the supersaturated ZnO on top of the Au-Zn nanopillar. Similar mechanism is also observed in Figure 6-5b, wherein the Au NP becomes unstable from its corners and mixes with the ZnO NW, thereby precipitating the supersaturated ZnO NW on top.

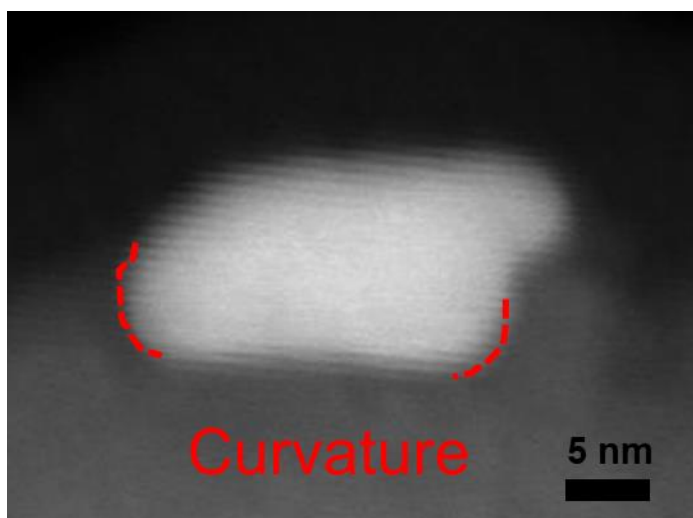


Figure 6-6. STEM image of the Au NP showing the curvature at RT

Figure 6-5c shows an isolated Au NP that is slightly in contact with the ZnO NW. Clearly, the Au NP doesn't undergo a major morphology change upon heating. However, its contrast becomes weaker, which is likely due to the Zn diffusion since the image contrast is roughly proportional to  $Z^2$ , evident by the EDS mapping. In contrast, the Au pillar, initially in contact with the ZnO pillar becomes a AuZn liquid alloy after heating the sample to 650°C. Similar results are also observed in Figure 6-5d in which the Au NP diffuses down along ZnO NW while ZnO diffuses to the Au NP to become Au-Zn liquid phase alloy. Therefore, two different mechanisms: (i) reverse VLS, and (ii) formation of AuZn solid solution take place upon vacuum annealing. The activation of the either mechanism can be attributed to the diameter of the ZnO NW at the Au-ZnO interface at room temperature. In the first case, when the Au-ZnO interfacial diameter is greater than a critical diameter (~10-11 nm), reverse VLS mechanism takes place. While, when the Au-ZnO interfacial diameter is less than the critical diameter, formation of the AuZn solid solution takes place. Since the smaller ZnO NW has the higher probability of getting reduced to Zn at the same

temperature and pressure as compared to the larger ZnO NW, it gets alloyed with Au to form a AuZn solid solution. The morphological changes in the sample take place mainly in two stages. Stage 1 is active till 400°C, where the microstructure is relatively stable. Further increasing the temperature above 400°C activates stage 2, where a rapid microstructural change is seen.

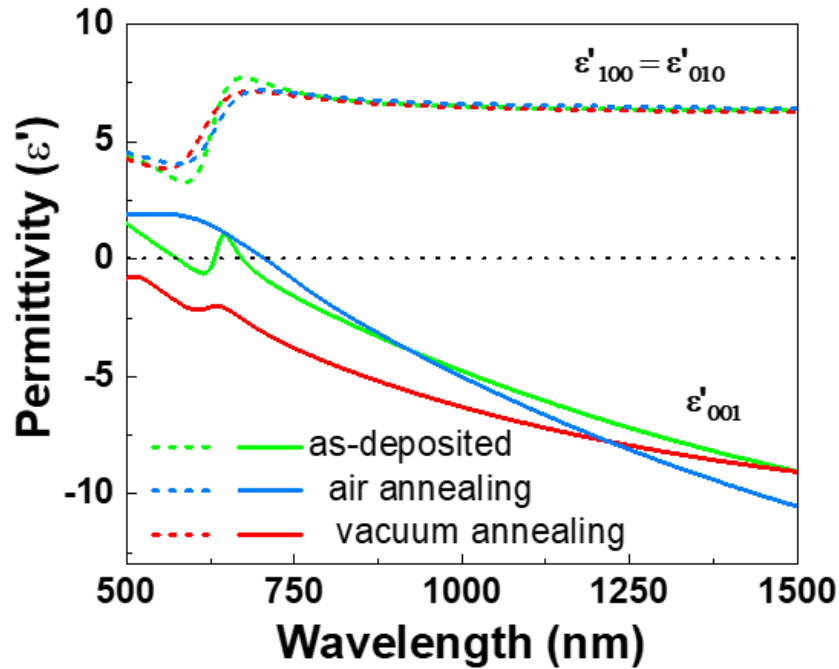


Figure 6-7. Tunable optical properties. Real part of the in-plane ( $\epsilon'_{100}=\epsilon'_{010}$ ) and out-of-plane ( $\epsilon'_{001}$ ) permittivity for the as-deposited, air-annealed, and vacuum annealed Au-BaTiO<sub>3</sub>-ZnO thin films.

The optical properties are closely related to the microstructural and morphological change in the sample. The angular dependent ellipsometry data of the three samples were measured and compared. The permittivity was modeled using an anisotropic model through the use of general oscillator models to enforce the Kramers-Kronig consistency. The real part of the in-plane ( $\epsilon'_{||}$ ) and out-of-plane permittivity ( $\epsilon'_{\perp}$ ) are plotted in Figure 6-7. Clearly, the  $\epsilon'_{||}$  for all the three samples show similar characteristics such as an absorption peak near 600 nm because of the plasmonic absorption by Au and remain positive throughout the wavelength regime. Interestingly, the  $\epsilon'_{\perp}$  show a pronounced difference in the visible wavelength regime. The as deposited sample show a resonant frequency near 600 nm which disappears after air and vacuum annealing. The resonant

frequency in the out-of-plane direction possibly arises due to the presence of Au NP capping the ZnO NW as observed earlier.<sup>106</sup> After vacuum annealing, the fraction of Au NPs present largely reduces and the most of the pillars are Au-Zn intermetallic which causes the out-of-plane permittivity to become negative throughout the wavelength range. Nonetheless, all the samples show negative  $\epsilon'_{\perp}$  in the near-infrared wavelength regime, thereby retaining the hyperbolic character. Thus, changes in the microstructure directly helps tune the optical properties of the three-phase nanocomposite.

The microstructure and phase composition of the three-phase nanocomposite before and after vacuum annealing is further analyzed with the high-resolution STEM images to understand the interface formation mechanism after the VLS growth mechanism. Figure 6-8a presents the HRSTEM image of BTO-ZnO vertical interface. A fast-Fourier transformed (FFT) image (Figure 6-8b) shows the domain matching relationship along the vertical interface. Several misfit dislocations are present at regular intervals, making the interface as semi-coherent. The BTO-ZnO vertical interface shows two types of domain matching epitaxy (DME): 5 BTO (002) with 4 ZnO (0002) and 6 BTO (002) with 5 ZnO (0002). O atom of ZnO binds alternatively with Ba and Ti atoms of BTO on either side of the ZnO pillar, making the energy of every layer to be similar. Such matching relationship also causes a slight tilt in the ZnO pillar. ZnO growth takes place along [0002] out-of-plane direction, with two domains growing with a 30° rotation in the in-plane direction with STO. The growth along [0002] out-of-plane exposes its low surface energy planes, specifically,  $(11\bar{2}0)$  and  $(10\bar{1}0)$ , in the vertical direction that is coupled with BTO. Such a growth orientation minimizes the strain and surface energy between the ZnO-BTO and ZnO-STO interfaces.

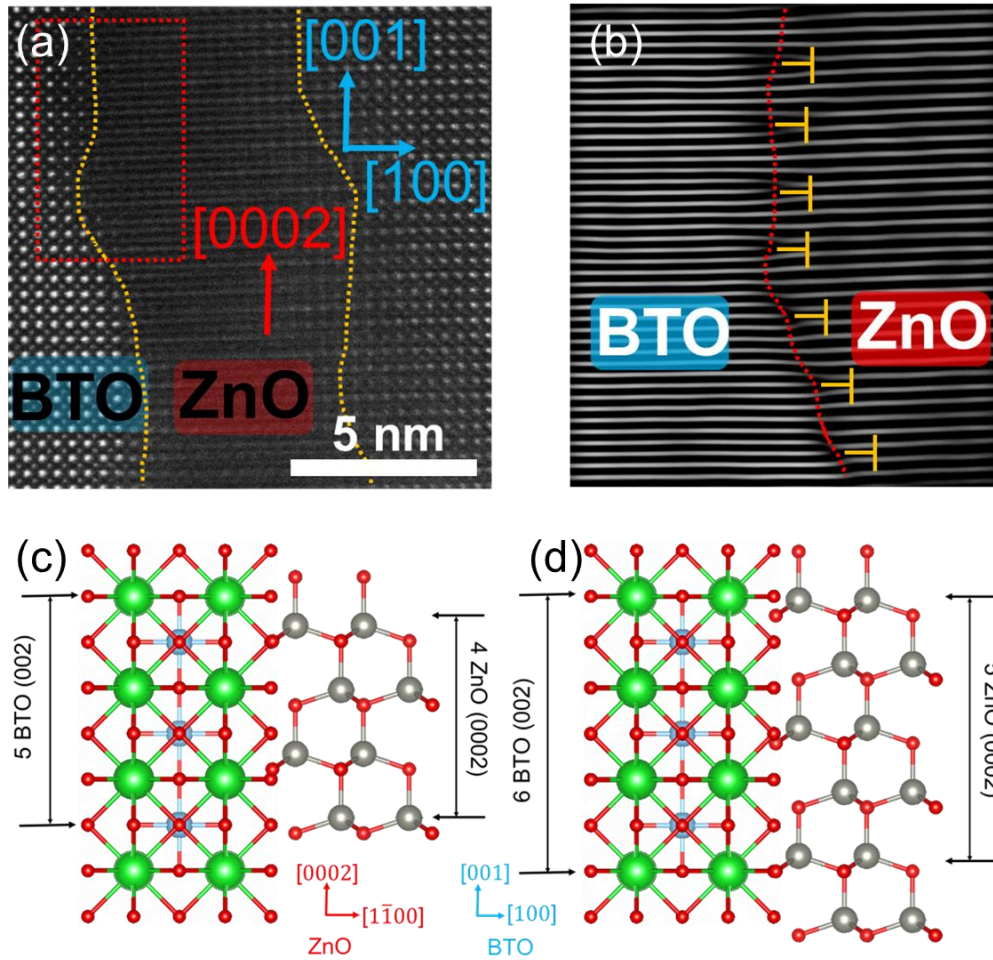


Figure 6-8. Microstructure of the as-deposited Au-BaTiO<sub>3</sub>-ZnO nanocomposite. (a) HR-STEM image of the BaTiO<sub>3</sub>-ZnO vertical interface and its corresponding (b) Fourier-transform image showing the presence of dislocations at the BaTiO<sub>3</sub>-ZnO vertical interface. Schematic illustration showing the two possible domain-matching epitaxy (DME) at the BaTiO<sub>3</sub>-ZnO vertical interface with (c) 5 BTO (002): 4 ZnO (0002) and (d) 6 BTO (002): 5 ZnO (0002) lattice matching relationship.

Figure 6-9a shows an EDS elemental map of a region containing three Au pillars: pure Au pillar and a pillar containing a solid solution of Au and Zn after vacuum annealing. The corresponding EDS line-profile is shown in Figure 6-9b. Clearly, the Zn phase is absent in the first two Au pillars (shown in red) while both Au and Zn are present in the third pillar. Further, using a k factor ( $k_{\text{AuL,ZnK}}$ ) of 3.0,<sup>234</sup> the composition of the AuZn alloy is determined to contain less than 10% atomic Zn. Figure 6-10 shows another EDS line-scan across several pillars, whose composition

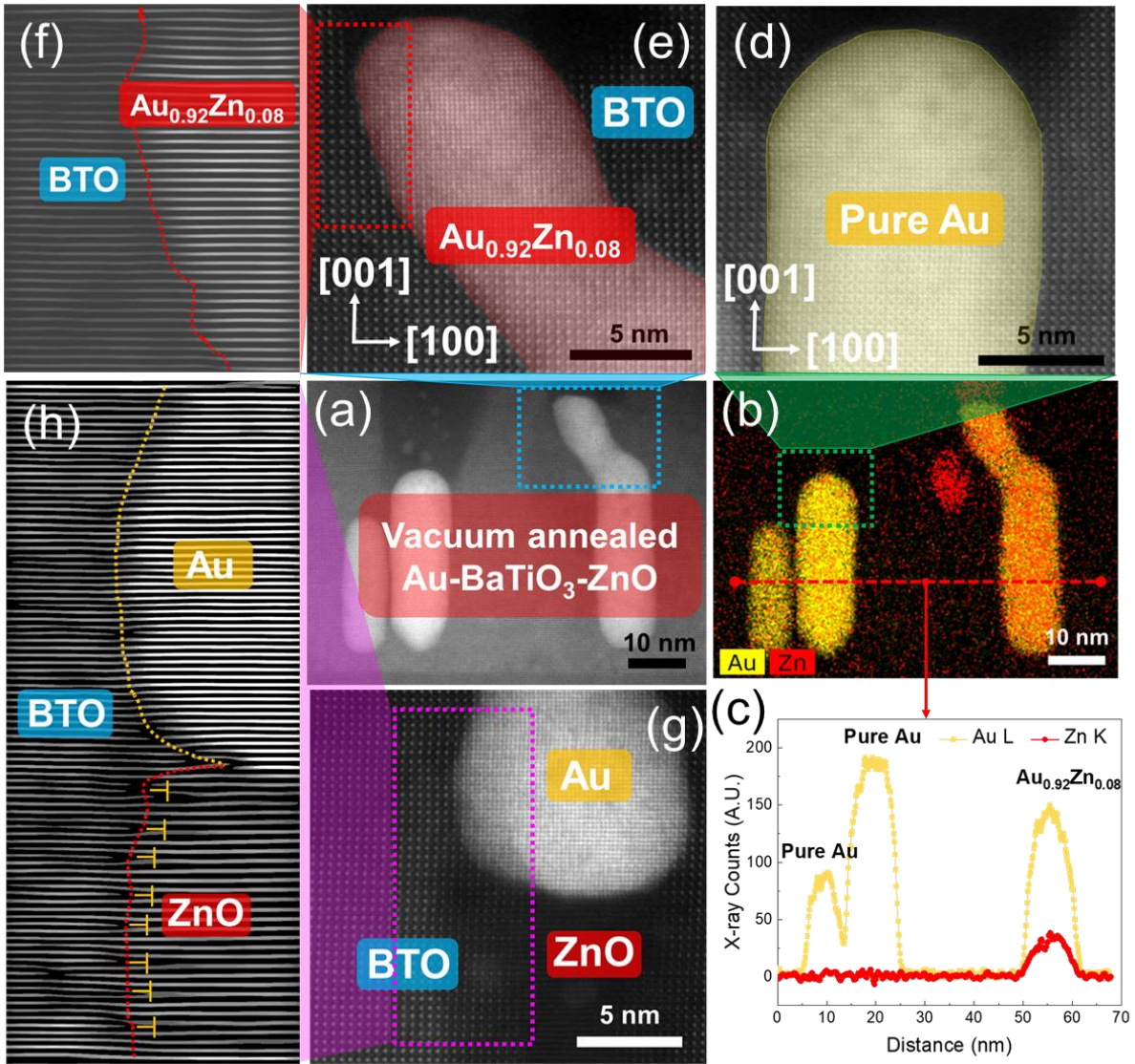


Figure 6-9. Microstructure of the vacuum-deposited Au-BaTiO<sub>3</sub>-ZnO nanocomposite. (a) STEM image of the vacuum-annealed Au-BaTiO<sub>3</sub>-ZnO nanocomposite, (b) its corresponding EDS elemental map and (c) EDS line-scan with the labeled stoichiometry. (d) HR-STEM image of the pure Au pillar and (e) of the pillar with stoichiometry Au<sub>0.92</sub>Zn<sub>0.08</sub> with its (f) corresponding Fourier-transform image. (g) HR-STEM image of Au-BaTiO<sub>3</sub> and BaTiO<sub>3</sub>-ZnO vertical interface with (h) its corresponding Fourier-transform image.

is marked in the map. Interestingly, all the AuZn alloys have composition of Zn less than 10% atomic Zn. Interestingly, the solubility of Au in Zn is 33.5 at% at 683°C and ~12 at% at room temperature from the bulk Au-Zn phase diagram (Figure 6-11).<sup>210</sup> The observed low Zn solubility can be attributed to the nanostructured Au and Zn formation, low cooling rate (20°C/min), and the presence of oxygen vacancies, which can cause a deviation of the solidus line from the bulk Au-

Zn phase diagram. Figure 6-9c and Figure 6-9d compares the atomic resolution STEM image of the Au pillar and  $\text{Au}_{0.92}\text{Zn}_{0.08}$ , respectively. The crystal structure of  $\text{Au}_{0.92}\text{Zn}_{0.08}$  is similar to the pure Au, confirming that the AuZn alloy is a solid solution with a FCC structure. The FFT image of the vertical interface between the AuZn solid solution and BTO is shown in Figure 6-9e. Clearly, no dislocations are formed, and the interface remains largely coherent. Figure 6-9f shows the HRSTEM image of one ZnO pillar capped by a Au NP after vacuum annealing. In order to compare the vertical interface before and after vacuum annealing, FFT image of the BTO-ZnO interface was analyzed and is presented in Figure 6-9g. Clearly, Au and BTO show an almost coherent interface with the presence of no misfit dislocations while the BTO-ZnO vertical interface shows similar DME as observed before annealing (Figure 6-8c and Figure 6-8d): 5 BTO (002) with 4 ZnO (0002) and 6 BTO (002) with 5 ZnO (0002).

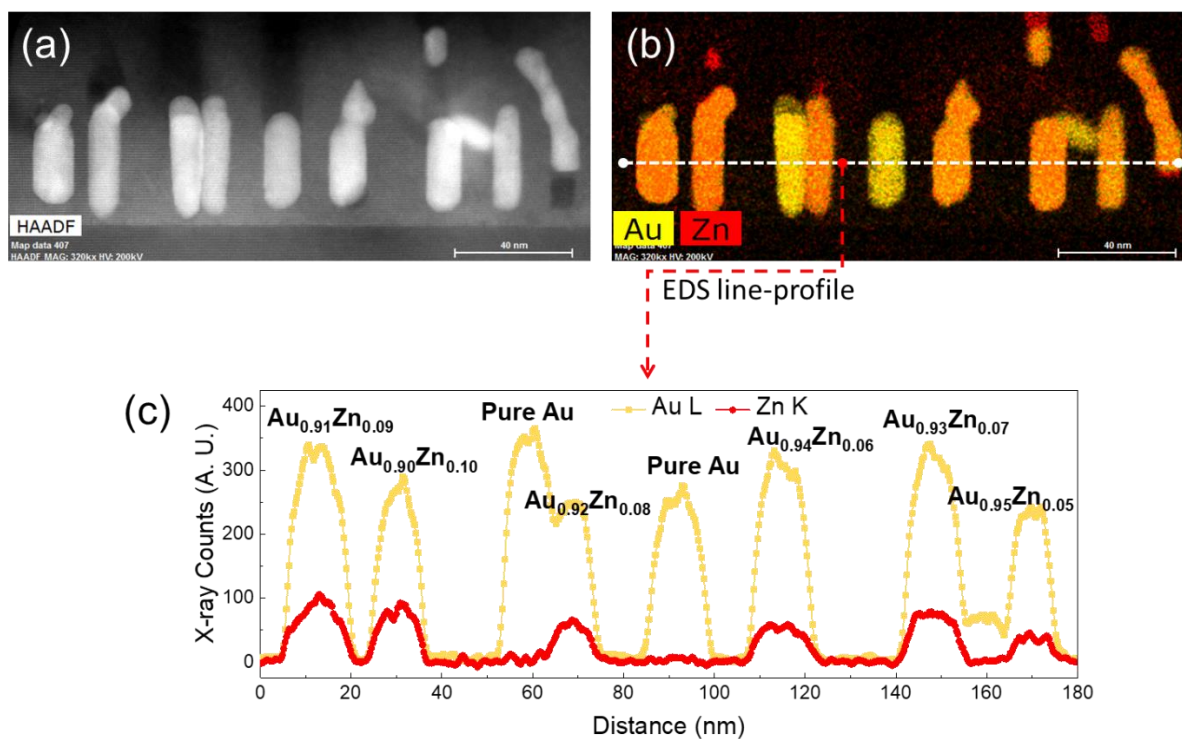


Figure 6-10. (a) STEM image of the vacuum annealed three-phase Au-BaTiO<sub>3</sub>-ZnO nanocomposite, (b) its corresponding EDS map and (c) the EDS line-scan showing the pillar compositions.

In situ heating experiments in TEM provides useful insights into the phase transformation and structure reconstruction during the annealing of the three-phase Au-BTO-ZnO ‘nanoman’

structure. The experiments also demonstrate the thermal stability and interfacial dynamics between the Au and ZnO at the nanoscale. Moreover, the in-situ heating experiments provide an opportunity to explore the growth mechanisms in other nanocomposite systems with different annealing environment and understand the factors influencing nanowire growth towards the successful fabrication of nanowire-based devices.

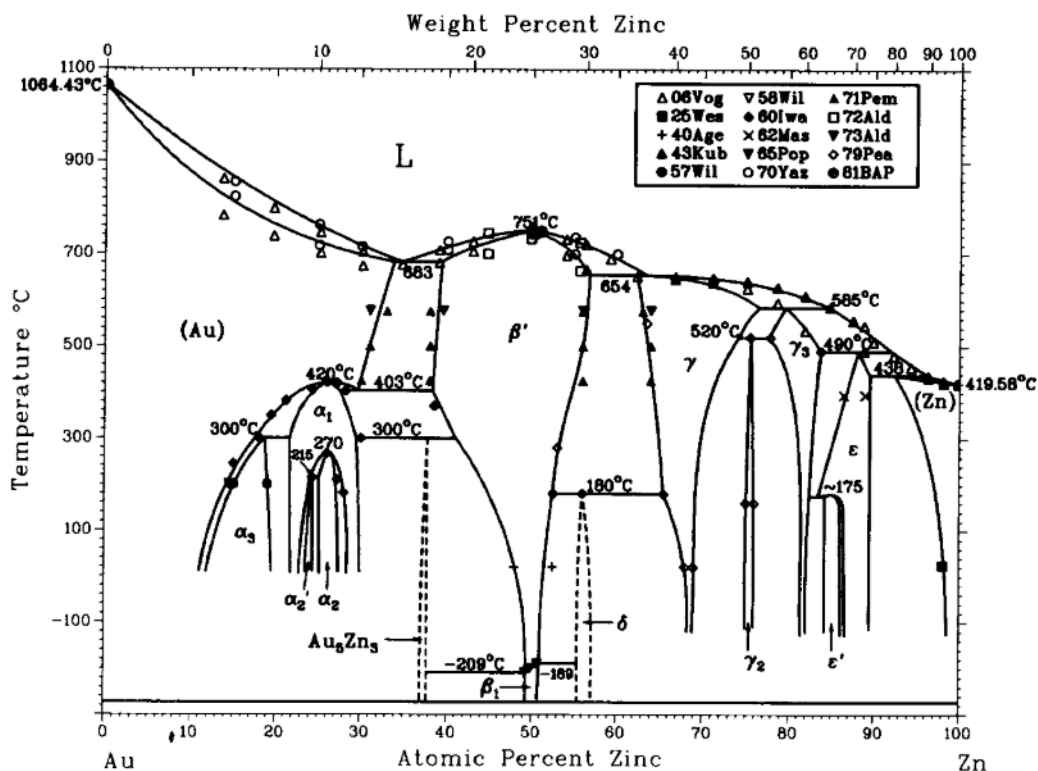


Figure 6-11. The Au-Zn (bulk) phase diagram<sup>210</sup>

## 6.4 Conclusions

In summary, thermal stability of self-assembled ordered three phase Au-BaTiO<sub>3</sub>-ZnO has been demonstrated by both ex situ annealing and in situ heating in TEM. The study reveals that different mechanisms are dominant while annealing in air (Ostwald ripening) and vacuum (reverse VLS and solid solution formation). In situ heating experiment in TEM confirms that the ZnO NW diameter at the Au-ZnO interface determines the activation of one of the either mechanism. The Zn atomic % in the AuZn solid solution is less than 10%, thus forming a FCC structure similar to that of pure Au. Such in situ heating in TEM provides a powerful tool for monitoring the

microstructure evolution at nanoscale and complement the existing factors influencing nanowire growth.

## 6.5 Experimental Details

*Thin Film Growth:* The self-assembled three-phase Au-BTO-ZnO nanocomposite thin films were deposited using a two-step growth using a templating method. Initially, an Au-BTO (1:1) thin film was deposited followed by the deposition of BTO-ZnO (1:1) thin film. The thin films were deposited on STO (001) single-crystal substrates using pulsed laser deposition (PLD) (with a KrF excimer laser, Lambda Physik Compex Pro 205,  $\lambda = 248$  nm). The films were deposited at the substrate temperature of 700 °C with a laser frequency of 2Hz and 40 mTorr oxygen pressure was maintained during the deposition.

*Structural Characterization:* The microstructure of the films were investigated by XRD (PANalytical Empyrean XRD), TEM, and high-resolution STEM (FEI TALOS 200X operated at 200 kV). Cross-section TEM samples were prepared using the manual grinding, polishing and thinning process followed by dimpling and ion milling using precision ion polishing system (PIPS II, Gatan). The in-situ heating experiments were conducted using a MEMS holder specifically designed for in situ heating. The sample was heated at the rate of 10°C/min and was cooled rapidly after reaching to 650°C.

*Optical characterization:* The dielectric permittivity of the films was measured using spectroscopic ellipsometer (JA Woollam RC2). The measurement was performed at three different angles: 55°, 65°, and 75°. A Raman microscope (Renishaw RM 2000) equipped with a 532 nm green laser was used for the Raman spectroscopy measurements.

## 7. SUMMARY AND FUTURE WORK

In this dissertation, a systematic study of the metal-dielectric nanocomposite ranging from the two-phase particle-in-matrix morphology to the three-phase VAN architecture for photocatalyst and metamaterial application was done. First, a one-step PLD deposition technique to deposit highly textured anatase  $\text{TiO}_2$ -Au nanocomposite thin films with highly tailorable shape and size of Au NPs by varying the growth temperature was demonstrated. Incorporation of Au NPs effectively tunes the band gap of  $\text{TiO}_2$ . The shape and size tuning of Au NPs increases the absorption efficiency over a broad optical spectrum. Photodegradation results conclude that the synergistic impact of lowering of the  $\text{TiO}_2$  band gap along with the plasmonic absorption of Au NPs plays a significant role in determining the photoactivity of the thin films.

Second, a new growth paradigm of three-phase nanocomposite (Au-BaTiO<sub>3</sub>-ZnO) with high degree of ordering has been achieved by the combined templating and VLS mechanism. This approach provides an alternative to the top-down fabrication approach for the growth of complex nanoscale metamaterials. The three-phase ordered microstructure tunes the isofrequency surfaces from ellipsoidal to hyperbolic, providing additional degree of freedom to control light-matter interaction at the nanoscale. Third, a strong tunability in the microstructure of the self-assembled ordered three-phase Au-BaTiO<sub>3</sub>-ZnO nanocomposite along with its optical properties, grown by a pulsed laser deposition method was demonstrated. Varying the growth temperature, deposition frequency and template thickness evolves the microstructure by tuning the Au and ZnO pillar geometry as well as the shape and size of the Au nanoparticle capping the ZnO nanowire. Finally, thermal stability of self-assembled ordered three phase Au-BaTiO<sub>3</sub>-ZnO has been demonstrated by both ex situ annealing and in situ heating in TEM. The study reveals that different mechanisms are dominant while annealing in air (Ostwald ripening) and vacuum (reverse VLS and solid solution formation). Such in situ heating in TEM provides a powerful tool for monitoring the microstructure evolution at nanoscale and complement the existing factors influencing nanowire growth.

Overall, metal-oxide nanocomposites offer unique advantages over oxide-oxide nanocomposites in terms of new functionalities and tunable microstructure. The nanoparticle size can be easily tuned in the particle-in-matrix design while the VAN architecture allows flexible

tunability of the pillar dimensions. Regarding the future research direction, selected focus directions are:

1. Owing to the large possibilities of materials combinations, a lot of metal-dielectric VAN systems are yet to be explored that can enable different multifunctionalities. Figure 1-26 provides a guideline on materials selection for designing VAN systems based on the in-plane strain compensation. Highly spatially ordered structures can be achieved by careful materials selection which provide an important building block for metamaterial application. However, domain matching epitaxy should also be considered while exploring potential VAN systems.
2. Most of the nanocomposite thin film systems have been reported on specific oriented single crystal substrates such as STO (001), LAO (001), Sapphire (0001), MgO (001) etc. Since these substrates are small and expensive, they are not ideal for scaling up device fabrication. Therefore, interesting and potential systems should be grown on Si substrates or flexible substrates such as Mica with the aim of achieving at par performance as reported earlier, which can be integrated in Si-based devices or flexible electronics. For example, several oxide-oxide based VAN systems have been successfully integrated on Si and Mica substrate and could be further extended to metal-dielectric nanocomposites.
3. Further work is needed in the exploration of three-phase nanocomposite for achieving greater design flexibility. Materials selection can be done by examining the bulk ternary, quaternary, or pseudo-binary phase diagrams for potential eutectic points or alloy formation.

## REFERENCES

1. O. Y. Gorbenko, S. V Samoilenkov, I. E. Graboy, and A. R. Kaul: Epitaxial Stabilization of Oxides in Thin Films. *Chem. Mater.* **14**, 4026 (2002).
2. J. L. Macmanus-driscoll: Self-Assembled Heteroepitaxial Oxide Nanocomposite Thin Film Structures : Designing Interface-Induced Functionality in Electronic Materials. *Adv. Funct. Mater.* **20**, 2035 (2010).
3. A. Chen and Q. Jia: Multiferroic Nanocomposite Thin Films. *Taylor Fr. Gr.* 189 (2016).
4. J. A. Venables, G. D. T. Spiller, and M. Hanbucken: Nucleation and growth of thin films. *Reports Prog. Phys.* **47**, 399 (1984).
5. L. W. Martin, Y. Chu, and R. Ramesh: Advances in the growth and characterization of magnetic , ferroelectric , and multiferroic oxide thin films. *Mater. Sci. Eng. R* **68**, 89 (2010).
6. J. Huang, J. L. Macmanus-driscoll, and H. Wang: New epitaxy paradigm in epitaxial self-assembled oxide vertically aligned nanocomposite thin films. *J. Mater. Res.* **32**(21), 4054 (2017).
7. Z. Chen, R. Gao, R. Xu, Y. Lee, X. Zhang, J. Yao, and L. W. Martin: Self-Assembled, Nanostructured, Tunable Metamaterials via Spinodal Decomposition. *ACS Nano* **10**, 10237 (2016).
8. J. Macmanus-driscoll, J. L. M. A. C. Manus-driscoll, P. Zerrer, H. Wang, H. A. O. Yang, and J. Yoon: Strain control and spontaneous phase ordering in vertical nanocomposite heteroepitaxial thin films Strain control and spontaneous phase ordering in vertical nanocomposite heteroepitaxial thin films. *Nat. Mater.* **7**, 314 (2008).
9. S. M. O. Malley, P. L. Bonanno, K. H. Ahn, A. A. Sirenko, A. Kazimirov, and M. Tanimura: Epitaxial checkerboard arrangement of nanorods in ZnMnGaO<sub>4</sub> films studied by x-ray diffraction. *Phys. Rev. B* **78**, 165424 (2008).
10. G. Sun, H. Zhou, X. Cao, R. Li, M. Tazawa, M. Okada, and P. Jin: Self-Assembled Multilayer Structure and Enhanced Thermo-chromic Performance of Spinodally Decomposed TiO<sub>2</sub>-VO<sub>2</sub> Thin Film. *ACS Appl. Mater. Interfaces* **8**, 7054 (2016).
11. J. Liu, X. Wu, W. N. Lennard, and D. Landheer: Surface-directed spinodal decomposition in hafnium silicate thin films. *Phys. Rev. B* **80**, 7 (2009).

12. W. Zhang, A. Chen, Z. Bi, Q. Jia, J. L. Macmanus-Driscoll, and H. Wang: Interfacial coupling in heteroepitaxial vertically aligned nanocomposite thin films: From lateral to vertical control. *Curr. Opin. Solid State Mater. Sci.* **18**(1), 6 (2014).
13. H. Zheng, J. Wang, S. E. Lofland, Z. Ma, T. Zhao, S. R. Shinde, S. B. Ogale, F. Bai, D. Viehland, Y. Jia, D. G. Schlom, M. Wuttig, A. Roytburd, and R. Ramesh: Multiferroic BaTiO<sub>3</sub>-CoFe<sub>2</sub>O<sub>4</sub> Nanostructures. *Science* (80-. ). **303**, 661 (2004).
14. A. Chen, H. Zhou, Z. Bi, Y. Zhu, Z. Luo, A. Bayraktaroglu, J. Phillips, E. Choi, J. L. Macmanus-driscoll, S. J. Pennycook, J. Narayan, Q. Jia, X. Zhang, and H. Wang: A New Class of Room-Temperature Multiferroic Thin Films with Bismuth-Based Supercell Structure. *Adv. Mater.* **25**, 1028 (2013).
15. E. Choi, T. Fix, A. Kursumovic, C. J. Kinane, D. Arena, S. Sahonta, Z. Bi, J. Xiong, L. Yan, J. Lee, H. Wang, S. Langridge, Y. Kim, A. Y. Borisevich, I. Maclaren, Q. M. Ramasse, M. G. Blamire, Q. Jia, and J. L. Macmanus-driscoll: Room Temperature Ferrimagnetism and Ferroelectricity in iFe<sub>0.5</sub>Mn<sub>0.5</sub>O<sub>3</sub>. *Adv. Funct. Mater.* **24**, 7478 (2014).
16. W. Zhang, M. Li, A. Chen, L. Li, Y. Zhu, Z. Xia, P. Lu, P. Boullay, L. Wu, Y. Zhu, J. L. Macmanus-driscoll, Q. Jia, H. Zhou, J. Narayan, X. Zhang, and H. Wang: Two-Dimensional Layered Oxide Structures Tailored by Self- Assembled Layer Stacking via Interfacial Strain. *ACS Appl. Mater. Interfaces* **8**, 16845 (2016).
17. K. J. Choi, M. Biegalski, Y. L. Li, A. Sharan, J. Schubert, R. Uecker, P. Reiche, Y. . Chen, X. Q. Pan, V. Gopalan, L.-Q. Chen, D. G. Schlom, and C. B. Eom: Enhancement of Ferroelectricity in Strained BaTiO<sub>3</sub> Thin Films. *Science* **306**, 1005 (2004).
18. H. Zheng, F. Straub, Q. Zhan, P. Yang, W. Hsieh, F. Zavaliche, Y. Chu, U. Dahmen, and R. Ramesh: Self-Assembled Growth of BiFeO<sub>3</sub> – CoFe<sub>2</sub>O<sub>4</sub> Nanostructures. *Adv. Mater.* **18**, 2747 (2006).
19. J. Gutierrez, A. Llodes, J. Gazquez, M. Gibert, N. Roma, S. Ricart, A. Pomar, F. Sandiumenge, N. Mestres, T. Puig, and X. Obradors: Strong isotropic flux pinning in nanocomposite superconductor films. *Nat. Mater.* **6**, 367 (2007).
20. A. Goyal, S. Kang, K. J. Leonard, P. M. Martin, A. A. Gapud, M. Varela, and M. Paranthaman: Irradiation-free, columnar defects comprised of self-assembled nanodots and nanorods resulting in strongly enhanced flux-pinning in YBa<sub>2</sub>Cu<sub>3</sub>O<sub>7-δ</sub> films. *Supercond. Sci. Technol.* **18**, 1533 (2005).

21. Y. Lu, C. Wang, R. Shi, Y. Cui, Z. Shi, S. Yang, Y. Cui, X. Liu, Y. Lu, C. Wang, R. Shi, Y. Cui, and Z. Shi: Predicting epitaxial orientations and lattice structure in ultrathin magnetic thin films. *APL Mater.* **4**, 076102 (2016).
22. M. Fan, B. Zhang, H. Wang, J. Jian, X. Sun, J. Huang, L. Li, X. Zhang, and H. Wang: Self-Organized Epitaxial Vertically Aligned Nanocomposites with Long-Range Ordering Enabled by Substrate Nanotemplating. *Adv. Mater.* **29**, 1606861 (2017).
23. A. Chen, Z. Bi, Q. Jia, J. L. Macmanus-Driscoll, and H. Wang: Microstructure, vertical strain control and tunable functionalities in self-assembled, vertically aligned nanocomposite thin films. *Acta Mater.* **61**(8), 2783 (2013).
24. V. Moshnyaga, B. Damaschke, O. Shapoval, A. Belenchuk, J. Faupel, O. I. Lebedev, J. Verbeeck, G. Van Tendeloo, M. Mücksch, V. Tsurkan, R. Tidecks, and K. Samwer: Structural phase transition at the percolation threshold in epitaxial  $(\text{La}_{0.7}\text{Ca}_{0.3}\text{MnO}_3)_{1-x}(\text{MgO})_x$  nanocomposite films. *Nat. Mater.* **2**(4), 247 (2003).
25. S. M. Stratulat, X. Lu, A. Morelli, D. Hesse, W. Erfurth, and M. Alexe: Nucleation-Induced Self-Assembly of Multiferroic  $\text{BiFeO}_3\text{-CoFe}_2\text{O}_4$  Nanocomposites. *Nano Lett.* **13**, 3884 (2013).
26. X. Gao, L. Li, J. Jian, H. Wang, M. Fan, J. Huang, X. Wang, and H. Wang: Vertically Aligned Nanocomposite  $\text{BaTiO}_3\text{:YMnO}_3$  Thin Films with Room Temperature Multiferroic Properties toward Nanoscale Memory Devices. *ACS Appl. Nano Mater.* **1**, 2509 (2018).
27. S. A. Harrington, J. Zhai, S. Denev, V. Gopalan, H. Wang, Z. Bi, S. A. T. Redfern, S. Baek, C. W. Bark, C. Eom, Q. Jia, M. E. Vickers, and J. L. Macmanus-driscoll: Thick lead-free ferroelectric films with high Curie temperatures through nanocomposite- induced strain. *Nat. Nanotechnol.* **6**, 491 (2011).
28. F. Khatkhatay, A. Chen, J. H. Lee, W. Zhang, H. Abdel-Raziq, and H. Wang: Ferroelectric properties of vertically aligned nanostructured  $\text{BaTiO}_3\text{-CeO}_2$  thin films and their integration on silicon. *ACS Appl. Mater. Interfaces* **5**(23), 12541 (2013).
29. X. Sun, Q. Li, J. Huang, J. Jian, P. Lu, X. Zhang, J. L. Macmanus-Driscoll, and H. Wang: Strain and property tuning of the 3D framed epitaxial nanocomposite thin films via interlayer thickness variation. *J. Appl. Phys.* **125**(8), 082530 (2019).

30. M. Fan, H. Wang, S. Misra, B. Zhang, Z. Qi, X. Sun, J. Huang, and H. Wang: Microstructure, Magnetic, and Magnetoresistance Properties of La<sub>0.7</sub>Sr<sub>0.3</sub>MnO<sub>3</sub>:CuO Nanocomposite Thin Films. *ACS Appl. Mater. Interfaces* **10**, 5779 (2018).
31. W. Zhang, L. Li, P. Lu, M. Fan, Q. Su, F. Khatkhatay, A. Chen, Q. Jia, X. Zhang, J. L. Macmanus-driscoll, and H. Wang: Perpendicular Exchange-Biased Magnetotransport at the Vertical Heterointerfaces in La<sub>0.7</sub>Sr<sub>0.3</sub>MnO<sub>3</sub>:NiO Nanocomposites. *ACS Appl. Mater. Interfaces* **7**, 21646 (2015).
32. J. Huang, Z. Qi, L. Li, H. Wang, S. Xue, B. Zhang, X. Zhang, and H. Wang: Self-assembled vertically aligned Ni nanopillars in CeO<sub>2</sub> with anisotropic magnetic and transport properties for energy applications. *Nanoscale* **10**(36), 17182 (2018).
33. F. Vidal, Y. Zheng, P. Schio, F. J. Bonilla, M. Barturen, J. Milano, D. Demaille, E. Fonda, A. J. A. De Oliveira, and V. H. Etgens: Mechanism of localization of the magnetization reversal in 3 nm wide Co nanowires. *Phys. Rev. Lett.* **109**(11), 117205 (2012).
34. Q. Su, W. Zhang, P. Lu, S. Fang, F. Khatkhatay, J. Jian, L. Li, and H. Wang: Self-Assembled Magnetic Metallic Nanopillars in Ceramic Matrix with Anisotropic Magnetic and Electrical Transport Properties. *ACS Appl. Mater. Interfaces* **8**, 20283(2016).
35. J. Huang, L. Li, P. Lu, Z. Qi, X. Sun, X. Zhang, and H. Wang: Self-assembled Co–BaZrO<sub>3</sub> nanocomposite thin films with ultra-fine vertically aligned Co nanopillars. *Nanoscale* **9**, 7970 (2017).
36. B. Zhang, J. Huang, B. Rutherford, P. Lu, S. Misra, M. Kalaswad, Z. He, X. Gao, X. Sun, L. Li, and H. Wang: Tunable room temperature multiferroic Fe-BaTiO<sub>3</sub> vertically aligned nanocomposite with perpendicular magnetic anisotropy. *Mater. Today Nano* **11**, 100083 (2020).
37. X. Weng, M. Hennes, A. Coati, A. Vlad, Y. Garreau, M. Sauvage-Simkin, E. Fonda, G. Patriarche, D. Demaille, F. Vidal, and Y. Zheng: Ultrathin Ni nanowires embedded in SrTiO<sub>3</sub>: Vertical epitaxy, strain relaxation mechanisms, and solid-state amorphization. *Phys. Rev. Mater.* **2**(10), 106003 (2018).
38. W. Zhang, A. Chen, J. Jian, Y. Zhu, L. Chen, P. Lu, Q. Jia, J. L. Macmanus-driscoll, X. Zhang, and H. Wang: Strong perpendicular exchange bias in epitaxial La<sub>0.7</sub>Sr<sub>0.3</sub>MnO<sub>3</sub>:BiFeO<sub>3</sub> nanocomposite films through vertical interfacial coupling. *Nanoscale* **7**, 13808 (2015).

39. J. Jian, X. Wang, S. Misra, X. Sun, Z. Qi, X. Gao, J. Sun, A. Donohue, D. G. Lin, V. Pol, J. Youngblood, H. Wang, L. Li, J. Huang, and H. Wang: Broad Range Tuning of Phase Transition Property in VO<sub>2</sub> Through Metal-Ceramic Nanocomposite Design. *Adv. Funct. Mater.* **29**, 1903690 (2019).
40. J. Huang, T. Jin, S. Misra, H. Wang, Z. Qi, Y. Dai, X. Sun, L. Li, J. Okkema, H. Chen, P. Lin, X. Zhang, and H. Wang: Tailorable Optical Response of Au – LiNbO<sub>3</sub> Hybrid Metamaterial Thin Films for Optical Waveguide Applications. *Adv. Opt. Mater.* **6**, 1800510 (2018).
41. L. Li, L. Sun, J. S. Gomez-Diaz, N. L. Hogan, P. Lu, F. Khatkhatay, W. Zhang, J. Jian, J. Huang, Q. Su, M. Fan, C. Jacob, J. Li, X. Zhang, Q. Jia, M. Sheldon, A. Alù, X. Li, and H. Wang: Self-assembled epitaxial Au-oxide vertically aligned nanocomposites for nanoscale metamaterials. *Nano Lett.* **16**(6), 3936 (2016).
42. J. Huang, X. Wang, X. L. Phuah, P. Lu, Z. Qi, and H. Wang: Plasmonic Cu nanostructures in ZnO as hyperbolic metamaterial thin films. *Mater. Today Nano* **8**, 100052 (2019).
43. R. L. Paldi, X. Sun, X. Wang, X. Zhang, and H. Wang: Strain-Driven In-plane Ordering in Vertically Aligned ZnO–Au Nanocomposites with Highly Correlated Metamaterial Properties. *ACS Omega* **5**, 2234 (2020).
44. R. Comes, H. Liu, M. Khokhlov, R. Kasica, J. Lu, and S. A. Wolf: Directed Self-Assembly of Epitaxial CoFe<sub>2</sub>O<sub>4</sub> – BiFeO<sub>3</sub> Multiferroic Nanocomposites. *Nano Lett.* **12**, 2367 (2012).
45. X. Sun, J. Huang, J. Jian, M. Fan, H. Wang, Q. Li, J. L. Macmanus-Driscoll, P. Lu, X. Zhang, and H. Wang: Three-dimensional strain engineering in epitaxial vertically aligned nanocomposite thin films with tunable magnetotransport properties. *Mater. Horizons* **5**, 536 (2018).
46. A. Chen, W. Zhang, F. Khatkhatay, Q. Su, C. F. Tsai, L. Chen, Q. X. Jia, J. L. Macmanus-Driscoll, and H. Wang: Magnetotransport properties of quasi-one-dimensionally channeled vertically aligned heteroepitaxial nanomazes. *Appl. Phys. Lett.* **102**(9), 093114 (2013).
47. S. Lee and J. L. MacManus-Driscoll: Research Update: Fast and tunable nanoionics in vertically aligned nanostructured films. *APL Mater.* **5**(4), 042304 (2017).
48. A. Fujishima and K. Honda: Electrochemical Photolysis of Water at a Semiconductor Electrode. *Nature* **238**(5358), 37 (1972).

49. S. U. M. Khan, M. Al-Shahry, and W. B. Ingler Jr.: Efficient Photochemical Water Splitting by a Chemically Modified n-TiO<sub>2</sub>. *Science* **297**(5590), 2243 (2002).
50. A. Mills, R. H. Davies, and D. Worsley: Water purification by semiconductor photocatalysis. *Chem. Soc. Rev.* **22**(6), 417 (1993).
51. Y. Zhang, Z.-R. Tang, X. Fu, and Y.-J. Xu: TiO<sub>2</sub>–Graphene Nanocomposites for Gas-Phase Photocatalytic Degradation of Volatile Aromatic Pollutant: Is TiO<sub>2</sub>–Graphene Truly Different from Other TiO<sub>2</sub>–Carbon Composite Materials? *ACS Nano* **4**(12), 7303 (2010).
52. U. Bach, D. Lupo, P. Comte, J. E. Moser, F. Weissörtel, J. Salbeck, H. Spreitzer, and M. Grätzel: Solid-State dye-sensitized mesoporous TiO<sub>2</sub> solar cells with high photon-to-electron conversion efficiencies. *Nature* **395**, 583 (1998).
53. D. B. Strukov, G. S. Snider, D. R. Stewart, and R. S. Williams: The missing memristor found. *Nature* **453**(7191), 80 (2008).
54. B. Karunagaran, P. Uthirakumar, S. J. Chung, S. Velumani, and E.-K. Suh: TiO<sub>2</sub> thin film gas sensor for monitoring ammonia. *Mater. Charact.* **58**(8–9), 680 (2007).
55. P. Bonhote, E. Gogniat, M. Gratzel, and P. . Ashrit: Novel electrochromic devices based on complementary nanocrystalline TiO<sub>2</sub> and WO<sub>3</sub> thin films. *Thin Solid Films* **350**(1), 269 (1999).
56. C. Euvananont, C. Junin, K. Inpor, P. Limthongkul, and C. Thanachayanont: TiO<sub>2</sub> optical coating layers for self-cleaning applications. *Ceram. Int.* **34**(4), 1067 (2008).
57. A. Jaroenworuluck, W. Sunsaneeyametha, N. Kosachan, and R. Stevens: Characteristics of silica-coated TiO<sub>2</sub> and its UV absorption for sunscreen cosmetic applications. *Surf. Interface Anal.* **38**, 473 (2006).
58. D. Hicks, M. J. Mehl, E. Gossett, C. Toher, O. Levy, R. M. Hanson, G. Hart, and S. Curtarolo: The AFLOW Library of Crystallographic Prototypes: Part 2. *Comput. Mater. Sci.* **161**, S1 (2019).
59. M. J. Mehl, D. Hicks, C. Toher, O. Levy, R. M. Hanson, G. Hart, and S. Curtarolo: The AFLOW Library of Crystallographic Prototypes: Part 1. *Comput. Mater. Sci.* **136**, S1 (2017).
60. J. Tian, Y. Sang, G. Yu, H. Jiang, X. Mu, and H. Liu: A Bi<sub>2</sub>WO<sub>6</sub>-based hybrid photocatalyst with broad spectrum photocatalytic properties under UV, visible, and near-infrared irradiation. *Adv. Mater.* **25**(36), 5075 (2013).

61. L. Liang, X. Kang, Y. Sang, and H. Liu: One-Dimensional Ferroelectric Nanostructures : Synthesis , Properties , and Applications. *Adv. Sci.* **3**, 1500358 (2016).
62. Y. L. Li and L. Q. Chen: Temperature-strain phase diagram for BaTiO<sub>3</sub> thin films. *Appl. Phys. Lett.* **88**, 072905 (2006).
63. W. Merz: The Dielectric Behavior of BaTiO<sub>3</sub> Single- Domain Crystals. *Phys. Rev.* **75**, 687 (1948).
64. A. von Hippel: Ferroelectricity, Domain Structure, and Phase Transitions of Barium Titanate. *Rev. Mod. Phys.* **22**(3), 221 (1950).
65. P. J. P. Espitia, N. de F. F. Soares, J. S. dos R. Coimbra, N. J. de Andrade, R. S. Cruz, and E. A. A. Medeiros: Zinc Oxide Nanoparticles: Synthesis, Antimicrobial Activity and Food Packaging Applications. *Food Bioprocess Technol.* **5**(5), 1447 (2012).
66. L. Schmidt-mende and J. L. Macmanus-driscoll: ZnO – nanostructures, defects, and devices. *Mater. Today* **10**(5), 40 (2007).
67. A. Janotti and C. G. Van De Walle: Fundamentals of zinc oxide as a semiconductor. *Reports Prog. Phys.* **72**, 126501 (2009).
68. R. E. Cohen: Origin of ferroelectricity in perovskite oxides. *Nature* **358**, 136 (1992).
69. A. F. Devonshire: Theory of ferroelectrics. *Adv. Phys.* **3**, 85 (1954).
70. W. Merz: The Dielectric Behavior of BaTiO<sub>3</sub> Single- Domain Crystals. *Phys. Rev.* **75**(687) (1949).
71. H. Moriwake, C. A. J. Fisher, A. Kuwabara, and T. Hashimoto: Anisotropic Permittivity of Tetragonal BaTiO<sub>3</sub> : A First-Principles Study. *Jpn. J. Appl. Phys.* **50**, 09NE02 (2011).
72. M. Han, M. S. J. Marshall, L. Wu, M. A. Schofield, T. Aoki, R. Twosten, J. Hoffman, F. J. Walker, C. H. Ahn, and Y. Zhu: Interface-induced nonswitchable domains in ferroelectric thin film. *Nat. Commun.* **5**, 4693 (2014).
73. L. Jiang, Z. Liang, J. Sun, Y. Jiang, and L. Jiang: Plasmonic Enhanced Optoelectronic Devices. *Plasmonics* **9**, 859 (2014).
74. B. W. A. Murray and W. L. Barnes: Plasmonic Materials. *Adv. Mater.* **19**, 3771 (2007).
75. M. Rycenga, C. M. Cobley, J. Zeng, W. Li, C. H. Moran, Q. Zhang, D. Qin, and Y. Xia: Controlling the Synthesis and Assembly of Silver Nanostructures for Plasmonic Applications. *Chem. Rev.* **111**, 3669 (2011).

76. H. A. R. Eddy, U. R. G. Uler, A. L. V. K. Ildishev, A. L. B. Oltasseva, and V. L. M. S. Halaev: Temperature-dependent optical properties of gold thin films. *Opt. Mater. Lett.* **6**(9), 2776 (2016).
77. A. Naldoni, U. Guler, Z. Wang, M. Marelli, F. Malara, X. Meng, L. V Besteiro, A. O. Govorov, A. V Kildishev, A. Boltasseva, and V. M. Shalaev: Broadband Hot-Electron Collection for Solar Water Splitting with Plasmonic Titanium Nitride. *Adv. Opt. Mater.* **5**(15), 1601031 (2017).
78. D. B. Ingram and S. Linic: Water splitting on composite plasmonic-metal/semiconductor photoelectrodes: Evidence for selective plasmon-induced formation of charge carriers near the semiconductor surface. *J. Am. Chem. Soc.* **133**(14), 5202 (2011).
79. Z. Zhang, L. Zhang, M. N. Hedhili, H. Zhang, and P. Wang: Plasmonic Gold Nanocrystals Coupled with Photonic Crystal Seamlessly on TiO<sub>2</sub> Nanotube Photoelectrodes for Efficient Visible Light Photoelectrochemical Water Splitting. *Nano Lett.* **13**, 14 (2013).
80. S. Linic, P. Christopher, and D. B. Ingram: Plasmonic-metal nanostructures for efficient conversion of solar to chemical energy. *Nat. Mater.* **10**(12), 911 (2011).
81. J. A. Schuller, E. S. Barnard, W. Cai, Y. C. Jun, J. S. White, and M. L. Brongersma: Plasmonics for extreme light concentration and manipulation. *Nat. Mater.* **9**(3), 193 (2010).
82. H. A. Atwater and A. Polman: Plasmonics for improved photovoltaic devices. *Nat. Mater.* **9**(3), 205 (2010).
83. S. Tan, A. Argondizzo, J. Ren, L. Liu, J. Zhao, and H. Petek: Plasmonic coupling at a metal/semiconductor interface. *Nat. Photonics* **11**, 806 (2017).
84. Z. Liu, H. Lee, Y. Xiong, C. Sun, and X. Zhang: Far-Field Optical Hyperlens Magnifying. *Science* **315**, 1686 (2007).
85. N. Fang, H. Lee, C. Sun, and X. Zhang: Sub-Diffraction-Limited Optical Imaging with a Silver Superlens. *Science* **308**, 534 (2005).
86. J. Yao, Z. Liu, Y. Liu, Y. Wang, C. Sun, G. Bartal, A. M. Stacy, and X. Zhang: Optical Negative Refraction in Bulk Metamaterials of Nanowires. *Science* **321**(5891), 930 (2008).
87. S. Zhang, W. Fan, N. C. Panoiu, K. J. Malloy, R. M. Osgood, and S. R. J. Brueck: Experimental Demonstration of Near-Infrared Negative-Index Metamaterials. *Phys. Rev. Lett.* **95**, 137404 (2005).

88. R. A. Shelby, D. R. Smith, and S. Schultz: Experimental Verification of a Negative Index of Refraction. *Science* **292**, 77 (2001).
89. D. R. Smith and D. Schurig: Electromagnetic Wave Propagation in Media with Indefinite Permittivity and Permeability Tensors. *Phys. Rev. Lett.* **90**, 5 (2003).
90. A. Poddubny, I. Iorsh, P. Belov, and Y. Kivshar: Hyperbolic metamaterials. *Nat. Photonics* **7**, 958 (2013).
91. E. E. Narimanov and A. V Kildishev: Naturally hyperbolic. *Nat. Photonics* **9**, 214 (2015).
92. L. Caspani, R. P. M. Kaipurath, M. Clerici, M. Ferrera, T. Roger, J. Kim, N. Kinsey, M. Pietrzyk, A. Di Falco, V. M. Shalaev, A. Boltasseva, and D. Faccio: Enhanced Nonlinear Refractive Index in  $\epsilon$ -Near-Zero Materials. *Phys. Rev. Lett.* **116**(23), 233901 (2016).
93. M. Z. Alam, I. De Leon, and R. W. Boyd: Large optical nonlinearity of indium tin oxide in its epsilon-near-zero region. *Science* **352**(6287), 795 (2016).
94. P. P. Iyer, M. Pendharkar, C. J. Palmstrøm, and J. A. Schuller: Ultrawide thermal free-carrier tuning of dielectric antennas coupled to epsilon-near-zero substrates. *Nat. Commun.* **8**(1), 2 (2017).
95. M. E. Nasir, S. Peruch, N. Vasilantonakis, W. P. Wardley, W. Dickson, G. A. Wurtz, and A. V. Zayats: Tuning the effective plasma frequency of nanorod metamaterials from visible to telecom wavelengths. *Appl. Phys. Lett.* **107**, 121110 (2015).
96. D. Zhang, S. Misra, L. Li, X. Wang, J. Jian, P. Lu, X. Gao, X. Sun, Z. Qi, M. Kalaswad, X. Zhang, and H. Wang: Tunable Optical Properties in Self-Assembled Oxide-Metal Hybrid Thin Films via Au-Phase Geometry Control: From Nanopillars to Nanodisks. *Adv. Opt. Mater.* **8**, 1901359 (2019).
97. S. Cho, J. Jang, L. Li, J. Jian, H. Wang, and J. L. Macmanus-driscoll: Self-Assembled Heteroepitaxial Oxide Nanocomposite for Photoelectrochemical Solar Water Oxidation. *Chem. Mater.* **28**, 3017 (2016).
98. J. Jian, X. Wang, L. Li, M. Fan, W. Zhang, J. Huang, Z. Qi, and H. Wang: Continuous Tuning of Phase Transition Temperature in VO<sub>2</sub> Thin Films on c - Cut Sapphire Substrates via Strain Variation. *ACS Appl. Mater. Interfaces* **9**, 5319 (2017).
99. J. Kim, Y. Kim, Y. S. Kim, J. L. Kim, D. Jung, J. Kim, Y. Kim, Y. S. Kim, and J. Lee: Large nonlinear dielectric properties of artificial superlattices Large nonlinear dielectric properties of artificial BaTiO<sub>3</sub>/SrTiO<sub>3</sub> superlattices. *Appl. Phys. Lett.* **80**, 3581 (2002).

100. L. Li, P. Boullay, J. Cheng, P. Lu, X. Wang, G. Steciuk, J. Huang, J. Jian, X. Gao, B. Zhang, S. Misra, X. Zhang, K. Yang, and H. Wang: Self-assembled two-dimensional layered oxide supercells with modulated layer stacking and tunable physical properties. *Mater. Today Nano* **6**, 100037 (2019).
101. L. Li, P. Boullay, P. Lu, X. Wang, J. Jian, J. Huang, X. Gao, S. Misra, W. Zhang, O. Perez, G. Steciuk, A. Chen, X. Zhang, and H. Wang: Novel Layered Supercell Structure from Bi<sub>2</sub>AlMnO<sub>6</sub> for Multifunctionalities. *Nano Lett.* **17**(11), 6575 (2017).
102. S. Misra, L. Li, X. Gao, J. Jian, Z. Qi, D. Zemlyanov, and H. Wang: Tunable physical properties in BiAl<sub>1-x</sub>Mn<sub>x</sub>O<sub>3</sub> thin films with novel layered supercell structures. *Nanoscale Adv.* **2**, 315 (2020).
103. K. Au, X. S. Gao, J. Wang, Z. Y. Bao, J. M. Liu, and J. Y. Dai: Enhanced resistive switching effect in Ag nanoparticle embedded BaTiO<sub>3</sub> thin films. *J. Appl. Phys.* **114**, 027019 (2013).
104. V. Schuler, F. J. Bonilla, D. Demaille, A. Coati, A. Vlad, Y. Garreau, M. Sauvage-Simkin, A. Novikova, E. Fonda, S. Hidki, V. Etgens, F. Vidal, and Y. Zheng: Huge metastable axial strain in ultrathin heteroepitaxial vertically aligned nanowires. *Nano Res.* **8**(6), 1964 (2015).
105. S. Misra, L. Li, J. Jian, J. Huang, X. Wang, D. Zemlyanov, J.-W. Jang, F. H. Ribeiro, and H. Wang: Tailorable Au Nanoparticles Embedded in Epitaxial TiO<sub>2</sub> Thin Films for Tunable Optical Properties. *ACS Appl. Mater. Interfaces* **10**, 32895 (2018).
106. S. Misra, L. Li, D. Zhang, J. Jian, Z. Qi, M. Fan, H. Chen, X. Zhang, and H. Wang: Self-Assembled Ordered Three-Phase Au – BaTiO<sub>3</sub> – ZnO Vertically Aligned Nanocomposites Achieved by a Templating Method. *Adv. Mater.* **31**, 1806529 (2018).
107. I. Fasaki, M. Kandyla, and M. Kompitsas: Properties of pulsed laser deposited nanocomposite NiO:Au thin films for gas sensing applications. *Appl. Phys. A Mater. Sci. Process.* **107**(4), 899 (2012).
108. I. Fasaki, M. Kandyla, M. G. Tsoutsouva, and M. Kompitsas: Optimized hydrogen sensing properties of nanocomposite NiO:Au thin films grown by dual pulsed laser deposition. *Sensors Actuators, B Chem.* **176**, 103 (2013).
109. S. Kawasaki, R. Takahashi, T. Yamamoto, M. Kobayashi, H. Kumigashira, J. Yoshinobu, F. Komori, A. Kudo, and M. Lippmaa: Photoelectrochemical water splitting enhanced by self-assembled metal nanopillars embedded in an oxide semiconductor photoelectrode. *Nat. Commun.* **7**, 11818 (2016).

110. V. Schuler, J. Milano, A. Coati, A. Vlad, M. Sauvage-Simkin, Y. Garreau, D. Demaille, S. Hidki, A. Novikova, E. Fonda, Y. Zheng, and F. Vidal: Growth and magnetic properties of vertically aligned epitaxial CoNi nanowires in (Sr, Ba)TiO<sub>3</sub> with diameters in the 1.8-6 nm range. *Nanotechnology* **27**, 495601 (2016).
111. P. Schio, F. Vidal, Y. Zheng, J. Milano, E. Fonda, D. Demaille, B. Vodungbo, J. Varalda, A. J. A. De Oliveira, and V. H. Etgens: Magnetic response of cobalt nanowires with diameter below 5 nm. *Phys. Rev. B - Condens. Matter Mater. Phys.* **82**(9), 094436 (2010).
112. M. Kahl, E. Voges, S. Kostrewa, C. Viets, and W. Hill: Periodically structured metallic substrates for SERS. *Sensors Actuators, B Chem.* **51**(1–3), 285 (1998).
113. M. Song and K. Furuya: Fabrication and characterization of nanostructures on insulator substrates by electron-beam-induced deposition. *Sci. Technol. Adv. Mater.* **9**(2), 023002 (2008).
114. Z. J. Zhao, S. H. Hwang, S. Jeon, B. Hwang, J. Y. Jung, J. Lee, S. H. Park, and J. H. Jeong: Three-dimensional plasmonic Ag/TiO<sub>2</sub> nanocomposite architectures on flexible substrates for visible-light photocatalytic activity. *Sci. Rep.* **7**(1), 8915 (2017).
115. A. Revaux, G. Dantelle, D. Decanini, A. M. Haghiri-Gosnet, T. Gacoin, and J. P. Boilot: Synthesis of YAG:Ce/TiO<sub>2</sub> nanocomposite films. *Opt. Mater. (Amst).* **33**(7), 1124 (2011).
116. D. Wang, R. Kou, D. Choi, Z. Yang, Z. Nie, J. Li, L. V. Saraf, D. Hu, J. Zhang, G. L. Graff, J. Liu, M. A. Pope, and I. A. Aksay: Ternary self-assembly of ordered metal oxide-graphene nanocomposites for electrochemical energy storage. *ACS Nano* **4**(3), 1587 (2010).
117. J. F. Lin, J. P. Bird, L. Rotkina, and P. A. Bennett: Classical and quantum transport in focused-ion-beam-deposited Pt nanointerconnects. *Appl. Phys. Lett.* **82**(5), 802 (2003).
118. S. Y. Chou and P. R. Krauss: Imprint lithography with sub-10 nm feature size and high throughput. *Microelectron. Eng.* **35**(1–4), 237 (1997).
119. M. Lee, S. Hong, and D. Kim: Chemical-free synthesis of electrically connected gold nanotubes/ nanoparticles from solution-infiltrated anodized aluminum oxide template. *Appl. Phys. Lett.* **89**(4), 043120 (2006).
120. L. Wen, R. Xu, Y. Mi, and Y. Lei: Multiple nanostructures based on anodized aluminium oxide templates. *Nat. Nanotechnol.* **12**(3), 244 (2017).

121. J. Huang, L. Li, P. Lu, Z. Qi, X. Sun, X. Zhang, and H. Wang: Self-assembled Co-BaZrO<sub>3</sub> nanocomposite thin films with ultra-fine vertically aligned Co nanopillars. *Nanoscale* **9**(23), 7970 (2017).
122. B. Schwarz, P. Reininger, D. Ristanić, H. Detz, A. M. Andrews, W. Schrenk, and G. Strasser: Monolithically integrated mid-infrared lab-on-a-chip using plasmonics and quantum cascade structures. *Nat. Commun.* **5**, 4085 (2014).
123. R. F. Aroca: Plasmon enhanced spectroscopy. *Phys. Chem. Chem. Phys.* **15**(15), 5355 (2013).
124. M. Fiebig, T. Lottermoser, D. Meier, and M. Trassin: The evolution of multiferroics. *Nat. Rev. Mater.* **1**(8), 1 (2016).
125. S. K. Gray: Surface plasmon-enhanced spectroscopy and photochemistry. *Plasmonics* **2**(3), 143 (2007).
126. L. Baldassarre, E. Sakat, J. Frigerio, A. Samarelli, K. Gallacher, E. Calandrini, G. Isella, D. J. Paul, M. Ortolani, and P. Biagioni: Midinfrared Plasmon-Enhanced Spectroscopy with Germanium Antennas on Silicon Substrates. *Nano Lett.* **15**(11), 7225 (2015).
127. C. L. Haynes and R. P. Van Duyne: Plasmon-sampled surface-enhanced Raman excitation spectroscopy. *J. Phys. Chem. B* **107**(30), 7426 (2003).
128. Y. Zhang, K. Aslan, M. J. R. Previte, and C. D. Geddes: Metal-enhanced fluorescence: Surface plasmons can radiate a fluorophore's structured emission. *Appl. Phys. Lett.* **90**(5), 053107 (2007).
129. C. K. Chen, A. R. B. de Castro, and Y. R. Shen: Surface-Enhanced Second-Harmonic Generation. *Phys. Rev. Lett.* **46**(2), 145 (1981).
130. T. Liebermann and W. Knoll: Surface-plasmon field-enhanced fluorescence spectroscopy. *Colloids Surfaces A Physicochem. Eng. Asp.* **171**(1–3), 115 (2000).
131. X. Sun, Q. Li, J. Huang, M. Fan, B. X. Rutherford, R. L. Paldi, J. Jian, X. Zhang, and H. Wang: Strain-driven nanodumbbell structure and enhanced physical properties in hybrid vertically aligned nanocomposite thin films. *Appl. Mater. Today* **16**, 204 (2019).
132. Q. Su, W. Zhang, P. Lu, S. Fang, F. Khatkhatay, J. Jian, L. Li, F. Chen, X. Zhang, J. L. MacManus-Driscoll, A. Chen, Q. Jia, and H. Wang: Self-Assembled Magnetic Metallic Nanopillars in Ceramic Matrix with Anisotropic Magnetic and Electrical Transport Properties. *ACS Appl. Mater. Interfaces* **8**, 20283 (2016).

133. S. Zhao, Y. Zhou, K. Zhao, Z. Liu, P. Han, S. Wang, W. Xiang, Z. Chen, H. Lü, B. Cheng, and G. Yang: Violet luminescence emitted from Ag-nanocluster doped ZnO thin films grown on fused quartz substrates by pulsed laser deposition. *Phys. B Condens. Matter* **373**(1), 154 (2006).
134. T. Sasaki, N. Koshizaki, J. W. Yoon, and K. M. Beck: Preparation of Pt/TiO<sub>2</sub> nanocomposite thin films by pulsed laser deposition and their photoelectrochemical behaviors. *J. Photochem. Photobiol. A Chem.* **145**(1–2), 11 (2001).
135. Z. Qi, J. Jian, J. Huang, J. Tang, H. Wang, V. G. Pol, and H. Wang: LiNi<sub>0.5</sub>Mn<sub>0.3</sub>Co<sub>0.2</sub>O<sub>2</sub>/Au nanocomposite thin film cathode with enhanced electrochemical properties. *Nano Energy* **46**, 290 (2018).
136. M. Lee, R. Arras, R. Takahashi, B. Warot-Fonrose, H. Daimon, M. J. Casanove, and M. Lippmaa: Noble Metal Nanocluster Formation in Epitaxial Perovskite Thin Films. *ACS Omega* **3**(2), 2169 (2018).
137. H. L. Skriver and N. M. Rosengaard: Surface energy and work function of elemental metals. *Phys. Rev. B* **46**(11), 7157 (1992).
138. K. Ikemiya, Y. Hirose, and T. Hasegawa: Fabrication and magnetic properties of fcc-Co nanorods embedded in epitaxial thin films of anatase TiO<sub>2</sub> as a transparent matrix. *J. Phys. Chem. C* **115**(5), 1776 (2011).
139. B. Zhang, M. Fan, L. Li, J. Jian, J. Huang, H. Wang, M. Kalaswad, and H. Wang: Tunable magnetic anisotropy of self-assembled Fe nanostructures. *Appl. Phys. Lett.* **112**, 013104 (2018).
140. F. J. Bonilla, A. Novikova, F. Vidal, Y. Zheng, E. Fonda, D. Demaille, V. Schuler, A. Coati, A. Vlad, Y. Garreau, M. Sauvage Simkin, Y. Dumont, S. Hidki, and V. Etgens: Combinatorial growth and anisotropy control of self-assembled epitaxial ultrathin alloy nanowires. *ACS Nano* **7**(5), 4022 (2013).
141. B. Zhang, J. Huang, J. Jian, B. X. Rutherford, L. Li, S. Misra, X. Sun, and H. Wang: Tuning magnetic anisotropy in Co-BaZrO<sub>3</sub> vertically aligned nanocomposites for memory device integration. *Nanoscale Adv.* **1**(11), 4450 (2019).
142. F. Vidal, Y. Zheng, J. Milano, D. Demaille, P. Schio, E. Fonda, and B. Vodungbo: Nanowires formation and the origin of ferromagnetism in a diluted magnetic oxide. *Appl. Phys. Lett.* **95**(15), 93 (2009).

143. R. K. Singh, O. W. Holland, and J. Narayan: Theoretical model for deposition of superconducting thin films using pulsed laser evaporation technique. *J. Appl. Phys.* **68**(1), 233 (1990).
144. J. Als-Nielsen and D. McMorrow: Elements of Modern X-Ray Physics (2011).
145. D. B. Williams and C. B. Carter: Transmission Electron Microscopy (2009).
146. <https://www.keysight.com/main/editorial.jsp?ckey=1774141&lc=eng&cc=US>: (n.d.).
147. D. Seol, B. Kim, and Y. Kim: Non-piezoelectric effects in piezoresponse force microscopy. *Curr. Appl. Phys.* **17**(5), 661 (2017).
148. <https://www.perkinelmer.com/product/lambda-1050-2d-system-l6020056>: (n.d.).
149. Y. Nishijima, K. Ueno, Y. Yokota, K. Murakoshi, and H. Misawa: Plasmon-Assisted Photocurrent Generation from Visible to Near-Infrared Wavelength Using a Au-Nanorods/TiO<sub>2</sub> Electrode. *J. Phys. Chem. Lett.* **1**, 2031 (2010).
150. Z. W. Seh, S. Liu, M. Low, S. Zhang, and Z. Liu: Janus Au-TiO<sub>2</sub> Photocatalysts with Strong Localization of Plasmonic Near-Fields for Efficient Visible-Light Hydrogen Generation. *Adv. Mater.* **24**, 2310 (2012).
151. Z. Xu, Y. Lin, M. Yin, H. Zhang, C. Cheng, L. Lu, X. Xue, H. J. Fan, X. Chen, and D. Li: Understanding the Enhancement Mechanisms of Surface Plasmon-Mediated Photoelectrochemical Electrodes: A Case Study on Au Nanoparticle Decorated TiO<sub>2</sub> Nanotubes. *Adv. Mater. Interfaces* **2**, 1500169 (2015).
152. H. Shi, X. Wang, M. Zheng, X. Wu, Y. Chen, and Z. Yang: Hot-Electrons Mediated Efficient Visible-Light Photocatalysis of Hierarchical Black Au-TiO<sub>2</sub> Nanorod Arrays on Flexible Substrate. *Adv. Mater. Interfaces* **3**, 1600588 (2016).
153. A. Kuzyk, R. Schreiber, H. Zhang, A. O. Govorov, T. Liedl, and N. Liu: Reconfigurable 3D plasmonic metamolecules. *Nat. Mater.* **13**(9), 862 (2014).
154. W. Cai, U. K. Chettiar, A. V. Kildishev, and V. M. Shalaev: Optical cloaking with metamaterials. *Nat. Photonics* **1**(4), 224 (2007).
155. D. E. Chang, A. S. Sorensen, P. R. Hemmer, and M. D. Lukin: Quantum optics with surface plasmons. *Phys. Rev. Lett.* **97**, 053002 (2006).
156. O. Neumann, A. D. Neumann, E. Silva, C. Ayala-Orozco, S. Tian, P. Nordlander, and N. J. Halas: Nanoparticle-mediated, light-induced phase separations. *Nano Lett.* **15**(12), 7880 (2015).

157. L. Zhou, Y. Tan, J. Wang, W. Xu, Y. Yuan, W. Cai, S. Zhu, and J. Zhu: 3D self-assembly of aluminium nanoparticles for plasmon-enhanced solar desalination. *Nat. Photonics* **10**(6), 393 (2016).
158. S. Mubeen, G. Hernandez-sosa, D. Moses, J. Lee, and M. Moskovits: Plasmonic Photosensitization of a Wide Band Gap Semiconductor : Converting Plasmons to Charge Carriers. *Nano Lett.* **11**, 5548 (2011).
159. D. C. Ratchford, A. D. Dunkelberger, I. Vurgaftman, C. Owrutsky, and P. E. Pehrsson: Quantification of Efficient Plasmonic Hot-Electron Injection in Gold Nanoparticle – TiO<sub>2</sub> Films. *Nano Lett.* **17**, 6047 (2017).
160. V. Subramanian, E. E. Wolf, and P. V Kamat: Influence of Metal / Metal Ion Concentration on the Photocatalytic Activity of TiO<sub>2</sub>-Au Composite Nanoparticles. *Langmuir* **19**, 469 (2003).
161. A. Tanaka, A. Ogino, M. Iwaki, K. Hashimoto, A. Ohnuma, F. Amano, B. Ohtani, and H. Kominami: Gold – Titanium ( IV ) Oxide Plasmonic Photocatalysts Prepared by a Colloid-Photodeposition Method: Correlation Between Physical Properties and Photocatalytic Activities. *Langmuir* **28**, 13105 (2012).
162. H. Tang, Y. Su, B. Zhang, A. F. Lee, M. A. Isaacs, K. Wilson, L. Li, Y. Ren, J. Huang, M. Haruta, B. Qiao, X. Liu, C. Jin, D. Su, J. Wang, and T. Zhang: Classical strong metal – support interactions between gold nanoparticles and titanium dioxide. *Sci. Adv.* **3**, e1700231 (2017).
163. W. Zhang, R. Ramesh, J. L. MacManus-Driscoll, and H. Wang: Multifunctional, self-assembled oxide nanocomposite thin films and devices. *MRS Bull.* **40**(09), 736 (2015).
164. T. Luttrell, S. Halpegamage, J. Tao, A. Kramer, E. Sutter, and M. Batzill: Why is anatase a better photocatalyst than rutile? - Model studies on epitaxial TiO<sub>2</sub> films. *Sci. Rep.* **4**, 4043 (2014).
165. T. Yoshida, T. Watanabe, F. Kikuchi, T. Tabuchi, I. Umezu, and M. Haraguchi: Pulsed-laser-deposited TiO<sub>2</sub> nanocrystalline films supporting Au nanoparticles for visible-light-operating plasmonic photocatalysts. *Appl. Phys. A* **122**(5), 510 (2016).
166. L. Duta, C. Popescu, A. Popescu, M. Motoc, C. Logofatu, A. Enesca, A. Duta, and E. Gyorgy: Nitrogen-doped and gold-loaded TiO<sub>2</sub> photocatalysts synthesized by sequential reactive pulsed laser deposition. *Appl. Phys. A Mater. Sci. Process.* **117**(1), 97 (2014).

167. T. Walther: A new experimental procedure to quantify annular dark field images in scanning transmission electron microscopy. *J. Microsc.* **221**, 137 (2006).
168. X. L. Wu, G. G. Siu, C. L. Fu, and H. C. Ong: Photoluminescence and cathodoluminescence studies of stoichiometric and oxygen-deficient ZnO films. Photoluminescence and cathodoluminescence studies of stoichiometric and oxygen-deficient ZnO films. *Appl. Phys. Lett.* **78**, 2295 (2005).
169. Z. S. Fishman, B. Rudshiteyn, Y. He, B. Liu, S. Chaudhuri, M. Askerka, G. L. Haller, V. S. Batista, and L. D. Pfe: Fundamental Role of Oxygen Stoichiometry in Controlling the Band Gap and Reactivity of Cupric Oxide Nanosheets. *J. Am. Chem. Soc.* **138**, 10978 (2016).
170. E. P. O. Reilly: Valence band engineering in strained-layer structures. *Semicond. Sci. Technol.* **4**, 121 (1989).
171. A. Ali, I. Ruzybayev, E. Yassitepe, A. Karim, S. I. Shah, and A. S. Bhatti: Phase Transformations in the Pulsed Laser Deposition Grown TiO<sub>2</sub> Thin Films as a Consequence of O<sub>2</sub> Partial Pressure and Nd Doping. *J. Phys. Chem. C* **119**(21), 11578 (2015).
172. Y. Shen: Carbothermal synthesis of metal-functionalized nanostructures for energy and environmental applications. *J. Mater. Chem. A* **3**(25), 13114 (2015).
173. A. Vittadini and A. Selloni: Small gold clusters on stoichiometric and defected TiO<sub>2</sub> anatase (101) and their interaction with CO: A density functional study. *J. Chem. Phys.* **117**(1), 353 (2002).
174. A. Mahmood and S. I. Woo: Enhancement of catalytic activity of Au/TiO<sub>2</sub> by thermal and plasma treatment. *Korean J. Chem. Eng.* **30**(10), 1876 (2013).
175. N. Lopez, J. K. Nørskov, T. V. W. Janssens, A. Carlsson, A. Puig-Molina, B. S. Clausen, and J. D. Grunwaldt: The adhesion and shape of nanosized Au particles in a Au/TiO<sub>2</sub> catalyst. *J. Catal.* **225**(1), 86 (2004).
176. Y. Tian and T. Tatsuma: Mechanisms and Applications of Plasmon-Induced Charge Separation at TiO<sub>2</sub> Films Loaded with Gold Nanoparticles. *J. Am. Chem. Soc.* **127**(16), 7632 (2005).
177. A. Furube, L. Du, K. Hara, R. Katoh, and M. Tachiya: Ultrafast Plasmon-Induced Electron Transfer from Gold Nanodots into TiO<sub>2</sub> Nanoparticles. *J. Am. Chem. Soc.* **129**, 14852 (2007).

178. G. D. Stucky, M. Moskovits, S. Mubeen, J. Lee, N. Singh, and S. Kra: An autonomous photosynthetic device in which all charge carriers derive from surface plasmons. *Nat. Nanotechnol.* **8**, 247 (2013).
179. C. Binek and B. Doudin: Magneto-electronics with magnetoelectrics. *J. Phys. Condens. Matter* **17**, L39 (2005).
180. S. Biehs and M. Tschikin: Hyperbolic Metamaterials as an Analog of a Blackbody in the Near Field. *Phys. Rev. Lett.* **109**, 104301 (2012).
181. W. Zhang, J. Jian, A. Chen, L. Jiao, F. Khatkhatay, L. Li, F. Chu, Q. Jia, J. Macmanus-driscoll, and H. Wang: Strain relaxation and enhanced perpendicular magnetic anisotropy in BiFeO<sub>3</sub> : CoFe<sub>2</sub>O<sub>4</sub> vertically aligned nanocomposite thin films. *Appl. Phys. Lett.* **104**, 062402 (2014).
182. A. Chen, Z. Bi, C. Tsai, J. Lee, Q. Su, X. Zhang, Q. Jia, J. L. Macmanus-driscoll, and H. Wang: Tunable Low-Field Magnetoresistance in LSMO:ZnO Self-Assembled Vertically Aligned Nanocomposite Thin Films. *Adv. Funct. Mater.* **21**, 2423 (2011).
183. A. V Kabashin, P. Evans, S. Pastkovsky, W. Hendren, G. A. Wurtz, R. Atkinson, R. Pollard, V. A. Podolskiy, and A. V Zayats: Plasmonic nanorod metamaterials for biosensing. *Nat. Mater.* **8**(11), 867 (2009).
184. A. A. Goyadinov and V. A. Podolskiy: Metamaterial photonic funnels for subdiffraction light compression and propagation. *Phys. Rev. B* **73**, 155108 (2006).
185. N. M. Aimon, H. K. Choi, X. Y. Sun, D. H. Kim, and C. A. Ross: Templated Self-Assembly of Functional Oxide Nanocomposites. *Adv. Mater.* **26**, 3063 (2014).
186. S. Misra, L. Li, J. Jian, J. Huang, X. Wang, D. Zemlyanov, J. Jang, F. H. Ribeiro, and H. Wang: Tailorable Au Nanoparticles Embedded in Epitaxial TiO<sub>2</sub> Thin Films for Tunable Optical Properties. *ACS Appl. Mater. Interfaces* **10**, 32895 (2018).
187. J. Huang, X. Wang, N. L. Hogan, S. Wu, P. Lu, Z. Fan, Y. Dai, B. Zeng, R. Starko-bowes, J. Jian, H. Wang, L. Li, R. P. Prasankumar, D. Yarotski, M. Sheldon, H. Chen, Z. Jacob, X. Zhang, and H. Wang: Nanoscale Artificial Plasmonic Lattice in Self-Assembled Vertically Aligned Nitride – Metal Hybrid Metamaterials. *Adv. Sci.* **5**(7), 1800416 (2018).
188. C. R. Robbins, M. K. Reser, H. F. McMurdie, and E. M. Levin: Phase Diagrams for Ceramists (1964).

189. C. Borchers, S. Mu, D. Stichtenoth, D. Schwen, and C. Ronning: Catalyst - Nanostructure Interaction in the Growth of 1-D ZnO Nanostructures. *J. Phys. Chem. B* **110**, 1656 (2006).
190. M. A. Khan and S. Sakrani: Synthesis of Cu<sub>2</sub>O and ZnO Nanowires and their Heterojunction Nanowires by Thermal Evaporation : A Short Review Jurnal Teknologi. *J. Teknol.* **5**, 83 (2014).
191. X. Wang, C. J. Summers, and Z. L. Wang: Large-Scale Hexagonal-Patterned Growth of Aligned ZnO Nanorods for Nano-optoelectronics and Nanosensor Arrays. *Nano Lett.* **4**, 423 (2004).
192. Y. Ding, P. X. Gao, and Z. L. Wang: Catalyst - Nanostructure Interfacial Lattice Mismatch in Determining the Shape of VLS Grown Nanowires and Nanobelts : A Case of Sn / ZnO. *J. Am. Chem. Soc.* **126**, 2066 (2004).
193. X. Duan and C. M. Lieber: Laser-Assisted Catalytic Growth of Single Crystal GaN Nanowires. *J. Am. Chem. Soc.* **122**, 188 (2000).
194. X. Duan and C. M. Lieber: General Synthesis of Compound Semiconductor Nanowires. *Adv. Mater.* **12**, 298 (2000).
195. Y. Wang, V. Schmidt, S. Senz, and U. Gosele: Epitaxial growth of silicon nanowires using an aluminium catalyst. *Nat. Nanotechnol.* **1**, 186 (2006).
196. A. M. Morales and C. M. Lieber: A Laser Ablation Method for the Synthesis of Crystalline Semiconductor Nanowires. *Science* **279**, 208 (1998).
197. B. M. Kayes, M. A. Filler, M. C. Putnam, M. D. Kelzenberg, N. S. Lewis, and H. A. Atwater: Growth of vertically aligned Si wire arrays over large areas with Au and Cu catalysts. *Appl. Phys. Lett.* **91**, 103110 (2007).
198. Y. Shen, S. Turner, P. Yang, G. Van Tendeloo, O. I. Lebedev, and T. Wu: Epitaxy-Enabled Vapor – Liquid – Solid Growth of Tin-Doped Indium Oxide Nanowires with Controlled Orientations. *Nano Lett.* **14**, 4342 (2014).
199. Y. C. Kong, D. P. Yu, B. Zhang, W. Fang, S. Q. Feng, Y. C. Kong, D. P. Yu, B. Zhang, W. Fang, and S. Q. Feng: Ultraviolet-emitting ZnO nanowires synthesized by a physical vapor deposition approach Ultraviolet-emitting ZnO nanowires synthesized by a physical vapor deposition approach. *Appl. Phys. Lett.* **78**, 407 (2001).

200. M. H. Huang, S. Mao, H. Feick, H. Yan, Y. Wu, H. Kind, E. Weber, and R. Russo: Room-Temperature Ultraviolet Nanowire Nanolasers. *Science* **292**, 1897 (2001).
201. M. H. Huang, Y. Wu, H. Feick, N. Tran, E. Weber, and P. Yang: Catalytic Growth of Zinc Oxide Nanowires. *Adv. Mater.* **13**(2), 113 (2001).
202. Q. Yan, P. Rinke, A. Janotti, M. Scheffler, and C. G. Van De Walle: Effects of strain on the band structure of group-III nitrides. *Phys. Rev. B* **90**, 125118 (2014).
203. Y. C. Yang, C. Song, X. H. Wang, F. Zeng, and F. Pan: Giant piezoelectric d33 coefficient in ferroelectric vanadium doped ZnO films. *Appl. Phys. Lett.* **92**, 012907 (2008).
204. X. Liu, B. Du, Y. Sun, M. Yu, Y. Yin, W. Tang, C. Chen, L. Sun, B. Yang, W. Cao, and M. N. R. Ashfold: Sensitive Room Temperature Photoluminescence-Based Sensing of H<sub>2</sub>S with Novel CuO – ZnO Nanorods. *ACS Appl. Mater. Interfaces* **8**, 16379 (2016).
205. X. Zhang and Z. Liu: Superlenses to overcome the diffraction limit. *Nature* **435** (2008).
206. J. B. Pendry: Negative Refraction Makes a Perfect Lens. *Phys. Rev. Lett.* **85**(18), 3966 (2000).
207. A. R. Rashed, B. Gudulluoglu, H. W. Yun, M. Habib, I. H. Boyaci, S. H. Hong, E. Ozbay, and H. Caglayan: Highly-Sensitive Refractive Index Sensing by Near-infrared Metatronic Nanocircuits. *Sci. Rep.* **8**, 11457 (2018).
208. M. E. Nasir, W. Dickson, G. A. Wurtz, W. P. Wardley, and A. V. Zayats: Hydrogen detected by the naked eye: Optical hydrogen gas sensors based on core/shell plasmonic nanorod metamaterials. *Adv. Mater.* **26**(21), 3532 (2014).
209. J. Valentine, J. Li, T. Zentgraf, G. Bartal, and X. Zhang: An optical cloak made of dielectrics. *Nat. Mater.* **8**(7), 568 (2009).
210. H. Okamoto and T. B. Massalski: The Au-Zn (Gold-Zinc) system. *Bull. Alloy Phase Diagrams* **10**(1), 59 (1989).
211. S. I. Shah, K. C. Cadien, and J. E. Greene: GaSb-Ge pseudobinary phase diagram. *J. Electron. Mater.* **11**(1), 53 (1982).
212. J. Zhang, Z. Fan, Y. Q. Wang, and B. L. Zhou: Equilibrium pseudobinary Al - Mg<sub>2</sub>Si phase diagram. *Mater. Sci. Technol.* **17**(5), 494 (2001).
213. K. Nireekshan Reddy, P. Y. Chen, A. I. Fernández-Domínguez, and Y. Sivan: Revisiting the boundary conditions for second-harmonic generation at metal-dielectric interfaces. *J. Opt. Soc. Am. B* **34**(9), 1824 (2017).

214. L. Cao, N. C. Panoiu, and R. M. Osgood: Surface second-harmonic generation from surface plasmon waves scattered by metallic nanostructures. *Phys. Rev. B - Condens. Matter Mater. Phys.* **75**, 205401 (2007).
215. D. H. Kim, X. Y. Sun, N. M. Aimon, J. J. Kim, M. J. Campion, H. L. Tuller, L. Kornblum, F. J. Walker, C. H. Ahn, and C. A. Ross: A Three Component Self-Assembled Epitaxial Nanocomposite Thin Film. *Adv. Funct. Mater.* **25**, 3091 (2015).
216. H. Gómez and M. Olvera de la L: Ga-doped ZnO thin films: Effect of deposition temperature, dopant concentration, and vacuum-thermal treatment on the electrical, optical, structural and morphological properties. *Mater. Sci. Eng. B* **134**(1), 20 (2006).
217. J. Kim, M. C. Kim, J. Yu, and K. Park: H<sub>2</sub>/Ar and vacuum annealing effect of ZnO thin films deposited by RF magnetron sputtering system. *Curr. Appl. Phys.* **10**, S495 (2010).
218. M. Gillet, K. Aguir, C. Lemire, E. Gillet, and K. Schierbaum: The structure and electrical conductivity of vacuum-annealed WO<sub>3</sub> thin films. *Thin Solid Films* **467**(1–2), 239 (2004).
219. J. Ederth, A. Hultåker, G. A. Niklasson, P. Heszler, A. R. Van Doorn, M. J. Jongerius, D. Burgard, and C. G. Granqvist: Thin porous indium tin oxide nanoparticle films: Effects of annealing in vacuum and air. *Appl. Phys. A Mater. Sci. Process.* **81**(7), 1363 (2005).
220. Y. Wang, P. Miska, D. Pilloud, D. Horwat, F. Mücklich, and J. F. Pierson: Transmittance enhancement and optical band gap widening of Cu<sub>2</sub>O thin films after air annealing. *J. Appl. Phys.* **115**, 073505 (2014).
221. M. G. Sousa, A. F. Da Cunha, and P. A. Fernandes: Annealing of RF-magnetron sputtered SnS<sub>2</sub> precursors as a new route for single phase SnS thin films. *J. Alloys Compd.* **592**, 80 (2014).
222. R. D. Weir, P. E. Hessop, and B. K. Garside: Growth and annealing of AgInSe<sub>2</sub> thin films. *Can. J. Phys.* **65**, 1033 (1987).
223. Y. M. Cho, W. K. Choo, H. Kim, D. Kim, and Y. Ihm: Effects of rapid thermal annealing on the ferromagnetic properties of sputtered Zn<sub>1-x</sub>(Co<sub>0.5</sub>Fe<sub>0.5</sub>)<sub>x</sub>O thin films. *Appl. Phys. Lett.* **80**(18), 3358 (2002).
224. G. S. Babu, Y. B. K. Kumar, P. U. Bhaskar, and V. S. Raja: Effect of post-deposition annealing on the growth of Cu<sub>2</sub>ZnSnSe<sub>4</sub> thin films for a solar cell absorber layer. *Semicond. Sci. Technol.* **23**(8), 085023 (2008).

225. W. Prellier, M. Rajeswari, T. Venkatesan, and R. L. Greene: Effects of annealing and strain on  $\text{La}_{1-x}\text{Ca}_x\text{MnO}_3$  thin films: A phase diagram in the ferromagnetic region. *Appl. Phys. Lett.* **75**(10), 1446 (1999).
226. T. P. Chow, A. J. Steckl, and D. M. Brown: The effect of annealing on the properties of silicidized molybdenum thin films. *J. Appl. Phys.* **52**(10), 6331 (1981).
227. D. Zhang, Z. Qi, J. Jian, J. Huang, X. L. Phuah, X. Zhang, and H. Wang: Thermally Stable Au–BaTiO<sub>3</sub> Nanoscale Hybrid Metamaterial for High-Temperature Plasmonic Applications. *ACS Appl. Nano Mater.* **3**, 1431 (2020).
228. K. Kodera, I. Kusunoki, and S. Shimizu: Dissociation Pressures of Various Metallic Oxides. *Bull. Chem. Soc. Jpn.* **41**, 1039 (1968).
229. E. a. Secco: Decomposition of zinc oxide. *Can. J. Chem.* **38**, 596 (1960).
230. J. B. Wagner, P. L. Hansen, A. M. Molenbroek, H. Topsøe, B. S. Clausen, and S. Helveg: In situ electron energy loss spectroscopy studies of gas-dependent metal - Support interactions in Cu/ZnO catalysts. *J. Phys. Chem. B* **107**(31), 7753 (2003).
231. J. D. Grunwaldt, A. M. Molenbroek, N. Y. Topsøe, H. Topsøe, and B. S. Clausen: In situ investigations of structural changes in Cu/ZnO catalysts. *J. Catal.* **194**(2), 452 (2000).
232. Z. L. Wang: Zinc oxide nanostructures: Growth, properties and applications. *J. Phys. Condens. Matter* **16**(25), 829 (2004).
233. Y. K. Mishra, V. S. K. Chakravadhanula, V. Hrkac, S. Jebril, D. C. Agarwal, S. Mohapatra, D. K. Avasthi, L. Kienle, and R. Adelung: Crystal growth behaviour in Au-ZnO nanocomposite under different annealing environments and photoswitchability. *J. Appl. Phys.* **112**, 064308 (2012).
234. J. E. Wood, D. B. Williams, and J. I. Goldstein: Experimental and theoretical determination of k<sub>AF</sub>e factors for quantitative X-ray microanalysis in the analytical electron microscope. *J. Microsc.* **133**(3), 255 (1984).

## PUBLICATIONS

1. **S. Misra**, H. Wang, *submitted*
2. **S. Misra**, D. Zhang, J. Jian, H. Wang, *to be submitted*
3. **S. Misra**, D. Zhang, Z. Qi, D. Li, H.-T Chen, H. Wang, *accepted, Crystal Growth and Design* (2020)
4. **S. Misra**, L. Li, X. Gao, J. Jian, Z. Qi, D. Zemlyanov, H. Wang, *Nanoscale Advances*, 2, 315-322 (2020)
5. **S. Misra**, M. Kalaswad, D. Zhang, H. Wang, *Materials Research Letters*, 8, 321 (2020)
6. **S. Misra**, L. Li, D. Zhang, J. Jian, Z. Qi, M. Fan, H.-T. Chen, X. Zhang and H. Wang, *Advanced Materials*, 31(7), 1806529 (2019)
7. **S. Misra**, L. Li, J. Jian, J. Huang, X. Wang, D. Zemlyanov, J. Jang, F.H. Ribeiro and H. Wang, *ACS Applied Materials and Interfaces*, 10(6), 5779-5784 (2018)
8. B. Zhang, J. Huang, B. Rutherford, P. Lu, **S. Misra**, M. Kalaswad, Z. He, X. Gao, X. Sun, L. Li, H. Wang, *Materials Today Nano*, 11, 100083 (2020)
9. Z. Qi, J. Tang, **S. Misra**, C. Fan, P. Lu, J. Jian, Z. He, V. G. Pol, X. Zhang, H. Wang, *Nano Energy*, 69, 104381 (2020)
10. X.L. Phuah, H. Wang, Z. Qi, **S. Misra**, M. Kalaswad, H. Wang, *Journal of the American Ceramics Society*, 103, 2309-2314 (2020)
11. L. Li, J. Cheng, H. Wang, J. Huang, X. Gao, X. Wang, **S. Misra**, B. Zhang, J. Jian, A. Chen, P. Lu, X. Qian, K. Yang, H. Wang, *Crystal Growth and Design*, 19, 7088 (2019)
12. Y. Ji, Z. Qi, **S. Misra**, R. Jin, Y. Liu, X. Ou, Y. Lin, H. Yang, H. Wang, *ACS Applied Materials and Interfaces*, 11, 44905-44912 (2019)
13. D. Zhang, **S. Misra**, L. Li, X. Wang, X. Gao, X. Sun, J. Jian, P. Lu, Z. Qi, M. Kalaswad, X. Zhang, H. Wang, *Advanced Optical Materials*, 1901359 (2019)
14. J. Jian, X. Wang, **S. Misra**, X. Sun, Z. Qi, X. Gao, J. Sun, A. Donohue, D. G. Lin, V. Pol, J. Youngblood, H. Wang, L. Li, J. Huang and H. Wang, *Advanced Functional Materials*, 1903690 (2019)
15. B. Zhang, J. Huang, J. Jian, B. Rutherford, L. Li, **S. Misra**, X. Sun, H. Wang, *Nanoscale Advances*, 1 (11), 4450-4458 (2019).

16. L. Li, P. Boullay, J. Cheng, P. Lu , X. Wang, G. Steciuk, J. Huang, J. Jian, X. Gao, B. Zhang, **S. Misra**, X. Zhang, K. Yang and H. Wang, *Materials Today Nano*, 6, 100037 (2019)
17. J. Wu, B. Gautam, M.A. Sebastian, V. Ogunjimi, **S. Misra**, J. Huang, J. Baca, J. Prestigiacomo, T. Haugan, H. Wang and M. Osofsky, *IEEE Transactions on Applied Superconductivity*, 29(5), 1-5 (2019)
18. M. Parekh, V. Parikh, P. Kim, **S. Misra**, Z. Qi, H. Wang and V. Pol, *Carbon*, 148, 36-43 (2019)
19. R. Xu, Y. Ji, R. Bouchilaoun, F. Qian, M. Li, X. Zhang, R. Tang, R. Zhao, **S. Misra**, H. Wang, W. Li, C. Kan, D. Shi, J. Fan, H. Yang, *Ceramics International*, 45(9), 11304-11308 (2019)
20. B. Gautam, M.A. Sebastian, S. Chen, **S. Misra**, J. Huang, F.J. Baca, R. Emergo, T. Haugan, Z. Xing, H. Wang, and J.Z. Wu, *Applied Physics Letters*, 113(21), 212602 (2018)
21. J. Huang, T. Jin, **S. Misra**, H. Wang, Z. Qi, Y. Dai, X. Sun, L. Li, J. Okkema, H.-T. Chen, P.-T. Lin, X. Zhang, and H. Wang, *Advanced Optical Materials*, 6(19), 1800510 (2018)
22. M. Fan, H. Wang, **S. Misra**, B. Zhang, Z. Qi, X. Sun, J. Huang and H. Wang, *ACS Applied Materials and Interfaces*, 10(6), 5779-5784 (2018)
23. L. Li, P. Boullay, P. Lu, X. Wang, J. Jian, J. Huang, X. Gao, **S. Misra**, W. Zhang, O. Perez, G. Steciuk, A. Chen, X. Zhang and H. Wang, *Nano Letters*, 17(11), 6575-6582 (2017)
24. O.L. Sanchez, D. Ovchinnikov, **S. Misra**, A. Allain and A. Kis, *Nano Letters*, 16(9), 5792-5797 (2016)